

K_L^0 - p INTERACTIONS BETWEEN 1 AND 20 GEV/C

by

Robert Frederick Theodore Barrey

A thesis presented for the degree of
Doctor of Philosophy of the University of London

Department of Physics,
Imperial College of Science and Technology,
London, S.W.7.

September 1978

K_L^0 - p INTERACTIONS BETWEEN 1 AND 20 GEV/C

by

Robert Frederick Theodore Barrey

A thesis presented for the degree of
Doctor of Philosophy of the University of London

Department of Physics,
Imperial College of Science and Technology,
London, S.W.7.

September 1978

ABSTRACT

This thesis describes the data reduction and analysis of a 400,000 picture exposure of $K_L^0 p$ interactions between land 20 Gev/c K_L^0 momentum in the C.E.R.N. 2 metre Hydrogen Bubble Chamber. The work is mainly concerned with the reaction $K_L^0 p \rightarrow K_S^0 \pi^+ \pi^- p$, with a visible decay of the K_S^0 .

The derivation of the K_L^0 momentum spectrum by a Monte-Carlo simulation of the five main decay modes of K_L^0 is described and the resulting spectrum is displayed together with the spectrum obtained independently by our Cambridge Collaborators. The experimental $(p_0')^2$ distribution is shown and used in the determination of the $K_{3\pi}$ branching ratio. Mass distributions, Dalitz Plots, angular distributions and cross-sections are presented for the Q region of the $(K_S^0 \pi^+ \pi^-)$ mass spectrum. Comparisons are made between Q^0 and \bar{Q}^0 states facilitated by the equal components of K^0 and \bar{K}^0 in the K_L^0 beam. The variation of the Q mass and width with incident beam momentum is investigated utilizing the broad K_L^0 momentum spectrum. Exponential fits to the four-momentum transfer squared t' distributions are given and a crossover in analogy with elastic scattering is obtained with $\bar{Q}^0 p$ having a steeper slope than $Q^0 p$. The mass and momentum dependence of the slopes of the t' distributions is studied and the effect of angular selections on the sign of the crossover is elaborated.

CONTENTS

	page
Abstract	2
Contents	3
List of Tables	6
Figure Captions	8
The $K^0 - \bar{K}^0$ system	17
<u>Chapter 1:</u> Extraction of Data from the K_L^0 film	25
Introduction	25
1.1 The K_L^0 Beam Line	28
1.2 Film Scanning	30
1.3 Film Measuring and Processing	32
1.4 Hypotheses Choicing and D.S.T. Production	38
1.5 Scanning and measuring efficiency determination	41
1.6 Event losses and corrections	47
1.7 K_S^0 mean lifetime determination	49
<u>Chapter 2:</u> K_L^0 Beam Spectrum Determination	77
2.1 Introduction	77
2.2 Removal of Background Events	78
2.3 K_L^0 Decay Matrix Elements	80
2.4 Form Factors	81
2.5 Derivation of the K_L^0 momentum Spectrum	82
2.6 Combination of the Monte-Carlo distributions	84
2.7 Fitting the p_{VIS} distribution	85
2.8 Beam flux weighting	87

<u>Chapter 3:</u>	The $(p'_0)^2$ variable and the $K_{3\pi}$ Branching Ratio	98
3.1	Introduction	98
3.2	$K_{3\pi}$ Branching Ratio	99
<u>Chapter 4:</u>	A study of the Q Mass Region in $K_L^0 p \rightarrow K_S^0 \pi^+ \pi^- p$	102
4.1	Introduction	102
4.2	Data Combination	103
4.3	Structure of the Q Enhancement	105
4.4	Mass Spectra and Scatter Plots	109
4.5	Dalitz Plots	112
4.6	Fitting the Mass Spectra	113
4.7	Momentum Dependence of the Q Mass and Width	115
4.8	Cross Sections	116
<u>Chapter 5:</u>	Momentum transfer studies in $K_L^0 p \rightarrow K_S^0 \pi^+ \pi^- p$ (Theory)	157
5.1	Introduction	157
5.2	The Crossover Phenomenon	158
5.3	The Reggeized Deck Model	161
5.4	The K^* Exchange Graph	164
5.5	Different Secondary Exchanges in the Q crossover	167
<u>Chapter 6:</u>	Momentum transfer studies in $K_L^0 p \rightarrow K_S^0 \pi^+ \pi^- p$ (Experiment)	177
6.1	Introduction	177
6.2	Determination of the Slopes	179
6.3	Slopes of the t' distributions for Q^0 and \bar{Q}^0	181

6.4	Strength of the Regge Contribution in the Q region	183
6.5	Momentum Dependence of the Slopes	185
6.6	Mass Dependence of the Slopes	188
6.7	Selection on angles	189
6.8	Summary and Conclusions	193
	References	217
	Acknowledgements	221

List of Tables

Chapter 1

- 1.1 Number of bubble chamber pictures taken at each π^- beam momentum
- 1.2 Topology distribution for the 400 frame test scan
- 1.3 Topology distribution for the total sample of Film scanned by I.C. (PASS 1 and PASS 3 combined)
- 1.4 Number of fits to each channel
- 1.5 Scanning efficiency for fits in each topology
- 1.6a Scanning efficiencies from a comparison of frames
- 1.6b Scanning efficiencies from a comparison of events
- 1.7 The Topology distribution for the 624 frames of PASS 1 and the common frames of PASS 2, for unassociated K_L^0 decays
- 1.8 Measuring efficiencies for each topology

Chapter 2

- 2.1 The fitted Spectrum Coefficients
- 2.2 The K_L^0 Beam Spectrum Values

Chapter 4

- 4.1 The fit parameters of the $(K_S^0 \pi)$ mass distributions
- 4.2 Number of fits to $K_L^0 p \rightarrow K_S^0 \pi^+ \pi^- p$ from Cambridge and I.C. D.S.T.'s
- 4.3 Properties of the Q_1 and Q_2 mesons
- 4.4 Fits to the $(K_S^0 \pi^+ \pi^-)$ diffractive mass spectrum
- 4.5 Fits to the Q^0 and \bar{Q}^0 diffractive mass spectra
- 4.6 Fits to the $(K_S^0 \pi^+ \pi^-)$ diffractive mass spectrum for various beam momentum cuts
- 4.7 Cross-sections for $K_L^0 p \rightarrow K_S^0 \pi^+ \pi^- p$ and $K_L^0 p \rightarrow Qp$

Chapter 6

- 6.1 Numbers of events in $K_L^0 p \rightarrow Qp$
- 6.2 Slope and Intercept parameters for the total data
- 6.3 Momentum dependence of the slopes
- 6.4 Mass dependence of the slopes
- 6.5 Angular dependence of the slopes

Figure Captions

Chapter 1

- 1.1 The K_L^0 beam line in diagram form
- 1.2 Photograph of the K_L^0 beam line
- 1.3 Photograph looking along the π^- beam incident at the copper target
- 1.4 Photograph of the copper target used to produce K_L^0
- 1.5 Photograph of the copper target from a different perspective
- 1.6 The Data Reduction flowchart for the K_L^0 film
- 1.7 Helix fit and best mass fit residuals from tracks reconstructed by the 'HYDRA GEOMETRY' program
- 1.8 Target position distribution in the Y and Z axes
- 1.9 $M(p\pi^-)$ and $M(\pi^+\pi^-)$ effective mass distributions from Λ and K_S^0 decays using measured momenta
- 1.10 Stretch distributions in dip, and azimuth for beam tracks only, from 6C fits
- 1.11 Stretch distributions in dip, azimuth and momentum for non-beam tracks only, from 6C fits
- 1.12 Probability distributions for 3C and 6C fits
- 1.13 The D.S.T. (Data Summary Tape) production flowchart
- 1.14 The Scanning and measuring passes flowchart for the K_L^0 film
- 1.15a Venn overlap diagram for pass 1 and pass 3
- 1.15b Venn overlap diagram for pass 1, pass 2 and pass 3
- 1.16a Venn overlap diagram for pass 1 and pass 2, for unassociated K_L^0 decays
- 1.16b Venn overlap diagram for pass 1 and pass 2, for K_L^0 decays scanned as associated
- 1.17 Diagram illustrating loss of events around fiducial volume boundaries arising from the scanner's 'conical' field of view
- 1.18 Distribution of projected decay lengths for I.C. and Cambridge data, from 3C and 6C fits to $K_L^0 p \rightarrow K_S^0 \pi^+ \pi^- p$

- 1.19 Distribution of decay weights for I.C. and Cambridge data, from 3C and 6C fits to $K_L^0 \rightarrow K_S^0 \pi^+ \pi^-$
- 1.20 Proper lifetime distribution of $K_S^0 \rightarrow \pi^+ \pi^-$ decays. The curve is the distribution predicted from a maximum likelihood estimate of the mean K_S^0 lifetime, for events satisfying the fiducial volume and length cuts.

Chapter 2

- 2.1 $M(e^+ e^-)$, $M(\pi^+ \pi^-)$, $M(p \pi^-)$ and $M(p^- \pi^+)$ effective mass distributions, from Geometry Data of V^0 s
- 2.2 Transverse momentum distributions for charged and missing neutral tracks, and the opening angle distribution, from Geometry Data of V^0 s.
- 2.3 The experimental p_{VIS} and opening angle distributions from K_L^0 s that survive the cuts
- 2.4 Hypothetical K_L^0 momentum spectrum, illustrating the consecutive momentum intervals
- 2.5 The set of p_{VIS} distributions of the K_L^0 momentum components, which represent the K_L^0 spectrum. The numbers on the right hand side are the K_L^0 momentum intervals (in GeV/c) and the X axis is the P_{VIS} scale (in GeV/c)
- 2.6 K_L^0 momentum spectrum obtained by the Monte-Carlo simulation (Total flux = 9.89 K_L^0)
- 2.7 Cambridge (starred point) and I.C. (dotted point) K_L^0 spectra compared (Total flux = 9 K_L^0)

Chapter 3

- 3.1 The $(p'_0)^2$ distribution. The curve represents the fit to the $(p'_0)^2$ distribution from a Monte-Carlo simulation of the five main visible decay modes of K_L^0

Chapter 4

- 4.1 Four-momentum transfer squared and K_L^0 momentum comparison, for fits to $K_L^0 p \rightarrow K_S^0 \pi^+ \pi^- p$
- 4.2 Misidentified mass distributions of $(\pi^+ \pi^-)$ in $K_L^0 p \rightarrow K_S^0 \pi^+ \pi^- p$
- 4.3 Fits to the combined $M(K_S^0 \pi^+)$ and $M(K_S^0 \pi^-)$ mass distributions
- 4.4 Mass structures in $\pi \rightarrow (\pi\pi\pi)$ and $K \rightarrow (K\pi\pi)$ transitions
- 4.5 Quantum numbers of the Q_A and Q_B mesons
- 4.6 Present status of the $L=1$ meson multiplet
- 4.7 Production and Formation graphs
- 4.8 The Deck effect
- 4.9 The total diffractive graph expressed by Deck, rescattering and resonant terms
- 4.10 $M(K_S^0 \pi^+ \pi^-)$ distribution for the combined data sample. The shaded sub-histogram is for events with $M(p\pi^+) > 1.34$ Gev and $-t'_{pp} < 0.5$ Gev².
- 4.11 Scatter Plot of $M(K_S^0 \pi^+ \pi^-)$ against K_L^0 momentum
- 4.12 Scatter Plot of $-t_{pp}$ against $M(K_S^0 \pi^+ \pi^-)$
- 4.13 Scatter Plot of $M(p\pi^+)$ against $M(K_S^0 \pi^-)$
- 4.14 Scatter Plot of $M(p\pi^-)$ against $M(K_S^0 \pi^+)$
- 4.15 Scatter Plot of $M(p\pi^+ \pi^-)$ against $M(K_S^0 \pi^+)$
- 4.16 Scatter Plot of $M(p\pi^+)$ against K_L^0 momentum
- 4.17 $M(p\pi^+)$ distribution for $p_{K_L^0} < 8$ Gev/c and the $M(p\pi^+)$ distribution for $p_{K_L^0} > 8$ Gev/c
- 4.18 $M(K_S^0 \pi^+ \pi^-)$ distribution with diffractive cuts, and also $p_{K_L^0} > 6$ Gev/c
- 4.19 Scatter Plot of $M(K_S^0 \pi^+ \pi^-)$ against K_L^0 momentum for events satisfying the diffractive cuts ($M(p\pi^+) > 1.34$ Gev and $-t'_{pp} < 0.5$ Gev²). The arrows denote the mass interval 1.8 - 1.9 Gev

- 4.20 $M(K_S^0 \pi^+ \pi^-)$ distribution with the diffractive cuts.
The shaded sub-histogram is for events satisfying the additional cut $0.86 < M(K_S^0 \pi) < 0.92$ Gev.
- 4.21 $M(K_S^0 \pi^+ \pi^-)$ distribution with the diffractive cuts.
The shaded sub-histogram is for events satisfying the additional cut $0.72 < M(\pi^+ \pi^-) < 0.82$ Gev.
- 4.22 $M(K_S^0 \pi^+ \pi^-)$ distribution with the diffractive cuts.
The shaded sub-histogram is for events satisfying the additional cut $1.32 < M(K_S^0 \pi) < 1.52$ Gev.
- 4.23 - 4.28 Dalitz Plots and Projections for the region $1.1 < M(K_S^0 \pi^+ \pi^-) < 1.5$ Gev
- 4.23 $M^2(\pi^+ \pi^-)$ against $M^2(K_S^0 \pi^-)$
- 4.24 $M^2(\pi^+ \pi^-)$ against $M^2(K_S^0 \pi^+)$
- 4.25 $M^2(K_S^0 \pi^-)$ against $M^2(K_S^0 \pi^+)$
- 4.26 $M^2(K_S^0 \pi^-)$ projection
- 4.27 $M^2(K_S^0 \pi^+)$ projection
- 4.28 $M^2(\pi^+ \pi^-)$ projection
- 4.29 - 4.34 Dalitz Plots and Projections for the region $1.1 < M(K_S^0 \pi^+ \pi^-) < 1.5$ Gev, $M(p\pi^+) > 1.34$ Gev, $-t_{pp}^+ < 0.5$ Gev²
- 4.29 $M^2(\pi^+ \pi^-)$ against $M^2(K_S^0 \pi^-)$
- 4.30 $M^2(\pi^+ \pi^-)$ against $M^2(K_S^0 \pi^+)$
- 4.31 $M^2(K_S^0 \pi^-)$ against $M^2(K_S^0 \pi^+)$
- 4.32 $M^2(K_S^0 \pi^-)$ projection
- 4.33 $M^2(K_S^0 \pi^+)$ projection
- 4.34 $M^2(\pi^+ \pi^-)$ projection

- 4.35 - 4.40 Dalitz Plots and Projections for the region
 $1.5 < M(K_S^0 \pi^+ \pi^-) < 2.0 \text{ GeV}$, $M(p\pi^+) > 1.34 \text{ GeV}$, $-t'_{pp} < 0.5 \text{ GeV}^2$.
- 4.35 $M^2(\pi^+ \pi^-)$ against $M^2(K_S^0 \pi^-)$
- 4.36 $M^2(\pi^+ \pi^-)$ against $M^2(K_S^0 \pi^+)$
- 4.37 $M^2(K_S^0 \pi^-)$ against $M^2(K_S^0 \pi^+)$
- 4.38 $M^2(K_S^0 \pi^-)$ projection
- 4.39 $M^2(K_S^0 \pi^+)$ projection
- 4.40 $M^2(\pi^+ \pi^-)$ projection
- 4.41 Fits to the mass distributions of figure (4.18)
- 4.42 Fits to the mass spectra for \bar{Q}^0 and Q^0
- 4.43 The ratio of $K^{*+} \pi^-$ to $K^{*-} \pi^+$ events as a function of $K^* \pi$ mass
- 4.44a) Fits to the $(K_S^0 \pi^+ \pi^-)$ diffractive mass spectrum for $p_{K_L^0} < 6 \text{ GeV}/c$
- b) Fits to the $(K_S^0 \pi^+ \pi^-)$ diffractive mass spectrum for $6 < p_{K_L^0} < 10 \text{ GeV}/c$
- c) Fits to the $(K_S^0 \pi^+ \pi^-)$ diffractive mass spectrum for $10 < p_{K_L^0} < 17 \text{ GeV}/c$
- 4.45a) Variation in the width of the Q enhancement with beam momentum (Non-Relativistic Breit-Wigner)
- b) Variation in the width of the Q enhancement with beam momentum (Relativistic Breit-Wigner)
- 4.46 Cross-section for $K_L^0 p \rightarrow K_S^0 \pi^+ \pi^- p$ by I.C.(dotted point) and by S.L.A.C.(starred point)
- 4.47 Cross-section for $K_L^0 p \rightarrow Q p$ (starred point) and for $K_L^0 p \rightarrow K_S^0 \pi^+ \pi^- p$ (dotted point)
- 4.48 Ratio $\sigma(K_L^0 p \rightarrow Q^0 p) / \sigma(K_L^0 p \rightarrow \bar{Q}^0 p)$ as a function of beam momentum

Chapter 5

- 5.1 Differential cross-sections for $K^\pm p$ elastic scattering at 13 GeV/c
- 5.2 Differential cross-sections for $\pi^\pm p \rightarrow (\pi^\pm \pi^+ \pi^-) p$ at 16 GeV/c

- 5.3 Differential cross-sections for $K^0 p \rightarrow Q^0 p$ (squares) and $\bar{K}^0 p \rightarrow \bar{Q}^0 p$ (circles) over the momentum range 4 to 12 Gev/c. The curves are from the following exponential fits:

$$\frac{d\sigma}{dt'}(Q^0 p) = 0.83 \exp(5.9t') \text{ mb/GeV}^2$$

$$\frac{d\sigma}{dt'}(\bar{Q}^0 p) = 1.36 \exp(9.7t') \text{ mb/GeV}^2$$

- 5.4 Differential cross-section for $K^\pm p \rightarrow Q^\pm p$ at 14 Gev/c
- 5.5 Diagram illustrating the kinematic variables for the process $ap \rightarrow a^* \pi N$
- 5.6 The Deck pion exchange graphs for $K^0 p \rightarrow K^{*+} \pi^- p$ and $\bar{K}^0 p \rightarrow K^{*-} \pi^+ p$. The ovals represent $\pi^- p$ and $\pi^+ p$ elastic scattering.
- 5.7 The Deck K^* exchange graphs for $K^0 p \rightarrow K^{*+} \pi^- p$ and $\bar{K}^0 p \rightarrow K^{*-} \pi^+ p$. The ovals represent $K^{*+} p$ and $K^{*-} p$ elastic scattering.
- 5.8 Slopes b for the differential cross-section $d\sigma/dt' = ce^{-bt'}$ obtained from Berger's Reggeized Deck model calculations as a function of beam momentum. The slope b^- is for $K^0 p \rightarrow K^{*+}(890)\pi^- p$ and the slope b^+ is for $\bar{K}^0 p \rightarrow K^{*-}(890)\pi^+ p$. In a) and b) the $K^* \pi$ mass is less than 1.5 Gev with the additional restriction in b) that $M(p\pi^+)$ is greater than 1.34 Gev. The slopes are fitted in the interval $0.02 < |t'| < 0.5 \text{ Gev}^2$
- 5.9 Diagram in which the s-channel decay angles (ϕ_s, θ_s) , in the $K^* \pi$ rest frame, are defined.
- 5.10 The Deck pion and baryon exchange graphs for $\pi^\pm p \rightarrow \pi^\pm (\pi^- \Delta^{++})$
- 5.11 The B and ω exchange graphs added to the pion exchange graphs.
- 5.12 The quark duality diagrams for $K^0 p \rightarrow K^{*+} \pi^- p$ and for $\bar{K}^0 p \rightarrow K^{*-} \pi^+ p$.

Chapter 6

- 6.1 $M(K_s^0 \pi^+)$ and $M(K_s^0 \pi^-)$ distributions
- 6.2 $M(K_s^0 \pi^+)$ and $M(K_s^0 \pi^-)$ distributions with the opposing $K^*(890)$ reflection removed.

- 6.3 Four-momentum transfer squared distribution, dN/dt' , for $K^0 p \rightarrow Q^0 p$ (circles) and $\bar{K}^0 p \rightarrow \bar{Q}^0 p$ (stars) over the momentum range 2.0 to 17 Gev/c. The curves result from the exponential fits.

$$\frac{dN}{dt'}(Q^0 p) = 942 \exp(5.56t') \text{ Events/GeV}^2$$

$$\frac{dN}{dt'}(\bar{Q}^0 p) = 1510 \exp(8.93t') \text{ Events/GeV}^2$$

- 6.4 Four-momentum transfer squared distribution dN/dt' , for $K^0 p \rightarrow Q^0 p$ (circles) and $\bar{K}^0 p \rightarrow \bar{Q}^0 p$ (stars) over the momentum range 2.0 to 17 Gev/c, with the opposing $K^*(890)$ reflection removed. The curves result from the exponential fits

$$\frac{dN}{dt'}(Q^0 p) = 700 \exp(5.0t') \text{ Events/GeV}^2$$

$$\frac{dN}{dt'}(\bar{Q}^0 p) = 1241 \exp(8.99t') \text{ Events/GeV}^2$$

- 6.5 Four-momentum transfer squared distribution, dN/dt' , for $K^0 p \rightarrow K^{*+} \pi^- p$ (Circles) and $\bar{K}^0 p \rightarrow K^{*-} \pi^+ p$ (Stars), with no Δ^{++} removal. The curves result from the exponential fits

$$\frac{dN}{dt'}(K^{*+} \pi^- p) = 1247 \exp(5.25t')$$

$$\frac{dN}{dt'}(K^{*-} \pi^+ p) = 1737 \exp(6.67t')$$

- 6.6 Momentum dependence of the slopes for $K^0 p \rightarrow Q^0 p$ (dotted point) and for $\bar{K}^0 p \rightarrow \bar{Q}^0 p$ (starred point). The average values over the whole momentum interval are shown as dashed lines and are $5.56 \pm 0.71 \text{ Gev}^{-2}$ and $8.93 \pm 0.88 \text{ Gev}^{-2}$ for $Q^0 p$ and $\bar{Q}^0 p$ respectively.

- 6.7 Momentum dependence of the slopes for $K^0 p \rightarrow K^{*+} \pi^- p$ (dotted point) and for $\bar{K}^0 p \rightarrow K^{*-} \pi^+ p$ (starred point), with no Δ^{++} removal. The average values over the whole momentum interval are shown as dashed lines and are $5.25 \pm 0.59 \text{ Gev}^{-2}$ and $6.67 \pm 0.60 \text{ Gev}^{-2}$ for $K^{*+} \pi^- p$ and $K^{*-} \pi^+ p$ respectively

- 6.8 Momentum dependence of the slopes for $K^0 p \rightarrow Q^0 p$ (dotted point) and for $\bar{K}^0 p \rightarrow \bar{Q}^0 p$ (starred point), with the opposing $K^*(890)$ reflection removed. The average values over the whole momentum interval are shown as dashed lines and are $5.0 \pm 0.77 \text{ Gev}^{-2}$ and $8.99 \pm 0.98 \text{ Gev}^{-2}$ for $Q^0 p$ and $\bar{Q}^0 p$ respectively.
- 6.9 Momentum dependence of the slopes for $K^0 p \rightarrow K^{*+} \pi^- p$ (dotted point) and for $\bar{K}^0 p \rightarrow K^{*-} \pi^+ p$ (starred point) with no Δ^{++} removal and the opposing $K^*(890)$ removed. The average values over the whole momentum interval are shown as dashed lines and are $4.82 \pm 0.67 \text{ Gev}^{-2}$ and $6.66 \pm 0.68 \text{ Gev}^{-2}$ for $K^{*+} \pi^- p$ and $K^{*-} \pi^+ p$ respectively.
- 6.10 Variation of the slopes with $M(K^*\pi)$ for $K^0 p \rightarrow K^{*+} \pi^- p$ (squares) and for $\bar{K}^0 p \rightarrow K^{*-} \pi^+ p$ (circles) averaged over the interval $4 < p_{\text{BEAM}} < 12 \text{ Gev}/c$. (S.L.A.C. K_L^0 data)
- 6.11 Mass dependence of the slopes for $K^- p \rightarrow K^- \pi^+ \pi^- p$ (white circles) and for $K^- p \rightarrow \bar{K}^0 \pi^- \pi^0 p$ (black circles) from $14 \text{ Gev}/c$ to $K^- p$.
- 6.12 Variation of the slopes with $M(K^*\pi)$ for $K^0 p \rightarrow K^{*+} \pi^- p$ (dotted point) and for $\bar{K}^0 p \rightarrow K^{*-} \pi^+ p$ (starred point) averaged between threshold and $17 \text{ Gev}/c$.
- 6.13 Variation of the slopes with $M(K^*\pi)$ for $K^0 p \rightarrow K^{*+} \pi^- p$ (dotted point) and for $\bar{K}^0 p \rightarrow K^{*-} \pi^+ p$ (starred point) with the opposing $K^*(890)$ removed, averaged between threshold and $17 \text{ Gev}/c$.
- 6.14 The ϕ_s angular distributions for $Q^0 \rightarrow K^{*+} \pi^-$ and for $\bar{Q}^0 \rightarrow K^{*-} \pi^+$.
- 6.15 Four-momentum transfer squared distribution, dN/dt' , for $K^0 p \rightarrow Q^0 p$ (circles) and $\bar{K}^0 p \rightarrow \bar{Q}^0 p$ (stars), for the regions $\cos \phi_s > 0$ and $\cos \phi_s < 0$ averaged between threshold and $17 \text{ Gev}/c$. The curves result from the exponential fits

$$\cos \phi_s > 0 \left\{ \begin{array}{l} \frac{dN}{dt'}(Q^0 p) = 464 \exp(5.39t') \text{ Events/GeV}^2 \\ \frac{dN}{dt'}(\bar{Q}^0 p) = 733 \exp(8.36t') \text{ Events/GeV}^2 \end{array} \right.$$

6.15 (contd)

$$\cos\phi_s < 0 \left\{ \begin{array}{l} \frac{dN}{dt} (Q^0 p) = 478 \exp(5.74t) \text{ Events/GeV}^2 \\ \frac{dN}{dt} (\bar{Q}^0 p) = 783 \exp(9.6t) \text{ Events/GeV}^2 \end{array} \right.$$

6.16 a) The two-dimensional decay phase space plot of $Q \rightarrow K^*\pi$ in terms of the s-channel decay angles (θ_s, ϕ_s) defined in figure (5.9). At high energies the π and K^* exchange graphs are concentrated in the corners shown in the diagram.

6.16 b) The two-dimensional decay phase space plot of $Q \rightarrow K^*\pi$ in terms of the t-channel decay angles (θ_t, ϕ_t) defined in figure (6.18). At high energies the π and K^* exchange graphs are concentrated in the corners shown in the diagram.

6.17 Scatter plot of $\cos\theta_s$ against ϕ_s for Q^0 and \bar{Q}^0

6.18 Diagram in which the t-channel decay angles (ϕ_t, θ_t) , in the $K^*\pi$ rest frame, are defined.

6.19 Scatter plot of $\cos\theta_t$ against ϕ_t for Q^0 and \bar{Q}^0

6.20 The ϕ_t angular distributions for $Q^0 \rightarrow K^{*+}\pi^-$ and for $\bar{Q}^0 \rightarrow K^{*-}\pi^+$

6.21 Numbers of events in the pion and K^* exchange corners of the $\cos\theta_s - \phi_s$ plot as a function of beam momentum

6.22 Numbers of events in the pion and K^* exchange corners of the $\cos\theta_t - \phi_t$ plot as a function of beam momentum

The $K^0 - \bar{K}^0$ system

As a consequence of the strangeness scheme of Gell-Mann and Nishijima, the K mesons can be classified into two isospin doublets as in figure (1), with K^- the antiparticle of K^+ and \bar{K}^0 the antiparticle of K^0 . K^0 and \bar{K}^0 were historically observed by their decay modes into 2π and 3π states (as well as into semileptonic channels),

$$\begin{array}{ll}
 K^0 \rightarrow \pi^0 \pi^0 & \bar{K}^0 \rightarrow \pi^0 \pi^0 \\
 K^0 \rightarrow \pi^+ \pi^- & \bar{K}^0 \rightarrow \pi^+ \pi^- \\
 K^0 \rightarrow \pi^0 \pi^0 \pi^0 & \bar{K}^0 \rightarrow \pi^0 \pi^0 \pi^0 \\
 K^0 \rightarrow \pi^+ \pi^- \pi^0 & \bar{K}^0 \rightarrow \pi^+ \pi^- \pi^0
 \end{array} \quad (1)$$

although the observation of these decays cannot by itself distinguish between K^0 and \bar{K}^0 . From a consideration of these decays of K^0 and \bar{K}^0 , Gell-Mann and Pais ⁽¹⁾ suggested that the K^0 and \bar{K}^0 mesons could be regarded as mixtures of systems with eigenstates of ± 1 under the 'CP' operation, where C is the charge conjugation operator and 'P' is the parity operator, with the eigenvalue of the CP operation ⁽²⁾ being conserved in weak decays ⁽³⁾. These eigenstates of CP called K_1^0 and K_2^0 are a linear superposition of the states K^0 and \bar{K}^0 and have CP eigenvalues of +1 and -1 respectively.

$$|K_1^0\rangle = \frac{1}{\sqrt{2}} \{ |K^0\rangle + |\bar{K}^0\rangle \} \quad \text{and} \quad |K_2^0\rangle = \frac{1}{\sqrt{2}} \{ |K^0\rangle - |\bar{K}^0\rangle \} \quad (2)$$

$$\text{CP} |K_1^0\rangle = |K_1^0\rangle \quad \text{CP} |K_2^0\rangle = -|K_2^0\rangle \quad (3)$$

The 2π and 3π decay products can also be shown to be eigenstates of CP with eigenvalues +1 and -1 respectively ⁽⁴⁾, so that although the base states K^0 and \bar{K}^0 cannot be distinguished by these decay modes, the CP eigenstates K_1^0 and K_2^0 can be, with K_1^0 decaying to the 2π state and K_2^0

to the 3π state. Because of the greater amount of phase space available in $K_1^0 \rightarrow 2\pi$ decays compared with $K_2^0 \rightarrow 3\pi$, the lifetime of the K_1^0 state is shorter than K_2 decays, with $\tau_1 = 0.89 \times 10^{-10}$ secs and $\tau_2 = 0.52 \times 10^{-7}$ secs.

Apart from being simply CP eigenstates, the origin of the K_1^0 and K_2^0 states arises out of the unique nature and properties of the $K^0-\bar{K}^0$ system. As the decay products of K^0 and \bar{K}^0 in (1) are identical, weak strangeness changing interactions can cause transitions to occur between K^0 and \bar{K}^0 and vice-versa, figure (2). This phenomenon is unknown for any other system in particle physics since charge or baryon conservation laws forbid otherwise possible transitions. Thus an initially pure state of K^0 will contain some \bar{K}^0 after a certain time 't' as a result of these $\Delta S = 2$ weak interactions connecting the opposite strangeness states. The time dependence of this system is governed by Schrödinger's equation

$$i\hbar \frac{\partial}{\partial t} |\psi\rangle = \hat{H}|\psi\rangle \quad (4)$$

where $|\psi\rangle$ is the overall wavefunction. Applied to $K^0-\bar{K}^0$, equation (4) takes the form (5)

$$i\hbar \frac{d}{dt} \begin{pmatrix} K^0 \\ \bar{K}^0 \end{pmatrix} = \begin{pmatrix} H_{11} & H_{12} \\ H_{21} & H_{22} \end{pmatrix} \begin{pmatrix} K^0 \\ \bar{K}^0 \end{pmatrix} \quad (5)$$

where the matrix in equation (5), known as the 'mass matrix' contains the terms ' H_{11} ', ' H_{22} ' identified with the mass of the K^0 and \bar{K}^0 , and the off-diagonal terms ' H_{12} ', ' H_{21} ' represent the transitions between the K^0 and \bar{K}^0 base states. As a solution to equation (5) the K^0 and \bar{K}^0 states 'oscillate' (6) in intensity with a frequency dependent upon the coupling strength between the two base states. The overall behaviour of the system is analogous to that of the NH_3 molecule (7) which can

have two possible configurations as in figure (2), rotating about the axis which passes through the middle of the plane and the nitrogen atom (ignoring other degrees of freedom). Quantum mechanical tunnelling causes transitions to occur between the two states $|1\rangle$ and $|2\rangle$ of the NH_3 molecule resulting in a similar oscillatory behaviour of the two configurations. Although the base states for the two different systems are continuously varying with time, a linear superposition of the base states is 'stationary' and therefore time independent. This linear superposition is,

$$6 \text{ a) } \quad \frac{1}{\sqrt{2}} (|1\rangle + |2\rangle) \quad \text{and} \quad \frac{1}{\sqrt{2}} (|1\rangle - |2\rangle) \quad \text{for } \text{NH}_3$$

$$6 \text{ b) } \quad \frac{1}{\sqrt{2}} (|K^0\rangle + |\bar{K}^0\rangle) \quad \text{and} \quad \frac{1}{\sqrt{2}} (|K^0\rangle - |\bar{K}^0\rangle) \quad \text{for } K^0 - \bar{K}^0$$

where the states in 6b) are identified with K_1^0 and K_2^0 . The frequency of the strangeness oscillation is determined by the minute mass difference between the K_1^0 and K_2^0 states ($\Delta m = 0.5349 \times 10^{10} \hbar \text{ sec}^{-1}$), which is typically the order of the uncertainty in the K_1^0 mass given by the uncertainty principle, where

$$\delta m \approx \frac{\hbar}{\tau_1} = 1.12 \times 10^{10} \hbar \text{ sec}^{-1} \approx 10^{-11} \text{ Mev}$$

This oscillation of the two base states together with the large difference in lifetimes between K_1^0 and K_2^0 causes a separation in both time and space of K_1^0 and K_2^0 decays. As a consequence, a strangeness state that is not originally present can be built up in time. This can be illustrated by considering the time development of an initial source

of K^0 , produced for example in associated production,



Inverting equations (2), the K^0 and \bar{K}^0 states can be expressed in terms of the stationary states K_1^0 and K_2^0 as

$$|K^0\rangle = \frac{1}{\sqrt{2}} \{ |K_1^0\rangle + |K_2^0\rangle \}$$

$$|\bar{K}^0\rangle = \frac{1}{\sqrt{2}} \{ |K_1^0\rangle - |K_2^0\rangle \}$$
(8)

If the terms in the brackets of equation (8) are replaced by their full time-dependent wave function taking into account losses from decays of K_1^0 and K_2^0 , then on taking the modulus squared of each amplitude, the intensities of K^0 and \bar{K}^0 after a proper time interval t are,

$$I(K^0) = \frac{1}{4} \left\{ e^{-t/\tau_1} + e^{-t/\tau_2} + 2e^{-(t/2\tau_1 + t/2\tau_2)} \cos\Delta mt \right\}$$

$$I(\bar{K}^0) = \frac{1}{4} \left\{ e^{-t/\tau_1} + e^{-t/\tau_2} - 2e^{-(t/2\tau_1 + t/2\tau_2)} \cos\Delta mt \right\}$$
(9)

This variation in K^0 and \bar{K}^0 intensity with time from equations (9) is shown in figure (3), where the modulation of the intensity distributions caused by the 'cos Δmt ' term is evident after a few K_1^0 lifetimes, together with the production of the opposite strangeness \bar{K}^0 state from an originally pure K^0 beam. After a time $t > 10\tau_1$ such that all the K_1^0 (or short lived K_S^0) component of the K^0 beam has decayed away, equal amounts of K^0 and \bar{K}^0 are left which in turn comprise

the remaining K_2^0 (or long lived K_L^0) component of the initially pure K^0 beam.

Two important features of the remaining K_L^0 component emerge from this brief résumé of the $K^0 - \bar{K}^0$ system. As the K_L^0 beam contains equal amounts of K^0 and \bar{K}^0 , two opposite strangeness reactions can take place within one experiment, so that the K_L^0 beam is particularly suitable for relative comparisons between opposite strangeness states that would otherwise require two separate experiments using charged kaon beams. K_L^0 is also an eigenstate of CP and hence in strong interactions of C with opposite sign to that of K_S^0 , facilitating the study of important reactions such as $K_L^0 p \rightarrow K_S^0 p$ where the change in C parity at the $K_L^0 - K_S^0$ vertex constrains the quantum number of the exchanged particle to $C = -1$. K_L^0 can therefore be used as a probe of C parity in studying reaction mechanisms.

References

- 1 M.Gell-Mann and A.Pais. Phys. Rev. 97, 1387, (1955)
- 2 The original argument was made using charge conjugation but subsequently changed to CP following the discovery of parity violation in weak interactions.
- 3 Ignoring the very small level of CP violation found in weak decays.
- 4 D.H.Perkins, Introduction to High Energy Physics, (Addison-Wesley Publishing Company, 1972), page 171.
- 5 G.Charpak and M.Gourdin, the $K^0 - \bar{K}^0$ system, C.E.R.N. Yellow Report, 67-18, (1967)
- 6 J.C.Sens, Quantum Mechanics of the System of Neutral Kaons, C.E.R.N. Report, 66-1087, (1966)
- 7 R.P.Feynmann, Lecture on Physics, (Addison-Wesley Publishing Co.1966), Vol III, page 8-11.

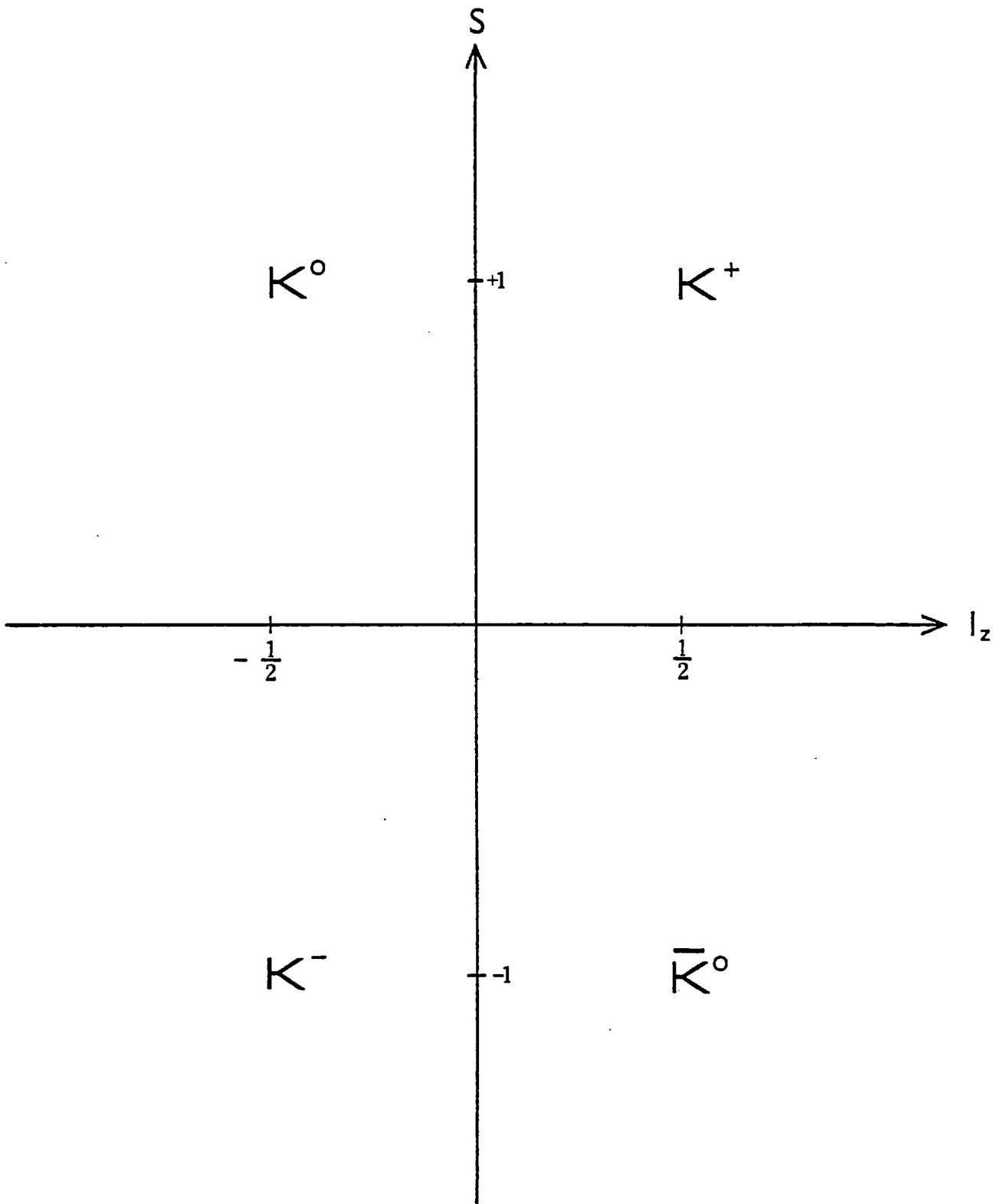
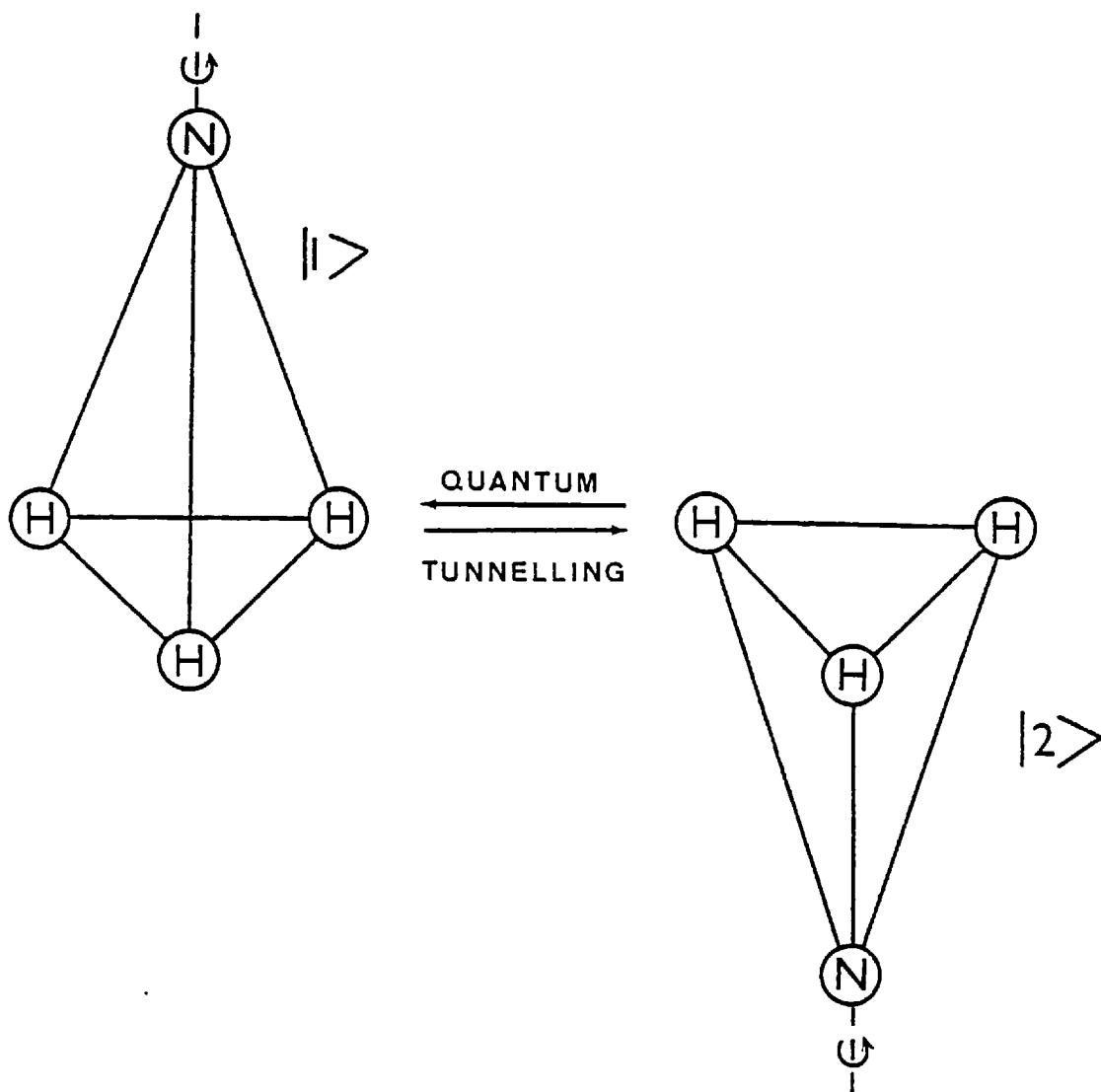


FIG.1



WEAK INTERACTION

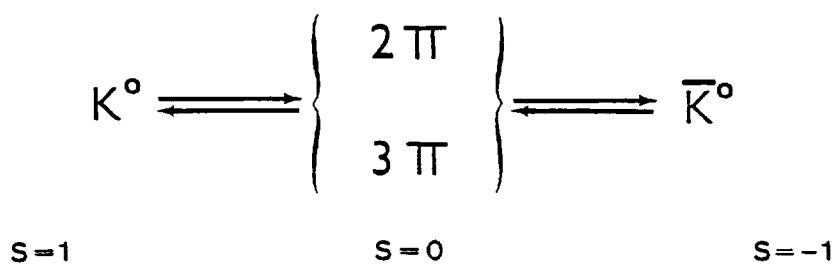
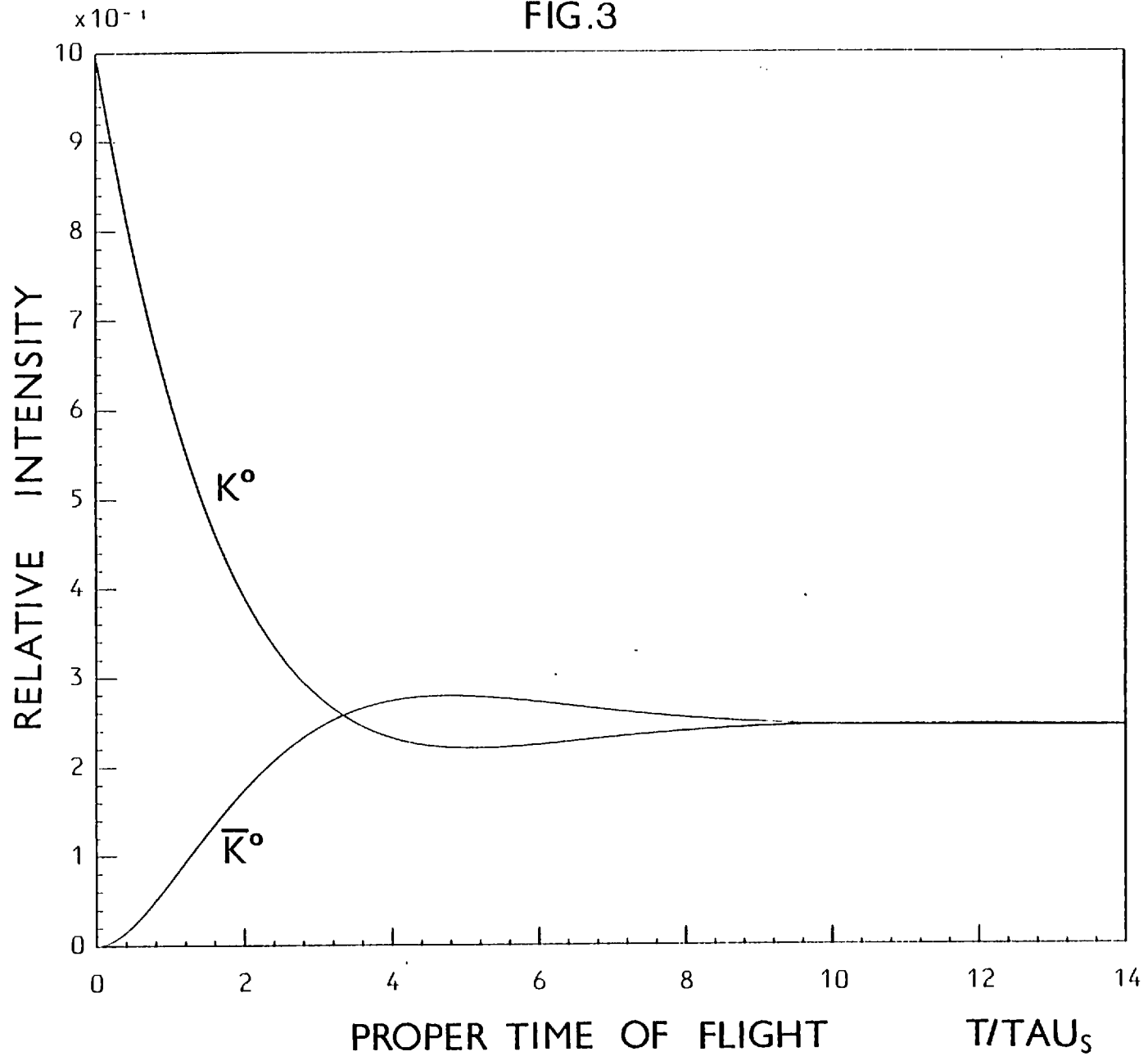


FIG.2

FIG.3



CHAPTER 1

Extraction of Data from the K_L^0 film

Introduction

Despite the several advantages that a K_L^0 beam offers as a probe of strong interactions, $K_L^0 p$ interactions remain a relatively unexplored area, as much effort has been expended on the equivalent charged Kaon beam experiments where the experimental problems associated with a neutral Kaon beam such as low particle fluxes and neutron background are avoided.

Counter experiments using K_L^0 beams have concentrated on high statistics measurement of forward differential cross-sections and regeneration amplitudes, whereas Bubble Chamber experiments have used their inherent 4π solid angle detection capability in the study of multi-body final states and measuring cross-sections over the range of 't' for elastic and inelastic channels. Previous experiments using a K_L^0 beam in conjunction with a Hydrogen Bubble Chamber have taken place at S.L.A.C. for K_L^0 momenta between 1 - 12 Gev/c and at D.E.S.Y. between 0.7 - 3.0 Gev/c, where in both experiments the K_L^0 has been produced by an electron beam hitting a metal target.

Current Physics interest in Kp strong interactions, centres around the study of the $K\pi\pi$ mass enhancement seen in the region $1.1 < M(K\pi\pi) < 1.5$ Gev and referred to as the 'Q'. Considerable effort has been expended to show whether the 'Q' is single, resonant, or a kinematic enhancement, culminating in evidence for the existence of two strangeness-one axial vector mesons from a partial wave analysis of high statistics data in $K^\pm p \rightarrow K^\pm \pi^+ \pi^- p$ at 13 Gev/c.

This has important consequences for the quark model of mesons where the Q is a possible candidate for the incomplete 1^+ nonet. An indirect but important guide to the nature of the Q enhancement comes from the observation of a 'crossover' in the differential cross-sections in $K_L^0 p \rightarrow Qp$ first seen in the S.L.A.C. K_L^0 experiment. It has become apparent that if the kinematic enhancement model of Q production is to be a viable alternative to a 'resonant' interpretation, then the sign of the crossover should be opposite to what is experimentally seen. Recent theoretical predictions have also been made on the basis of the 'Deck' or kinematic enhancement model and show that the sign of the crossover may depend upon angular selections done in the Q rest frame. In the light of these considerations and the interesting S.L.A.C. results which left some questions unanswered, particularly over the removal of background events and the effect of angular selections on the data, a collaboration was set up between Imperial College and Cambridge University Bubble Chamber Groups to propose a K_L^0 experiment that would be a natural extension of the S.L.A.C. experiment to a higher K_L^0 momentum of 20 GeV/c. A formal proposal describing the Physics case for the experiment was forwarded to the C.E.R.N. Track Chamber Committee and a 400,000 picture exposure was approved for film taking in March 1974.

The author joined the Imperial College Bubble Chamber Group in October 1973 and was present at the K_L^0 Beam Run in C.E.R.N. Apart from some initial help in setting up the data reduction programs and in the determination of the scanning efficiencies, the author was responsible for all aspects of the experiment. This thesis which is based on the author's research work in the department, is constructed as follows.

Chapter 1. Describes the data reduction program chain and the extraction of Physics data from the Bubble Chamber film.

Chapter 2. Explains how the K_L^0 momentum spectrum is obtained from the decays of K_L^0 beam particles.

Chapter 3. Shows how the information present in these beam decays is used to obtain a value of the $K_{3\pi}$ branching ratio.

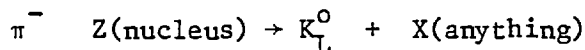
Chapter 4. Presents the experimental $(K_S^0 \pi^+ \pi^-)$ mass distributions for various cuts and the fits to the $(K_S^0 \pi^+ \pi^-)$ mass spectra.

Chapter 5. Gives a full account of the crossover predictions based on the Deck model, and selections on decay angles in the rest frame of the Q are discussed as a method of isolating specific exchanges.

Chapter 6. Exponential fits to the four momentum transfer squared distributions are presented and the crossovers obtained compared with the theoretical predictions.

1.1 The K_L^0 Beam Line

The K_L^0 beam line is shown in diagram form in figure (1.1) and by photograph in figure (1.2). An unseparated π^- beam of about 1.3×10^5 particles, produced from a burst of 1×10^{11} 26 Gev/c protons from the P.S. incident on a copper target, was transported along the U5 beam line to a (10 x 20 x 150 mm) copper target, figures (1.3-1.5), situated 15 metres from the 2m. H.B.C. centre and aligned on the chamber axis. Production of K_L^0 can be represented as



The flux of π^- estimated from scintillator activation techniques was lower than expected ($1.5 \times 10^6 \pi^-$), however the K_L^0/π^- ratio (0.7×10^{-4}) appears to be roughly as predicted. In order to obtain a hard K_L^0 momentum spectrum, previous experimental data on inclusive K^0 production⁽¹⁾ had shown the importance of using as small an angle between the π^- and K^0 beam as possible. This requirement meant that any gamma ray background from electrons in the negative beam was directed towards the 2 metre chamber. The K_L^0 beam line therefore had to be designed so that any tracks in the chamber produced by such beam contamination were reduced as far as possible, facilitating easy scanning and measuring of events.

Charged particles from interactions in the copper target and decays of the incident π^- beam were removed by a collimator and three vertical 2metre bending magnets with centres 13.5, 10.5 and 7 metres from the 2metre chamber centre figure (1.1). Gamma rays produced by bremsstrahlung of e^- beam impurity in the target and from π^0 decay were removed by a photon filter consisting of 5 cms of lead placed at the entrance of the third sweeping magnet nearest the chamber, so that any charged secondaries

produced in the photon filter would also be swept away. The thickness of lead was kept at a minimum, consistent with scannable pictures, to reduce the proportion of K_L^0 scattered in the filter. Lead shielding of length 1500 mm and with aperture 100 x 200 mm was mounted on the axis between the final bending magnet and the bubble chamber yoke, so as to obscure any part of the chamber not obscured by the yoke.

A total of 400,000 pictures were taken with incident π^- beam momentum as given in table (1.1), and were divided equally between Cambridge and Imperial College Bubble Chamber Groups.

1.2 Film Scanning

As the K_L^0 beam is not charged, particle interactions in the bubble chamber have no visible beam track and an odd number of charged secondary tracks. Two prong events can be decays of locally produced K_S^0 or Λ , K_L^0 beam decays or e^+e^- pairs from gamma contamination in the beam.

In order to establish a priority for the scanning and measuring of bubble chamber events, the Imperial College film sample was first subjected to a preliminary scan of 400 frames, which yielded the topology distribution in table (1.2), where an event with 'I' charged outgoing tracks from the production vertex, 'J' charged decays and 'K' neutral decays is assigned the topology 'IJK'. It is apparent that the '300' class topology events are a high proportion (69%) of the total. After geometrical reconstruction and kinematic fitting of an initial sample, it was found that over half of the '300' interactions gave fits to the channel $n\bar{p} \rightarrow p\bar{p}\pi^-$, the remainder giving fits to the channel $K_L^0 p \rightarrow K^+ p\pi^+$, with a large fraction of events ambiguous between these two reactions. Scanning has therefore been restricted to events where a V^0 association could be made such as '301' and '501' topologies where the background problems are less severe. Wherever possible a V^0 was associated with a production vertex and measured. Unassociated or 'free' V^0 's such as beam decays were also recorded and measured, for future use in beam flux determination. Secondary interactions were only included if they were elastic, ie. two pronged, and the sagitta of the connecting track was less than 2 mm on the scan table. To help distinguish between obvious e^+e^- pairs and V^0 's, a simple 'template' was constructed, the arms having radii of curvature 315 mms corresponding to a muon track having 1.5 [150 Mev/c] times minimum ionization, this being the lowest ionization which could

be properly distinguished from minimum by the scanners. For an associated V^0 to be an electron pair candidate, both tracks were required to be minimum ionizing, to have zero opening angle on all three views and to have at least one track outside the template arms. For a free V^0 to be classified as an electron pair both tracks had to lie outside the template arms. If a V^0 associated with a production vertex or unassociated was shown conclusively using these criteria to be an electron pair, then the V^0 was rejected from measurement. Similarly a V^0 with one track identified positively as an electron was never associated with a production vertex. Table (1.3) gives the topology distribution on master list for the total sample of film scanned by Imperial College.

1.3 Film Measuring and Processing

The extraction of Physics Data from the K_L^0 bubble chamber film proceeded through the following sequence and as illustrated in figure (1.6). Using the scanning criteria defined in the previous section the interesting events are located on each frame and their topology noted. At the same time rough measurement of production, decay vertices and two points along the event tracks takes place for all three camera views. In addition measurement of fiducial crosses on the chamber walls is made, which serve to define the scale and axes for the events.

After ordering the output tape in increasing R.FM.No (ONMIST, ONEDIT) and correcting mistakes, a 'master list' is updated containing a five word entry, so that a 'book-keeping' account can be kept of each event as it passes through successive stages. Automatic measurement of events takes place on a H.P.D. (Hough-Powell Device), which operates in a 'Road Guidance Mode', that is rough measurements performed initially on the tables, are utilized by a program called 'MIST' to construct 'Roads' for the H.P.D. to follow. These Roads are sections across the film that contain the event tracks which help the H.P.D. to distinguish from background tracks and film scratches. Under operation of the Program 'HAZE' the H.P.D. scans the three film views separately with a laser spot, and a photo-multiplier detects obscuration of the light by bubbles in the track. It is then possible using a Moiré Fringe digitiser system to determine the coordinates of the track points. If the H.P.D. fails to detect a track within a road, it is possible to redefine the position of the track using a light-pen facility 'RESCUE'.

Geometry

After merging the digitizings of the three separate camera views back onto a single output tape 'SMOG', Geometrical reconstruction of events using the 'HYDRA GEOMETRY' ⁽²⁾ program package took place to determine the curvature, dip and azimuth of particle tracks and event coordinates from the three separate views. In order to relate the film measurements to the bubble chamber frame, 'optical' constants such as refractive indices, lens distortion parameters, camera and fiducial positions have to be provided as 'Titles' for HYDRA. These quantities were obtained from a fit of measured fiducials to fiducial positions from a telescope survey of the chamber.

In a magnetic field each track of an event will in general form a helix in space and HYDRA in reconstructing the track makes a mass dependent allowance for ionization energy loss as well as Multiple Coulomb scattering track errors. The quality of measurement and reconstruction can be tested by looking at the r.m.s. residual distances between the measured points and the projection on the film of the reconstructed track. These helix fit residuals from HYDRA are shown in figure (1.7), peak around four microns, and selecting on the best mass fits peak around three microns.

Using geometry tapes as input, a 'Remeasures' program produced a list of all those events that failed Geometrical reconstruction together with events listed as unassociated V^0 's but with effective mass consistent with that of K_S^0 or Λ decays. The latter class were re-examined at the scan table for an association vertex, and where possible were re-classified as an associated V^0 event and re-measured along with the failed Geometry events.

Kinematics

After successful geometrical reconstruction of an event, kinematic fitting of the event can proceed. This involves momentum and energy conservation at each vertex leading to four equations of constraint in p_x , p_y , p_z and E . Since Geometry output supplies only the momentum components of the measured tracks, a list of mass assumptions for the event has to be supplied to the kinematics program 'GRIND' (3), so that energy conservation can take place. These mass assignments or 'hypotheses' for each topology incorporate charge, strangeness and baryon conservation, the beam and target masses as well as taking into account one missing neutral track if required. Also range-energy tables, magnetic field values, convergence criteria and probability cut offs are supplied in the form of Titles to GRIND.

If there are no missing neutral tracks for an event, then there are four equations of constraint and no unknowns, giving a degree of 'over-determination', and instead of simply solving these equations, GRIND uses the momenta from Geometry as starting values in a fit for the correct mass hypothesis. Because of measurement errors these initial values are altered slightly by GRIND to conserve momentum and energy exactly and at the same time to minimize a chi-squared function defined in terms of the track errors.

As the K_L^0 beam can have no experimentally measured momentum components, three unknowns ($|p|$, λ , ϕ) are introduced into the four equations of energy and momentum conservation at the vertex of a beam interaction, leaving one overall constraint equation. A fit to an event under these circumstances is known as a 1 Constraint (1C) fit. Extrapolating back the fitted K_L^0 momentum components, the position of

the target relative to the centre of the 2m.HBC can be found. This yields the distributions shown in figure (1.8). If the target positions relative to all three chamber axes are known by GRIND, then this serves to fix the direction of the K_L^0 beam in dip and azimuth, leaving only the momentum undetermined, which can then be found from a 3C fit. For events with one or more missing neutral particles no fit can be achieved, since one missing particle involves the loss of three constraints, giving at best an overall 0C fit. For events with more than one vertex as for example, in $K_L^0 p \rightarrow K_S^0 p \pi^+ \pi^-$, with a visible decay of the K_S^0 , GRIND fits the vertices in time reverse order, that is the decay vertex of the K_S^0 is fitted first to determine the K_S^0 momentum and direction, which is then fed back to the production vertex, so as to fit for the K_L^0 momentum. Finally an overall '6C' multivertex fit is made in which all the measured values take part.

Effective Mass Distributions

As a check on the Magnetic field Maps in the Geometry and Kinematics Titles, that determine the momenta of the tracks from their curvature in the bubble chamber, the effective mass distribution of K_S^0 and Λ decays was plotted using the measured momenta of the decay tracks figure (1.9) and fitted to a Gaussian plus polynomial background. The K_S^0 and Λ mass values obtained from the fit are in excellent agreement with the accepted values in the Particle Properties Handbook ⁽⁴⁾, and there is no evidence of any shift in mass values. [$M_{K_S^0} = 0.4984 \pm 0.0001 \text{ Gev}$, $M_{\Lambda} = 1.116 \pm 0.0001 \text{ Gev}$]

Target Positions

Target positions were continuously redetermined throughout the data reduction stage. The early distributions in these quantities were broadened by the presence of spurious 1 Constraint fits where any imbalance of momentum or energy was compensated for by an off-axis apparent K_L^0 beam direction. From previous fitting those events which were known to give more reliable 3C fits were refitted on a 1C basis to give a more precise determination of the target positions. Finally all geometry data was refitted on a 3C basis using the updated target positions. This process yielded improved probability and stretch distributions for the fits.

Target Sizes

The target size which determines the errors on dip and phi of the beam tracks, was found by a study of the stretches on these quantities. The stretch functions for these quantities are defined (5) as

$$S(X) = \frac{X^{MEAS} - X^{FIT}}{\sqrt{(\text{err}_{MEAS}^2 - \text{err}_{FIT}^2)}} \quad \text{where } X \text{ is } \frac{1}{p}, \lambda, \phi. \quad 1.1$$

If the errors are correctly estimated and measurements unbiased, the stretch functions for the three quantities should be a Gaussian centred at zero with standard deviation of unity. To achieve this optimum it was found necessary to increase the effective target size to twice physical value, as a result of the beam K_L^0 s being scattered in the lead photon filter and thus 'blurring' and enlarging the true target size. Increasing the target size beyond the optimum value, resulted in a 5% increase in the

number of 3 Constraint fits, although at the expense of narrow stretches and a probability distribution peaked towards the high probability end, showing that the beam errors had been overestimated. For each different trial value for the beam errors, the momentum transfer squared t-distribution and K_L^0 momentum distribution for 3C fits to the relatively unambiguous channel $K_L^0 p \rightarrow K_S^0 p \pi^+ \pi^-$ were plotted and compared with previous settings and with our collaborators D.S.T. values, showing an uniform increase in events over the range in t and momentum and yielding a constant ratio for these variables between Imperial College and Cambridge. The stretch distributions corresponding to the optimum beam error settings are shown in figures (1.10-1.11) together with the reference gaussian curves. The probability distributions for 3C and 6C fits are shown in figure (1.12) and apart from the low probability peaks, are consistent with uniformity.

1.4 Hypotheses Choicing and D.S.T. Production

For the final D.S.T. preparation stage, all OC fits and events that failed geometrical reconstruction were excluded. In addition a probability cut-off was imposed at the GRIND Kinematics stage, requiring all events to exceed 0.001 before further study.

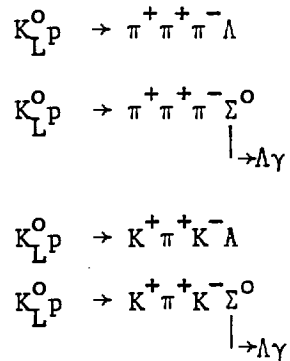
GRIND will not always give an unique fit to an event, so to help resolve any ambiguities between different hypotheses, the GRIND kinematics tapes were used as input to a program which listed out all ambiguous fits together with relevant physical quantities, and in addition punched out a 'Slice' card consisting of an eight word summary of each possible fit.

Some of these ambiguities can be resolved by comparing the observed ionization with the theoretical ionization projected onto the xy plane for a particular mass hypothesis and fitted momentum.

$$I_{xy} = \left(1 + \frac{m^2}{p^2}\right) \frac{1}{\cos\lambda} \quad \begin{array}{l} m = \text{mass of track.} \\ p = \text{momentum of track.} \\ \lambda = \text{dip of track.} \end{array} \quad 1.2$$

For the channel $K_L^0 p \rightarrow K_S^0 p^+ \pi^-$ which has a diffractive type contribution, the recoiling proton has a low momentum compared with the positive pion, so that differences in ionization are usually easily observed. Track ambiguity between the outgoing K and π mesons as in the equivalent charged Kaon beam experiments between K^+ and π^+ , does not occur in this channel because the K_S^0 is immediately identifiable from its decay into $\pi^+ \pi^-$. For other channels such as $K_L^0 p \rightarrow K^+ \pi^+ K^- \Lambda$, distinguishing between fits with pion/kaon interchange is more difficult particularly above 0.7 GeV/c where the differences in ionization become too small for the scanners to notice.

A further class of ambiguous fits which cannot be separated on ionization grounds are events which give both Λ and Σ fits in, for example, the channels

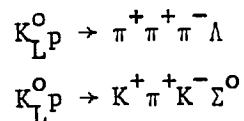


where the Σ decays electromagnetically to Λ and γ . For fits to the above reactions, the following selection rules were agreed upon between the collaborations involved and are based upon Monte-Carlo simulations of 'Faked' events (6).

(1) Where the probability of the fit at the production vertex of a 6C fit exceeded that of the $4C\Sigma^0$ fit, only the 6C Λ fit was passed forward to the D.S.T.

(2) Conversely if the probability at the production vertex of the Λ fit was less than the corresponding probability for the Σ^0 fit, both fits were forwarded. Further separation can be achieved using angular tests in the Σ^0 rest frame (7).

(3) When a 6C Λ fit is ambiguous with a $4C\Sigma^0$ fit to a different channel, such as



then if ionization cannot distinguish, only the $6C\Lambda$ fit is forwarded.

(4) For $4C\Sigma^0$ fits to different channels such as

$$K_L^0 p \rightarrow K^+ \pi^+ K^- \Sigma^0$$

$$K_L^0 p \rightarrow \pi^+ \pi^+ \pi^- \Sigma^0$$

the fit with the highest production probability was chosen.

Using the final list of selected hypotheses, a further program 'edits' out the correct SLICE cards, which in conjunction with the GRIND kinematics tape is used in the production of the final SLICE D.S.T. (8) For events with more than one final fit an additional weight is assigned equal to the reciprocal of the number of final fits. The number of fits to each channel is given in table (1.4). Figure (1.13) illustrates the various stages of D.S.T. production from the GRIND kinematics tapes.

1.5 Scanning and measuring efficiency determination

The K_L^0 scanning and measuring sequences are illustrated schematically in figure (1.14). As described previously, the film was initially scanned and measured (PASS 1), the 'ONEDIT' tape produced, updated a master list resident on disk, so that each event was described by a five word entry including topology, x-y co-ordinates and ROLL-FRAME Numbers. Subsequent geometrical reconstruction and kinematic fitting yielded kinematics tapes containing successful fits corresponding to this 1st pass. A second 'off-line' scan (PASS 2) was later performed on every 5th ROLL of the film sample so that scanning efficiencies could be monitored, using the same scanning criteria as in the previous scan. The scan cards produced, formed a second master list where however no co-ordinate information was included. From the results of this and the first scan, giving a scanning efficiency determination, it was decided to rescan the complete film sample. The scan cards produced from this 3rd scan (PASS 3) were compared with the ONEDIT output from the 1st pass and a list was compiled of new events that had been missed on the 1st scan. These new events were measured at the tables along with remeasures from the 1st pass, and a corresponding kinematics TAPE was obtained for this 3rd pass.

Scanning efficiency determination for fits

To determine the scanning efficiencies for particular scans, any common sample of events can be used, the most suitable being events which give kinematic fits, since a knowledge of the scanning efficiency

for this class of events would give a more reliable estimate for cross-sections and avoids the problems that scanners have of gamma ray interpretation. The complete scans corresponding to passes 1 and 3 can be represented by two overlapping circles as in figure (1.15a) where,

$$N'_1 = \text{No. of fits found only on pass 1.}$$

$$N'_3 = \text{No. of fits found only on pass 3.}$$

$$N'_{13} = \text{No. of fits found on pass 1 and pass 3.}$$

The overall efficiencies for passes 1 and 3 could in principle be obtained from these numbers since

$$e_1 = \frac{N'_{13}}{(N'_{13} + N'_3)} \qquad e_3 = \frac{N'_{13}}{(N'_{13} + N'_1)}$$

However no common fit information ' N'_{13} ' is available, since only events that were missed on pass 1 and found on pass 3 were processed through the data chain. There are therefore three unknowns N'_{13} , e_1 and e_3 and two equations, therefore to solve them a further assumption is made that the scanning efficiency for pass 3 is identical to that of pass 2. The area of overlap in figure (1.15b) for the three scans is valid only for those rolls that were scanned on scan 2, namely every 5th ROLL. The scanning efficiencies e_2 and e_3 can be calculated from figure (1.15b) as,

$$e_2 = \frac{N_{12} + N_{123}}{(N_1 + N_{13}) + (N_{12} + N_{123})} \qquad e_3 = \frac{N_{13} + N_{123}}{(N_1 + N_{12}) + (N_{13} + N_{123})}$$

where,

- N_1 = No. of fits found on pass 1 only
- N_2 = No. of fits found on pass 2 only
- N_3 = No. of fits found on pass 3 only
- N_{12} = No. of fits common to pass 1 and pass 2
- N_{23} = No. of fits common to pass 2 and pass 3
- N_{123} = No. of fits common to pass 1, pass 2 and pass 3.

For $e_2 = e_3$, then $N_{12} = N_{13}$ and $N_2 = N_3$ in order for e_1 to be identical in both pass 1 and pass 3. The remaining numbers can be found by comparing the kinematics D.S.T. for pass 1 and pass 3 with the Master list for pass 2 and evaluating the common fits. This procedure can be repeated for various topologies and the numbers together with the overall efficiencies are given in table (1.5).

Scanning efficiency for K_0 -L's and events

In order to reduce the scanning load in the 3rd pass, it was decided to omit from the scan unassociated V^0 s such as K_L^0 beam decays, since a sufficiently large sample of these events (4100) was already available from the results of the first pass. Therefore in deriving a value for the scanning efficiency, only results from the first two passes will be used.

Because of the lack of co-ordinate information on the second pass, it is not possible to specify whether an event seen on the 1st pass corresponds to an identical event seen on the 2nd pass and vice-versa. Rather than use individual events, then it is more meaningful to compare

'frames' and require whether an event of the same topology has been seen on the same frame for the other pass. The results of the two separate passes are given in table (1.6), where both common and missing frames and events of the two scans are displayed.

The low values for the scanning efficiencies calculated from these numbers, are due in part to the fact that some scanners using past experience will reject or include e^+e^- pairs from gamma materializations as beam decays or as associated with beam interaction vertices in different ways, inspite of scanning instructions and template information. This has implications for the determination of the K_L^0 -decay scanning efficiencies, where inclusion of e^+e^- pairs as potential beam decays will 'dilute' the true K_L^0 contribution giving a low value.

Beam decays can however be separated from e^+e^- pairs, K_S^0 and Λ decays at the post-geometry stage of pass 1, where by effective mass and transverse momentum cuts a sample of K_L^0 s can be obtained and used as an independent scanning sample. K_L^0 beam decays fall into two categories. Those scanned as unassociated which are in a majority (3314), and those scanned initially as associated with a production vertex, but after subsequent analysis using geometry tapes, are shown to be consistent with beam decays (780). The ROLL, FRAME-No. of these two classes of events which fall within the limits of pass 2 can be used to determine the scanning efficiency for pass 2.

Comparison of the two scans showed that out of 624 frames which were scanned on pass 1 as having an unassociated K_L^0 beam decay, 467 frames on pass 2 have at least one event seen on them, figure (1.16a). This represents an upper scanning efficiency limit for pass 2 as $467/624 = 0.75 \pm 0.05$. The condition that the K_L^0 s must be scanned as unassociated on pass 2 is relaxed, as there is no guarantee that all K_L^0 s will be scanned

as associated or unassociated in the same way as pass 1. The topology distribution corresponding to the scan of pass 1 is given in table (1.7) and noting that the proportion of K_L^0 s to the total numbers of events for the 624 frames on scan 1 is $624/868 = 0.72$ which for the scan of pass 2 would give $(0.72 \times 605) = 436 K_L^0$ s and a scanning efficiency estimate of 70% within the estimate obtained by comparing frames.

Similar reasoning applied to K_L^0 s scanned as associated gives a value of 0.67 ± 0.09 . Since no geometry processing of events for pass 2 was done, no estimate of the scanning efficiency for K_L^0 s in pass 1 is available.

Measuring efficiencies

By comparing the numbers of events on the master list to the number that reach a final geometry D.S.T., the measuring efficiency for a given topology defined as

$$e_M^{-1} = \frac{\text{No. scanned}}{\text{No. on D.S.T.}}$$

can be obtained. The D.S.T. used is a geometry D.S.T. rather than a D.S.T. containing kinematical fits, as a considerable proportion of events scanned will have apparent gamma associations where a fit is not required. The measuring efficiency gives for each topology the fraction of events scanned that survive the data reduction stages through to successful geometrical reconstruction, and is used in conjunction with scanning efficiencies in the determination of cross-sections. Events can be lost through poor rough digitisings at the measuring tables, HAZE-H.P.D. not giving

adequate digitisings or events failing geometrical reconstruction. It is worth remarking that because of the essentially automatic manner in which the H.P.D. operates, it is at a disadvantage as regards measurement of events, compared with interactive operator controlled measuring machines such as 'SWEEPNIK' and 'ERASME' where failed or difficult events can command additional attention on the part of the operator, to produce a higher measuring efficiency. The measuring efficiencies are given in table (1.8) for each topology together with the numbers on the master list and geometry D.S.T.

1.6 Event losses and corrections

The set of fiducial crosses which define the scanning and measuring volumes are used as reference marks for the scanners for including or rejecting an event for measurement, however since the scanner views a 'conical' projection of events onto the xy plane figure (1.17), the distribution of events as a function of bubble chamber co-ordinates will not be uniform but will show losses around the boundaries of the fiducial volume. To ensure uniform detection efficiency a flat 'box-like' x-co-ordinate distribution is imposed (within statistics), and for the y and z axes events in the tails are removed. Cuts on event coordinates are done at the post Geometry stage, where the distribution of events in all three coordinates are available and any losses clearly visible. On the basis of these distributions for production and decay vertices, the following volume boundaries were chosen

<u>Production Volume</u>	<u>Decay Volume</u>
-76 < x < 32 cms	-76 < x < 48 cms
-13 < y < 15 cms	-16 < y < 19 cms
-38 < z < -13 cms	-40 < z < -10 cms

These volumes in addition ensure that there is sufficient track length for measurement and that the events are in the well-illuminated region of the chamber.

Decay losses and decay weights

Losses of associated V^0 events can occur when the K_S^0 fails to decay in for example the minimum of 16 cms downstream distance provided between the two fiducial volume regions, or if the K_S^0 decays so close to the production vertex that the event is classified as a non V^0 event. The size of these losses were estimated using events falling within the production and decay fiducial volumes specified previously. Events were removed if the projected distance (on the xy plane) between production and decay vertices was less than a distance ' ℓ_{\min} ', where ℓ_{\min} was varied between 0 and 2 cms. The remaining events were weighted up by the reciprocal of the probability of decay between ℓ_{\min} and the intersection of the K_S^0 path with the decay fiducial volume.

$$\text{Weight} = \frac{1}{(e^{-\ell_{\min}/L \cos \lambda} - e^{-\ell_{\text{pot}}/L})} \quad 1.3$$

where ℓ_{\min} = minimum projected length

λ = dip of K_S^0 with respect to the xy plane

L = mean free path

ℓ_{pot} = distance from production vertex to the intersection of K_S^0 path with decay fiducial volume boundary.

The minimum projected length cut ℓ_{\min} was found to be 1 cm for K_S^0 decays of '301' type topology events for which the weighted number of events became independent of the choice of ℓ_{\min} . This value is compatible with that obtained from the distribution of projected lengths in figure (1.18) for 6C fits to $K_L^0 p \rightarrow K_S^0 p \pi^+ \pi^-$, where losses are clearly visible in the first bin. The distribution of decay weights resulting from this procedure is

shown in figure (1.19), for 6C fits to $K_L^0 \rightarrow K_S^0 p \pi^+ \pi^-$, giving an average weight of 1.2 to the Imperial College data and 1.17 to the Cambridge data.

1.7 K_S^0 mean lifetime determination

A maximum likelihood determination of the mean K_S^0 lifetime was undertaken for 3C and 6C fits to the channel $K_L^0 \rightarrow K_S^0 p \pi^+ \pi^-$, satisfying the fiducial volume and projected length cuts outlined in the previous section. The quantity

$$L = \prod_{i=1, n} \frac{1}{c\tau} \frac{e^{-(ct_i - ct_i^{\min})/c\tau}}{(1 - e^{-(ct_i^{\max} - ct_i^{\min})/c\tau})} \quad \begin{array}{l} \text{'i' = i}^{\text{th}} \text{ event} \\ 1.4 \\ n = \text{no. events} \end{array}$$

was maximized, or alternatively $-\log L$ was minimized, ct_i^{\min} being the proper lifetime corresponding to ' l_{\min} ' the minimum projected length cut equal to 1 cm and ct_i^{\max} is the proper lifetime corresponding to ' l_{\max} ' the maximum projected length cut equal to 30 cms, or the proper lifetime to reach the edge of the fiducial volume if this is smaller.

The value of $c\tau$ required to minimize $-\log L$ was found to be 2.60 ± 0.155 cms for 629 events surviving the cuts, in agreement within errors of the accepted value of 2.68 cms ⁽⁴⁾. Figure (1.20) shows the experimental proper lifetime distribution together with the theoretical estimate from the maximum likelihood determination.

Table 1.1 Number of bubble chamber pictures
 taken at each π^- beam momentum

π^- Beam Momentum Gev/c	Number of pictures taken
14.0	37,800
17.0	316,872
18.5	6,184
20.0	38,722

Table 1.2 Topology distribution for
 the 400 frame test scan.

Topology	Number scanned
300	508
500	113
700	20
900	1
001	52
101	7
301	16
310	10
311	3
501	3
510	3

Table 1.3 Topology distribution for the total sample
of Film scanned by Imperial College

Topology	Number scanned on PASS 1 and PASS 3	Topology	Number scanned on PASS 1 and PASS 3
001	34620	502	196
101	13170	503	7
102	829	511	281
103	30	512	19
111	239	521	8
112	24	531	1
301	16765	701	711
302	813	702	27
303	26	703	2
304	2	711	64
311	883	712	1
312	45	713	1
313	4	901	69
321	20	902	2
501	4428	911	2

Table 1.4 Number of fits to each channel

Channel	Numbers of fits (Unambiguous)	Numbers of fits (Ambiguous)
$K_{L}^0 \rightarrow K_{S}^0 p$	156	-
$K_{L}^0 \rightarrow \Lambda \pi^+$	101	30
$K_{L}^0 \rightarrow \Sigma^0 \pi^+$	64	30
$K_{L}^0 \rightarrow K_{S}^0 \pi^+ \pi^- p$	865	5
$K_{L}^0 \rightarrow \pi^+ \pi^+ \pi^- \Lambda$	160	58
$K_{L}^0 \rightarrow \pi^+ \pi^+ \pi^- \Sigma^0$	108	56
$K_{L}^0 \rightarrow K^+ p K^- K_{S}^0$	28	6
$K_{L}^0 \rightarrow K^+ \pi^+ K^- \Lambda$	32	24
$K_{L}^0 \rightarrow K^+ \pi^+ K^- \Sigma^0$	47	16
$np \rightarrow p K^+ \pi^- \Lambda$	56	39
$np \rightarrow p K^+ \pi^- \Sigma^0$	49	30
$np \rightarrow p p K^- K_{S}^0$	15	6
$K_{L}^0 \rightarrow K_{S}^0 \pi^+ \pi^+ \pi^- \pi^- p$	108	6
$K_{L}^0 \rightarrow \pi^+ \pi^+ \pi^+ \pi^- \pi^- \Lambda$	28	9
$K_{L}^0 \rightarrow \pi^+ \pi^+ \pi^+ \pi^- \pi^- \Sigma^0$	19	8

Unambiguous = one unique fit to an event.

Ambiguous = more than one fit to an event.

(Numbers refer to 17 GeV/c data only)

Table 1.5 Scanning efficiency for fits in each topology

Topology	N_1	N_{12}, N_{13}	N_{123}	N_2, N_3	N_{23}	e_2, e_3	e_1
101	83	101	166	73	87	0.59 ± 0.05	0.63 ± 0.05
301	73	108	416	70	101	0.74 ± 0.04	0.75 ± 0.04
501	23	41	98	8	7	0.68 ± 0.08	0.90 ± 0.11
701							
901							

Table 1.6a Scanning efficiencies from a comparison of frames

Topology	No. Frames on PASS 1	No. Common Frames on PASS 1 and PASS 2	No. Frames on PASS 2	E_1	E_2
001	4443	2028	3361	0.60 ± 0.02	0.46 ± 0.01
101	1397	591	1330	0.44 ± 0.02	0.42 ± 0.02
301	1956	1109	1763	0.63 ± 0.02	0.57 ± 0.02
501	629	320	565	0.57 ± 0.04	0.51 ± 0.03
701	115	55	96	0.57 ± 0.10	0.48 ± 0.08

Table 1.6b Scanning efficiencies from a comparison of events

Topology	No.Events on PASS 1	No.Common Events on PASS 1 and PASS 2	No.Events on PASS 2	E ₁	E ₂
001	4929	2281	3690	0.62±0.02	0.46±0.01
101	1499	614	1376	0.45±0.02	0.41±0.02
301	2082	1173	1848	0.63±0.02	0.56±0.02
501	643	326	576	0.57±0.04	0.51±0.03
701	115	55	96	0.57±0.10	0.48±0.08

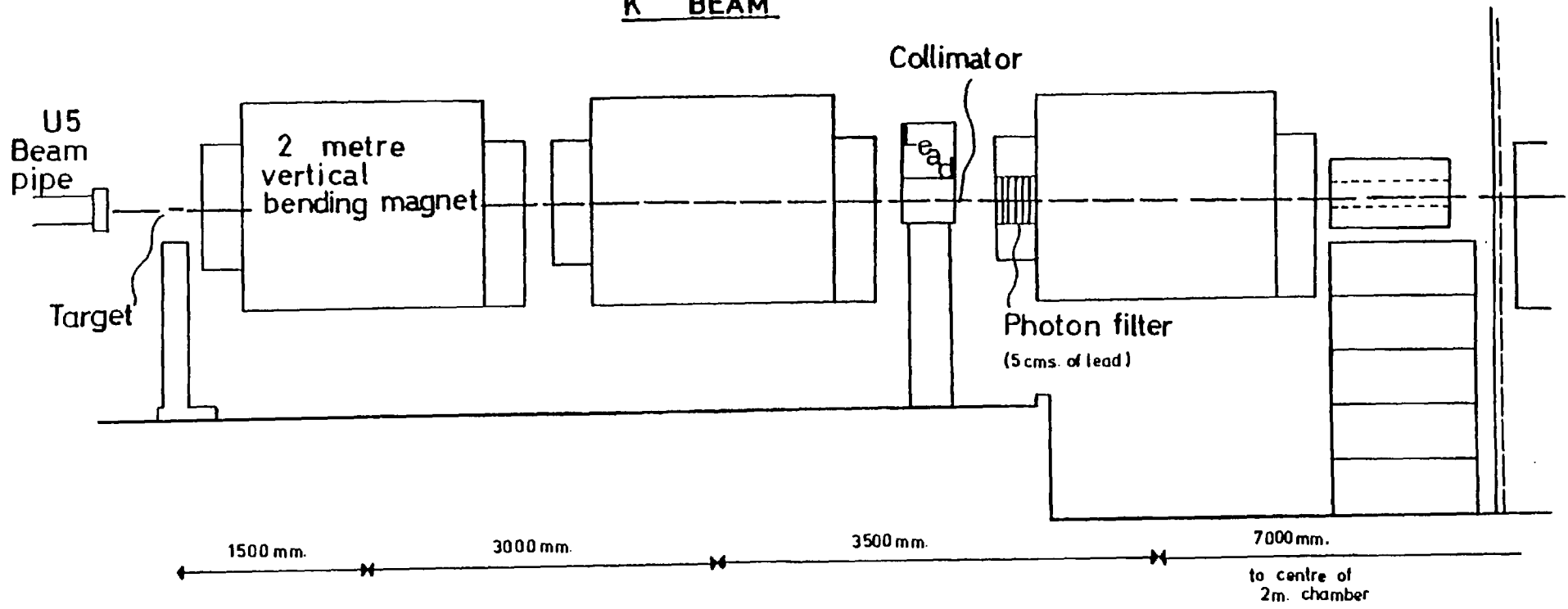
Table 1.7 The Topology distribution for the 624 frames of PASS 1
and the common frames of PASS 2

Topology	No.Events on the 624 frames of PASS 1	No.Events on the 467 common frames of PASS 2
001	736	423
101	36	76
301	74	84
501	19	19
701	3	3
	(Total = 868)	(Total = 605)

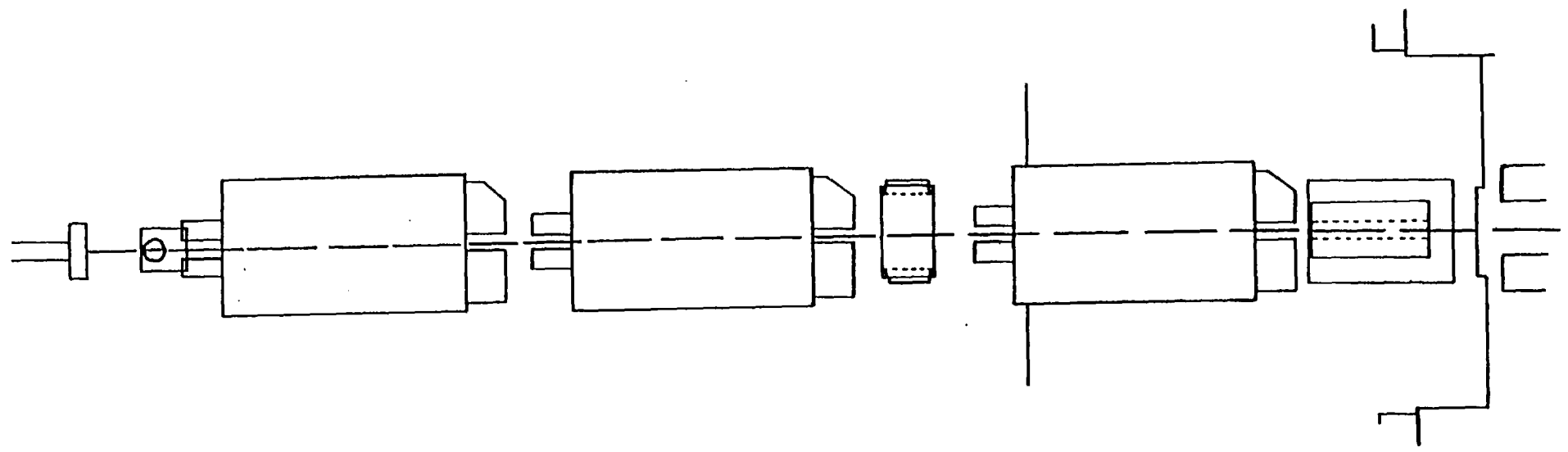
Table 1.8 Measuring efficiencies for each topology

Topology	Number on Master List	Number on Geometry D.S.T.	Measuring efficiency
001	34620	29475	0.85±0.01
101	10112	7840	0.78±0.01
301	13544	9926	0.73±0.01
501	4131	2771	0.67±0.02
701	679	392	0.58±0.04
100+ (at least) (1 assoc V^0)	11013	8506	0.77±0.01
300+ (")	15036	10910	0.73±0.01
500+ (")	4605	3065	0.67±0.02
700+ (")	772	438	0.57±0.03

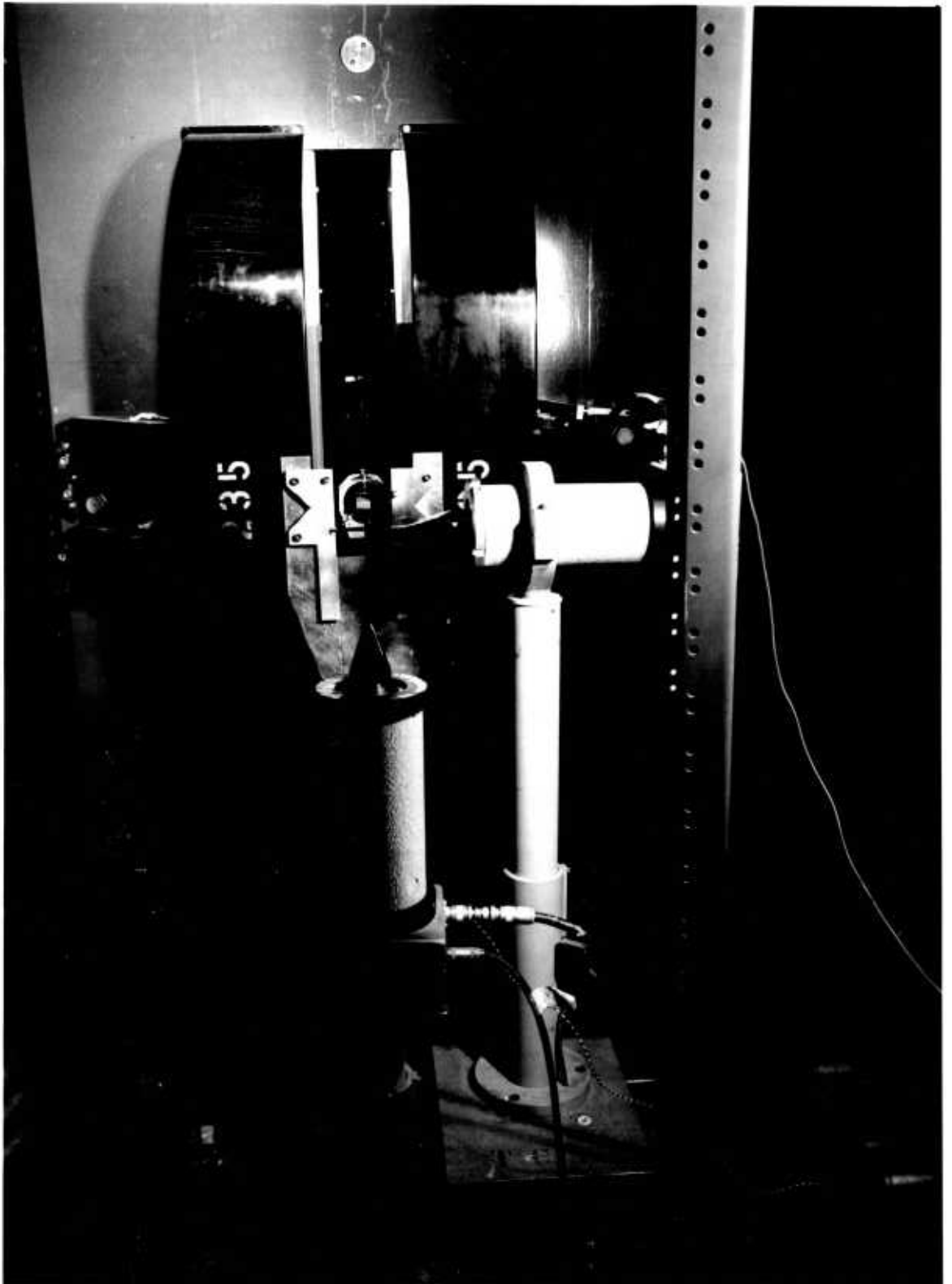
K⁰ BEAM



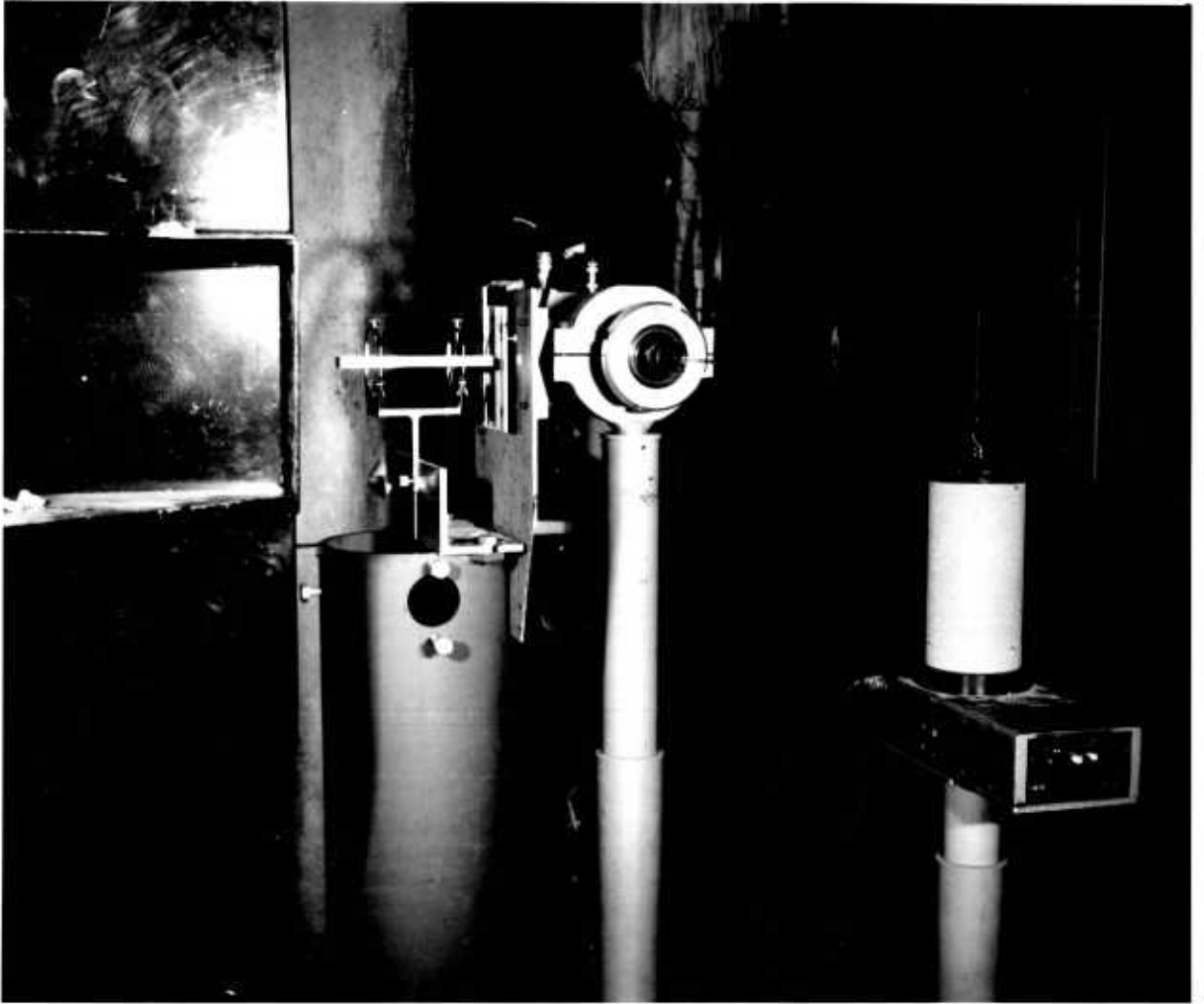
-56-

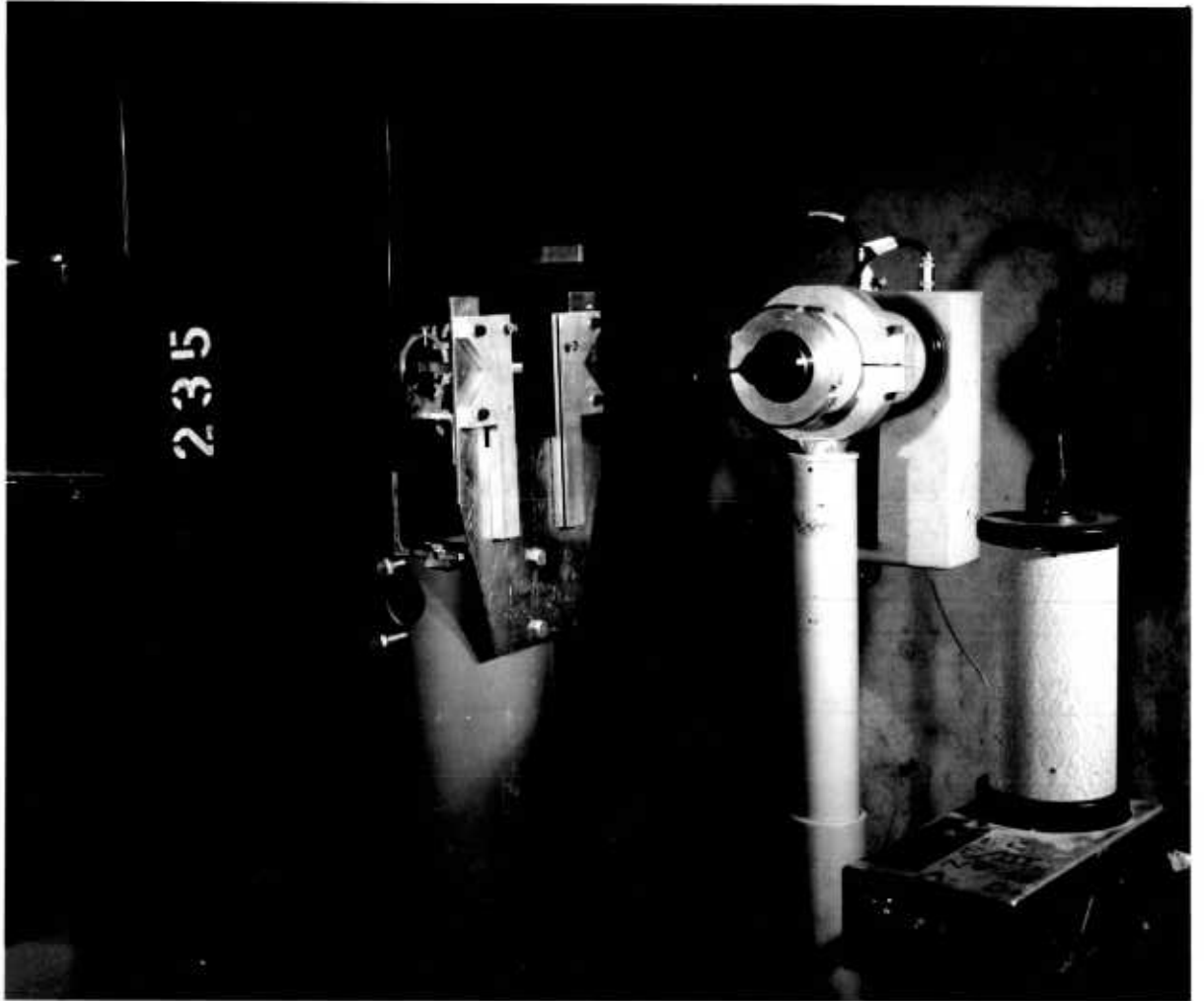




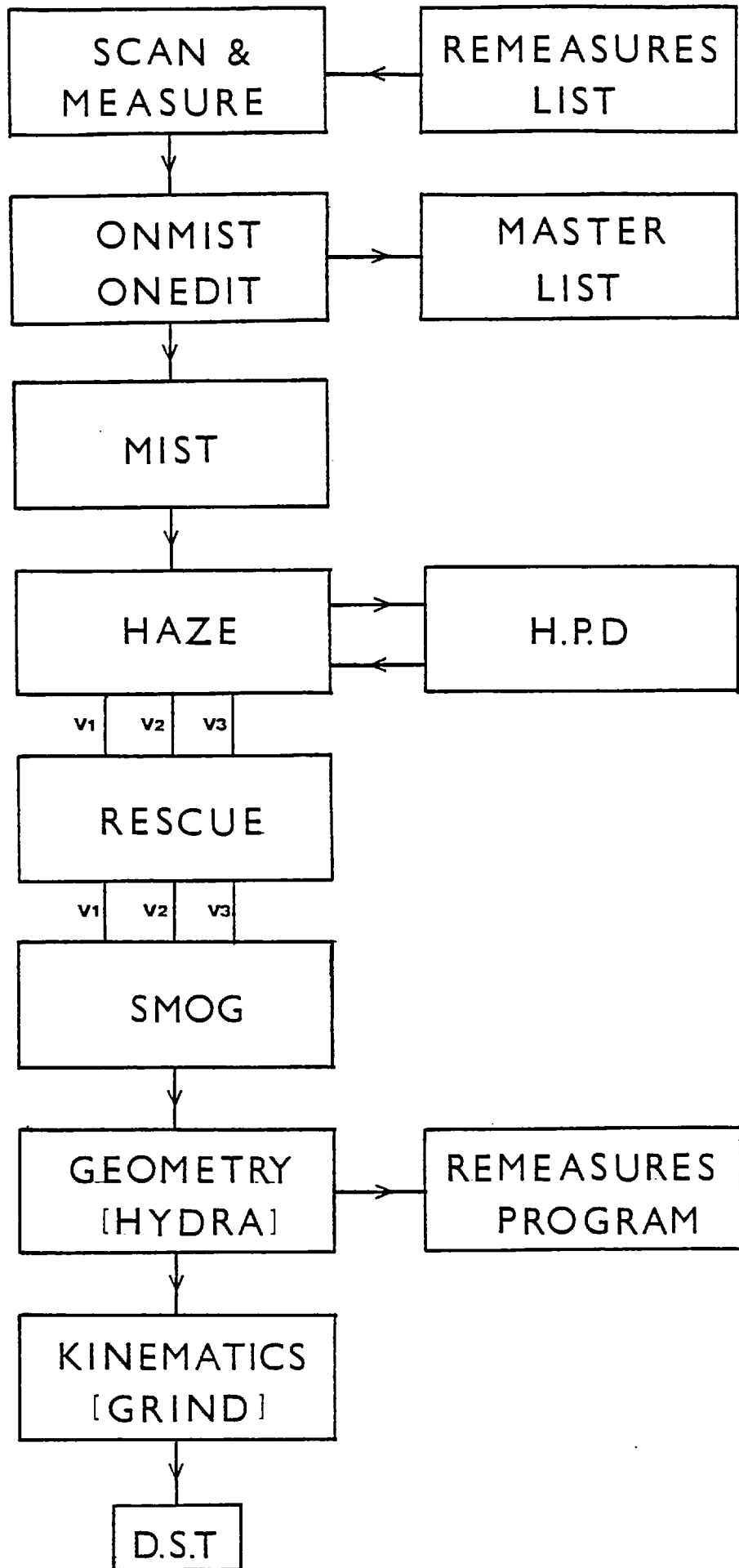


1.3

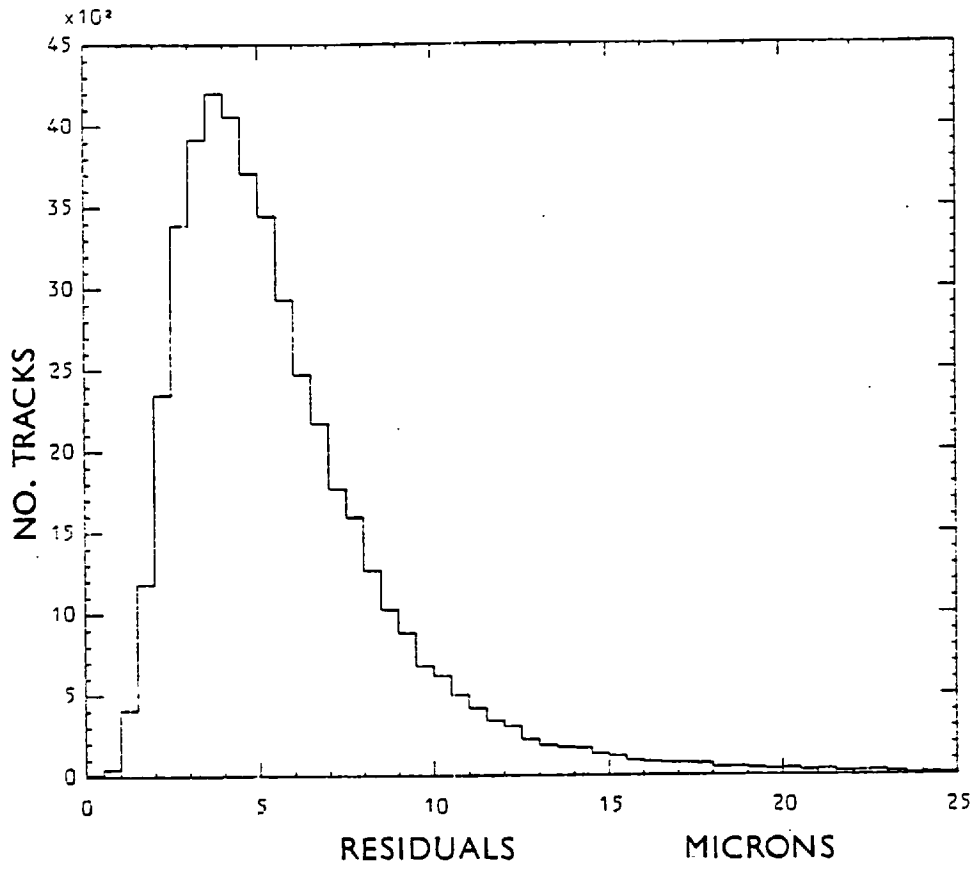




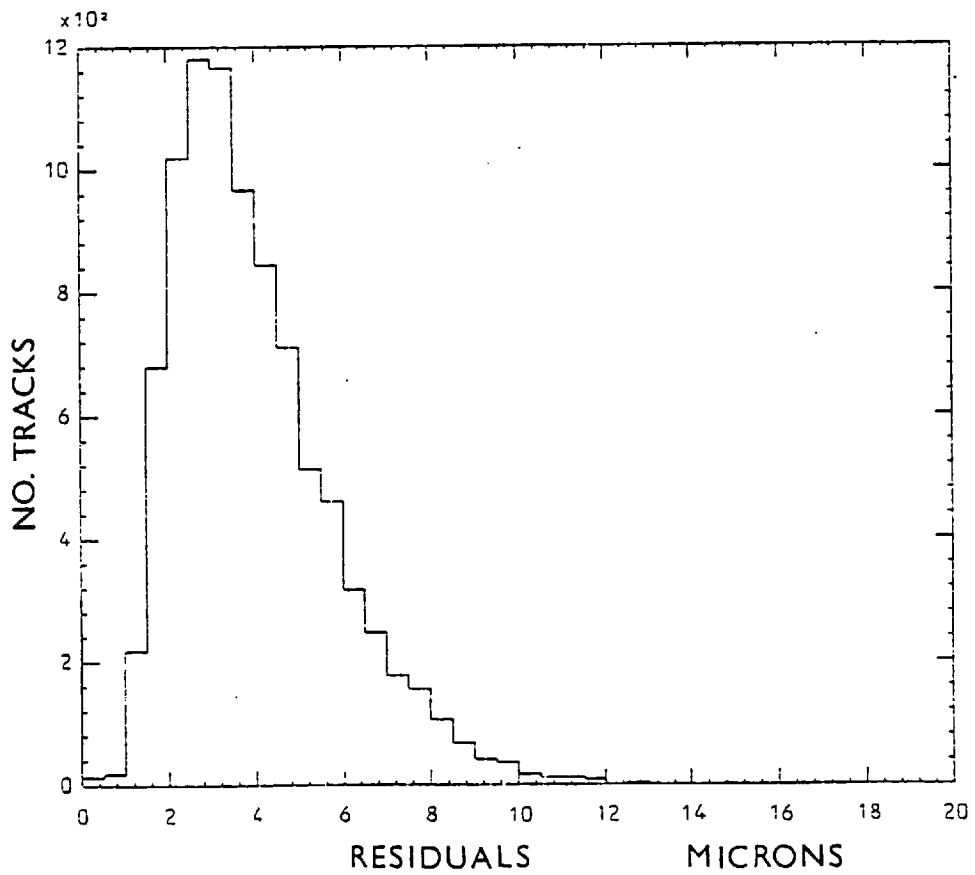
1.5



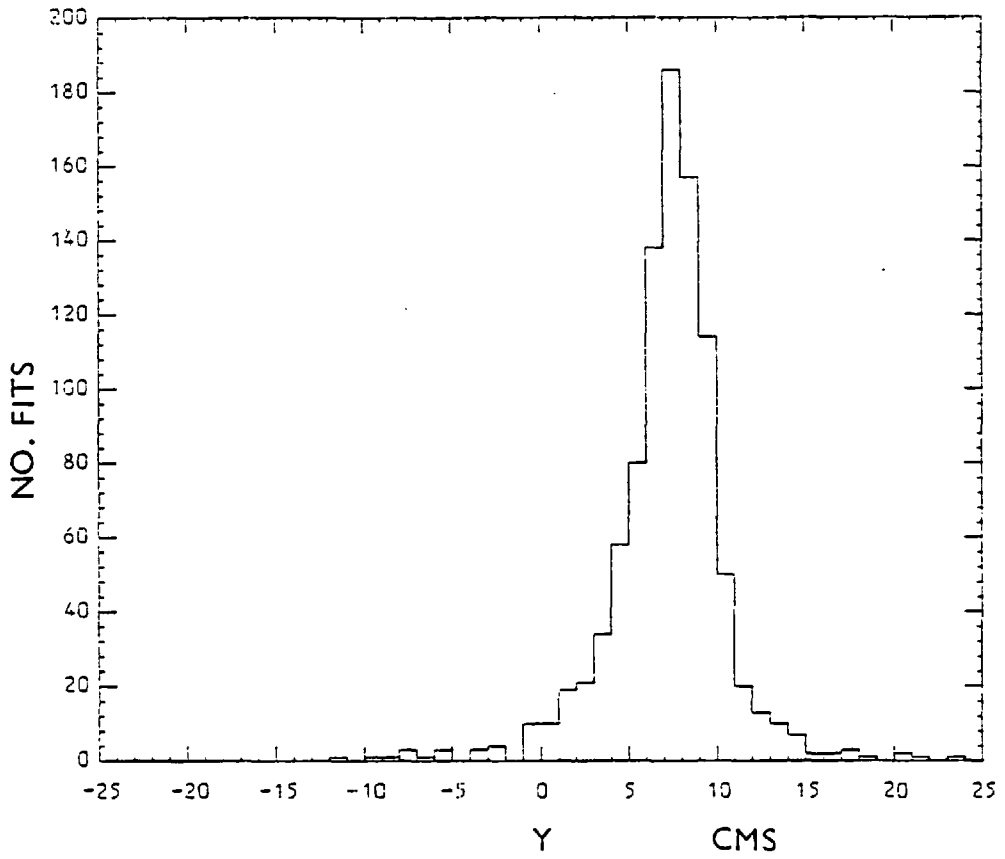
HELIX FIT RESIDUALS



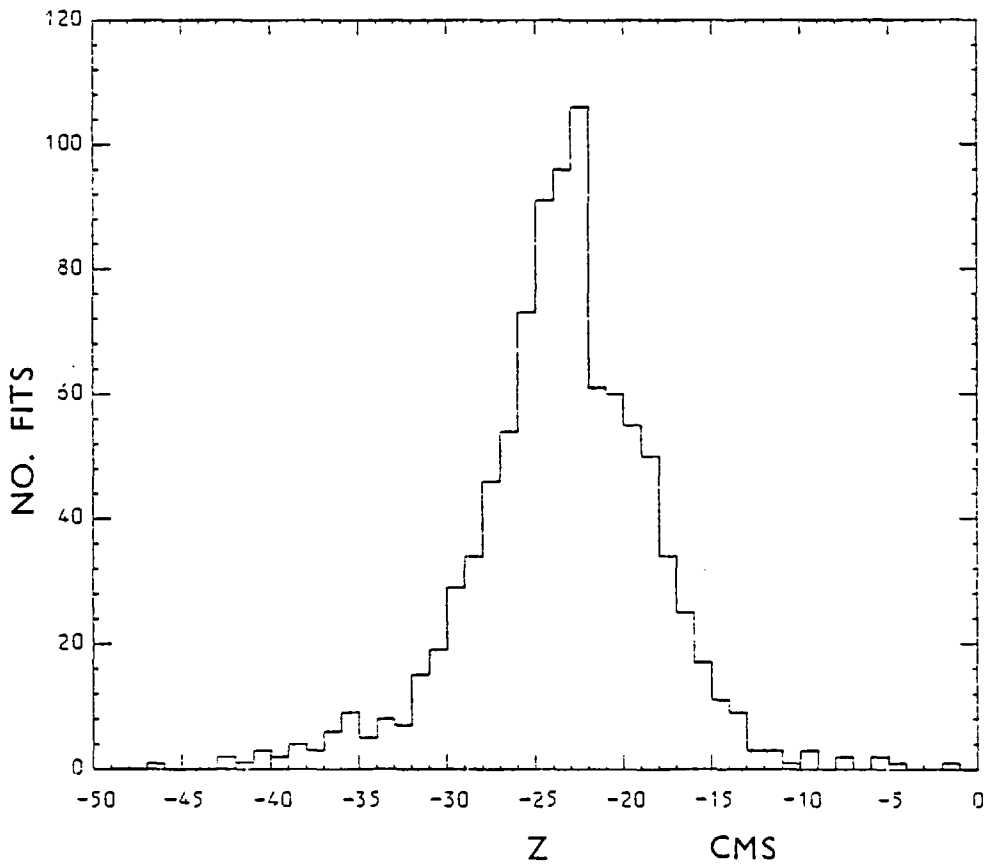
BEST MASS FIT RESIDUALS



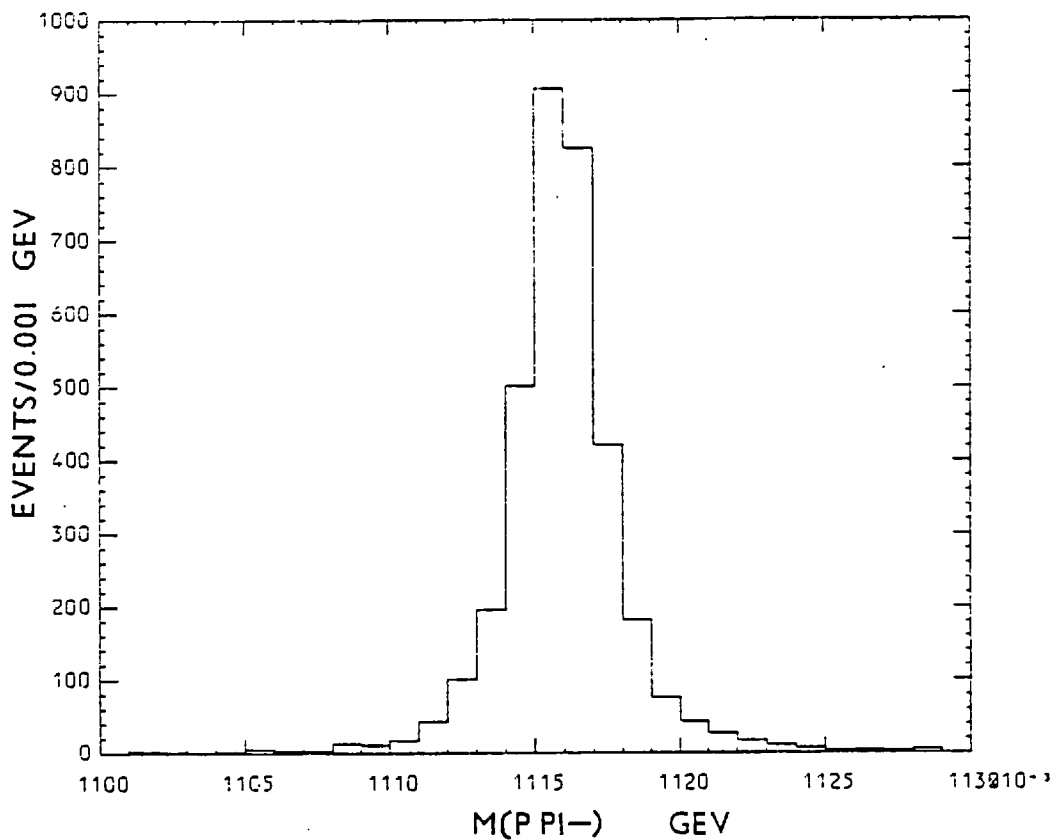
Y-AXIS TARGET PLOT FROM 1C FITS



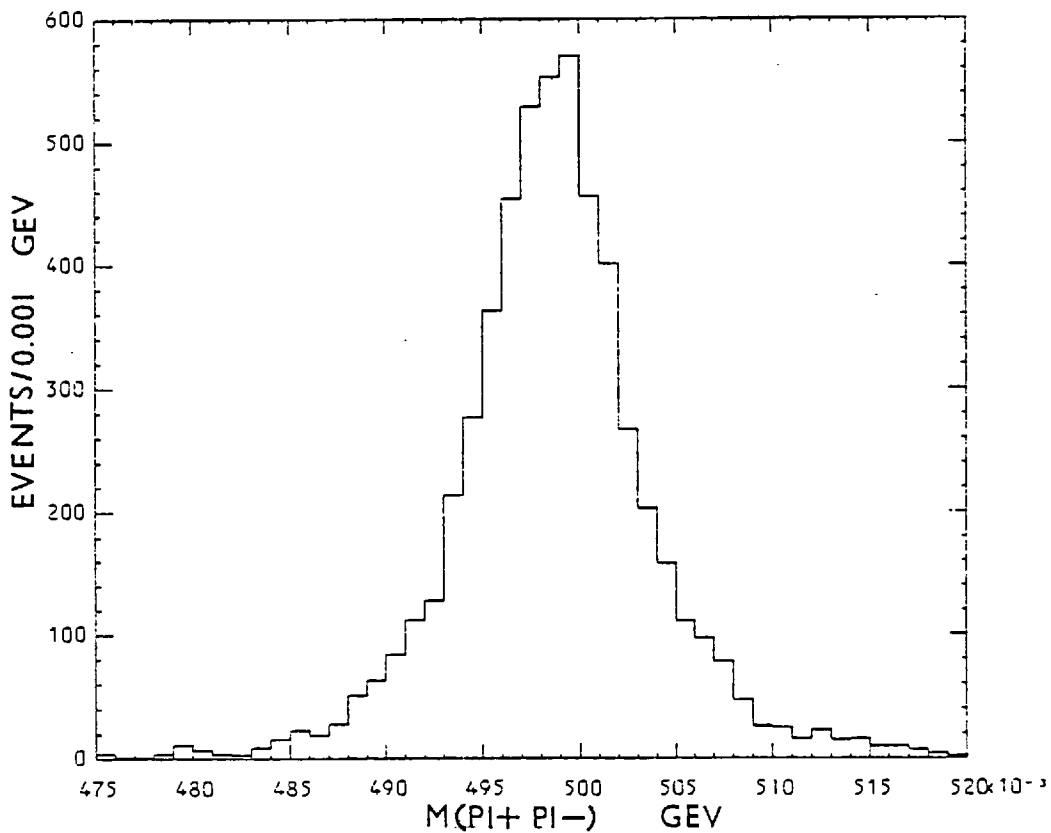
Z-AXIS TARGET PLOT FROM 1C FITS



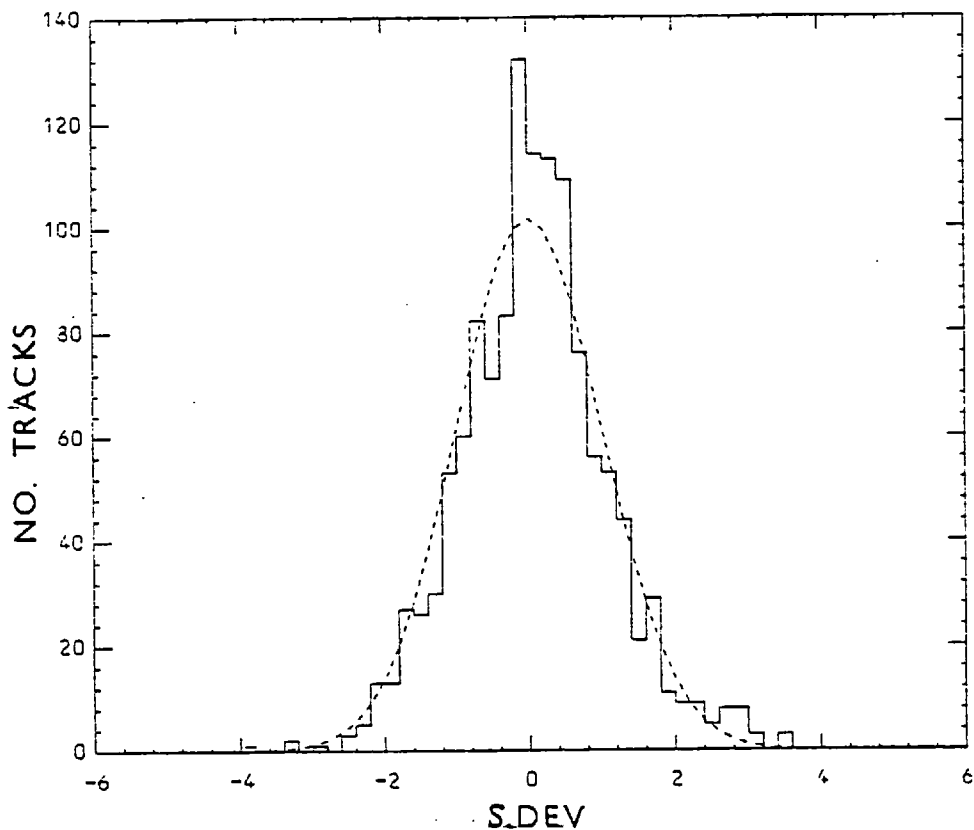
P PI- EFFECTIVE MASS PLOT



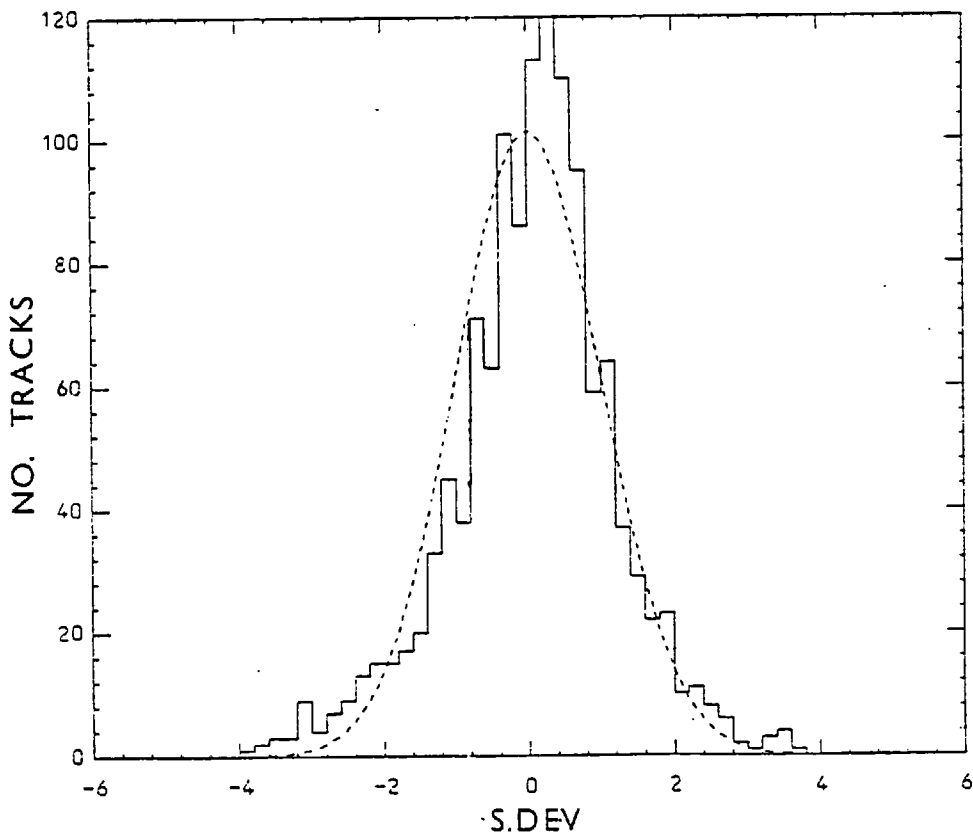
$\pi^+ \pi^-$ EFFECTIVE MASS PLOT



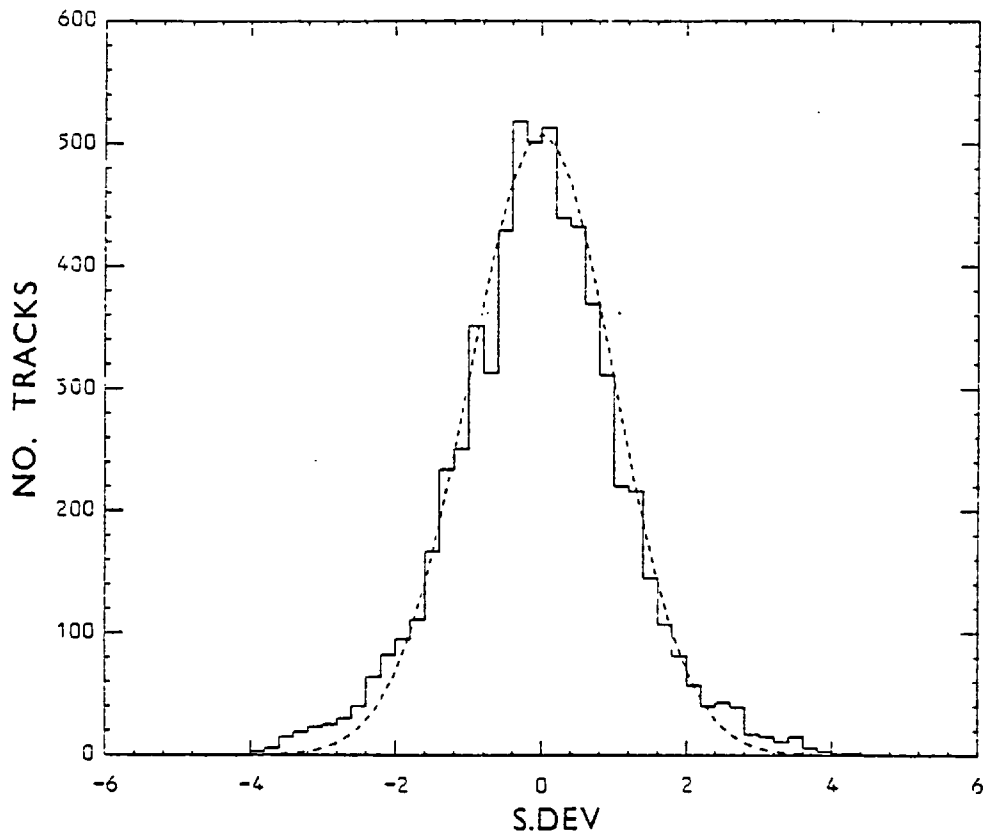
STRETCH FOR BEAM DIP



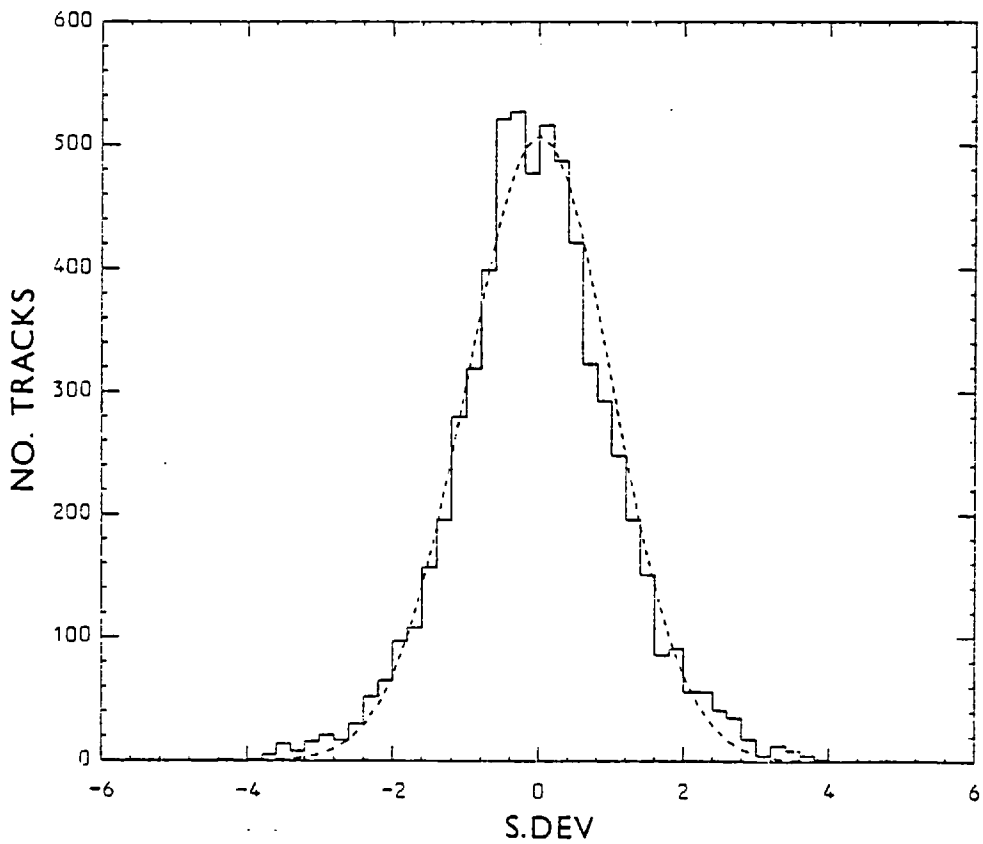
STRETCH FOR BEAM PHI



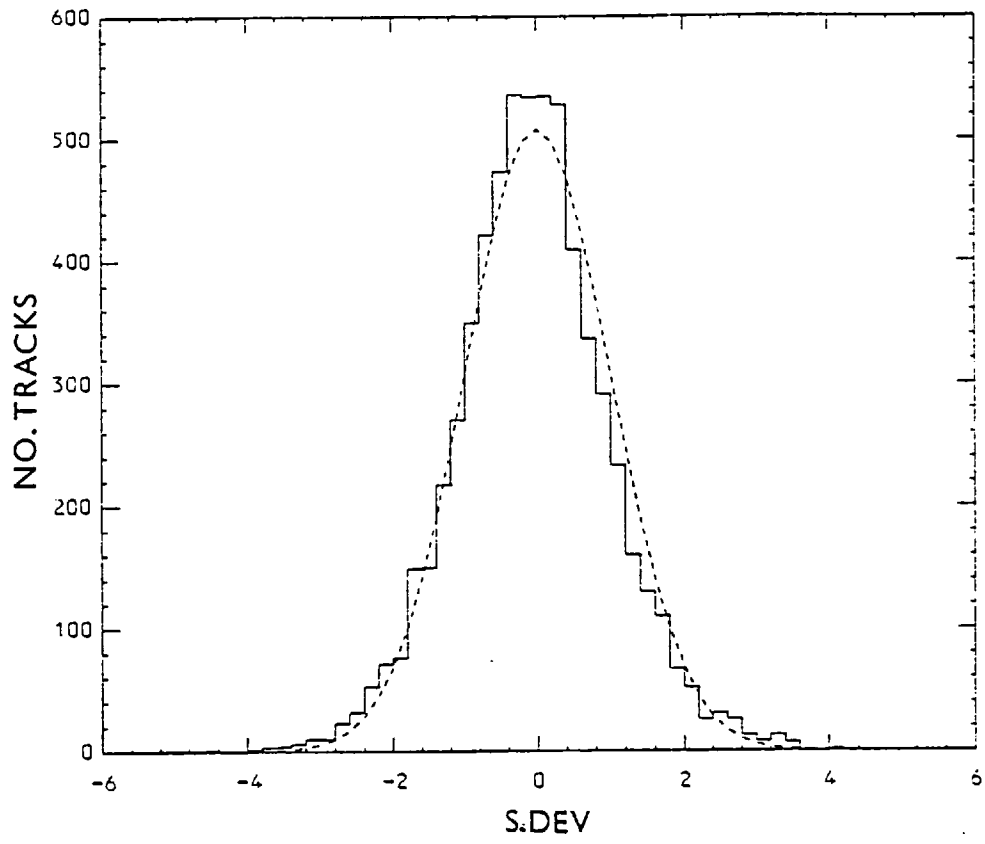
STRETCH FOR DIP, NO BEAM



STRETCH FOR PHI, NO BEAM

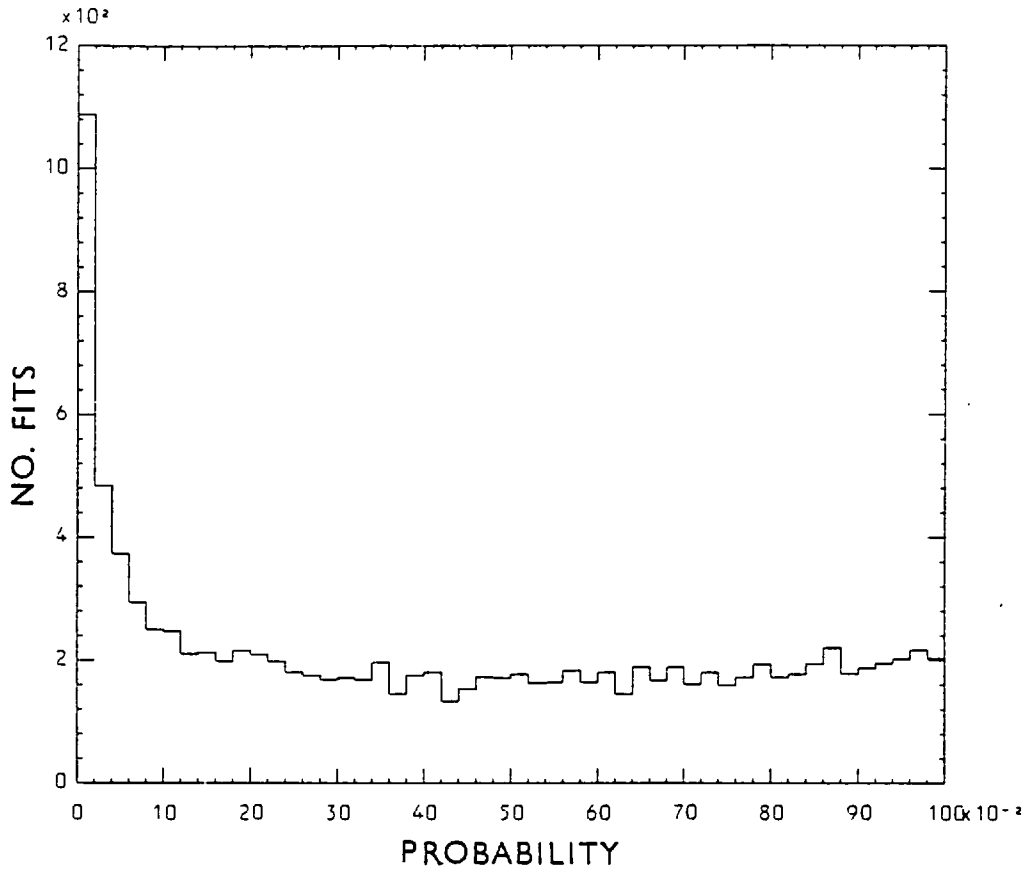


STRETCH FOR 1/P, NO BEAM

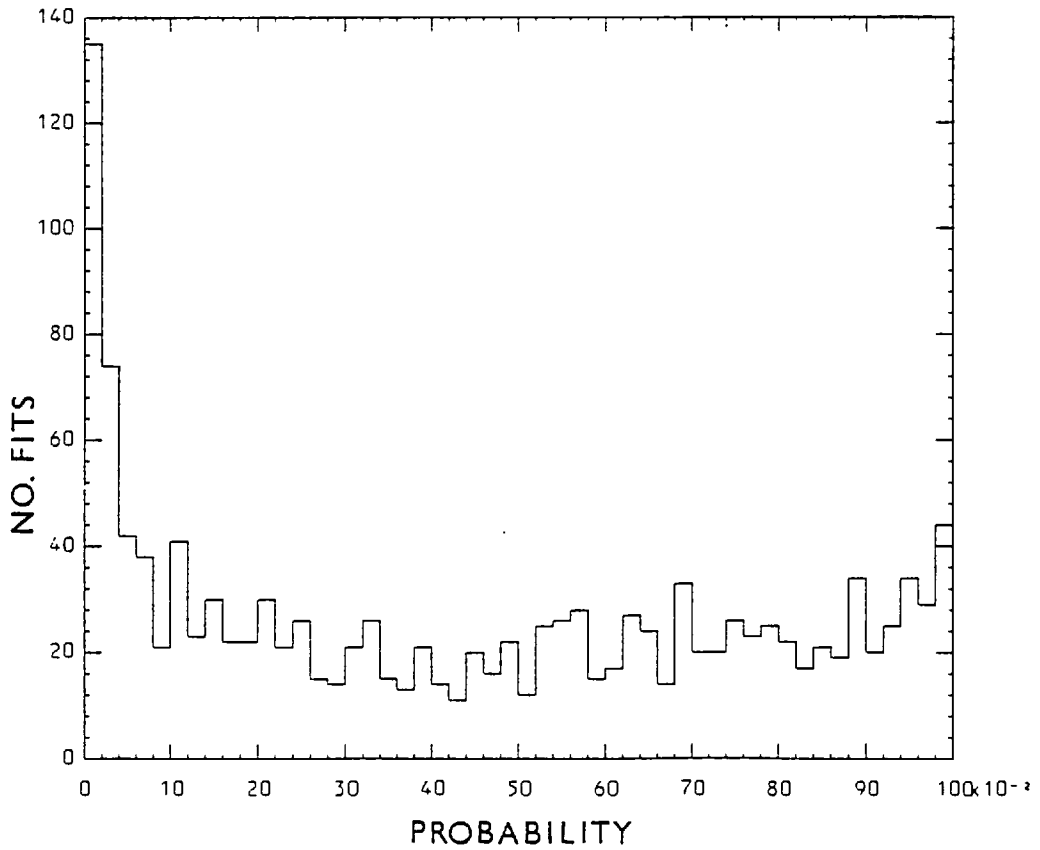


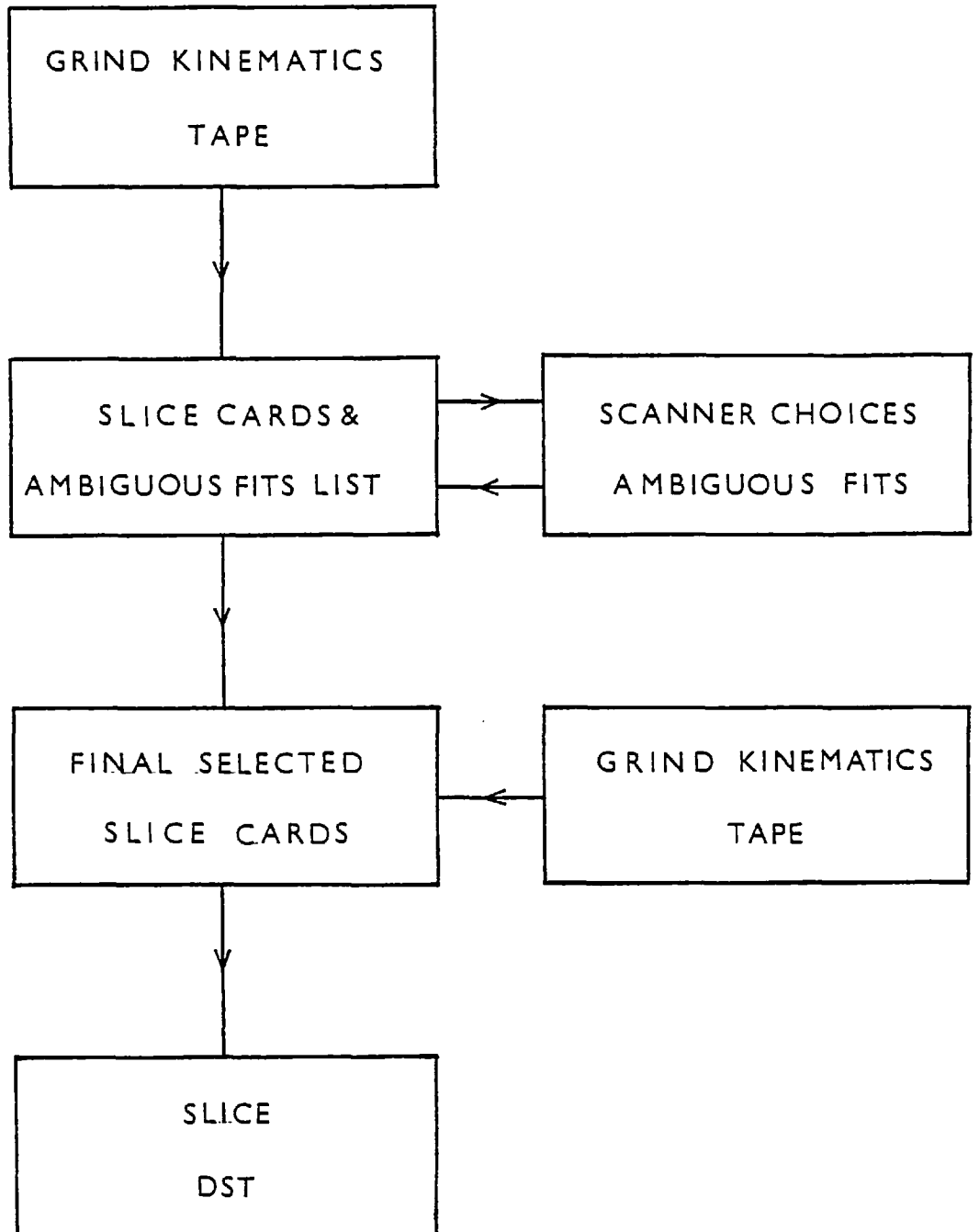
1.11 CONTD.

PROBABILITY PLOT OF 3C FITS

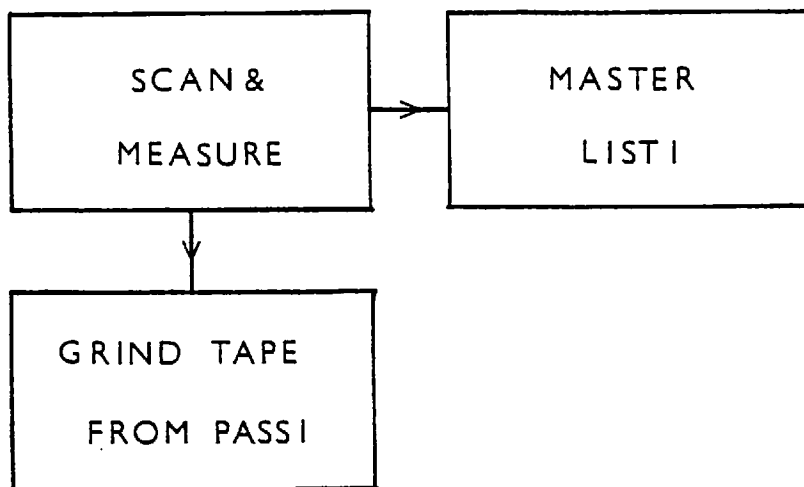


PROBABILITY PLOT OF 6C FITS

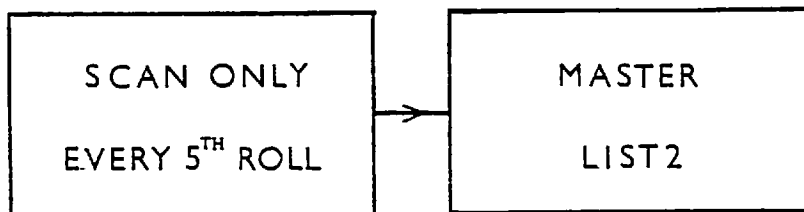




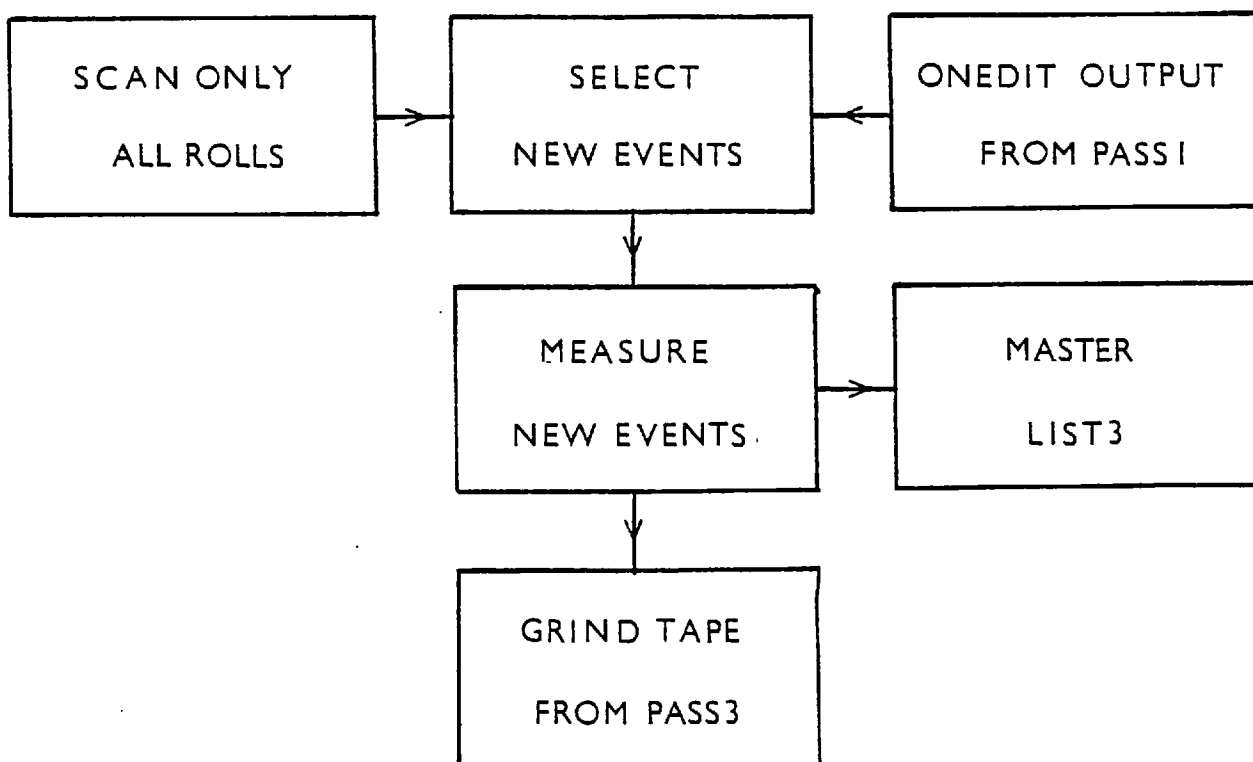
PASS 1

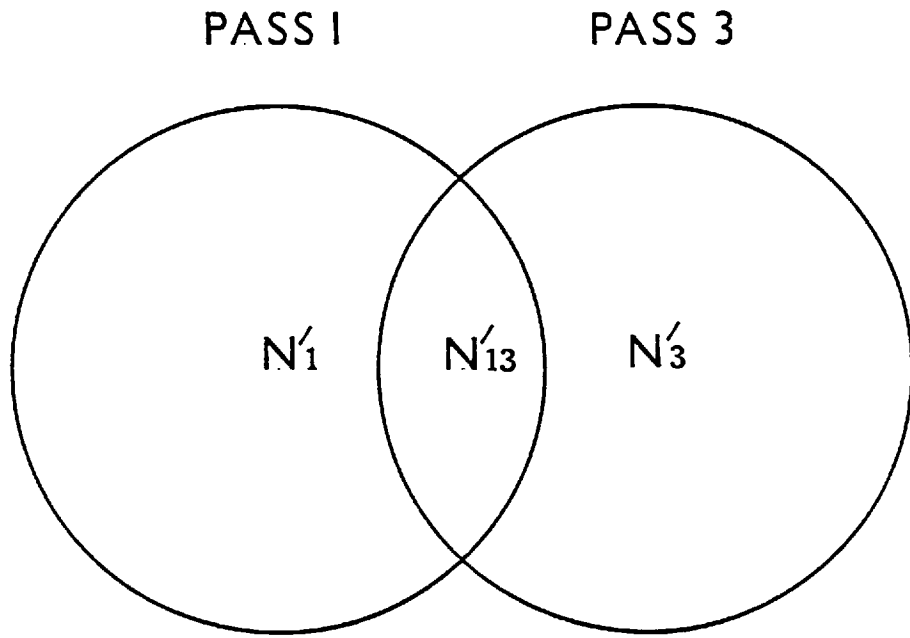


PASS 2

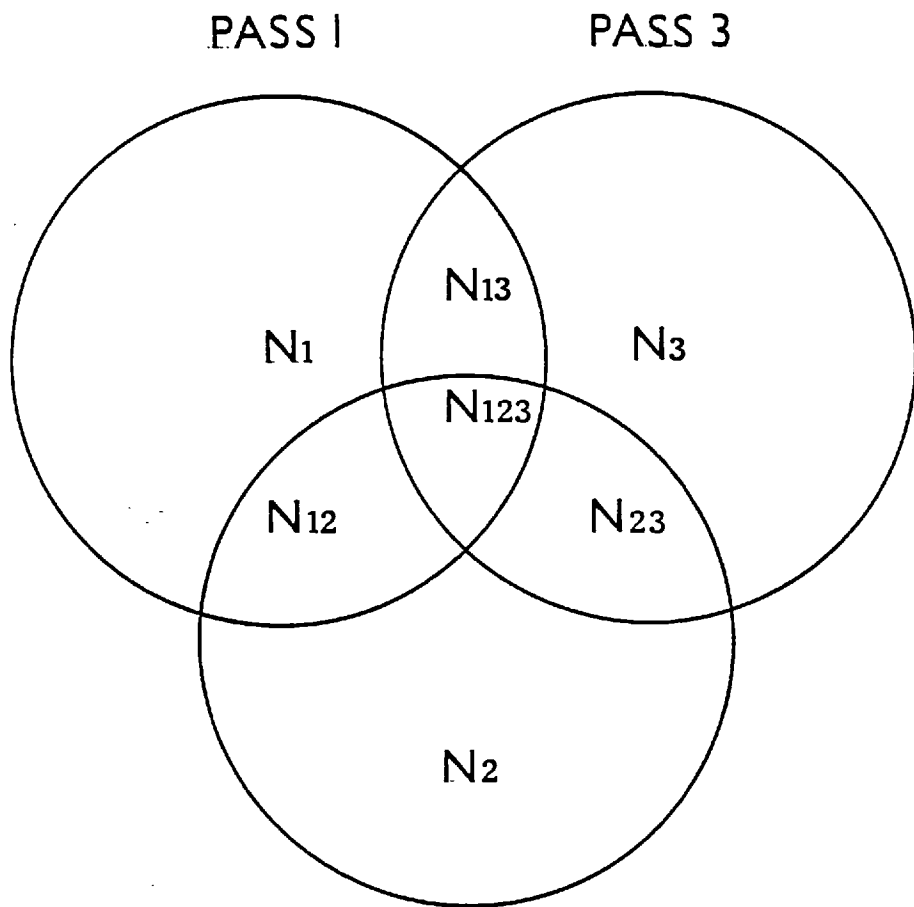


PASS 3





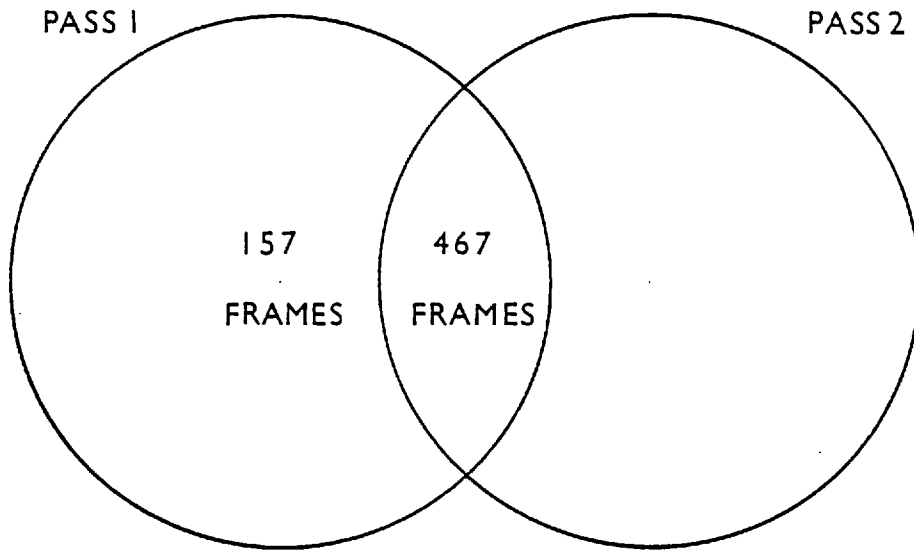
1.15a



PASS 2

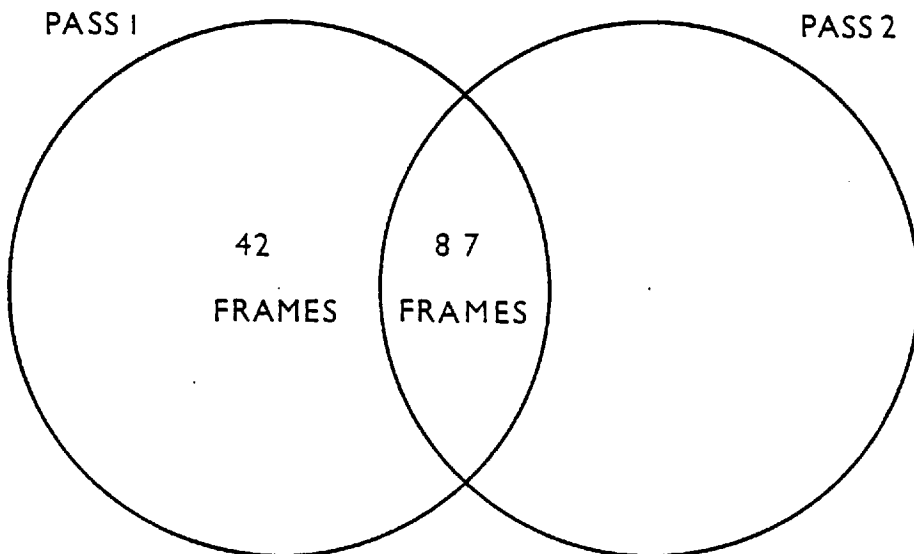
1.15b

UNASSOCIATED K_L^0
DECAYS

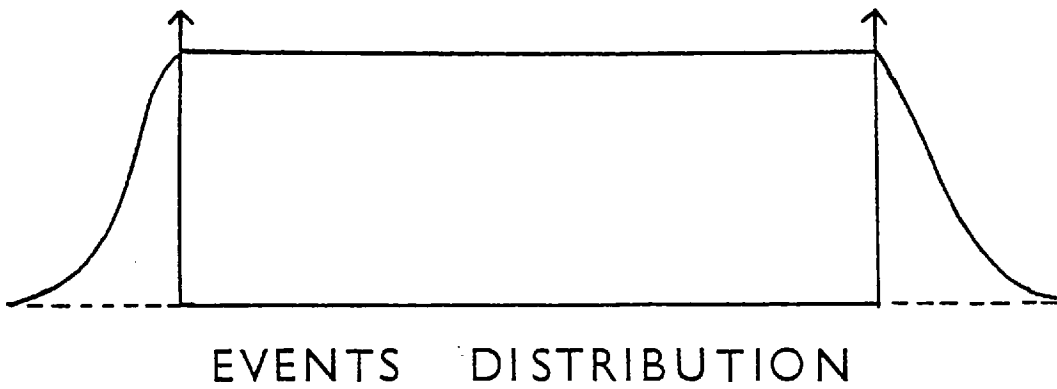
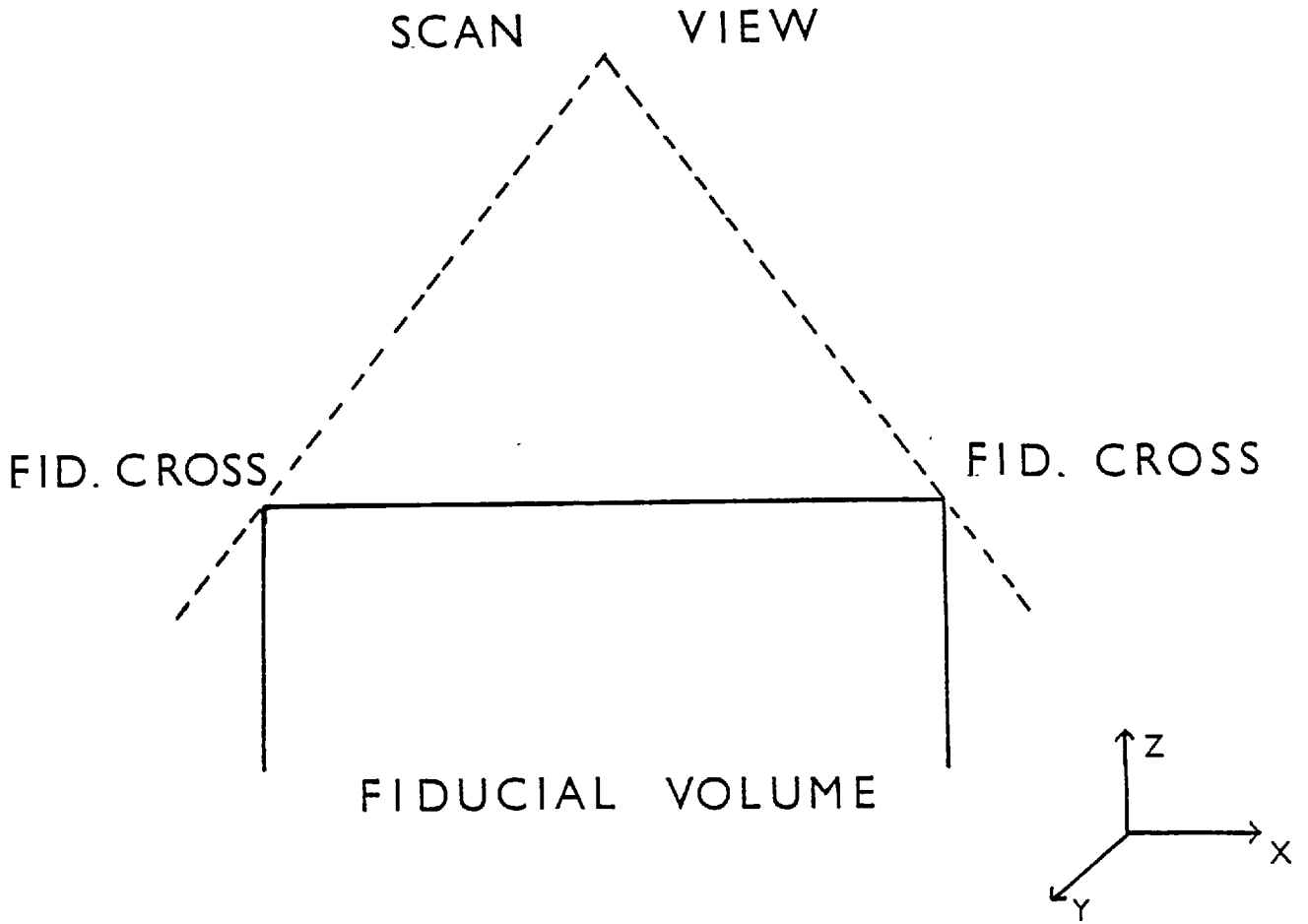


1.16a

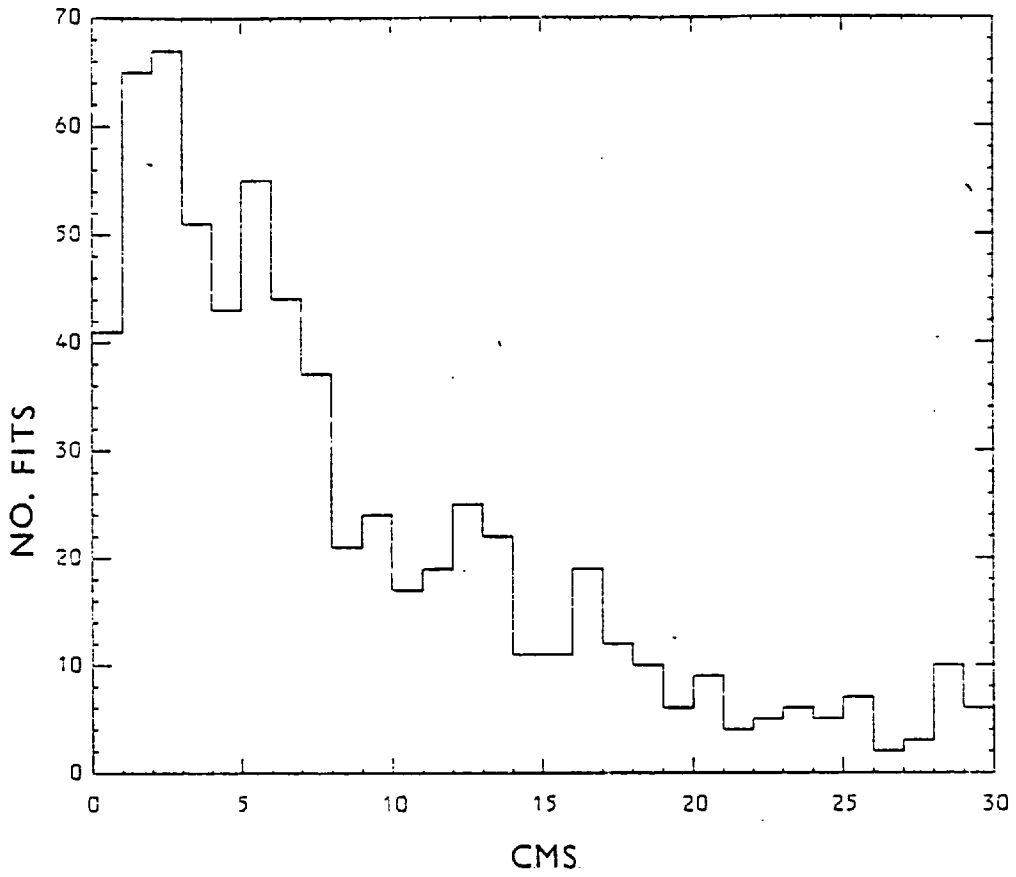
ASSOCIATED K_L^0
DECAYS



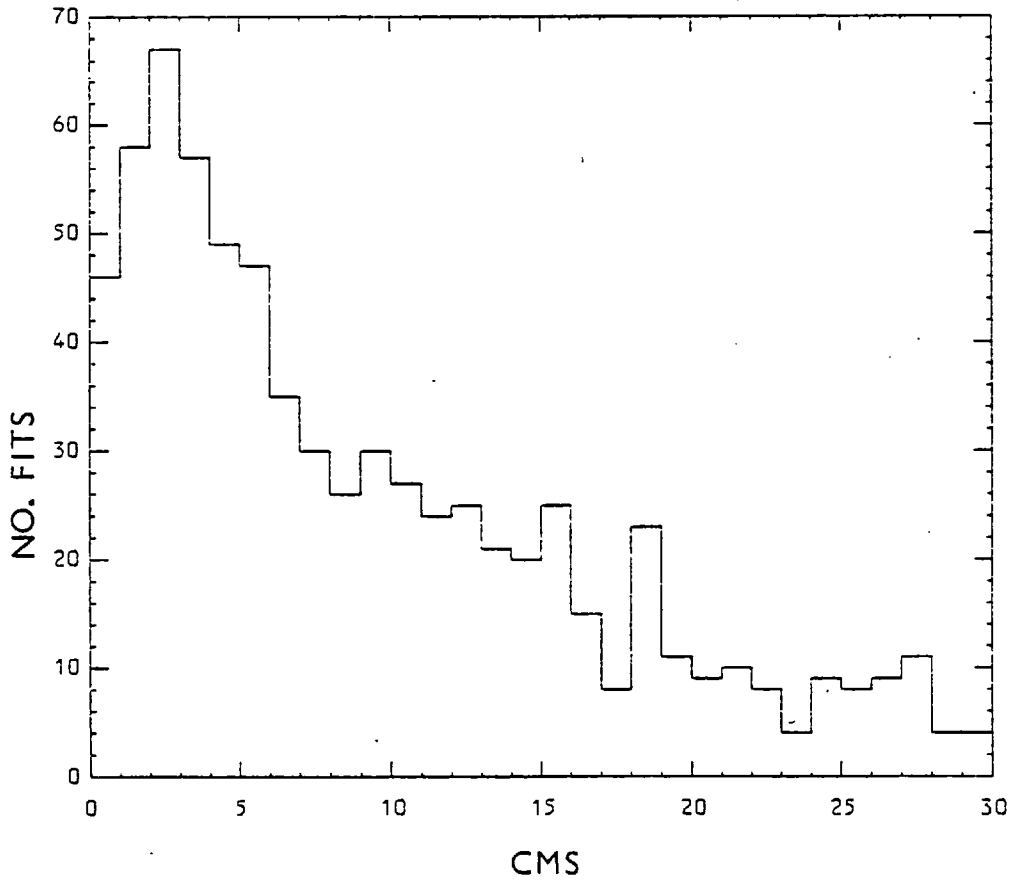
1.16b



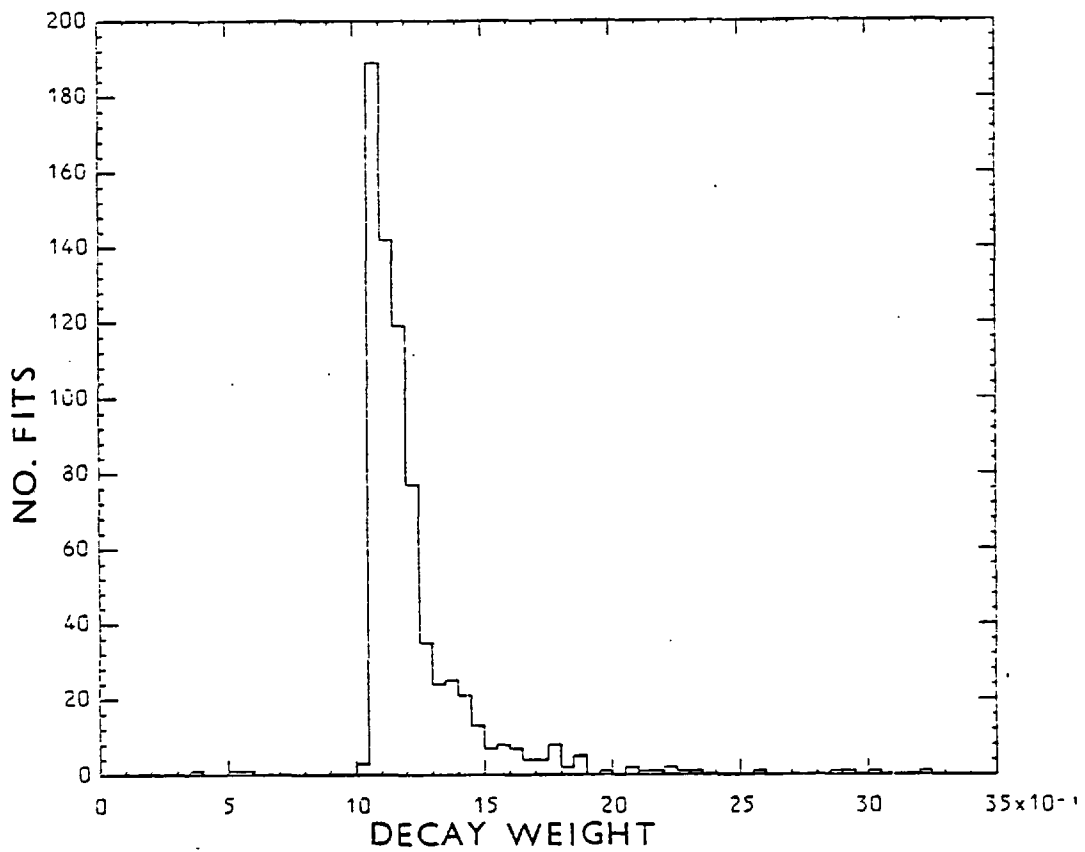
PROJ.-DECAY DISTANCE FOR I.C.



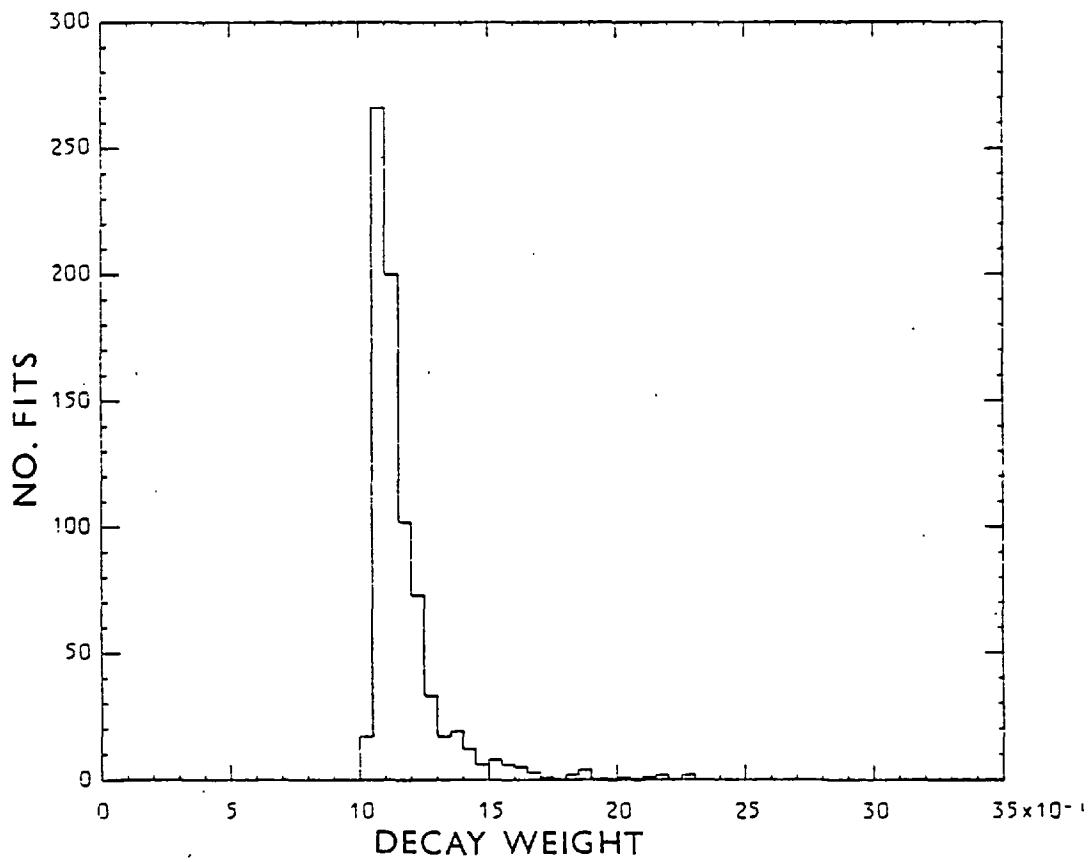
PROJ.-DECAY DISTANCE FOR CAMB

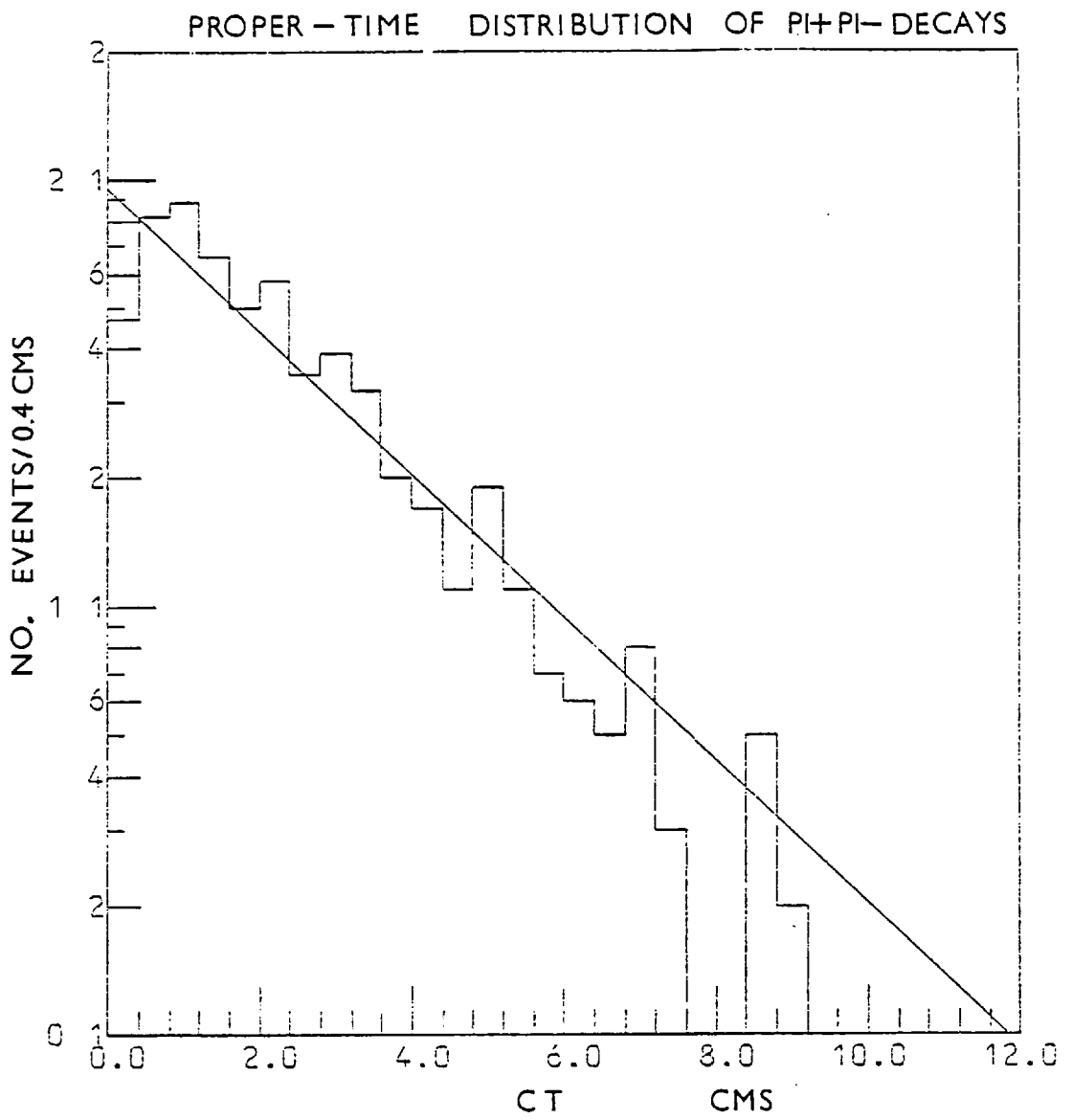


DISTRIBUTION OF I.C.DECAY WEIGHTS



DISTRIBUTION OF CAMB.DECAY WEIGHTS





1.20

CHAPTER 2

K_L^0 Beam Spectrum Determination

2.1 Introduction

Cross-section normalisation for the K_L^0 experiment is achieved using the information present in the decay of K_L^0 beam particles. As the products of these decays contain a neutral particle and the K_L^0 beam momentum is unknown, they cannot be fitted and fall under the zero constraint category. The K_L^0 momentum spectrum is instead obtained by a Monte-Carlo simulation of the five main visible decay modes of K_L^0 .

$$K_L^0 \rightarrow \pi^\pm e^\mp \bar{\nu}_e$$

$$K_L^0 \rightarrow \pi^\pm \mu^\mp \bar{\nu}_\mu$$

$$K_L^0 \rightarrow \pi^+ \pi^- \pi^0$$

These decays appear mainly as two-prong events un-associated with any interaction in the chamber together with a small fraction of events (18%) scanned initially as associated with an interaction but which are subsequently reclassified as beam decays after measurement and geometrical reconstruction.

A sensitive Monte-Carlo variable from which the K_L^0 beam spectrum can be simulated and fitted to the data is, ' p_{VIS} '⁽¹⁾, the visible longitudinal momentum for each decay event, defined as

$$p_{VIS} = (\vec{p}_1 + \vec{p}_2) \cdot \hat{n} \quad 2.1$$

where \vec{p}_1 and \vec{p}_2 are the three-momenta of the two charged tracks and \hat{n} is a unit vector along the beam direction. Another variable that will also be used in simulation is the opening angle between the two charged tracks, ' θ_{op} ', defined as

$$\cos \theta_{op} = \frac{\vec{p}_1 \cdot \vec{p}_2}{|\vec{p}_1| |\vec{p}_2|} \quad 2.2$$

2.2 Removal of Background Events

To remove decays of K_S^0 , Λ , $\bar{\Lambda}$ and gamma materialisations from the K_L^0 decay data, the appropriate masses were assigned to the charged tracks of the V^0 and the effective mass computed. Any V^0 whose effective mass fell within the limits defined in (1-4) was removed from the data sample, figure (2.1).

- (1) $0.480 < M(\pi^+ \pi^-) < 0.510$ Gev
- (2) $1.105 < M(p \pi^-) < 1.125$ Gev
- (3) $1.105 < M(\bar{p} \pi^+) < 1.125$ Gev
- (4) $M(e^+ e^-) < 0.025$ Gev;

To reduce other sources of background, V_S^0 were required to satisfy the following conditions (a-c), figure (2.2).

- (a) Transverse momentum to the beam direction was less than 0.240 Gev/c for both charged decay tracks and the neutral track, so that the K_L^0 decay was consistent from having come from the target.

- (b) The opening angle between the two charged tracks was less than 40° , so as to eliminate wide angle decays such as $\pi^\pm \rightarrow \mu^\pm \nu$ simulating a true K_L^0 decay.

- (c) The momenta of both charged tracks was greater than $0.050 \text{ Gev}/c$ to exclude events such as $\pi^\pm p \rightarrow \pi^\pm p$ with a proton range less than a millimeter.

The V^0 decay volume boundaries were chosen on the basis of the coordinate distributions to be,

$$\begin{aligned} -72 < x < 46 & \text{ cms} \\ -13 < y < 15 & \text{ cms} \\ -18 < z < -33 & \text{ cms} \end{aligned}$$

The final V^0 decay sample contained 4088 events and figure (2.3) shows the experimental p_{VIS} and opening angle distribution. The cuts outlined above, however remove a fraction of true K_L^0 decays but are also applied to the Monte-Carlo events so that there is no bias in the determination of the K_L^0 momentum spectrum.

2.3 K_L^0 Decay Matrix Elements

The Monte-Carlo program FOWL⁽²⁾ which outputs the theoretical distributions of p_{VIS} and θ_{op} , includes USER subroutines which calculate the matrix elements squared of the main K_L^0 decay modes. These serve to weight the phase space distributions generated by the program. For $K_L^0 \rightarrow \pi^+ \pi^- \pi^0$ the form of the matrix element squared was⁽³⁾,

$$|M|^2 = 1 + g \frac{(S3 - S0)}{m_{\pi^\pm}^2} \quad 2.3$$

$$S3 = (m_{K_L^0} - m_{\pi^0})^2 - 2m_{K_L^0} (E_{\pi^0} - m_{\pi^0})$$

$$S0 = \frac{(m_{K_L^0}^2 + 2m_{\pi^\pm}^2 + m_{\pi^0}^2)}{3}$$

$$g = 0.64$$

For the leptonic decays of K_L^0 the form used was⁽⁴⁾,

$$|M|^2 = (A + B\xi(t) + C\xi^2(t))f^+(t) \quad 2.4$$

where A, B and C are kinematic variables defined below, $\xi(t)$ and $f^+(t)$ are 'form' factors and are functions of four-momentum transfer squared t between the K_L^0 and the pion.

$$A = m_{K_L^0} (2E_\nu E_\ell - m_{K_L^0} E'_\pi) + m_\ell^2 \left(\frac{E'_\pi}{4} - E_\nu \right)$$

$$B = m_\ell^2 \left(E_\nu - \frac{E'_\pi}{2} \right)$$

$$C = m_\ell^2 \frac{E'_\pi}{4}$$

$$E_{\pi}^{\prime} = E_{\pi}^{\max} - E_{\pi}$$

$$E_{\pi}^{\max} = \frac{m_{K_L^0}^2 + m_{\pi}^2 - m_{\ell}^2}{2m_{K_L^0}}$$

$$t = m_{K_L^0}^2 - 2m_{K_L^0} E_{\pi} + m_{\pi}^2$$

and 'l' is the lepton e, μ in $K_L^0 \rightarrow \pi^{\pm} e^{\mp} \bar{\nu}_e$

$$K_L^0 \rightarrow \pi^{\pm} \mu^{\mp} \bar{\nu}_{\mu}$$

2.4 Form Factors

Previous experimental results and parameterisation of the form factors are conflicting. The ' λ^+ , $\xi(o)$ ' parameterisation (5) has been used for both leptonic decays with λ^- set to zero. The form factors $\xi(t)$ and $f^+(t)$ can be expanded in terms of the four-momentum transfer squared t and the form factor constants λ^+ and $\xi(o)$ as

$$\xi(t) = \frac{f^-(t)}{f^+(t)} = \xi(o) \left(1 - \frac{\lambda^+ t}{2m_{\pi}^2}\right)$$

$$f^+(t) = f^+(o) \left(1 + \frac{\lambda^+ t}{2m_{\pi}^2}\right) \tag{2.5}$$

The values chosen for λ^+ and $\xi(o)$ are the world average values (6)

$$\underline{K_L^0 \rightarrow \pi\mu\nu}$$

$$\lambda_+ = 0.034$$

$$\xi(o) = -0.17$$

$$\underline{K_L^0 \rightarrow \pi e\nu}$$

$$\lambda_+ = 0.0288$$

$$\xi(o) = -0.17$$

The theoretical Monte-Carlo distributions for p_{VIS} and θ_{op} generated using phase space only are not substantially different from those using the variable matrix elements described above. For the leptonic decay mode $K_L^0 \rightarrow \pi^\pm e^\mp \nu$, terms containing m_μ^2 which are B and C in equation (2.4) are very small compared with term A, and there is therefore only a very weak dependence on the form factors λ^+ and $\xi(o)$.

2.5 Derivation of the K_L^0 momentum Spectrum

The K_L^0 beam spectrum can be considered as being constructed from consecutive momentum intervals as illustrated schematically in figure (2.4). An infinite number of such momentum bands would be needed to describe the spectrum profile precisely, however statistical limitations on the data and computing time needed to generate sufficient events restrict the number used. Each momentum band as input to the program FOWL will generate a corresponding p_{VIS} and θ_{op} distribution and it is the task of the fitting program to decide what combination of these theoretical distributions, corresponding to each successive momentum interval, best fits the experimental data.

Considerable experience was gained in deciding the optimum number

and width of the momentum intervals for eg., a few wide momentum bands spanning the known K_L^0 momentum range, failed to give an adequate fit to the p_{VIS} data and it became apparent that to fit this distribution well, particularly in the region under 3 Gev/c where the p_{VIS} bins are heavily populated figure (2.3), the width of the K_L^0 momentum intervals in figure (2.4) would need to decrease towards zero K_L^0 momentum, because these bins in low p_{VIS} receive contributions from successively more K_L^0 momentum components. As the K_L^0 momentum increases, the momentum intervals in figure (2.4) can be widened as the corresponding p_{VIS} distributions shift towards higher momenta and need relatively fewer momentum components to describe sufficiently well. The rapid rise in the K_L^0 momentum spectrum figure (2.4) also requires the width of the momentum intervals to decrease towards zero momentum, and for the first and last momentum bins a 'sawtooth' shape profile is generated to simulate the rapid rise in the beam profile.

In addition to the matrix element squared term in FOWL, a weighting factor equal to $1/p_{K_L^0}$ is added to allow for the relative decay probability of K_L^0 s with momentum $p_{K_L^0}$ inside some finite momentum interval between $p_{K_L^0}$ and $p_{K_L^0} + \Delta p_{K_L^0}$. The Monté-Carlo events are Lorentz transformed from the K_L^0 centre of mass to the laboratory frame, after which the same cuts are applied to the theoretical p_{VIS} and θ_{op} events as were made on the corresponding experimental data. The distributions for each momentum interval and decay mode are normalized to unity and are combined by a factor depending on the known branching ratios for each decay mode and the fraction of events for each mode that survive the cuts.

2.6 Combination of the Monte-Carlo distributions

If α^i , β^i and γ^i are the fractions of generated events that survive the cuts for each mode at momentum interval 'i' (estimated from FOWL) and ϵ_1 , ϵ_2 and ϵ_3 are the branching ratios for each decay mode, where

$$\begin{aligned} \epsilon_1 &= \frac{K_L^0 \rightarrow (\pi^+ \pi^- \pi^0)}{K_L^0 \rightarrow (\text{charged})} = 0.1564 \\ \epsilon_2 &= \frac{K_L^0 \rightarrow (\pi^\pm \mu^\mp \bar{\nu}_\mu)}{K_L^0 \rightarrow (\text{charged})} = 0.3461 \\ \epsilon_3 &= \frac{K_L^0 \rightarrow (\pi^\pm e^\mp \bar{\nu}_e)}{K_L^0 \rightarrow (\text{charged})} = 0.4975 \end{aligned}$$

Then $(\alpha^i \epsilon_1 + \beta^i \epsilon_2 + \gamma^i \epsilon_3)$ is the fraction of all seen K_L^0 modes that survive the cuts at momentum interval 'i'. In general this quantity is less than unity, so that in combining the distributions of the different decay modes, the final branching fractions used were

$$\frac{\alpha^i \epsilon_1}{(\alpha^i \epsilon_1 + \beta^i \epsilon_2 + \gamma^i \epsilon_3)} \quad \text{for } K_L^0 \rightarrow \pi^+ \pi^- \pi^0$$

$$\frac{\beta^i \epsilon_2}{(\alpha^i \epsilon_1 + \beta^i \epsilon_2 + \gamma^i \epsilon_3)} \quad \text{for } K_L^0 \rightarrow \pi^\pm \mu^\mp \bar{\nu}_\mu$$

$$\frac{\gamma^i \epsilon_3}{(\alpha^i \epsilon_1 + \beta^i \epsilon_2 + \gamma^i \epsilon_3)} \quad \text{for } K_L^0 \rightarrow \pi^\pm e^\mp \bar{\nu}_e$$

2.7 Fitting the p_{VIS} distribution

The program MINUIT ⁽⁷⁾ performs a chi-squared minimization procedure in fitting the set of theoretical distributions of p_{VIS} to the experimental data. For an initial set of ' X_j ' which represents the amount of each distribution in p_{VIS} at momentum interval j , the number of events in each theoretical bin of p_{VIS} denoted by index 'i' is given by,

$$T_i = \sum_j X_j H_{ij} \quad 2.6$$

where H_{ij} is the matrix of Monte-Carlo $p_{VIS} - p_{K_L^0}$ values. The best set of X_j is found by minimising $\chi^2(X_1, X_2 \dots X_N)$ where χ^2 is given by,

$$\chi^2 = \sum_{i=1,n} \frac{(T_i - N_i)^2}{N_i} \quad 2.7$$

and the summation in 'i' is over the total number of p_{VIS} bins. Because of the requirement in fitting to have at least ten events per bin ⁽⁸⁾ (0.2 Gev/c), the bins in the experimental p_{VIS} distribution beyond 12 Gev/c are combined together so as to satisfy this condition, resulting in a total of sixty-eight bins. To ensure a continuous behaviour in the ' X_j ' coefficients with K_L^0 momentum, a smoothing parameter proportional to

$$\sum_j \left(\frac{(X_{j+1} - X_j)}{\Delta p_j} - \frac{(X_j - X_{j-1})}{\Delta p_{j-1}} \right)^2 \quad 2.8.$$

where ' Δp_j ' is the width of momentum interval j , was added to the term on the right hand side of equation (2.7). This additional term ⁽⁹⁾, whose constant of proportionality was chosen empirically, constrains a

a smooth behaviour on the coefficients X_j without significantly adding to the chi-squared contribution. Twenty-five coefficients corresponding twenty-five consecutive momentum intervals were used in the description of the K_L^0 beam spectrum from 0-17 Gev/c, and the final fitted values of these coefficients required to minimize the chi-squared function are given in table (2.1). The fit to the p_{VIS} distribution is shown in figure (2.3), giving a $\chi^2 = 54.83$ for forty-two degrees of freedom. The set of p_{VIS} distributions corresponding to the fitted values of X_j , which comprise the fit to the total p_{VIS} data are shown in figure (2.5). The theoretical opening angle distribution is obtained from the fitted X_j and the Monte-Carlo θ_{op} distributions and provides a satisfactory fit to the experimental opening angle distribution figure (2.3).

To determine the statistical errors on the X_j coefficients, the experimental p_{VIS} distribution in each bin is independently altered from its original value N^i to $N^i \pm \delta N^i$, where δN^i is the product of a Gaussian distributed random number and the standard deviation of the original bin equal to $\sqrt{N_i}$. This procedure is repeated twenty-five times and the standard deviation of the corresponding coefficients X_j obtained by refitting the separate p_{VIS} distributions is taken as the statistical error, table (2.1).

2.8 Beam flux weighting

To obtain the absolute flux of K_L^0 at the entrance of the chamber, the coefficients X_j have to be weighted by the inverse probability of K_L^0 s decaying within the fiducial volume length 'L' specified in 2.2.

Allowance must also be made for unseen decay modes of K_L^0 , scanning and measuring efficiency losses and K_L^0 s lost by the action of the cuts.

The flux at the chamber, ' $N_j(p_{K_L^0})$ ', is related to $X_j(p_{K_L^0})$ by

$$N_j(p_{K_L^0}) = \frac{1}{e_s e_m r C(p_{K_L^0})} (1 - e^{-L/\lambda(p_{K_L^0})})^{-1} X_j(p_{K_L^0}) \quad 2.9$$

where e_s = scanning efficiency for K_L^0 s
 e_m = measuring efficiency for K_L^0 s
 r = branching ratio, $\frac{K_L^0 \rightarrow (\text{charged})}{K_L^0 \rightarrow (\text{all})}$

$C(p_{K_L^0})$ = fraction of visible K_L^0 decay modes that survive the cuts.

$$\lambda(p_{K_L^0}) = \frac{p_{K_L^0}}{m_{K_L^0}} c\tau_{K_L^0}, \quad K_L^0 \text{ mean decay length}$$

L = length of decay volume (118 cms)

As no geometry processing of events from pass 2 was done, no estimate for the K_L^0 scanning efficiency of pass 1 is available as explained in chapter 1 section 1.5, instead the scanning efficiency estimate for pass 2 is assumed. The scanning and measuring efficiency values to be used in equation (2.9) are complicated by the fact that the K_L^0 s comprising the p_{VIS} data sample fall into two categories as discussed in the previous

chapter, namely those scanned and measured as unassociated V^0 s (3314) and a smaller number scanned and measured as associated with an interaction vertex (779). Because of the low statistics involved in the determination of K_L^0 s scanned as associated (0.67 ± 0.09), it was decided to use the more reliable estimate for the unassociated V^0 sample (0.75 ± 0.05), as in any case combining the statistics of the two samples yields an average K_L^0 scanning efficiency of (0.74 ± 0.04). The measuring efficiency of the V^0 s scanned as unassociated from table(1.8) is (0.85 ± 0.01) and the measuring efficiency of V^0 s scanned and measured as associated is taken as the mean of efficiencies of events with at least one associated V^0 (0.73 ± 0.01). The total 'throughput' efficiency ($e_s e_m$) is then a weighted mean of the respective values equal to (0.62 ± 0.04). The momentum dependent factor $C(p_{K_L^0})$ which is equal to the fraction of K_L^0 that survive the cuts is estimated from the FOWL Monte-Carlo output at each different momentum interval. Suitable units with which to express the K_L^0 flux at the two metre chamber entrance are K_L^0 per frame, where the total number of frames corresponding to the sample of K_L^0 used is 154600 frames. The K_L^0 momentum histogram is rebinned into more convenient momentum intervals in table(2.2) and the resulting K_L^0 beam spectrum is shown in figure (2.6).

The estimated total K_L^0 flux per frame is 9.89 ± 0.67 the error on flux estimate reflecting the uncertainty in the K_L^0 throughput efficiency $e_s e_m$. Using a different fitting procedure our collaborators obtained a flux estimate of $9K_L^0$ per frame with an overall throughput efficiency of 0.83. Normalizing the I.C. spectrum to $9K_L^0$ per frame as in figure (2.7) shows that apart from the 2-3 GeV/c interval where the spectrum is rising rapidly, the two profiles are in good agreement.

The fitted Spectrum Coefficients

Table 2.1

K_L^0 momentum intervals (Gev/c)	Spectrum Coefficient ' X_j ' (K_L^0 s)	Weighted Spectrum Coefficients ' N_j ' (K_L^0 s / frame)
0.1 - 0.4	6.14 ± 3.68	0.041 ± 0.244
0.4 - 0.6	0.05 ± 2.86	0.0 ± 0.008
0.6 - 0.8	19.04 ± 5.72	0.028 ± 0.008
0.8 - 1.0	65.13 ± 8.18	0.064 ± 0.008
1.0 - 1.4	122.29 ± 11.45	0.095 ± 0.009
1.4 - 1.8	219.22 ± 15.94	0.172 ± 0.013
1.8 - 2.2	269.21 ± 14.72	0.248 ± 0.014
2.2 - 2.6	289.07 ± 10.22	0.309 ± 0.011
2.6 - 3.0	299.90 ± 13.90	0.367 ± 0.017
3.0 - 3.4	313.31 ± 19.21	0.433 ± 0.027
3.4 - 4.2	327.86 ± 22.48	0.531 ± 0.036
4.2 - 5.0	334.34 ± 20.03	0.650 ± 0.039
5.0 - 5.8	296.86 ± 21.26	0.673 ± 0.048
5.8 - 6.6	242.46 ± 18.80	0.628 ± 0.049
6.6 - 7.4	203.04 ± 20.44	0.593 ± 0.059
7.4 - 8.2	174.61 ± 19.62	0.566 ± 0.064
8.2 - 9.0	150.12 ± 16.76	0.536 ± 0.060
9.0 - 10.0	128.17 ± 19.21	0.505 ± 0.076
10.0 - 11.0	103.54 ± 16.76	0.450 ± 0.073
11.0 - 12.0	94.03 ± 14.31	0.447 ± 0.068
12.0 - 13.0	90.95 ± 19.62	0.470 ± 0.102
13.0 - 14.0	89.71 ± 16.76	0.501 ± 0.094
14.0 - 15.0	85.90 ± 15.13	0.514 ± 0.091
15.0 - 16.0	84.61 ± 13.08	0.541 ± 0.084
16.0 - 17.0	78.40 ± 16.76	0.529 ± 0.113
	(Total=4088 K_L^0 s)	(Total=9.89 K_L^0 s / frame)

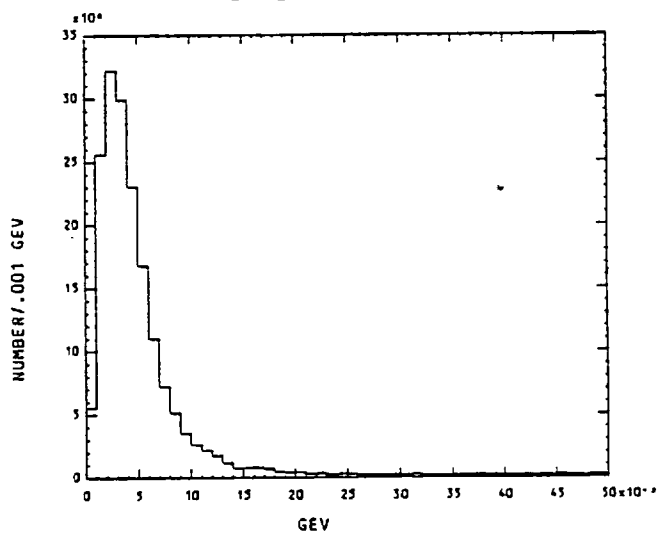
Table 2.2

The K_L^0 Beam Spectrum Values

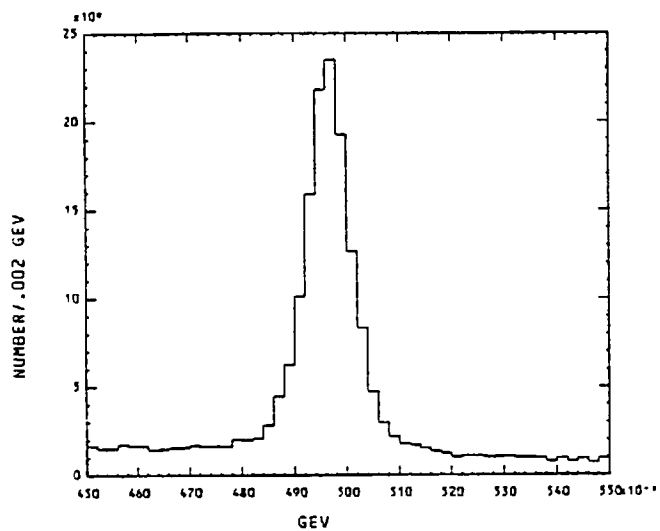
K_L^0 momentum intervals (Gev/c)	K_L^0 flux (K_L^0 / frame / Gev/c)
0.0 - 1.0	0.133 ± 0.027
1.0 - 2.0	0.392 ± 0.017
2.0 - 3.0	0.80 ± 0.021
3.0 - 4.0	0.831 ± 0.038
4.0 - 5.0	0.782 ± 0.040
5.0 - 6.0	0.830 ± 0.049
6.0 - 7.0	0.768 ± 0.047
7.0 - 8.0	0.721 ± 0.056
8.0 - 9.0	0.678 ± 0.062
9.0 - 10.0	0.505 ± 0.076
10.0 - 11.0	0.450 ± 0.073
11.0 - 12.0	0.447 ± 0.068
12.0 - 13.0	0.470 ± 0.102
13.0 - 14.0	0.501 ± 0.094
14.0 - 15.0	0.514 ± 0.091
15.0 - 16.0	0.541 ± 0.084
16.0 - 17.0	0.529 ± 0.113

(Total flux = 9.89 K_L^0 s)

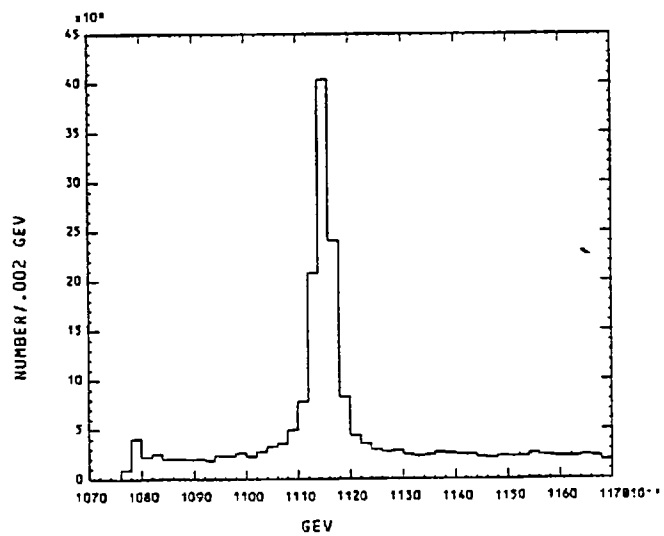
M(E+ E-) DISTRIBUTION



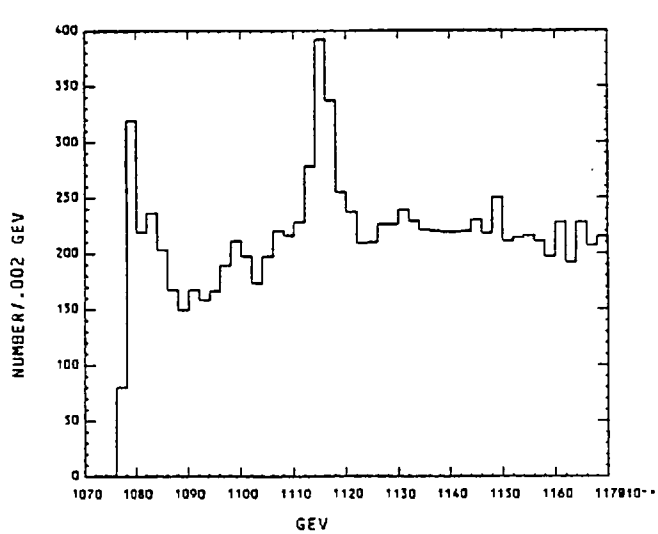
M(PI+ PI-) DISTRIBUTION



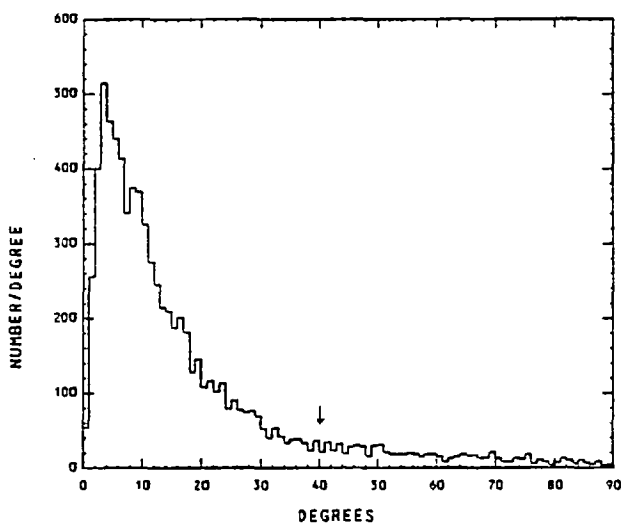
M(P PI-) DISTRIBUTION



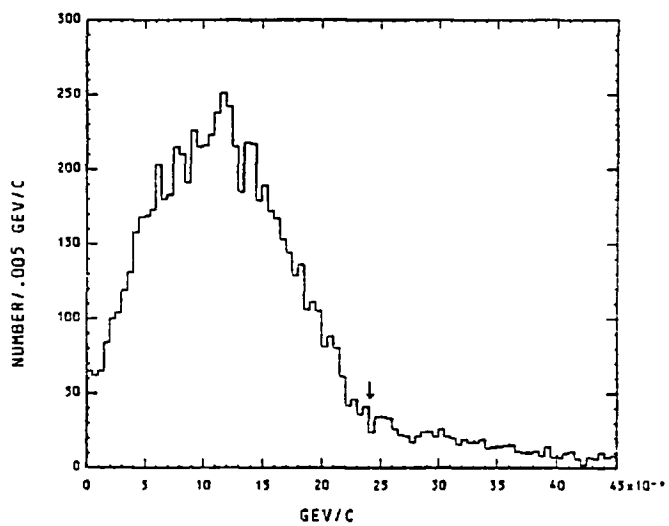
M(PBAR PI+) DISTRIBUTION



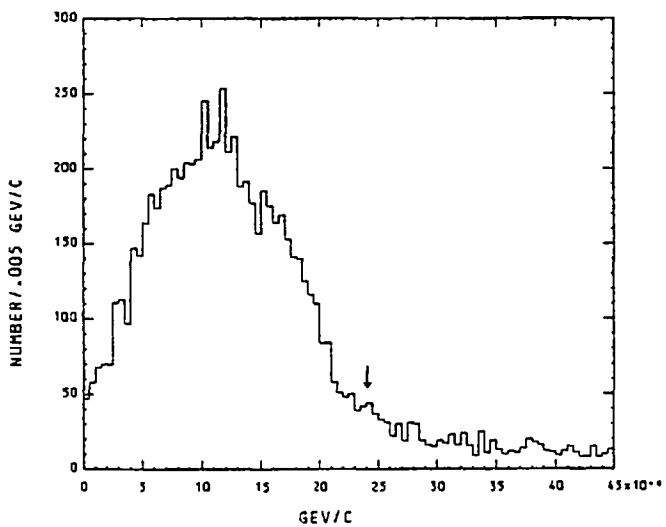
OPENING ANGLE DISTRIBUTION



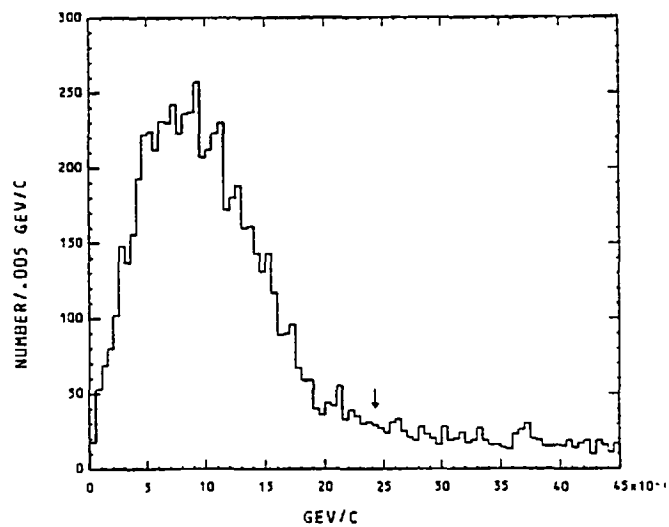
PT OF NEGATIVE TRACK



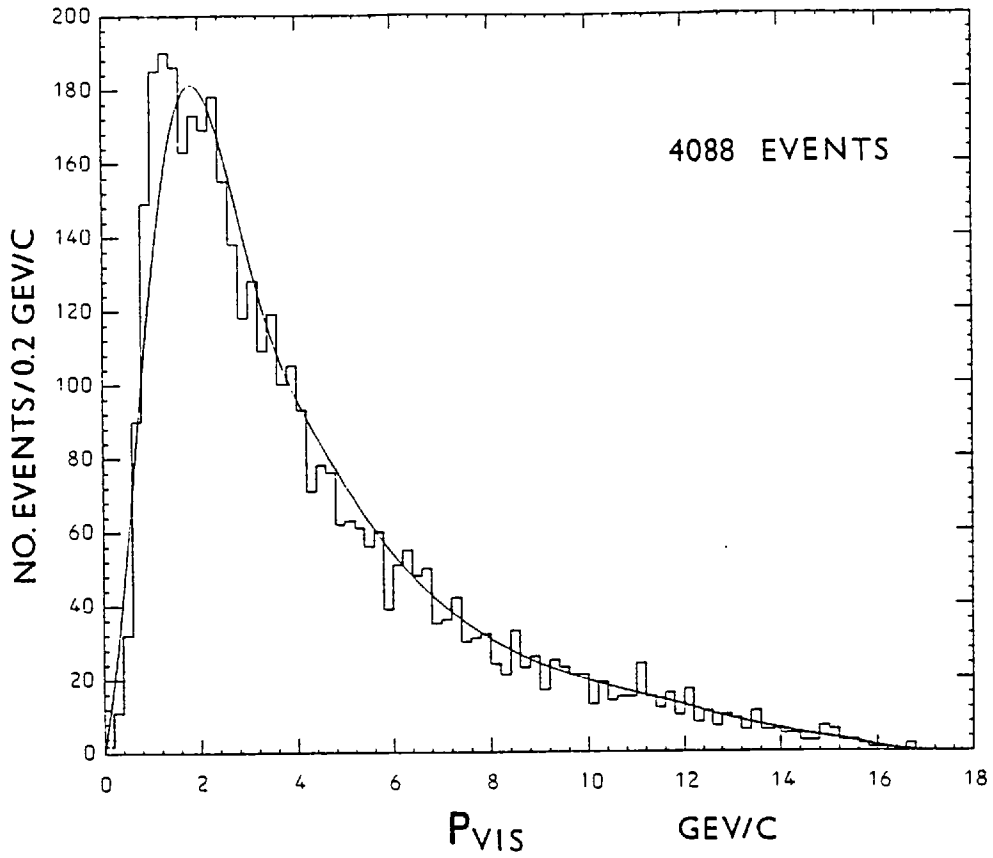
PT OF POSITIVE TRACK



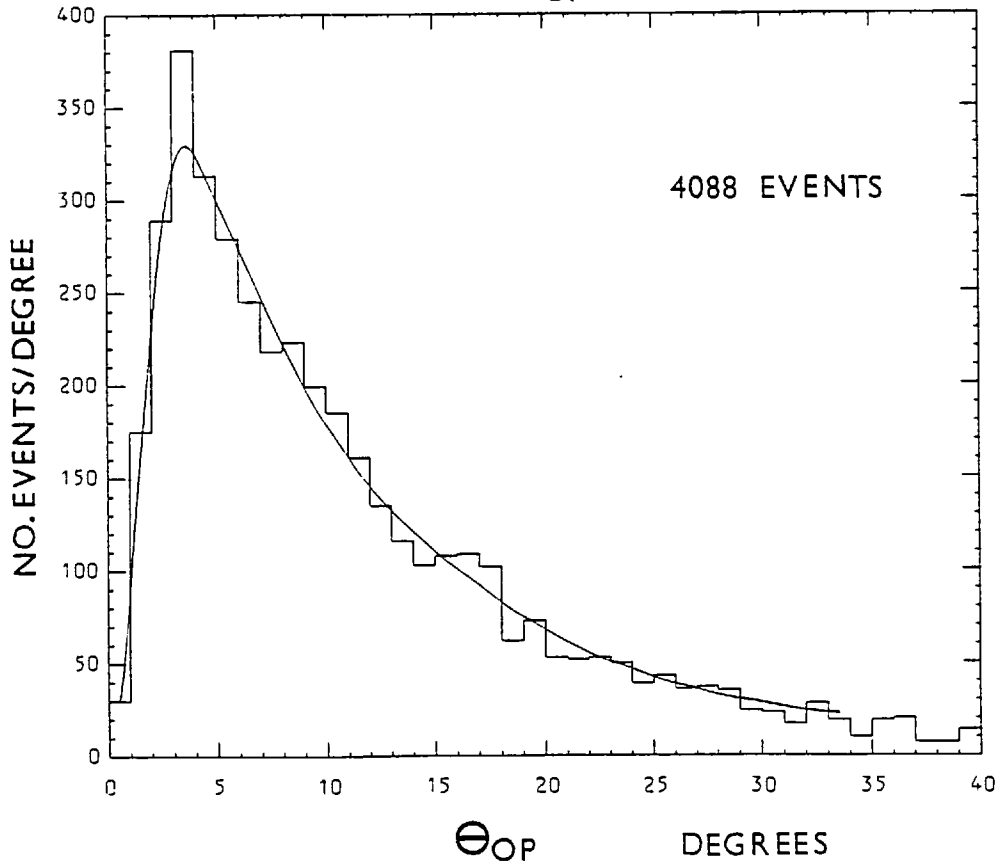
PT OF NEUTRAL TRACK



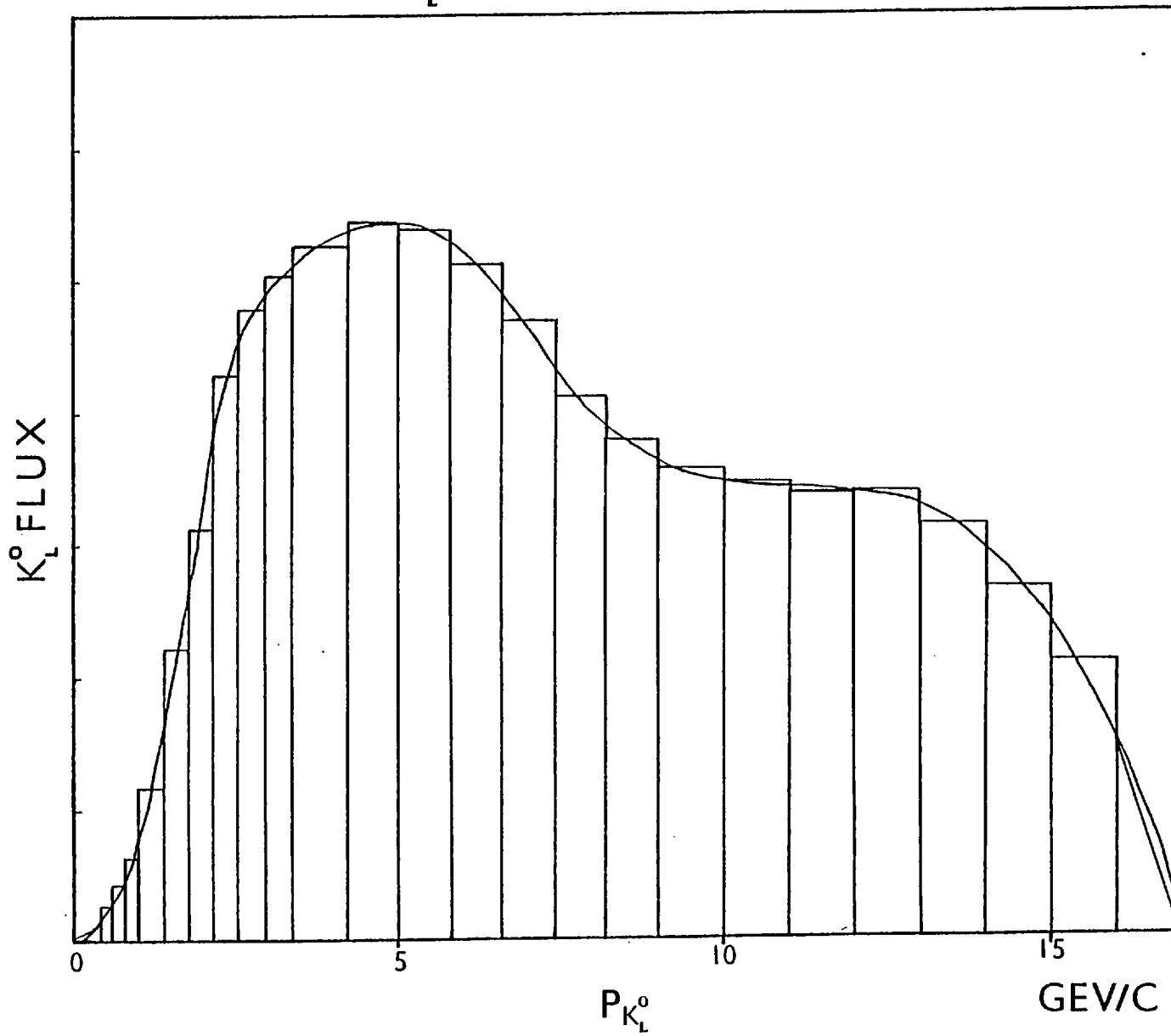
EXPERIMENTAL P_{VIS} DISTRIBUTION



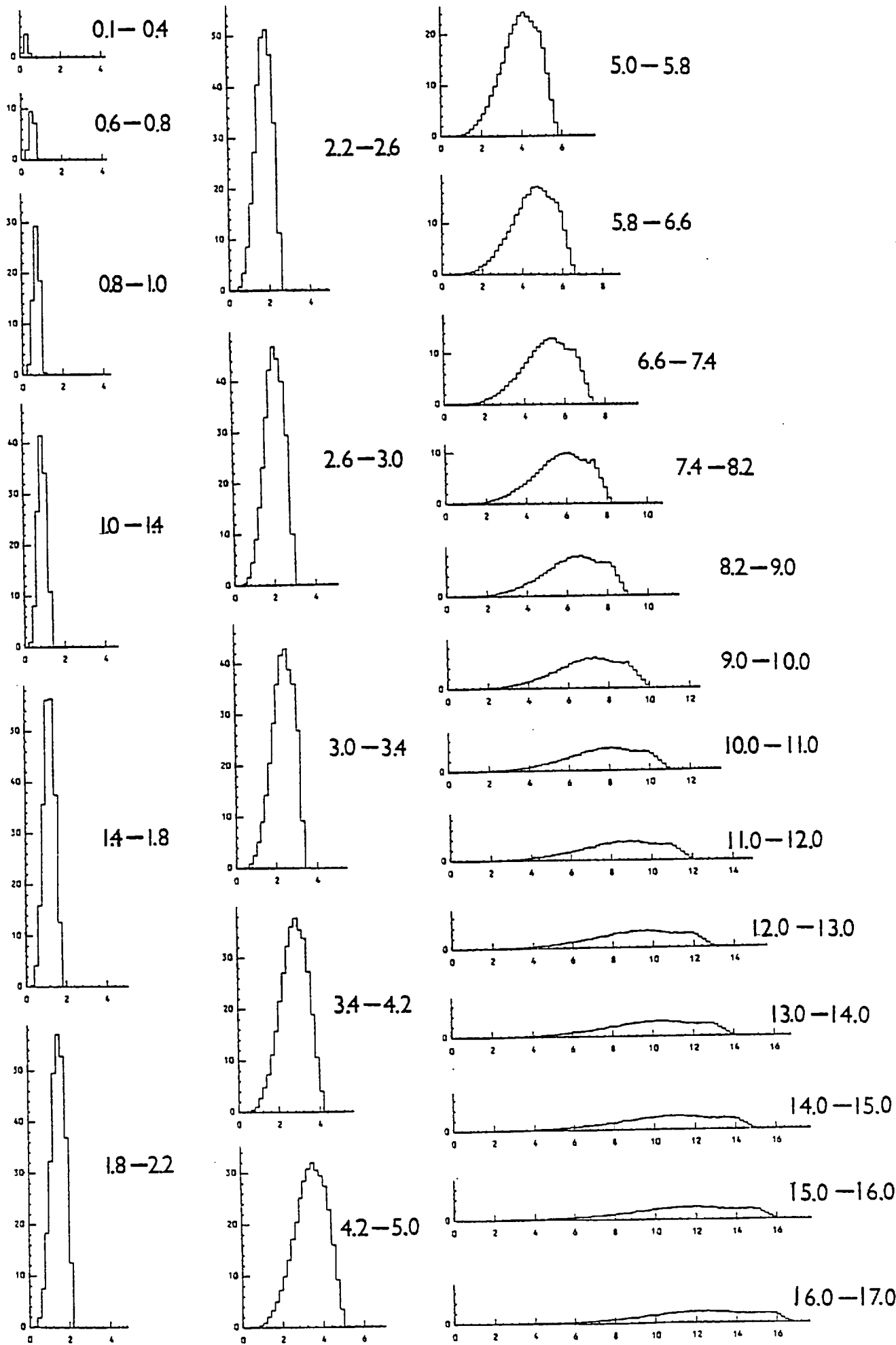
EXPERIMENTAL Θ_{OP} DISTRIBUTION

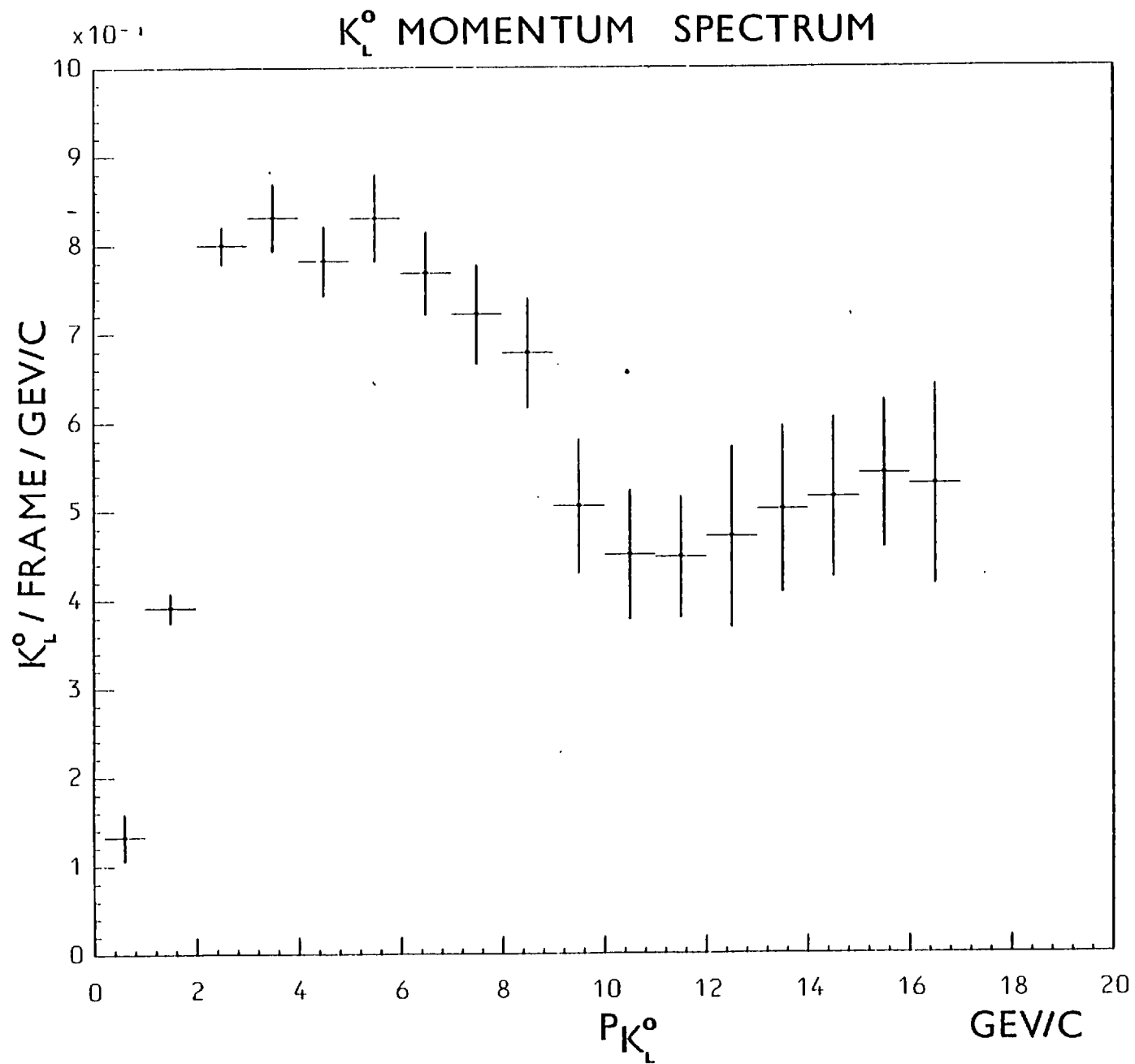


K_L^0 MOMENTUM BANDS

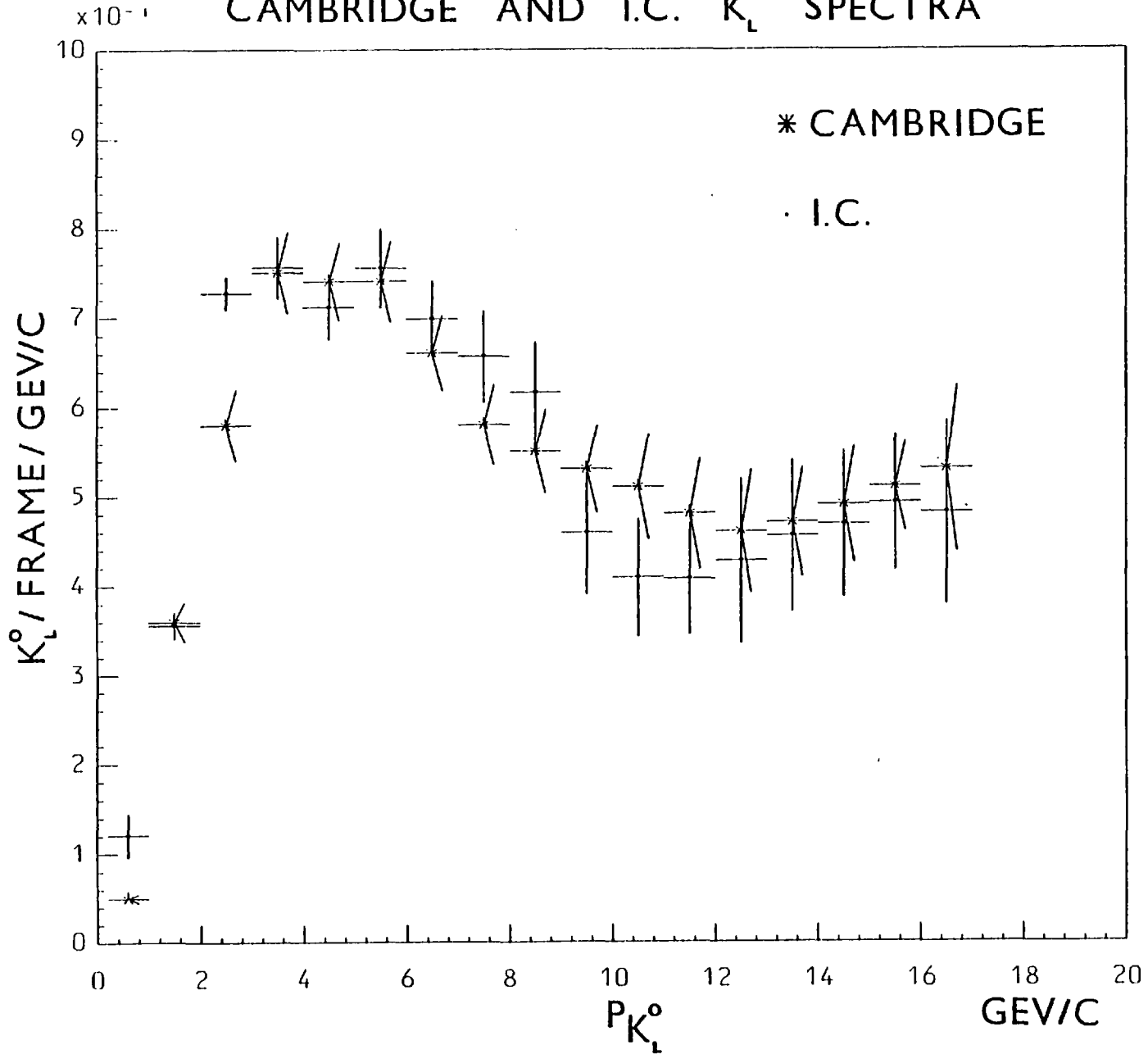


P_{VIS} DISTRIBUTIONS OF THE K_L⁰ MOMENTUM COMPONENTS





CAMBRIDGE AND I.C. K_L^0 SPECTRA



CHAPTER 3

The $(p'_0)^2$ variable and the $K_{S\pi}$ Branching Ratio

3.1 Introduction

A useful kinematic variable for partially separating leptonic three body decays of $K_L^0 (\pi^\pm \mu^\mp \nu_\mu, \pi^\pm e^\mp \nu_e)$ from 'tau' decays ($\pi^+ \pi^- \pi^0$) is the invariant quantity $(p'_0)^2$ (1), defined as the K_L^0 momentum squared in the frame where the combined momentum of the charged pair is transverse to the K_L^0 beam direction assuming a tau decay.

$$(p'_0)^2 = \frac{(m_{K_L^0}^2 - m_\pi^2 - m^2)^2 - 4m_\pi^2 m^2 - 4m_{K_L^0}^2 p_T^2}{4(p_T^2 + m^2)} \quad 3.1$$

where p_T = the transverse momentum of the charged pair

m = effective mass of the charged pair misidentified as π^\pm .

This variable can be rewritten in a more transparent form as (2)

$$(p'_0)^2 = \frac{m_{K_L^0}^2}{(p_T^2 + m^2)} (p_{\pi^0}^{*2} - p_T^2) \quad 3.2$$

$$p_{\pi^0}^{*2} = \frac{(m_{K_L^0}^2 + m_\pi^2 - m^2)^2}{4m_{K_L^0}^2} - m_\pi^2$$

where $p_{\pi^0}^*$ = π^0 momentum in the K_L^0 rest frame assuming a tau decay.

Ignoring resolution effects, true $K_L^0 \rightarrow \pi^+ \pi^- \pi^0$ decays are limited to positive values of $(p'_0)^2$ by equation 3.2, since p_T cannot exceed $p_{\pi^0}^*$.

Leptonic decays which can have a higher transverse momentum than tau

decays, give rise to a large peak at negative $(p'_0)^2$ with a falling tail extending into positive regions of $(p'_0)^2$. The observed $(p'_0)^2$ distribution is shown in figure (3.1).

3.2 $K_{3\pi}$ Branching Ratio

The branching ratio $\alpha = \frac{\Gamma(K_L^0 \rightarrow \pi^+ \pi^- \pi^0)}{\Gamma(K_L^0 \rightarrow \text{charged})}$ can be found by

comparing the experimental $(p'_0)^2$ distribution with a theoretical distribution obtained from a Monte-Carlo simulation of the five main visible decay modes of K_L^0 . Similar cuts were imposed on both the experimental and Monte-Carlo data to remove non- K_L^0 decay events as described in section 2.2 on the determination of the K_L^0 beam spectrum. The Monte-Carlo program also makes allowance for measuring and multiple coulomb scattering errors as described in the program FAKE (3). The resulting experimental sample after cuts contained 4686 events. The theoretical and experimental $(p'_0)^2$ distributions were compared in the interval $-0.051 < (p'_0)^2 < 0.015^*$ and using the established value of the branching ratio $x = \frac{\Gamma(K_L^0 \rightarrow \pi\mu\nu)}{\Gamma(K_L^0 \rightarrow \pi e\nu)}$, set equal to 0.696 (4), the best

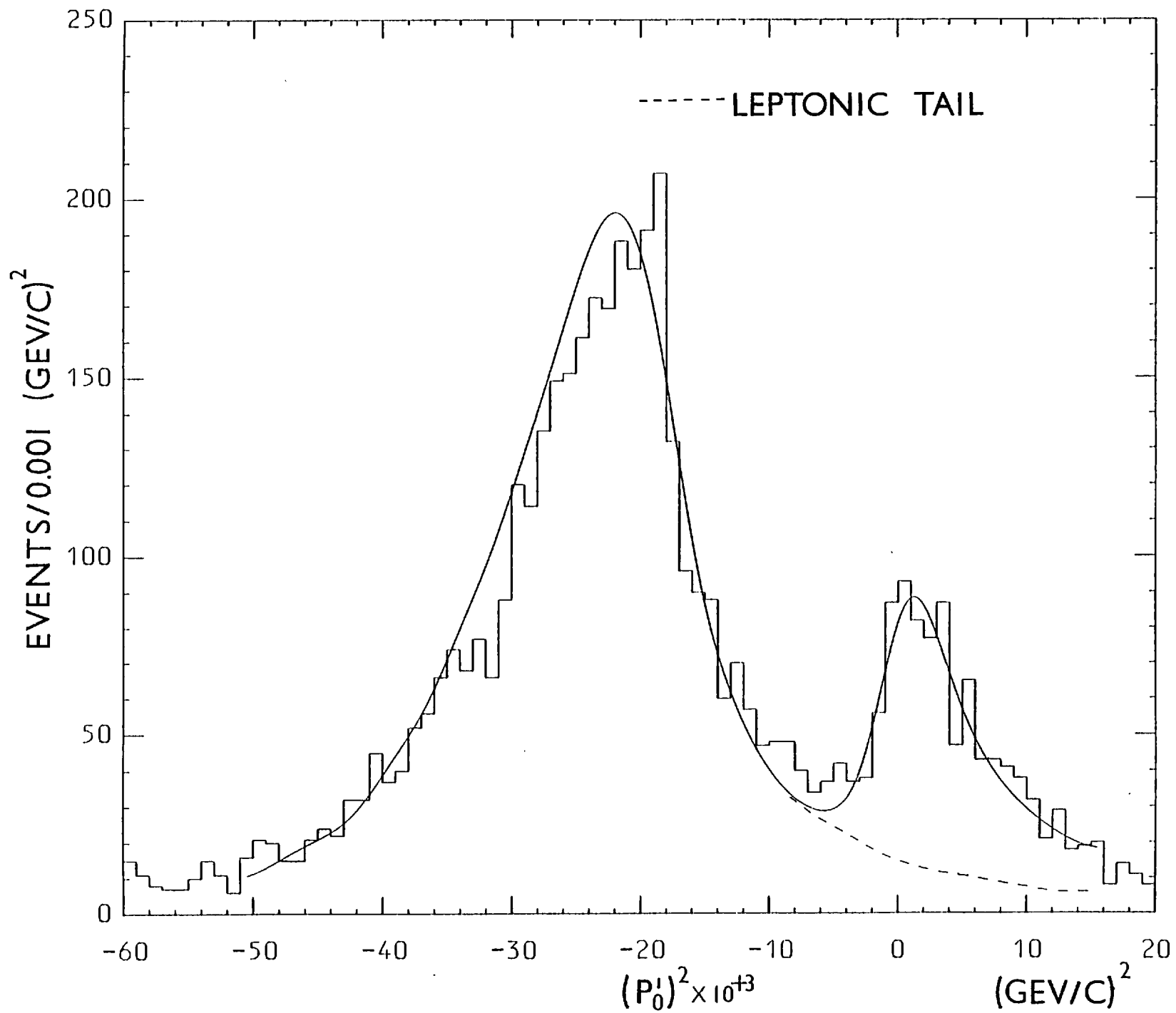
value of the branching ratio α was found using a chi-squared minimisation procedure, yielding a value for α of 0.1551 ± 0.0064 for $\chi^2 = 108.6$ and N.D.F. = 66. The expression for the statistical error on α is given by,

$$\sqrt{\frac{\alpha(1-\alpha)}{N}} = 0.0053 \quad N = \text{number of events}$$

* Units are $[\text{Gev}/c]^2$

The fit to the experimental $(p'_0)^2$ distribution is also shown in figure (3.1). The value of α obtained was found to be independent of the choice of the branching ratio x within wide limits and the fit was repeated using different $M(\pi^+\pi^-)$ cuts as any remaining decays of $K_S^0 \rightarrow \pi^+\pi^-$ would be expected to populate negative regions of $(p'_0)^2$ and thus decrease the branching ratio α . The ratio was not significantly changed as a result of these different cuts. The value of the branching ratio α found is to be compared with the world average result ⁽⁴⁾ of 0.1564 ± 0.0022 and with a previous measurement at S.L.A.C. ⁽²⁾ of 0.146 ± 0.004 from a K_L^0 beam in the momentum interval $4 < p_{K_L^0} < 12$ Gev/c.

THE $(P_0)^\pm$ DISTRIBUTION



CHAPTER 4

A Study of the Q Mass Region

$$\text{in } \underline{K_L^0 p \rightarrow K_S^0 \pi^+ \pi^- p}$$

4.1 Introduction

Data from kinematic fits to the channel,

$$K_L^0 p \rightarrow K_S^0 \pi^+ \pi^- p \quad (4.1)$$

was used in a study of the 'Q' region of the $K_S^0 \pi^+ \pi^-$ mass spectrum. Because of the natural composition of the K_L^0 beam, the production of opposite strangeness states Q^0 and \bar{Q}^0 can be compared in,

$$\begin{aligned} K^0 p \rightarrow Q^0 p \\ \qquad \qquad \qquad \rightarrow K_S^0 \pi^+ \pi^- p \\ \bar{K}^0 p \rightarrow \bar{Q}^0 p \end{aligned} \quad (4.2)$$

free of relative normalisation problems found in comparing charged kaon beam experiments. Previous knowledge of the Q region has been mainly acquired from the reactions,

$$K^+ p \rightarrow Q^+ p \rightarrow K^+ \pi^+ \pi^- p \quad (4.3)$$

$$K^- p \rightarrow \bar{Q}^- p \rightarrow K^- \pi^- \pi^+ p$$

at a variety of different momenta, the only previous experiment investigating Q^0 and \bar{Q}^0 production using the unique properties of the K_L^0 beam, was that of Brandenburg et al.⁽¹⁾, for beam momenta in the interval

$4 < p_{K_L^0} < 12$ Gev/c. Although one kinematic constraint is lost in fitting for the K_L^0 momentum, the broad K_L^0 spectrum allows the study of effective mass and momentum transfer squared distributions as a function of beam momentum. Fits to reaction (4.1) are characterized by the decay of a K_S^0 and do not suffer the same degree of kinematic ambiguity as fits in the corresponding charged beam process (4.3) where a charged pion/kaon permutation is involved. As a consequence reaction (4.1) is a 'clean' channel where less than 2% of the events are ambiguous.

4.2 Data Combination

As the total K_L^0 film sample was divided equally between Cambridge and Imperial College laboratories, some regard and attention was given to the eventual recombination of the separate data samples, since different scanning, measuring and fitting procedures were used. To ensure therefore that the final D.S.T. (Data Summary Tape) information for fits to reaction (4.1) from the two Groups was compatible and could be combined together, a number of simple data consistency and quality checks were performed on the two individual data samples, outlined in (a-d).

- (a) The K_L^0 beam momentum and four-momentum transfer squared t_{pp} (between target and scattered proton) for fits to reaction (4.1) were compared and found to be equivalent over the whole momentum interval, figure (4.1).
- (b) The charged outgoing tracks of reaction (4.1) identified as pions, were misassigned and given the charged kaon mass, and the resulting effective

mass of the charged pair plotted, figure (4.2). If the event had been fitted incorrectly one could expect a signal around $M(K^+K^-) = 1.020$ Gev to be present corresponding to ' ϕ ' production and decay to K^+ and K^- . It is apparent from these distributions for both laboratories that the signal in the ϕ mass interval is only just noticeable above statistics and only constitutes a 1% level of contamination.

(c) The distribution of the azimuthal angle between the normal to the scattering plane and the bubble chamber z axis for fits to reaction (4.1) was plotted to check whether any losses occurred when the normal vector was perpendicular to the plane of the cameras. No such losses within statistics were observed.

(d) The $K_S^0\pi$ mass distributions from reaction (4.1) for both laboratories were combined and fitted to a single Breit-Wigner resonance shape and polynomial background so as to compare the widths and masses of the $K^*(890)$ with the established values. The parameters of the fit are summarized in table (4.1) and the fit to the data is shown in figure (4.3), showing no significant deviation from the accepted mass and width values in the Particle Data Handbook.

As a result of these comparisons and tests, it was established that the data from the two laboratories was bias free and could be combined together. The number of three and six constraint fits to reaction (4.1) in the total data sample ($p_{K_L^0} < 17$ Gev/c) was 1690 of which 1494 satisfied the fiducial volume and projected length cuts outlined in the first chapter. These remaining fits were then weighted up by the inverse of the K_S^0 decay probabilities in the respective fiducial volumes as described in chapter 1, section (1.6), to give 1788 weighted events. The numbers of fits

to reaction (4.1) from each laboratory are given in table (4.2) together with those extra fits from 14 and 20 GeV/c film exposures.

4.3 Structure of the Q Enhancement

The mass spectra of pion induced diffraction dissociation processes have some interesting similarities with that of kaon induced processes indicative of a common underlying mechanism in both cases. Both sets of mass spectra exhibit common features of a rapid rise from threshold to reach a maximum followed by a steep fall off. The 3π mass spectra shows three major structures the A_1 , A_2 and A_3 peaks corresponding to the Q, $K^*(1420)$ and L in the $K\pi\pi$ spectrum. Both $K^*(1420)$ and the A_2 have had their resonance status confirmed in many experiments ⁽²⁾ but the Q and L (and their pion analogues A_1 and A_3) have not exhibited any characteristics of simple Breit-Wigner resonance behaviour and appear to be more complex objects, figure (4.4).

Analysis of decay angular distributions and fitting of the Dalitz Plot have shown that the Q is predominantly $J^P = 1^+$ ⁽³⁾ and the absence of a $K\pi$ decay mode confirms its unnatural spin parity assignment. Isospin conservation requires the Q to have $I = \frac{1}{2}$ since the enhancement is absent in $(K\pi\pi)^{++}$ from K^+ beams and its production is by isoscalar exchange as it is not seen in the charge exchange process $K^-p \rightarrow (K^0\pi^+\pi^-)_n$ ⁽⁴⁾. The potential resonance standing of the Q enhancement is particularly important because the quark model of mesons predicts in the mass region of the Q, two axial vector 1^+ nonets ⁽⁵⁾, formed by coupling the quark-antiquark

total spin with $L = 1$ orbital angular momentum to give the ' A_1 ' nonet with $J^{PC} = 1^{++}$ and the 'B' nonet with $J^{PC} = 1^{+-}$, figure (4.5). Apart from the assignment of the $I = 1$ B meson, firm candidates for the remaining states have remained elusive, figure (4.6).

This difficulty in identifying possible meson resonances in many body final states where there may be a large background or competing processes taking place, is partly due to the fact that because no stable meson targets exist, such processes have to take place in 'production' type reactions figure (4.7) with inherent problems in analysis such as exchange parameterisation and rescattering effects. This has resulted in a generally less complete picture of meson classification than their baryon counterparts which can be viewed in simpler 'formation' type reactions. To analyse these complicated meson final states, sophisticated Partial Wave Analysis (P.W.A.) programmes such as the Ascoli three body program (6) have been developed and applied to high statistics data. Such programs have been used in the determination of the spin structure of the $(K\pi\pi)^\pm$ mass spectrum and have shown that the Q mass enhancement is a composite structure of a series of unnatural spin parity states 0^- , 1^+ , 2^- produced by exchange of a system with natural parity (7). This is just the spin parity series one would expect from a diffractive type process where for a 0^- incident particle (K or π), orbital angular momentum ' ℓ ' and parity $(-1)^\ell$ is exchanged, to produce states with $J = \ell$ and $P = (-1)^{\ell+1}$. The Q system is usually identified with the dominant 1^+ wave produced with $M_Z = 0$ with respect to incident kaon, and decaying in an S wave state via the $K^*(890)\pi$ and ρK channels. The behaviour of the relative $\rho K/K^*\pi$ amplitude which rises very rapidly just above the ρK threshold to about unity and then drops by a factor of two in the interval (8) 1.2-1.4 Gev, together with the observation that two different production mechanisms are

responsible for the ρK and $K^*\pi$ decay modes, which are predominantly S-channel helicity conserving (S.C.H.C.) and t-channel helicity conserving (T.C.H.C.) respectively ⁽⁹⁾, is suggestive that the Q is composed of two 1^+ strange mesons. However attempts to detect any Breit-Wigner resonant phase motion in the major spin waves accompanied by narrow peaks in the mass spectrum, had met until recently with little or no success. The difficulty in extracting any resonant phase motion in the Q has often been explained in terms of a large 1^+ non resonant kinematic enhancement of the Deck ⁽¹⁰⁾ type, figure (4.8), which may account for a large part of the Q mass. The total diffractive data might include large Deck and rescattering contributions together with a small resonant signal which P.W.A. programs have difficulty in establishing, figure (4.9). Reactions in which the Q is not produced diffractively as in non-K induced

$$(1) \quad \pi^- p \rightarrow \Lambda \quad K\pi\pi \tag{4.4}$$

$$(2) \quad p\bar{p} \rightarrow \bar{K} \quad K\pi\pi$$

avoid complications due to the Deck effect, at the expense of lower Q cross-sections and hence poorer statistics. The $K\pi\pi$ mass spectrum from (1) and (2) show the presence of an enhancement, parameterized by a Breit-Wigner resonance shape with

$$M = 1.28 \pm 0.004 \text{ Gev}$$

$$\Gamma = 0.052 \pm 0.013 \text{ Gev}$$

and with ρK as the main decay mode ⁽¹¹⁾. It has been argued ⁽¹²⁾ that there is at least one resonance coupled to ρK with a similar mass as above present

in the diffractive data, which would account for the rapid rise in the $\rho K/K^*\pi$ ratio around the ρK threshold and with production that is mainly S.C.H.C.. The $K^*\pi$ mode which is compatible with T.C.H.C. would then be a consequence of the pion exchange Deck effect.

Recent results from a very high statistics wire spark chamber experiments ⁽¹³⁾ using the magnetic spectrometer facility at S.L.A.C. and studying both K^+ and K^- reactions at 13 Gev/c in

$$K^+_p \rightarrow K^+\pi^+\pi^-p \quad (72,000 \text{ events})$$

$$K^-_p \rightarrow K^-\pi^+\pi^-p \quad (56,000 \text{ events})$$

have succeeded in finally confirming a resonant phase motion in both $1^+K^*\pi$ and $1^+K\rho$ waves. Further analysis ⁽¹⁴⁾ has shown that the main features of the data can be explained by a model incorporating two Q mesons, one with mass 1.3 Gev coupling mainly to the ρK channel ' Q_1 ' and the other of mass 1.4 Gev coupling mainly to $K^*\pi$ ' Q_2 '. Table (4.3) gives the results of the model fit to the data together with decay modes to $K\omega$, $K\pi$ and $K\varepsilon$, where ' K ' and ' ε ' are S-wave $K\pi$ and $\pi\pi$ systems. The strange members of the A and B nonets predicted by the quark model and denoted by ' Q_A ' and ' Q_B ' would, if similar in mass, be expected to undergo SU_3 breaking interactions and 'mix' to give the observed Q_1 and Q_2 states such that

$$\begin{aligned} |Q_1\rangle &= \cos\theta_Q |Q_A\rangle + \sin\theta_Q |Q_B\rangle \\ |Q_2\rangle &= -\sin\theta_Q |Q_A\rangle + \cos\theta_Q |Q_B\rangle \end{aligned} \quad (4.5)$$

where ' θ_Q ' is the mixing angle, determined from fits to the data as nearly 45° ($41^\circ \pm 4^\circ$). As a consequence ⁽¹⁵⁾, although Q_A and Q_B can decay via

both $K^*\pi$ and ρK , the Q_1 and Q_2 states are effectively decoupled from $K^*\pi$ and ρK decay modes respectively, table (4.3). The masses of the eigenstates Q_A and Q_B are related to the masses of the mixed states Q_1 and Q_2 (12) by,

$$\begin{aligned} M_A^2 &= \frac{1}{2}(M_1^2 + M_2^2 + (M_1^2 - M_2^2) \cos 2\theta_Q) \\ M_B^2 &= \frac{1}{2}(M_1^2 + M_2^2 - (M_1^2 - M_2^2) \cos 2\theta_Q) \end{aligned} \quad (4.6)$$

resulting in the nearly degenerate masses for Q_A and Q_B as

$$\begin{aligned} M(Q_A) &= 1.34 \pm 0.030 \text{ Gev} \\ M(Q_B) &= 1.355 \pm 0.030 \text{ Gev} \end{aligned}$$

4.4 Mass Spectra and Scatter Plots

The effective mass distribution of the $K_S^0 \pi^+ \pi^-$ system in reaction (4.1) defined as

$$M(K_S^0 \pi^+ \pi^-) = \sqrt{\left(\sum_{i=1,3} E_i \right)^2 - \left| \sum_{i=1,3} \vec{p}_i \right|^2} \quad (4.7)$$

is shown in figure (4.10) for the combined 17 Gev/c data sample. The figure shows the familiar broad 'Q' enhancement in the mass interval (1.1 - 1.5) Gev seen in previous charged and neutral kaon experiments. followed by a rapid fall-off at higher masses. The scatter plot of

$M(K_S^0 \pi^+ \pi^-)$ against K_L^0 momentum figure (4.11) shows that this enhancement (defined by the two arrows) is produced almost evenly up to high beam momenta. The Q can be considered as the 'diffraction dissociation' product of the incident K_L^0 beam, mediated by the exchange of a particle in the t-channel possessing the quantum members of the vacuum ($I = 0$, $S = 0$, $C = +1$) known as the 'Pomeron' (17). Such diffractive processes are characterised by cross-sections which vary weakly with energy thus explaining Q production at high momenta, and a strong forward $d\sigma/dt$ peak (18). The peripheral nature of these processes is illustrated in figure (4.12) where the four-momentum transfer squared t_{pp} is plotted against $M(K_S^0 \pi^+ \pi^-)$, the mass of the diffractive system and it can be seen that the bulk of the Q system is produced at $|t_{pp}|$ less than 0.5 GeV^2 .

In order to estimate the contribution of non-diffractive background events in reaction (4.1) the scatter plots of

- (1) $M(p\pi^+)$ vs $M(K_S^0 \pi^-)$
- (2) $M(p\pi^-)$ vs $M(K_S^0 \pi^+)$
- (3) $M(p\pi^+ \pi^-)$ vs $M(K_S^0 \pi^+)$

are displayed in figures (4.13 - 4.15). In figure (4.13) a distinct cluster of events at low $M(p\pi^+)$ corresponding to $\Delta^{++}(1236)$ is visible, whilst the projection on the vertical shows the presence of a strong $K^{*-}(890)$ signal, the region of overlap corresponding to $K_L^0 p \rightarrow K^{*-}(890) \Delta^{++}(1236)$. In figure (4.14) the $K^{*+}(890)$ is present on the vertical axis with similar intensity as the K^{*-} , whilst on the horizontal axis there is little evidence of $\Delta^0(1236)$. Diffraction dissociation at the proton vertex which is significant in $K_p^\pm \rightarrow K^\pm(p\pi^+ \pi^-)$ (19), is forbidden in

$K_L^0 p \rightarrow K_S^0 p \pi^+ \pi^-$ because of the $C = +1$ nature of the Pomeron and the change in C of -1 at the $K_L^0 - K_S^0$ vertex. This is confirmed in figure (4.15) where no structure in $M(p\pi^+\pi^-)$ is visible. The scatter of $M(p\pi^+)$ against beam momentum in figure (4.16) shows that the $\Delta^{++}(1236)$, which constitutes the main source of background in reaction (4.1), is produced mainly at low K_L^0 momenta and above 8 Gev/c is greatly reduced in intensity, figure (4.17).

The shaded histogram of figure (4.10) shows the $K_S^0 \pi^+ \pi^-$ mass distribution for events satisfying the cuts $M(p\pi^+) > 1.34$ Gev to eliminate the $\Delta^{++}(1236)$ and $|t'_{pp}| = |t_{pp} - t_{min}| < 0.5$ Gev² to ensure peripherality. These cuts significantly enhance the Q signal with respect to the background and result in 1017 events being removed. A momentum cut requiring $P_{K_L^0} > 6$ Gev/c in figure (4.18) reduces further any background and enhances the diffractive signal. The Q mass enhancement in figure (4.18) does not appear split into two distinct peaks as in reference (20). No visible 'L' enhancement (21) is present in the 1.7 - 1.8 Gev region of the $M(K_S^0 \pi^+ \pi^-)$ spectrum, instead interesting structure is observed in the adjacent mass region 1.8 - 1.9 Gev, which becomes clearer when the $P_{K_L^0} > 6$ Gev/c cut is made. This structure is seen in both independent laboratory data and is not visible in the equivalent S.L.A.C. mass distributions. The scatter of $M(K_S^0 \pi^+ \pi^-)$ against K_L^0 momentum for events satisfying the diffractive cuts ($M(p\pi^+) > 1.34$ Gev and $|t'_{pp}| < 0.5$ Gev²) figure (4.19), shows that for this mass interval, (denoted by the two arrows), there is with the present statistics only weak evidence for a possible resonance band.

Figures (4.20-4.22) show the $K_S^0 \pi^+ \pi^-$ mass spectrum with the diffractive cuts, and the shaded histogram in each figure displays those events that satisfy the additional requirements that,

- (1) A $K_S^0\pi$ mass combination is within the $K^*(890)$ mass interval, $0.86 < M(K_S^0\pi) < 0.92$ Gev, figure (4.20).
- (2) The $\pi^+\pi^-$ mass combination is within the ρ mass interval, $0.72 < M(\pi^+\pi^-) < 0.82$ Gev, figure (4.21).
- (3) A $K_S^0\pi$ mass combination is within the $K^*(1420)$ mass interval, $1.32 < M(K_S^0\pi) < 1.52$ Gev, figure (4.22).

4.5 Dalitz Plots

The Dalitz plots for the Q decay are presented in figures (4.23-4.25) together with the projections, figures (4.26-4.28), where the Q is defined by the region $1.1 < M(K_S^0\pi^+\pi^-) < 1.5$ Gev. The curves in these figures show the contours for the mass limits in each plot. In figures (4.23-4.24) ρ and $K^*(890)$ crossing bands are visible and in figure (4.25) strong $K^{*+}(890)$ and $K^{*-}(890)$ bands are present and show approximate symmetry about the diagonal line. There is evidence for some destructive interference along this line where $M(K_S^0\pi^-)$ is equal to $M(K_S^0\pi^+)$. Similar features are also present for the Q Dalitz plots with the additional diffractive cuts ($M(p\pi^+) > 1.34$ Gev, $|t_{pp}^-| < 0.5$ Gev²), figures (4.29-4.34). The Dalitz plots are also displayed for the mass interval $1.5 < M(K_S^0\pi^+\pi^-) < 2.0$ Gev and for events satisfying the diffractive cuts, figures (4.35-4.40). The ρ signal to background ratio appears particularly high in this mass interval, figure (4.40), when compared with the previous Q mass interval, figure (4.34).

4.6 Fitting the Mass Spectra

The mass spectra in figure (4.18) were fitted to an incoherent superposition of two Breit-Wigner resonance shapes and a polynomial background. For a particular mass value m , the form used was proportional to

$$\sum_i f_i BW_i(m, m_i^0, \Gamma_i) + (1 - \sum_i f_i) BG(m) \quad (4.8)$$

where ' f_i ' the resonance ' i ' fraction, ' m_i^0 ' the resonance ' i ' mass value and ' Γ_i ' the fullwidth of resonance ' i ', were varied so as to minimize a chi-squared function, the constant of normalisation being determined by the numbers of events in the data sample. The form of the Breit-Wigner ' BW_i ' and the order of the polynomial background ' BG ' in equation (4.8) were varied in the fitting, but were found to have an insignificant effect (within errors) on the final fitted values. The parameters of the fit are given in table (4.4) and the fit to the mass distributions shown in figure (4.41). The Breit-Wigner contribution of the second higher mass resonance to the total fit is denoted in figure (4.41) by the dashed line. Single resonance and background only fits were attempted but were found to give a poorer fit than the two resonance parameterisation particularly at large $K\pi\pi$ mass where the interesting structure is observed. From table (4.4) the Q enhancement has a Breit-Wigner mass and width of

$$M_Q \approx 1.32 \pm 0.010 \text{ Gev}$$

$$\Gamma_Q \approx 0.270 \pm 0.030 \text{ Gev}$$

The mass value appears compatible with that found in previous experiments, but is difficult given the simplicity of the model fit to identify with

either the lower mass Q_1 or the Q_A and Q_B eigenstates. The other 'resonance' which attempts to reproduce the structure in the mass region 1.8-2.0 Gev has a mass and width of

$$M_X \sim 1.89 \pm 0.025 \text{ Gev}$$

$$\Gamma_X \sim 0.100 \pm 0.100 \text{ Gev}$$

This mass is too high to associate with the L enhancement at 1.76 Gev, however it is worth remarking that it is not incompatible with the expected mass of a $J^{PC} = 3^{++}$ state (1.9-2.0 Gev depending on the Regge Slope) produced by diffraction dissociation of the beam and lying on the same Regge trajectory as the Q meson, separated by two units of angular momentum.

The $K_S^0 \pi^+ \pi^-$ mass spectra corresponding to Q^0 and \bar{Q}^0 production are shown in figure (4.42), where Q^0 and \bar{Q}^0 are separated by selecting on $K^{*-} \pi^+$ and $K^{*+} \pi^-$ final states and the K^* cut is defined by $0.84 < M(K_S^0 \pi) < 0.94$ Gev. The ratio of $K^{*-} \pi^+$ to $K^{*+} \pi^-$ events, figure (4.43) is constant within statistics across the $K_S^0 \pi^+ \pi^-$ mass range and is consistent with unity. The $K^{*-} \pi^+$ distribution appears wider than the $K^{*+} \pi^-$ region within the Q mass interval and this is confirmed in the mass fits to these distributions of a single Breit-Wigner and polynomial background shown in figures (4.42) and summarized in table (4.5). Although with present statistics this result is questionable, interference and mixing between Q_A and Q_B could result in different mass spectra between Q^0 and \bar{Q}^0 .

4.7 Momentum Dependence of the Q Mass and Width

The broad K_L^0 spectrum gives one the opportunity to study how the mass and width of the Q enhancement varies with incident momentum within one experiment. Similar studies with charged kaon beams have not been undertaken in any detail because of the problems in comparing experiments at different momenta using different cuts and analysis techniques. To investigate this further fits to reaction (4.1) were divided into three consecutive beam momentum intervals spanning the K_L^0 spectrum such that there were approximately the same number in each interval.

$$p_{K_L^0} < .6 \text{ GeV/c} \quad (257 \text{ events})$$

$$6 < p_{K_L^0} < 10 \text{ GeV/c} \quad (247 \text{ events})$$

$$10 < p_{K_L^0} < 17 \text{ GeV/c} \quad (266 \text{ events})$$

The $K_S^0 \pi^+ \pi^-$ mass spectra satisfying these selection criteria and the diffractive cuts outlined previously, were fitted to a single Breit-Wigner resonance and polynomial background to give a mass and width for each set of data. The fitted parameters are given in table (4.6), and the experimental distributions and fit to the data are shown in figure (4.44), the dashed line in each diagram denoting the contribution of the Breit-Wigner resonance to the total fit. The observed variation in the width of the Q enhancement is shown in figures (4.45) for two different Breit-Wigner forms (relativistic and non-relativistic), the dashed line giving the width value averaged over the whole momentum interval. The resonance mass value obtained from the fit remains constant within errors across the momentum range.

These features in figures (4.45) can be partially understood on the basis of a model of the Q enhancement composed of the $Q_A (J^{PC}=1^{++})$ and $Q_B (J^{PC}=1^{+-})$. Assuming that the charge conjugation number is applicable in describing the coupling between the Q system and the Pomeron ($J^{PC}=0^{++}$), one would expect the cross-section of the 1^{++} state to remain constant with increasing beam momentum, with the 1^{+-} component decreasing, thus suggesting a momentum dependent width for the Q.

4.8 Cross-sections

The cross-section for reaction (4.1) between threshold and 17 GeV/c beam momentum is given in table (4.7) and shown in figure (4.46), together with the cross-section values obtained in the S.L.A.C. K_L^0 experiment. The cross-section values are given by the expression

$$\sigma = \frac{N_{INT}}{N_{K_L^0}} \left(\frac{10^{30}}{e_s e_m \rho_{H_2} l_{INT} \epsilon N} \right) \mu BS \quad (4.9)$$

where

N_{INT} = The number of events of reaction (4.1)

$N_{K_L^0}$ = The K_L^0 flux

e_s = Scanning efficiency for '301' topology

e_m = Measuring efficiency for '301' topology

ρ_{H_2} = Density of liquid hydrogen

l_{INT} = Interaction length for reaction (4.1)

ϵ = Branching ratio, $\frac{(K_s^0 \rightarrow \text{visible})}{(K_s^0 \rightarrow \text{all})}$

N = Avogadro's number

The cross-sections have been corrected for the neutral decay modes of K_S^0 and for scanning and measuring efficiencies using events of reaction (4.1) with the weighting procedure described in the 1st Chapter. Some allowance has also been made for events missed in scanning with short recoil protons having $|t_{pp}| < 0.04 \text{ GeV}^2$, figure (4.1). This loss has been estimated by fitting the t_{pp} distributions to single exponentials in the range $0.04 < |t_{pp}| < 0.5 \text{ GeV}^2$ and extrapolating to $|t_{pp}| = 0$ for three consecutive momentum intervals between threshold and 17 GeV/c. This correction added 6% to the total number of weighted events of reaction (4.1). The overall normalisation of the K_L^0 flux has been fixed at $9K_L^0$ s per frame to agree with the Cambridge flux estimate and the errors shown in figure (4.46) include the statistical errors in the numbers of events and the uncertainties in the K_L^0 momentum spectrum given by the error bars in figure (2.7). The overall scale of the cross-sections is lower than the S.L.A.C. values but is within the 15% systematic uncertainty quoted by them. The cross-section rises sharply from threshold to reach a maximum around 3 - 4 GeV/c and then decreases beyond 6 GeV/c. For momenta greater than 12 GeV/c outside the S.L.A.C. momentum range, the cross-section behaviour is consistent with uniformity.

The cross-section for Q production is shown in figure (4.47) together with the cross-section for reaction (4.1). For the Q signal, the following cuts are made on data of reaction (4.1).

$$\begin{aligned}
 &1) |t_{pp}'| < 0.5 \text{ GeV}^2 \\
 &2) 1.1 < M(K_S^0 \pi^+ \pi^-) < 1.5 \text{ GeV} \\
 &3) M(p\pi^+) > 1.34 \text{ GeV}
 \end{aligned}
 \tag{4.10}$$

Further selection into Q^0 and \bar{Q}^0 states can be achieved by selecting subsamples of $K^{*+}\pi^-$ and $K^{*-}\pi^+$ within the Q mass region where the K^* selection is 0.86 to 0.92 Gev. The cross-sections have been adjusted for the neutral K_S^0 decay mode and for the scanning and measuring efficiencies discussed previously. The cut $M(p\pi^+) > 1.34$ Gev in addition to removing the Δ^{++} (1236) will remove true Q events. In order to make appropriate corrections, a simple 'background' subtraction was done for events satisfying the first two cuts of (4.10), using the scatter plots of $M(K_S^0\pi^-)$ against $M(p\pi^+)$ and $M(K_S^0\pi^+)$ against $M(p\pi^+)$. The average number of events in the adjacent mass regions of $0.80 < M(K_S^0\pi) < 0.86$ Gev and $0.92 < M(K_S^0\pi) < 0.98$ Gev for $M(p\pi^+) < 1.34$ Gev was taken as a measure of the background and subtracted from the signal in the region $0.86 < M(K_S^0\pi) < 0.92$ Gev corresponding to Q^0 and \bar{Q}^0 production. The cross-section for Q production in figure (4.47) shows only a weak dependence with energy as expected for a diffractively produced state. The ratio of cross-sections for Q^0p and \bar{Q}^0p states is shown in figure (4.48) and is consistent with unity over the whole momentum interval, in agreement with the result found in the S.L.A.C. K_L^0 experiment.

Table 4.1 Fit parameters of the $K_S^0 \pi$ mass distributions

$$M(K^{*+}) = 0.893 \pm 0.001 \text{ Gev}$$

$$\Gamma(K^{*+}) = 0.037 \pm 0.006 \text{ Gev}$$

(Breit-Wigner and 3rd order polynomial)

$$M(K^{*+}) = 0.894 \pm 0.002 \text{ Gev}$$

$$\Gamma(K^{*+}) = 0.045 \pm 0.008 \text{ Gev}$$

(Breit-Wigner and 2nd order polynomial)

$$M(K^{*-}) = 0.889 \pm 0.001 \text{ Gev}$$

$$\Gamma(K^{*-}) = 0.048 \pm 0.003 \text{ Gev}$$

(Breit-Wigner and 3rd order polynomial)

$$M(K^{*-}) = 0.889 \pm 0.002 \text{ Gev}$$

$$\Gamma(K^{*-}) = 0.047 \pm 0.004 \text{ Gev}$$

(Breit-Wigner and 2nd order polynomial)

Table 4.2 Number of fits to $K_L^0 p \rightarrow K_S^0 \pi^+ \pi^- p$

Film exposure	I.C.data	Cambridge data
17 Gev/c:	864	826
14,18.5,20 Gev/c:	128	-

Table 4.3 Properties of the Q_1 and Q_2 mesons

	Q_1 meson	Q_2 meson
Mass (Mev)	1290 \pm 25	1400 \pm 10
Width (Mev)	210 \pm 80	190 \pm 85

Partial Widths (Mev)

$K^*\pi$	12 \pm 12	154 \pm 52
$K\rho$	100 \pm 35	2 \pm 1
$K\omega$	32 \pm 11	\approx 0
$K\pi$	35 \pm 13	\approx 0
$K\varepsilon$	29 \pm 10	31 \pm 11

Table 4.4 Fits to the $(K_S^0 \pi^+ \pi^-)$ diffractive mass spectrum

$(1.1 < M(K_S^0 \pi^+ \pi^-) < 2.45 \text{ Gev} , M(p\pi^+) > 1.34 \text{ Gev}, |t_{pp}^-| < 0.5 \text{ Gev}^2)$

710 events

Fits to two Resonances and a 3rd order polynomial Background

<u>Quantity</u>	<u>Non-Rel. Breit-Wigners</u>	<u>Rel. Breit-Wigners</u>
M_Q	1.320 ± 0.008	1.324 ± 0.011
Γ_Q	0.276 ± 0.028	0.262 ± 0.052
fraction _Q	0.738 ± 0.023	0.670 ± 0.147
M_X	1.852 ± 0.039	1.835 ± 0.052
Γ_X	0.443 ± 0.149	0.544 ± 0.170
fraction _X	0.221 ± 0.013	0.286 ± 0.174
Prob.of fit	0.11	0.10

Fits to the $(K_S^0 \pi^+ \pi^-)$ diffractive mass spectrum

$(1.1 < M(K_S^0 \pi^+ \pi^-) < 2.3 \text{ Gev} , M(p\pi^+) > 1.34 \text{ Gev}, |t_{pp}^-| < 0.5 \text{ Gev}^2, \vec{K}_L^0 > 6 \text{ Gev}/c)$

443 events

Fits to two Resonances and a 3rd order polynomial Background

<u>Quantity</u>	<u>Non-Rel. Breit-Wigners</u>	<u>Rel. Breit-Wigners</u>
M_Q	1.315 ± 0.013	1.323 ± 0.013
Γ_Q	0.315 ± 0.035	0.274 ± 0.077
fraction _Q	0.768 ± 0.030	0.619 ± 0.156
M_X	1.893 ± 0.025	1.892 ± 0.024
Γ_X	0.103 ± 0.089	0.064 ± 0.120
fraction _X	0.069 ± 0.028	0.048 ± 0.042
Prob.of fit	0.06	0.065

Masses and widths are in Gev.

Table 4.5 Fits to the Q^0 diffractive mass spectrum

$(1.1 < M(K_S^0 \pi^+ \pi^-) < 1.9 \text{ GeV}, 0.84 < M(K_S^0 \pi^+) < 0.94 \text{ GeV}, M(p\pi^+) > 1.34 \text{ GeV}, |t_{pp}'| < 0.5 \text{ GeV}^2)$

250 events

Fits to a single Resonance and a quadratic background

<u>Quantity</u>	<u>Non-Rel.Breit-Wigner</u>	<u>Rel.Breit-Wigner</u>
M_{Q^0}	1.319 \pm 0.009	1.322 \pm 0.011
Γ_{Q^0}	0.204 \pm 0.027	0.208 \pm 0.026
fraction $_{Q^0}$	0.915 \pm 0.08	0.943 \pm 0.029
Prob.of fit	0.18	0.15

Fits to the \bar{Q}^0 diffractive mass spectrum

$(1.1 < M(K_S^0 \pi^+ \pi^-) < 1.9 \text{ GeV}, 0.84 < M(K_S^0 \pi^-) < 0.94 \text{ GeV}, M(p\pi^+) > 1.34 \text{ GeV}, |t_{pp}'| < 0.5 \text{ GeV}^2)$

251 events

Fits to a single Resonance and a 3rd order polynomial Background

<u>Quantity</u>	<u>Non-Rel.Breit-Wigner</u>	<u>Rel.Breit-Wigner</u>
$M_{\bar{Q}^0}$	1.314 \pm 0.017	1.315 \pm 0.015
$\Gamma_{\bar{Q}^0}$	0.318 \pm 0.045	0.303 \pm 0.038
fraction $_{\bar{Q}^0}$	0.965 \pm 0.038	0.904 \pm 0.036
Prob.of fit	0.05	0.05

Masses and widths are in GeV.

Table 4.6 Fits to the ($K_S^0 \pi^+ \pi^-$) diffractive mass spectrum

($1.15 < M(K_S^0 \pi^+ \pi^-) < 2.1$ Gev, $p_{K_L^0} < 6$ Gev/c, $M(p\pi^+) > 1.34$ Gev, $|t_{pp}^-| < 0.5$ Gev²)

238 events

Fits to a single Resonance and a 3rd order polynomial Background

<u>Quantity</u>	<u>Non-Rel.Breit-Wigner</u>	<u>Rel.Breit-Wigner</u>
M_Q	1.324 ± 0.017	1.325 ± 0.015
Γ_Q	0.187 ± 0.082	0.198 ± 0.044
fraction _Q	0.539 ± 0.236	0.564 ± 0.050
Prob.of fit	0.48	0.47

Fits to the ($K_S^0 \pi^+ \pi^-$) diffractive mass spectrum

($1.1 < M(K_S^0 \pi^+ \pi^-) < 2.05$ Gev, $6 < p_{K_L^0} < 10$ Gev/c, $M(p\pi^+) > 1.34$ Gev, $|t_{pp}^-| < 0.5$ Gev²)

199 events

Fits to a single Resonance and a 3rd order polynomial Background

<u>Quantity</u>	<u>Non-Rel.Breit-Wigner</u>	<u>Rel.Breit-Wigner</u>
M_Q	1.318 ± 0.025	1.316 ± 0.017
Γ_Q	0.278 ± 0.052	0.289 ± 0.052
fraction _Q	0.670 ± 0.056	0.692 ± 0.051
Prob.of fit	0.16	0.18

Masses and widths are in Gev

Table 4.6 Fits to the($K_S^0 \pi^+ \pi^-$) diffractive mass spectrum
 Contd.,

($1.15 < M(K_S^0 \pi^+ \pi^-) < 1.95$ Gev, $10 < p_{K_L^0} < 17$ Gev/c, $M(p\pi^+) > 1.34$ Gev, $|t_{pp}^+| < 0.5$ Gev²)

203 events

Fits to a single Resonance and a 3rd order polynomial Background

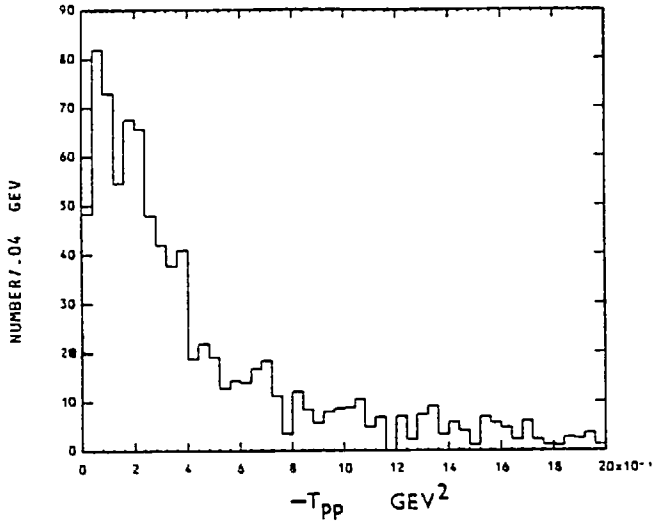
<u>Quantity</u>	<u>Non-Rel.Breit-Wigner</u>	<u>Rel.Breit-Wigner</u>
M_Q	1.330 ± 0.022	1.328 ± 0.015
Γ_Q	0.347 ± 0.061	0.311 ± 0.054
fraction _Q	0.718 ± 0.088	0.779 ± 0.058
Prob.of fit	0.05	0.06

Masses and widths are in Gev.

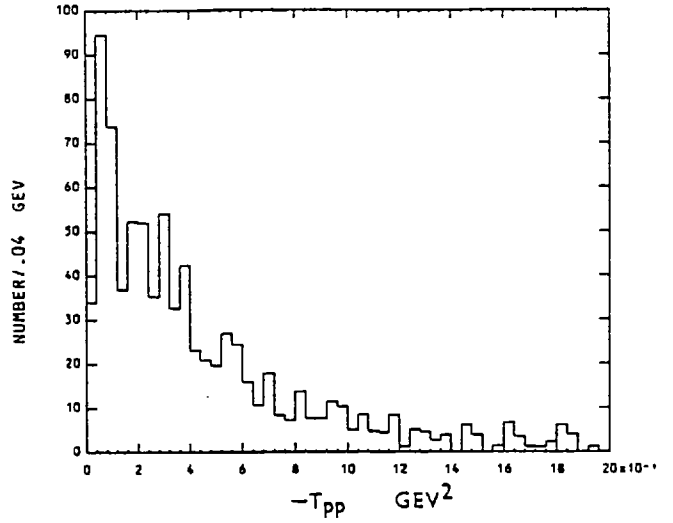
Table 4.7 Cross-sections

K_L^0 momentum interval (Gev/c)	Cross-section for $K_L^0 p \rightarrow K_S^0 \pi^+ \pi^- p$ (μ bs)	Cross-section for $K_L^0 p \rightarrow Qp$ (μ bs)
0 - 2	135 ± 48	-
2 - 4	503 ± 43	90 ± 17
4 - 6	481 ± 43	73 ± 16
6 - 8	362 ± 39	68 ± 16
8 - 10	300 ± 45	56 ± 17
10 - 12	324 ± 60	69 ± 21
12 - 14	253 ± 55	62 ± 20
14 - 17	217 ± 40	55 ± 15

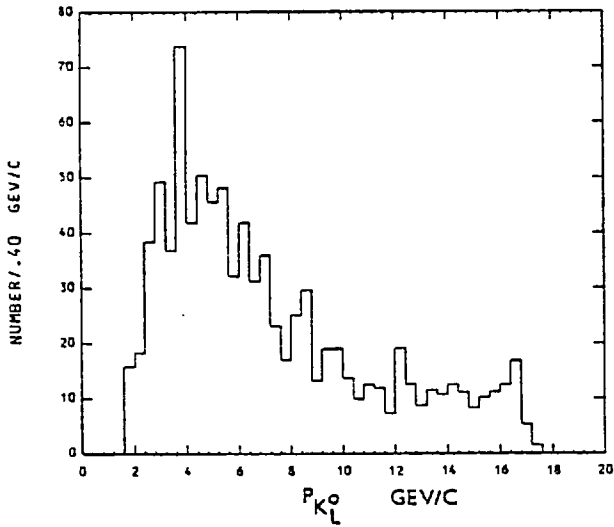
CAMB T-PP DISTRIBUTION



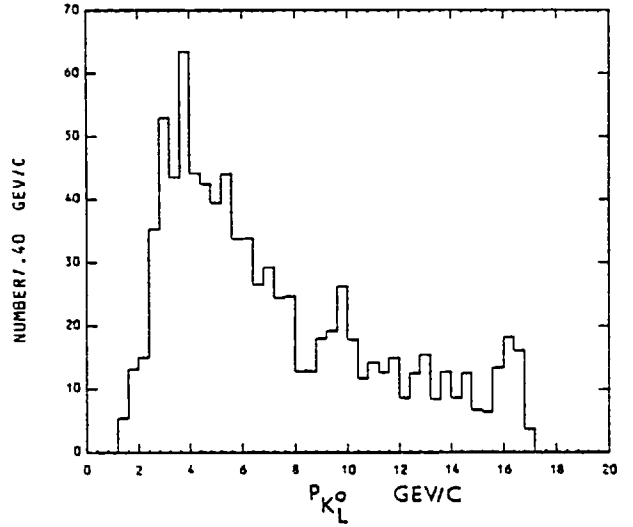
IC T-PP DISTRIBUTION



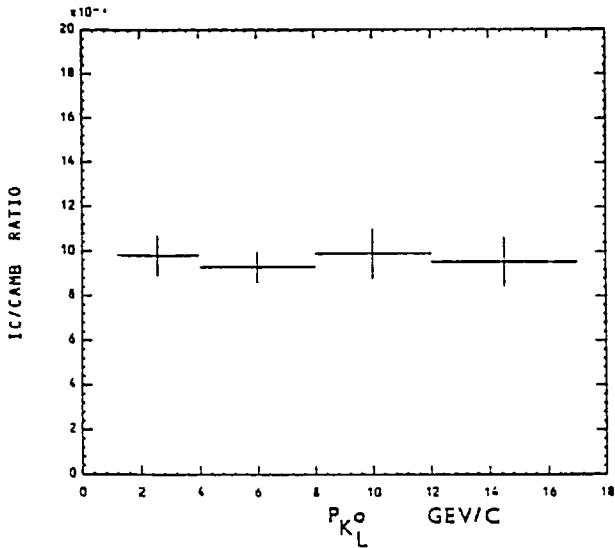
CAMB KOL MOMENTUM



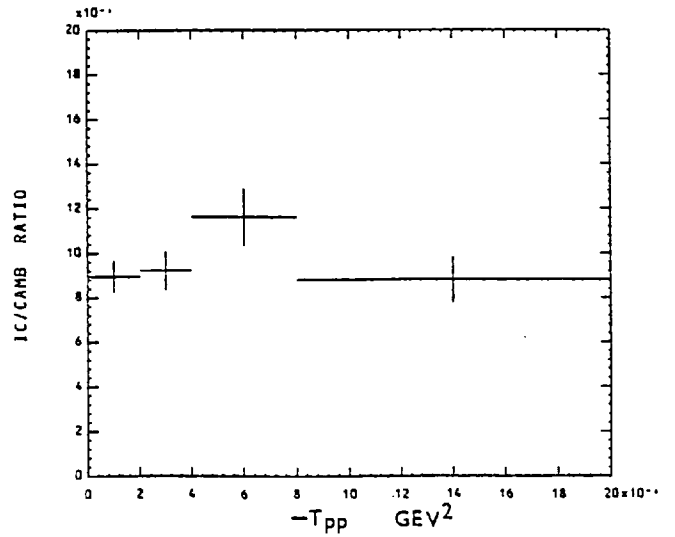
IC KOL MOMENTUM



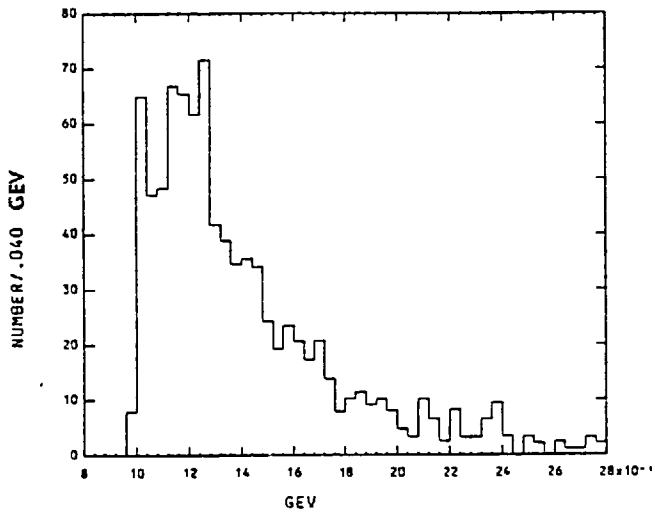
KOL MOM. RATIO FOR IC AND CAMB



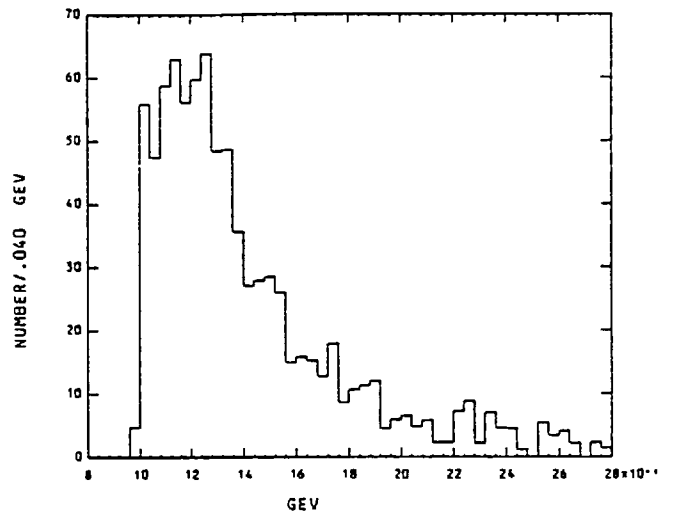
T-PP RATIO FOR IC AND CAMB



CAMB PI+ PI- MISIDENTIFIED MASS

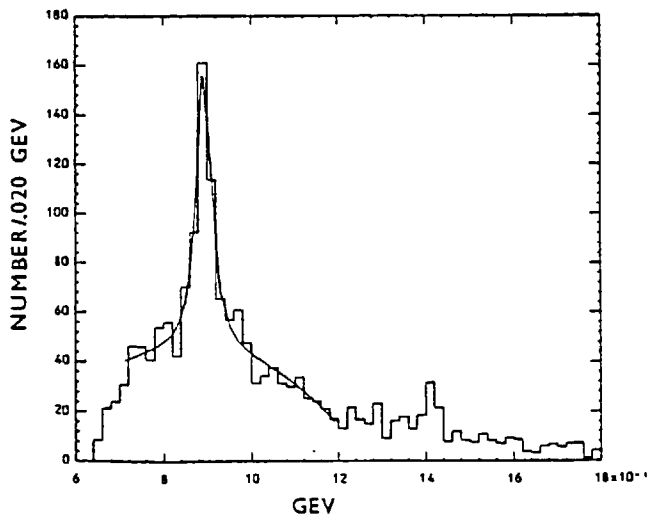


IC PI+ PI- MISIDENTIFIED MASS

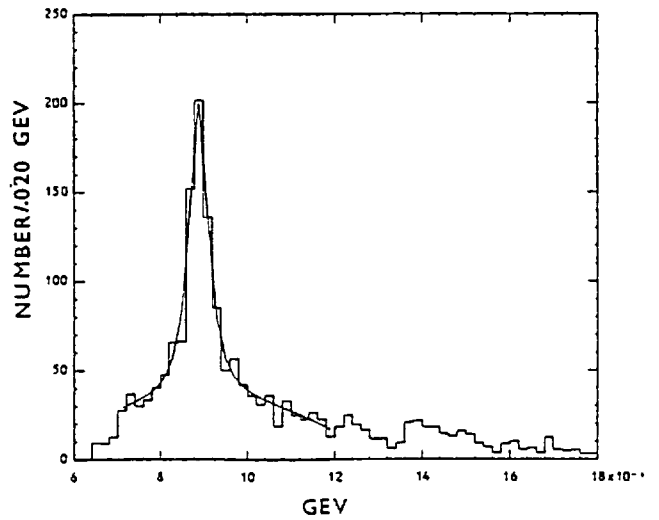


4.2

M(KOS PI+) DISTRIBUTION



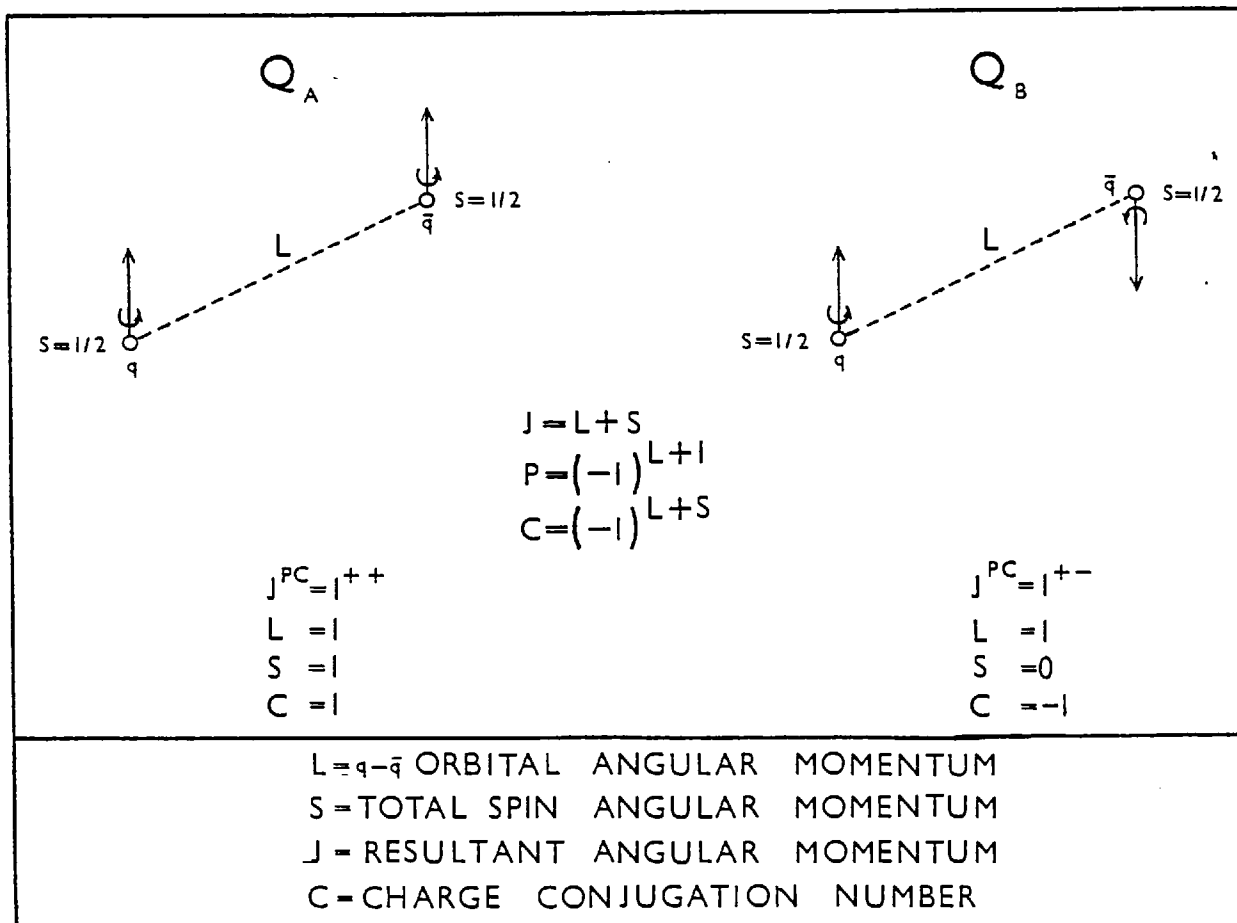
M(KOS PI-) DISTRIBUTION



4.3

TRANSITION	PEAK	MASS GEV	J^P	MAIN DECAY CHANNEL
$K \rightarrow (K\pi\pi)$	Q	1.3	1^+	$K^*(890)\pi$
	$K^*(1420)$	1.42	2^+	$K^*(890)\pi$
	L	1.77	2^-	$K^*(1420)\pi$
$\pi \rightarrow (\pi\pi\pi)$	A_1	1.1	1^+	$\rho\pi$
	A_2	1.31	2^+	$\rho\pi$
	A_3	1.64	2^-	$f\pi$

4.4



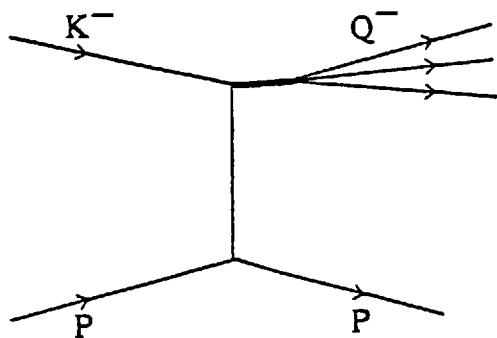
4.5

STATUS OF L=1 MULTIPLET

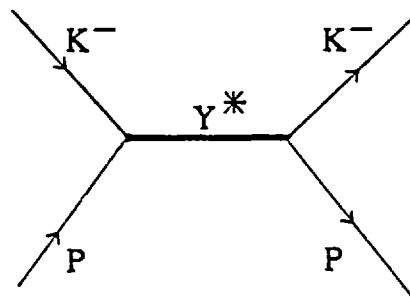
J^{PC}	$I=1$	$I=1/2$	$I=0$	$I=0$
2^{++}	A_2	K^*	f	f'
1^{++}	A_1	Q_A		
0^{++}				
1^{+-}	B	Q_B		

4.6

PRODUCTION

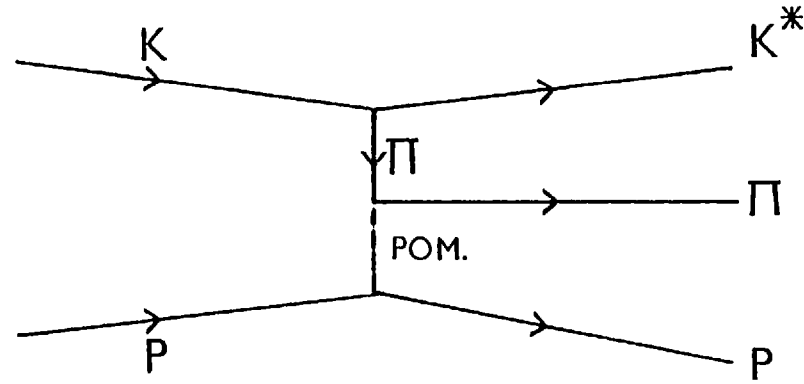


FORMATION

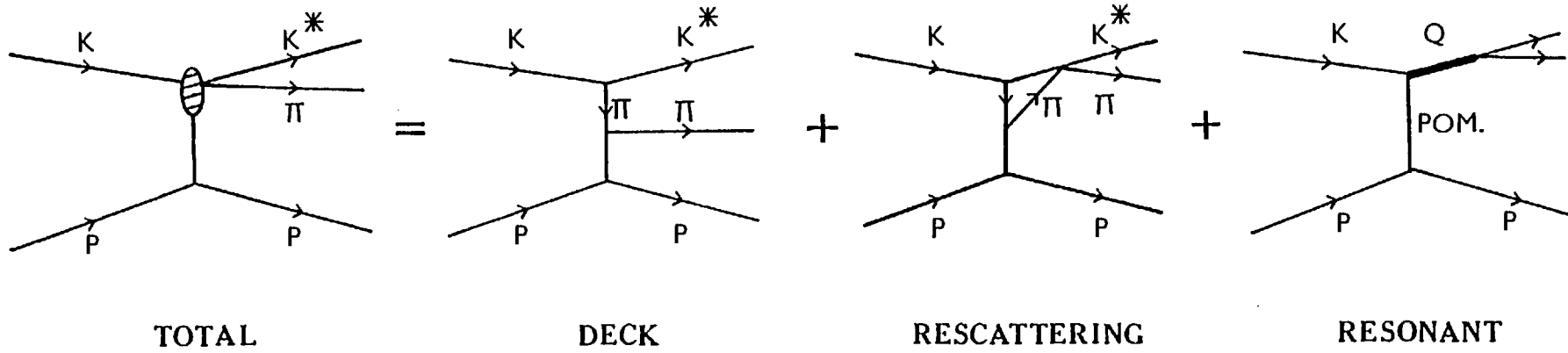


4.7

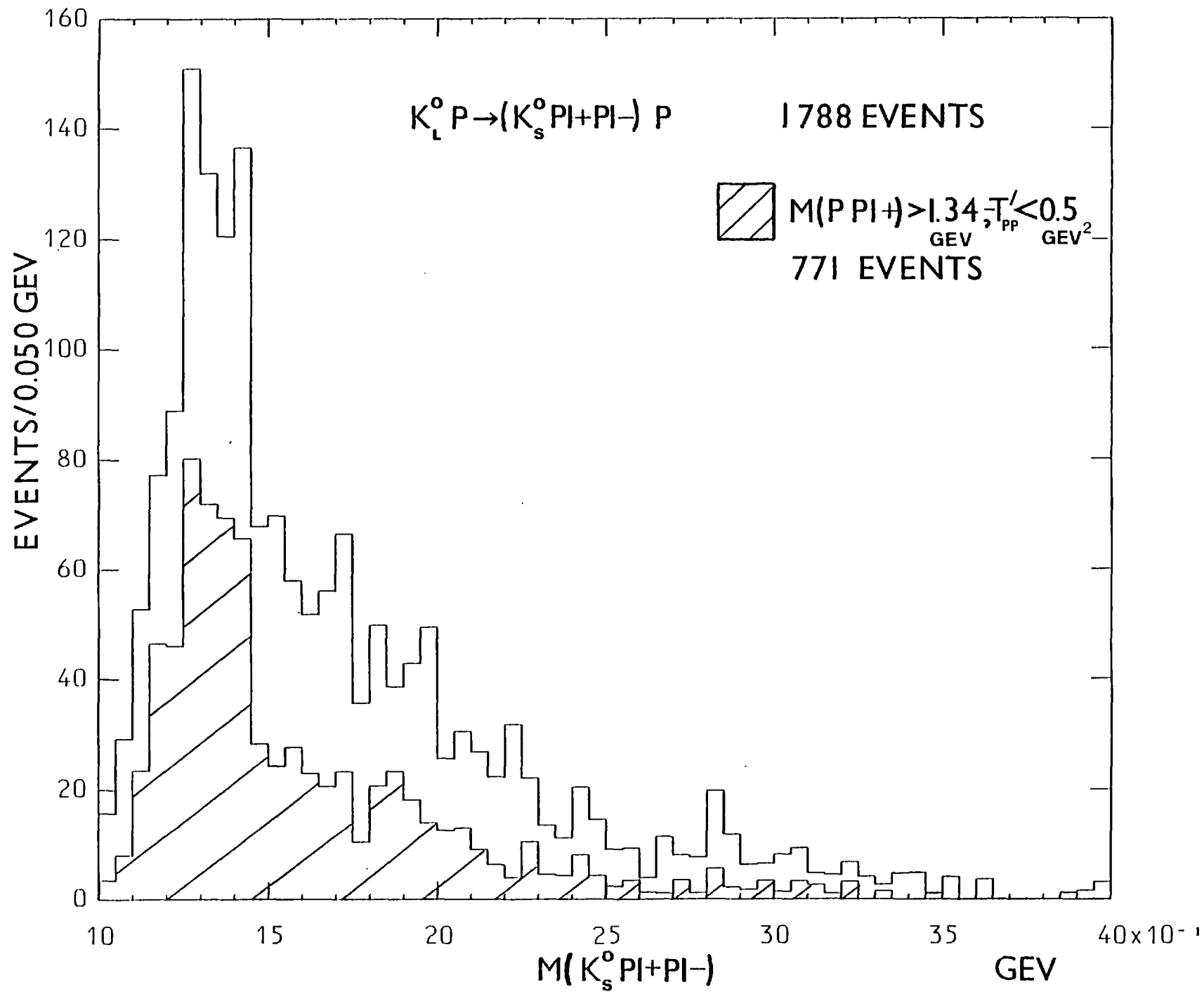
THE DECK EFFECT

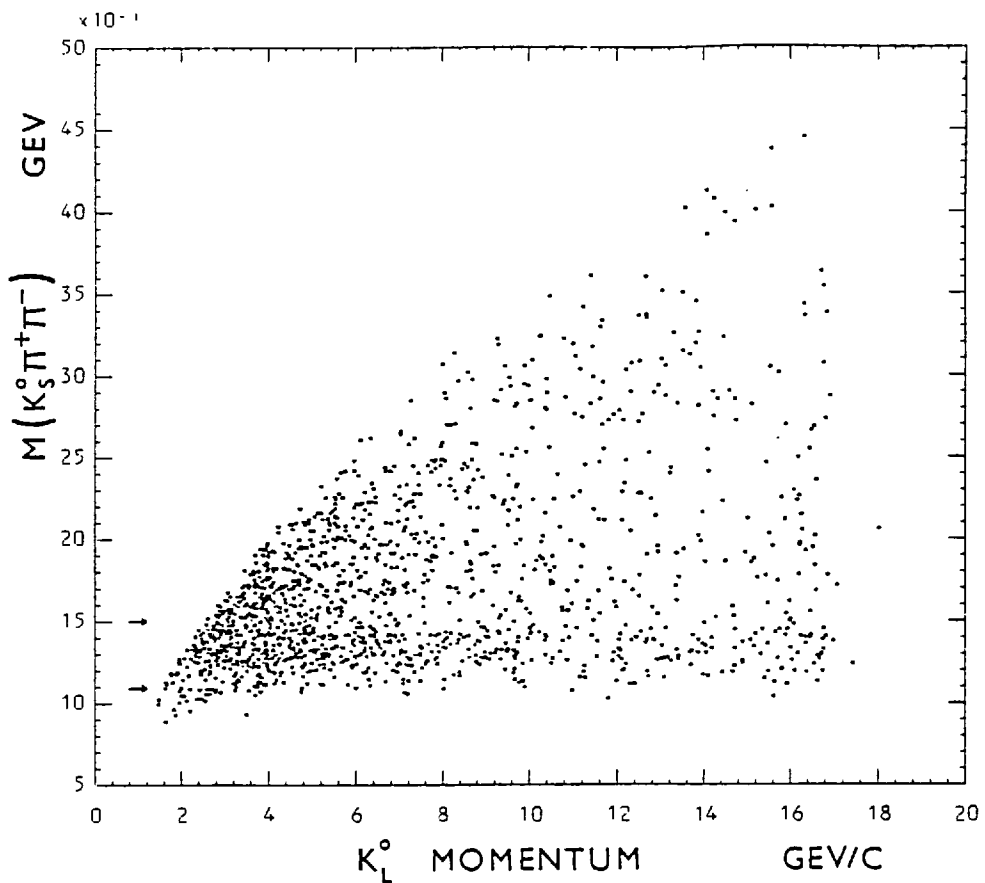


4.8

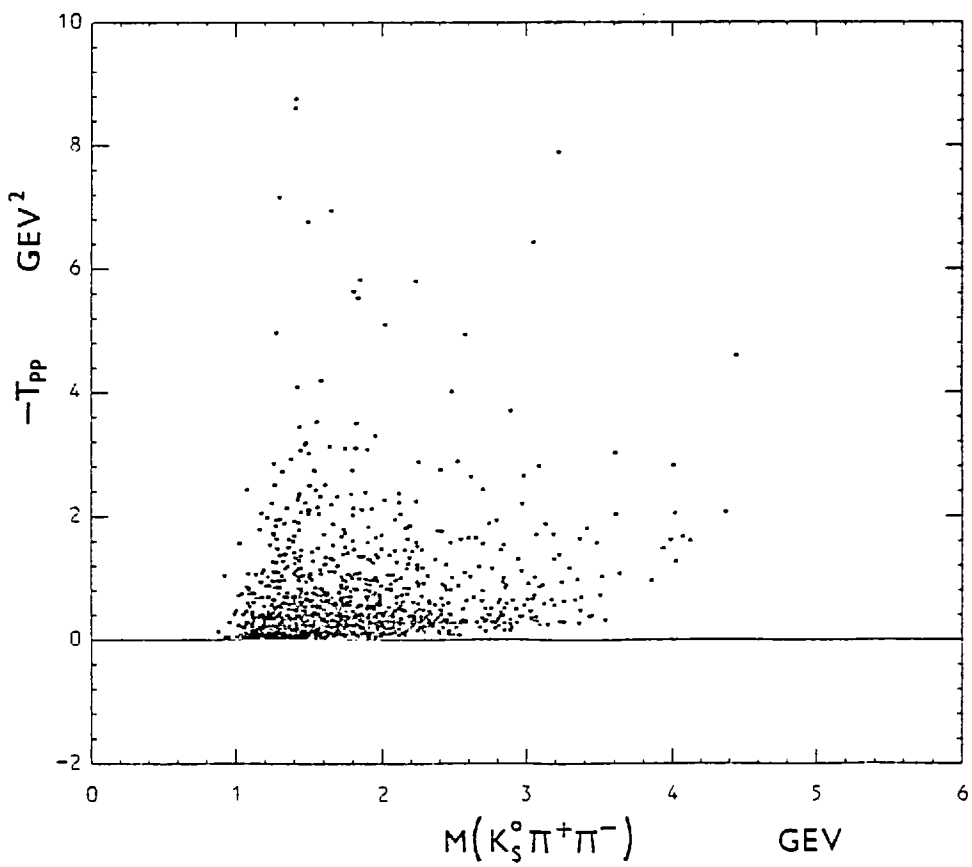


4.9

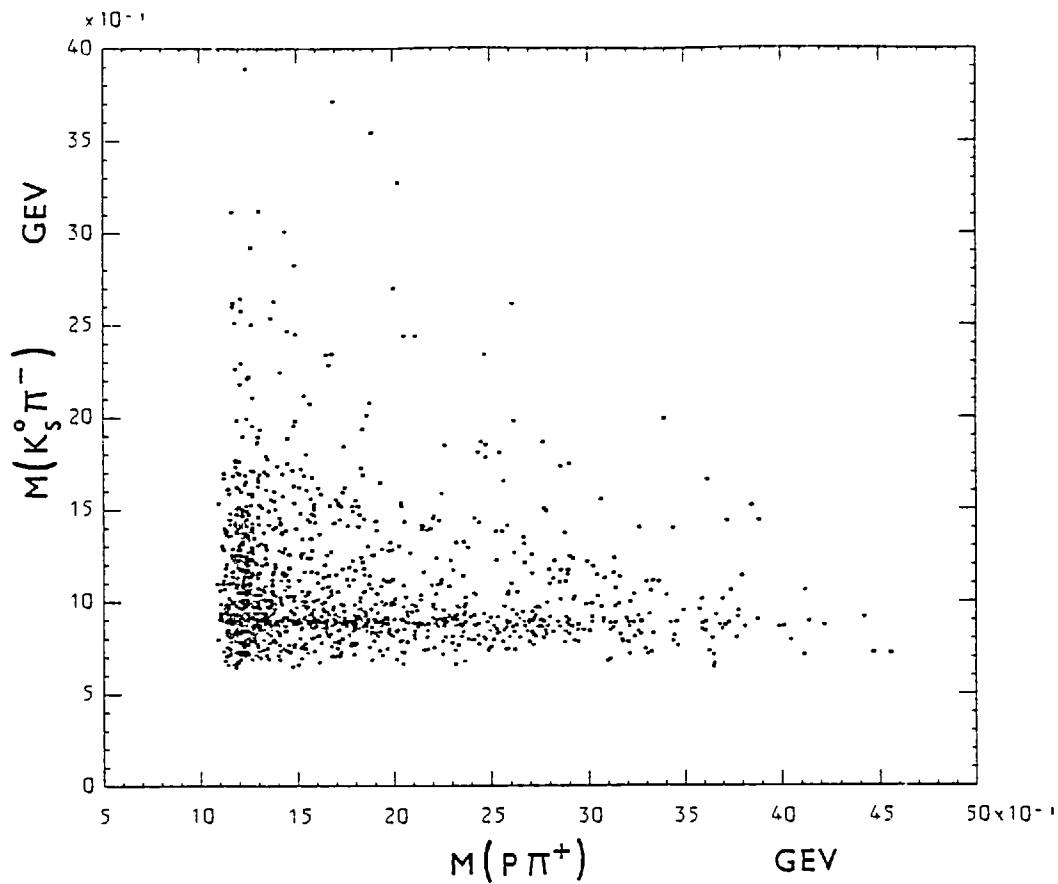




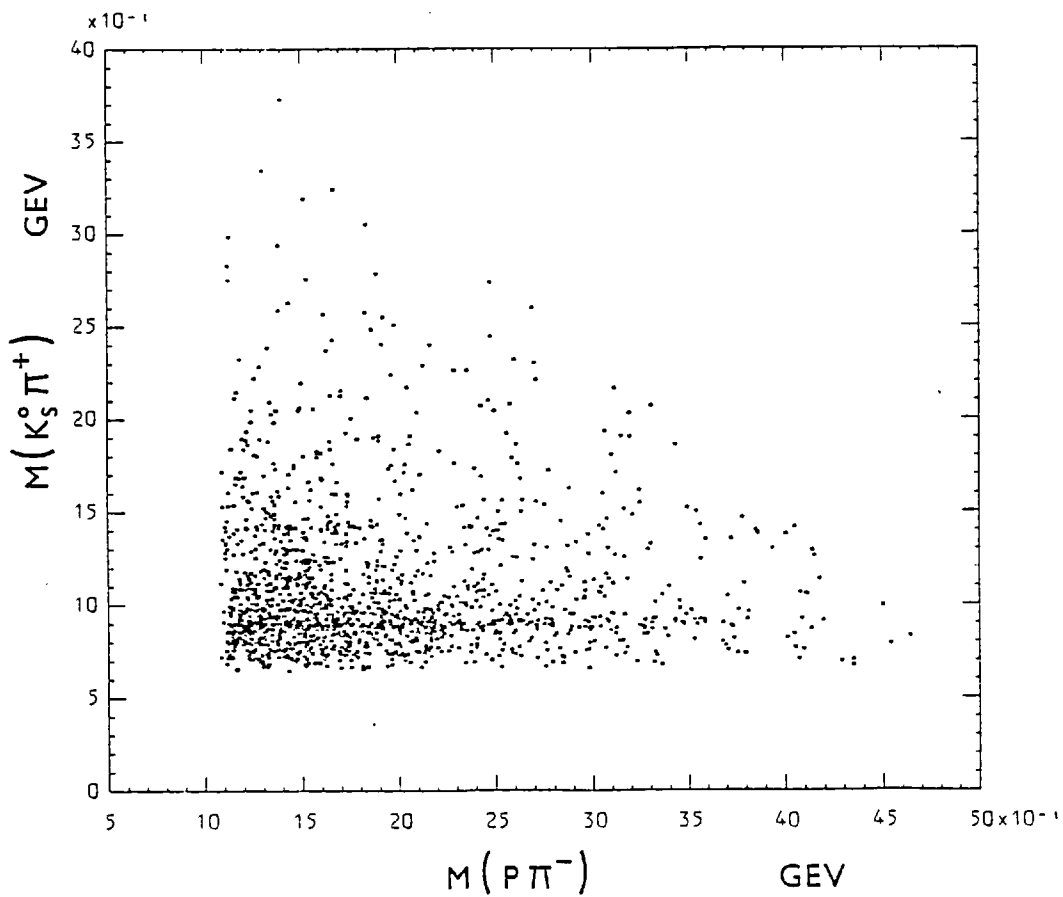
4.11



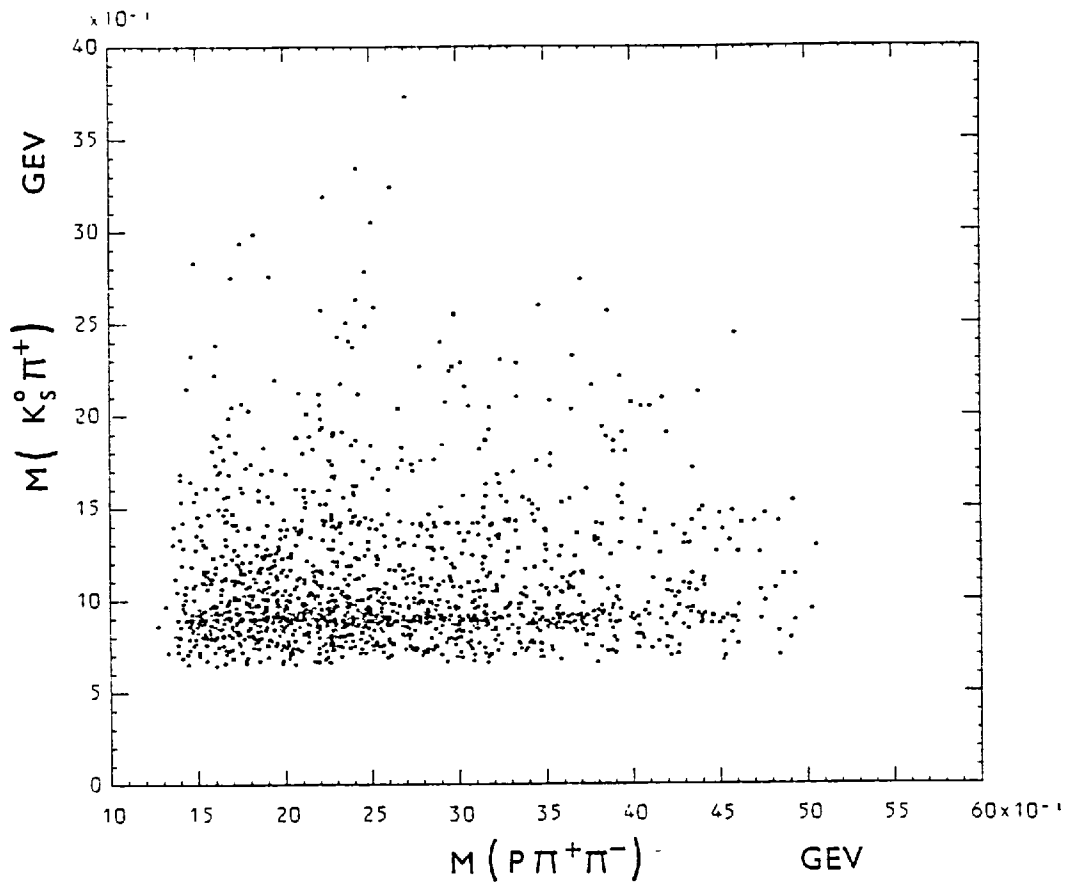
4.12



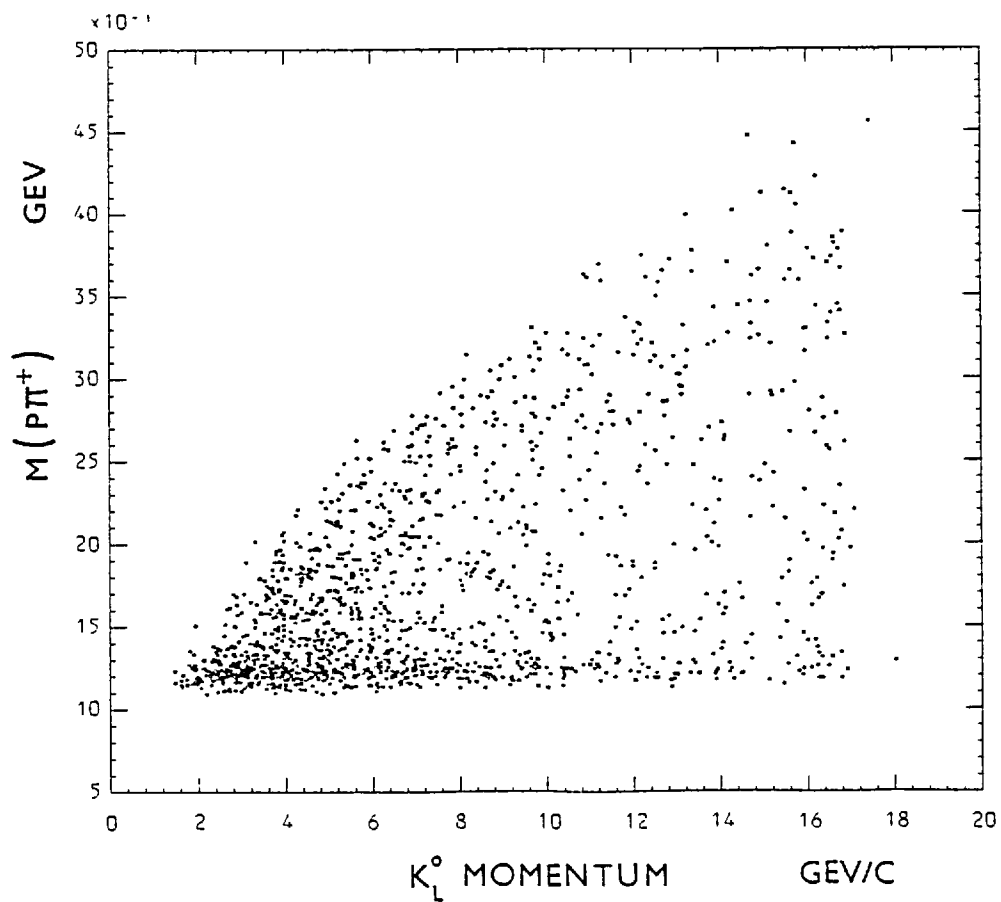
4.13



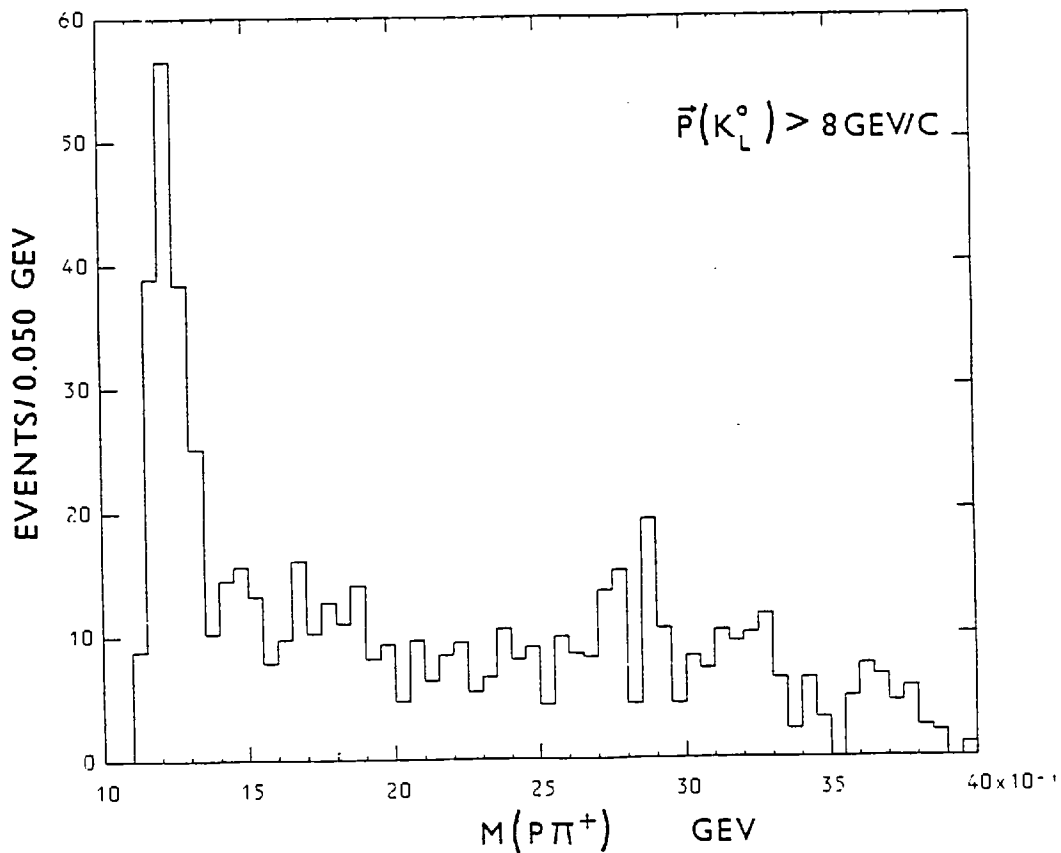
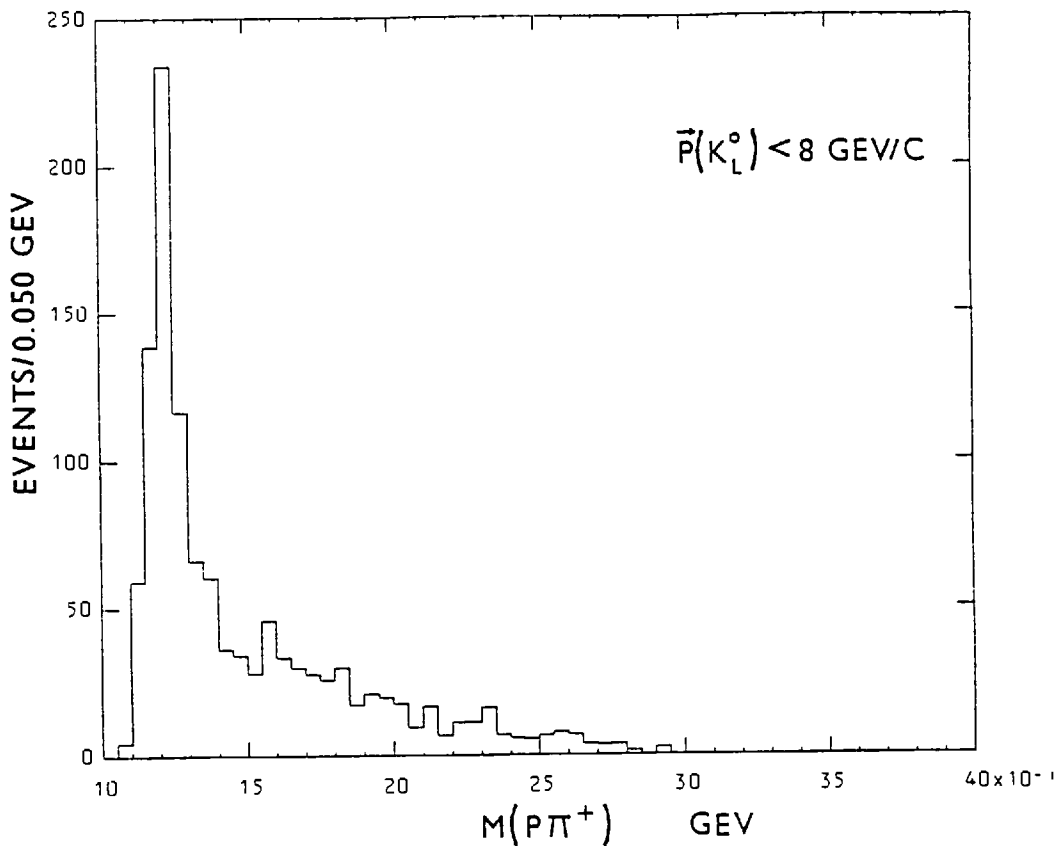
4.14

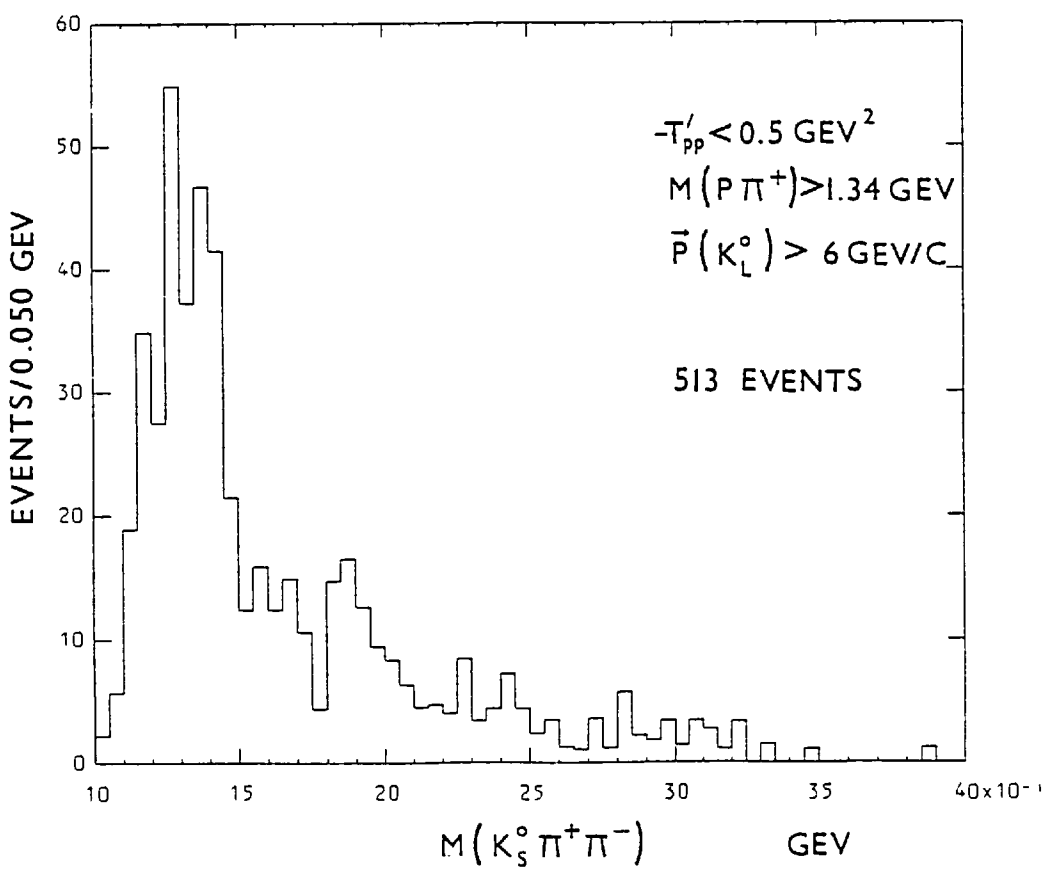
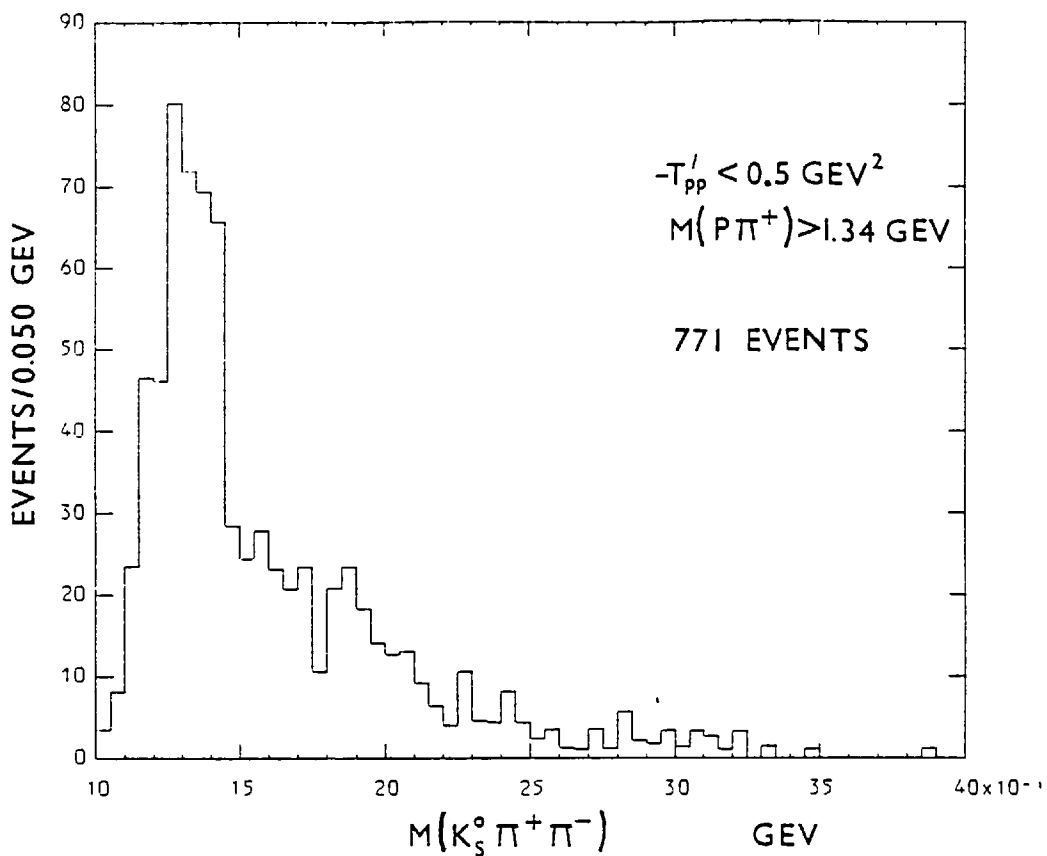


4.15

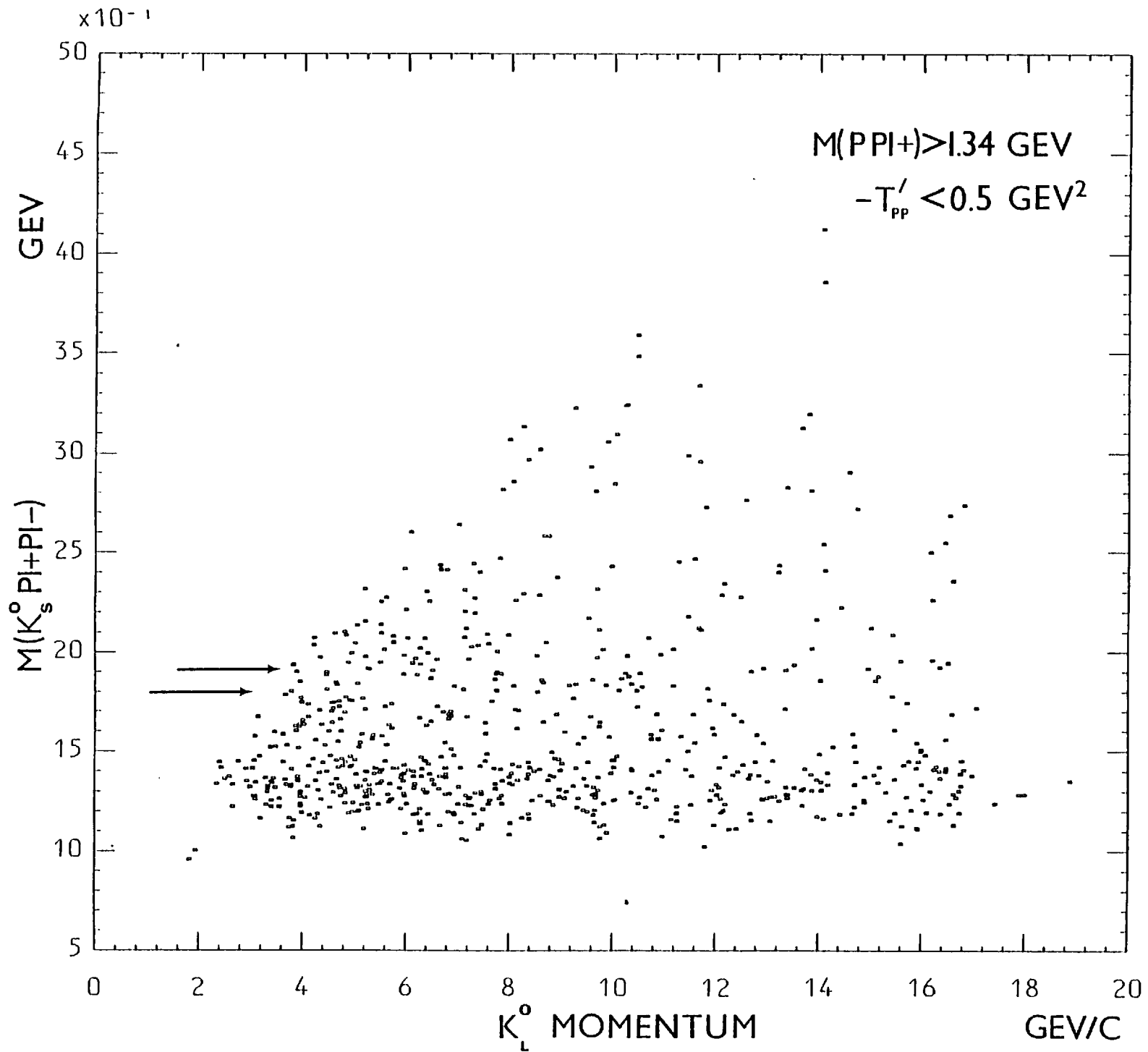


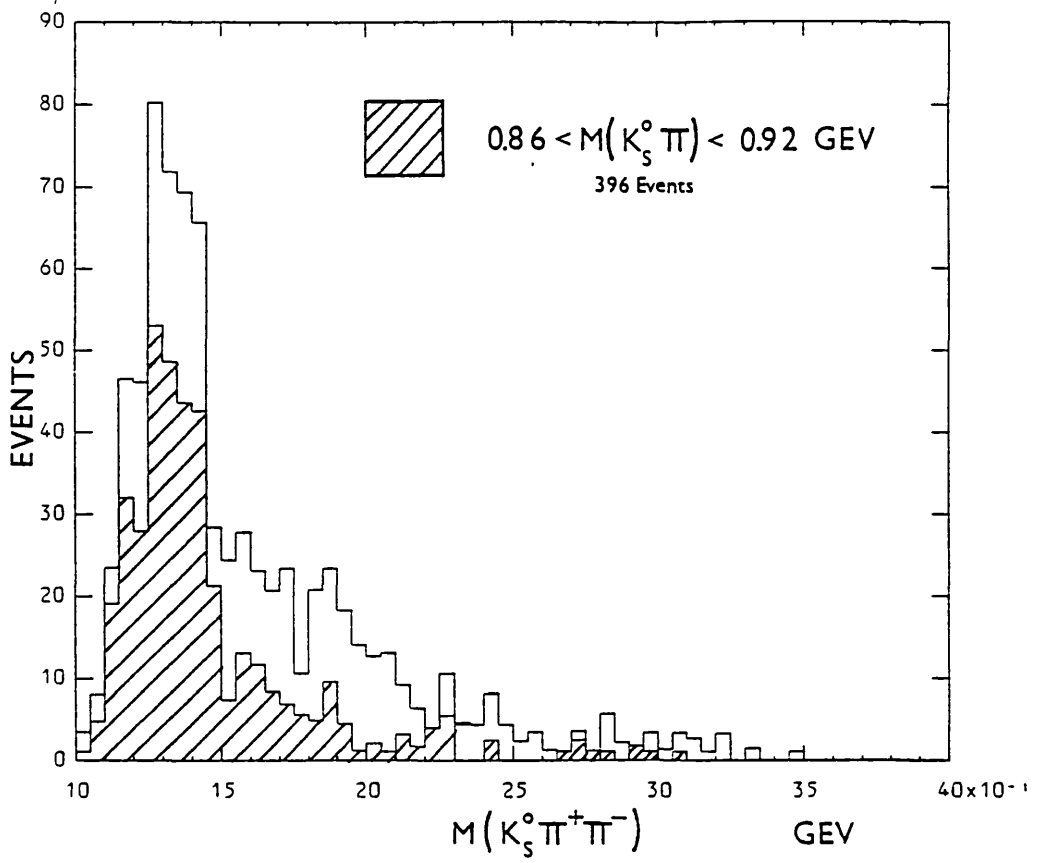
4.16



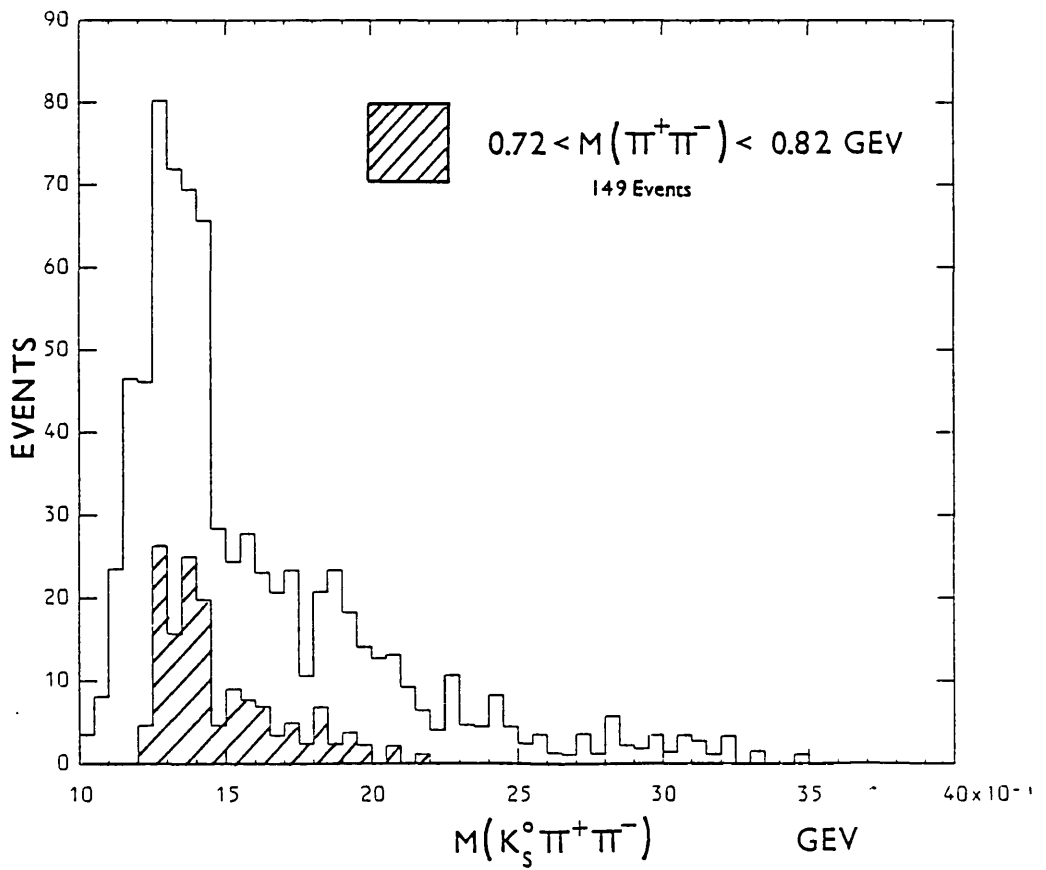


4.19

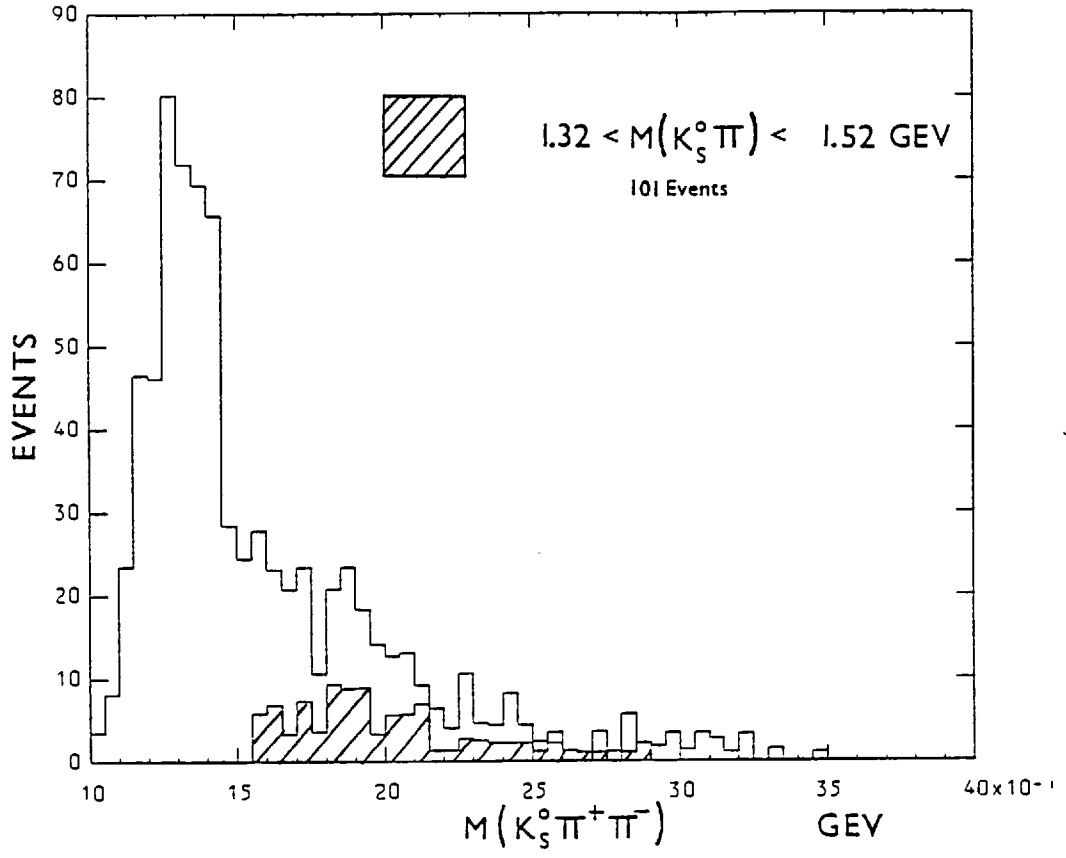




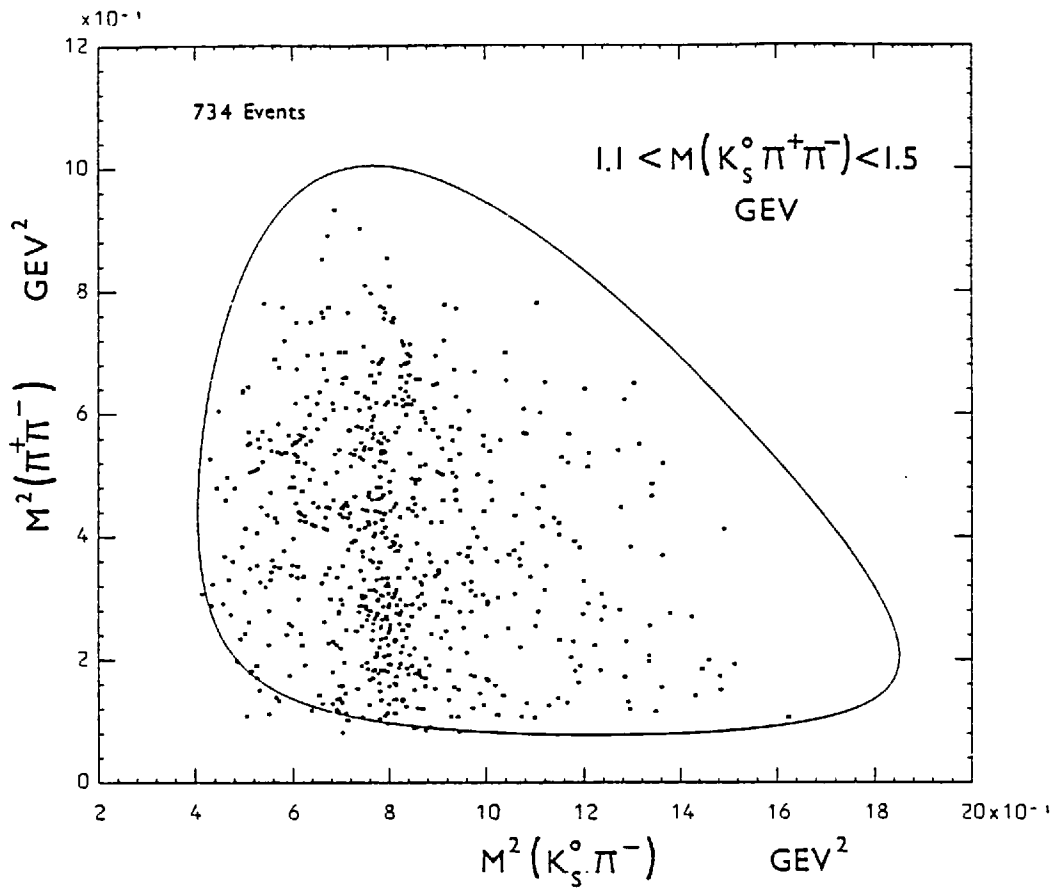
4.20



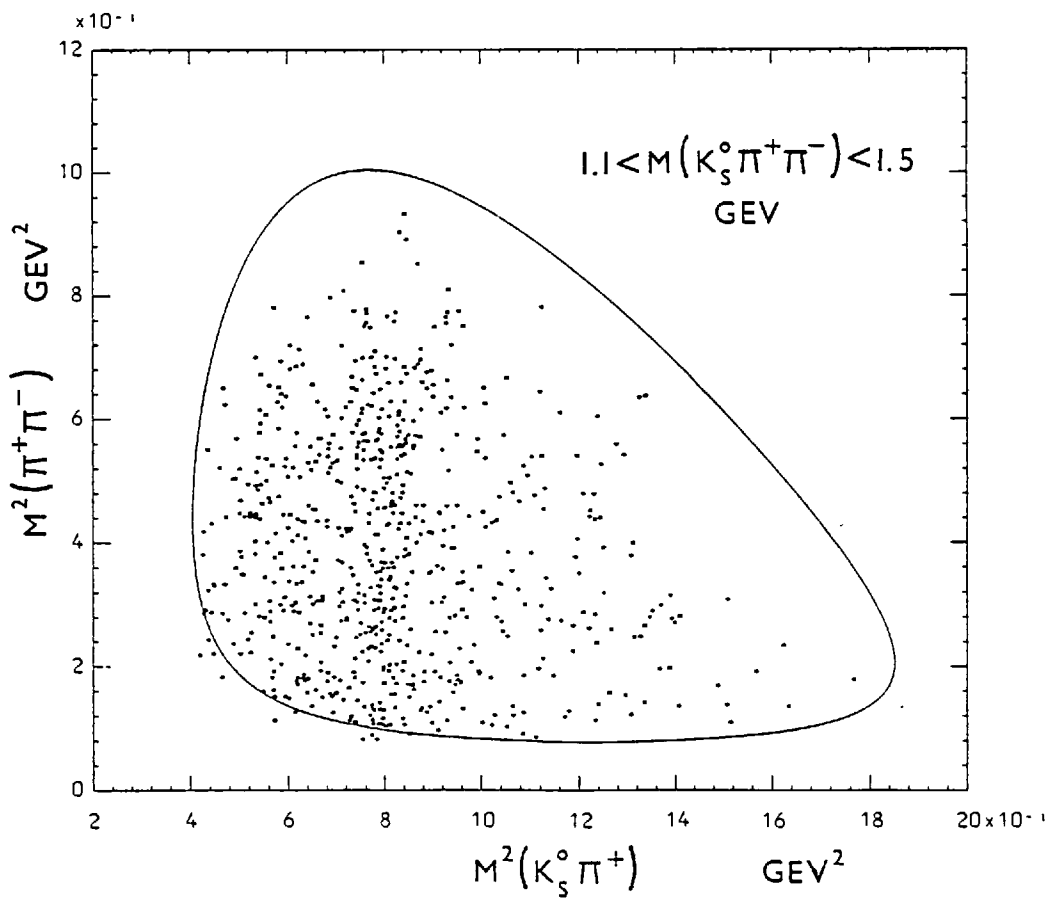
4.21



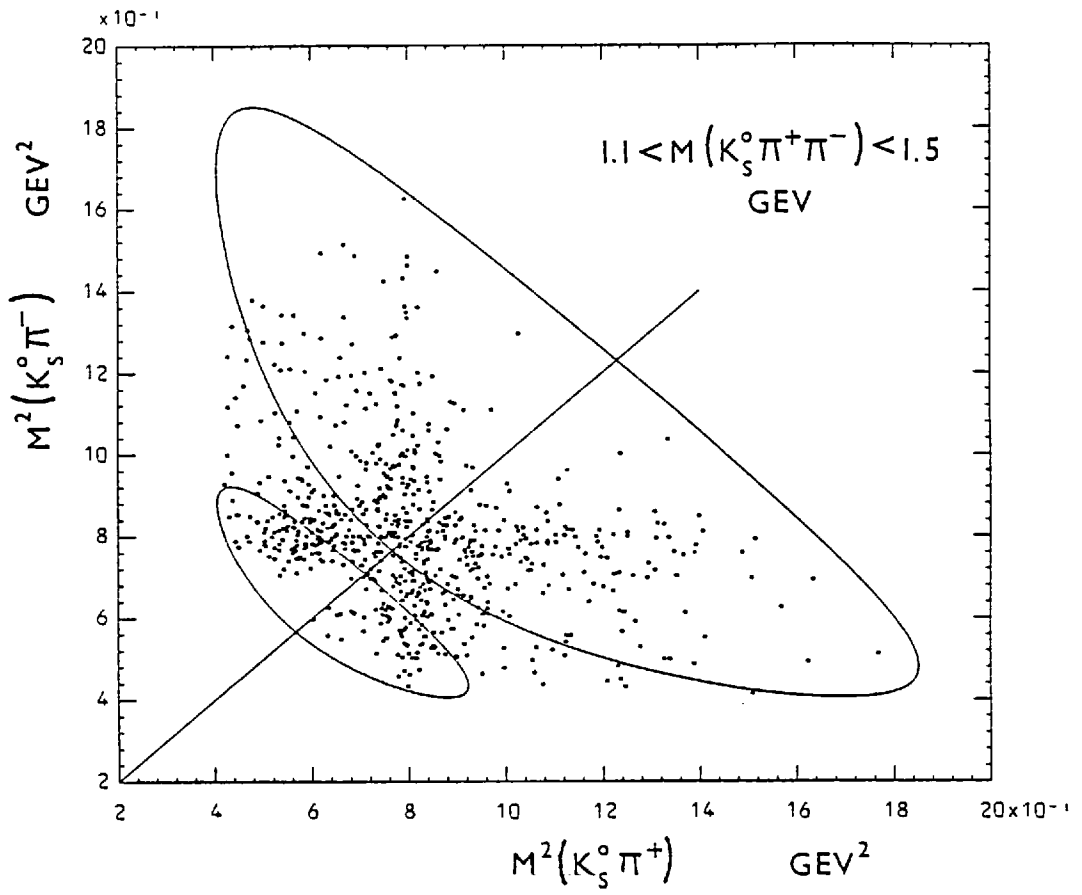
4.22



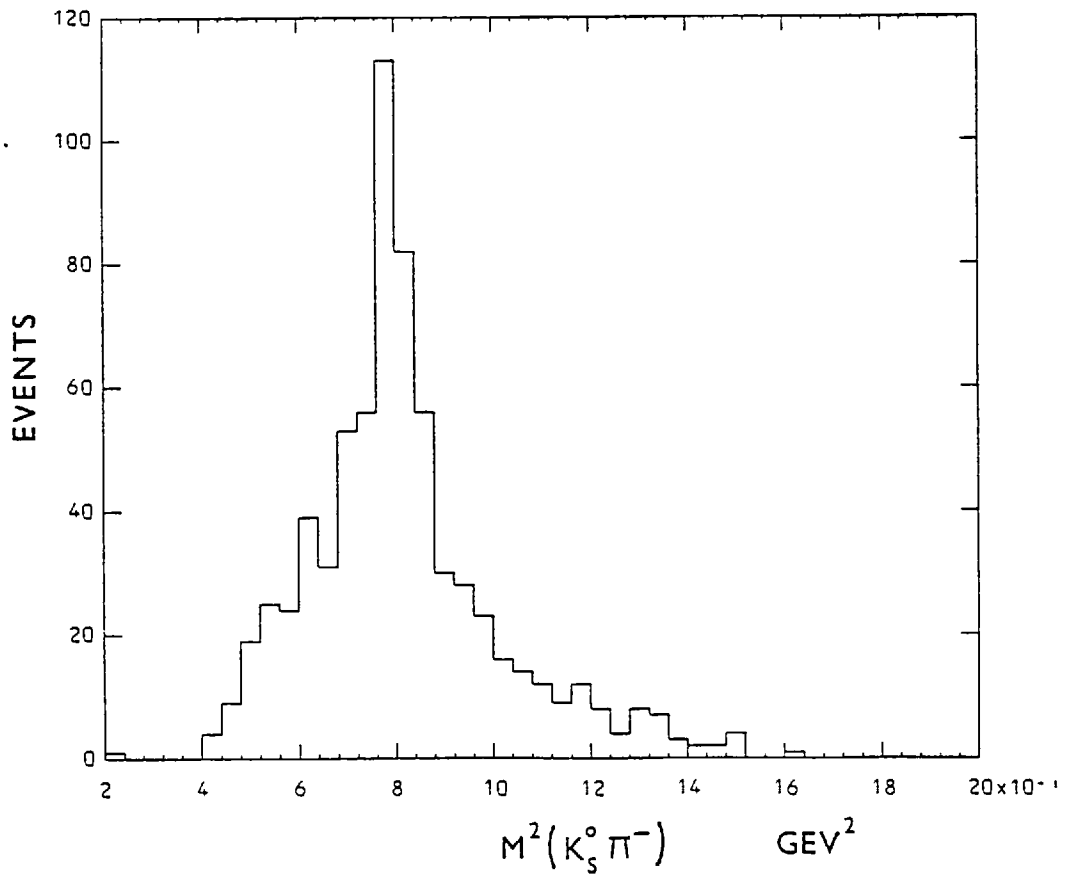
4.23



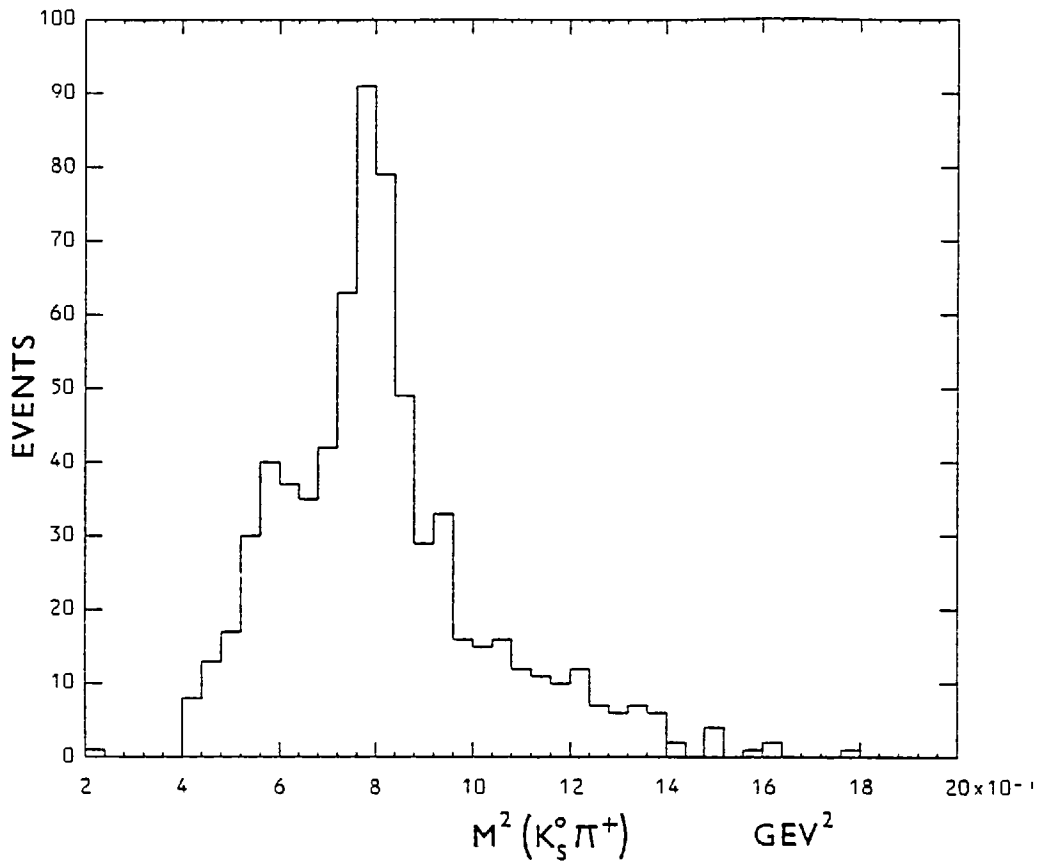
4.24



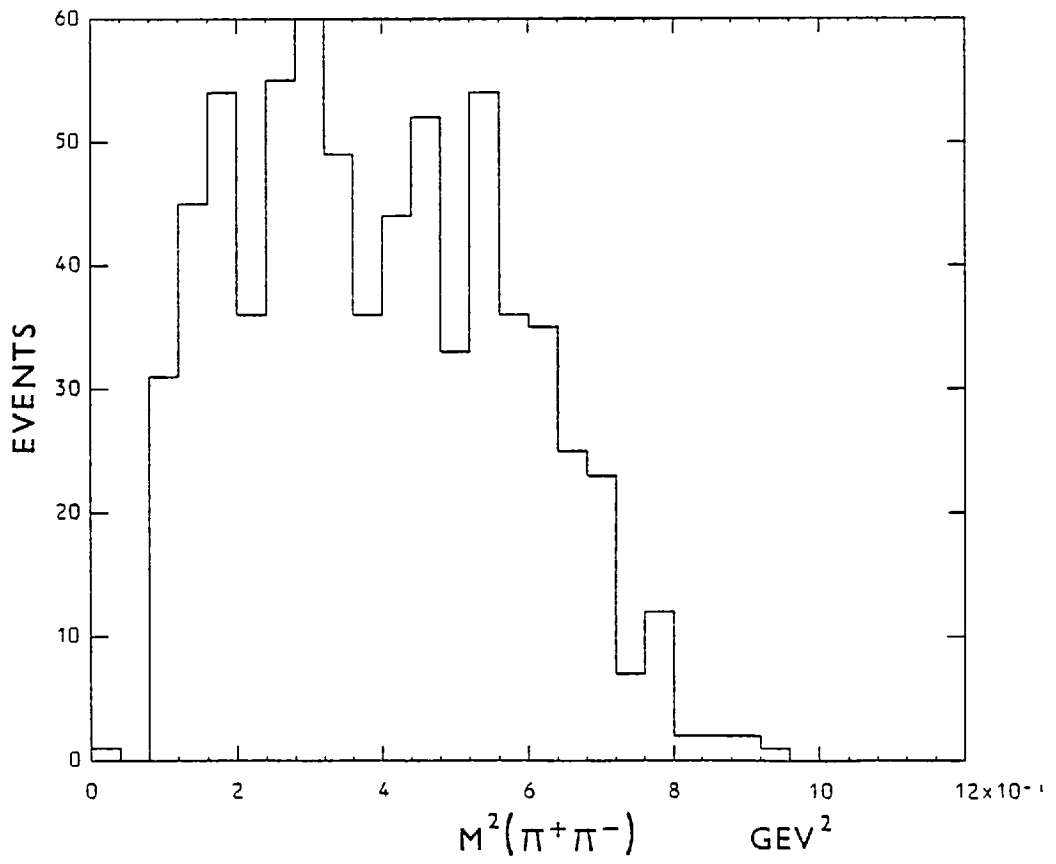
4.25



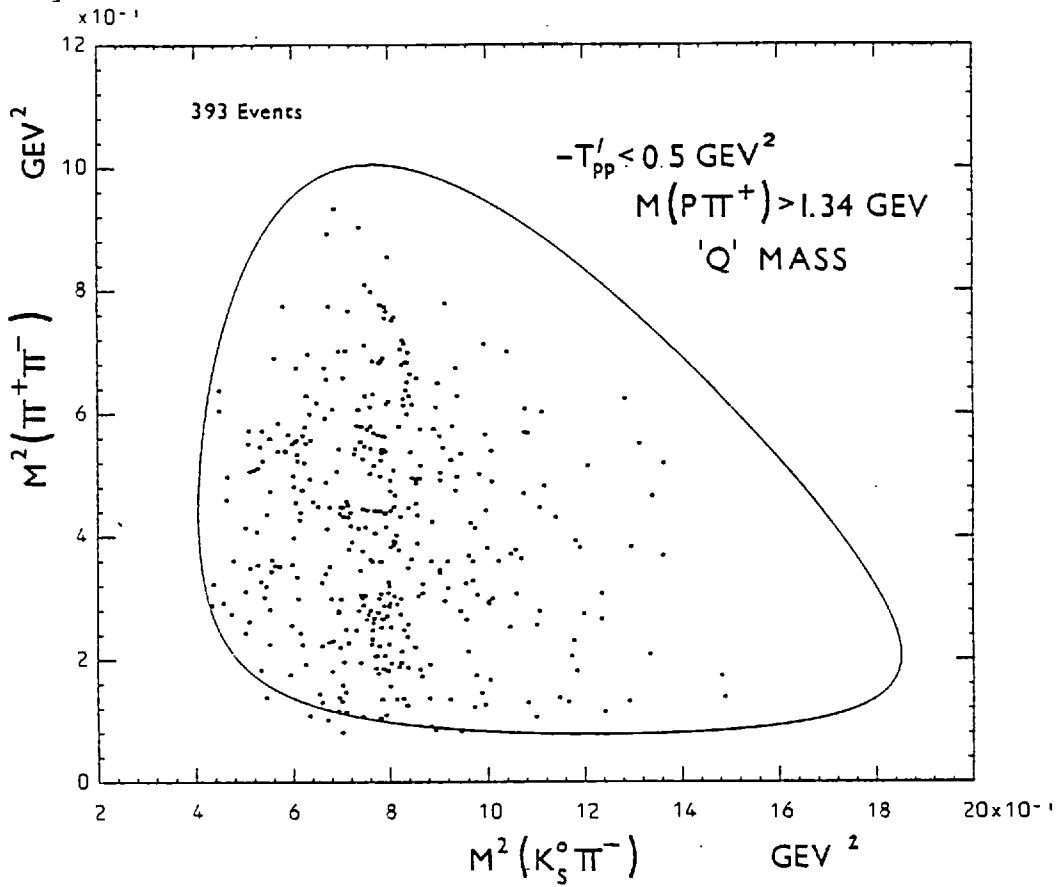
4.26



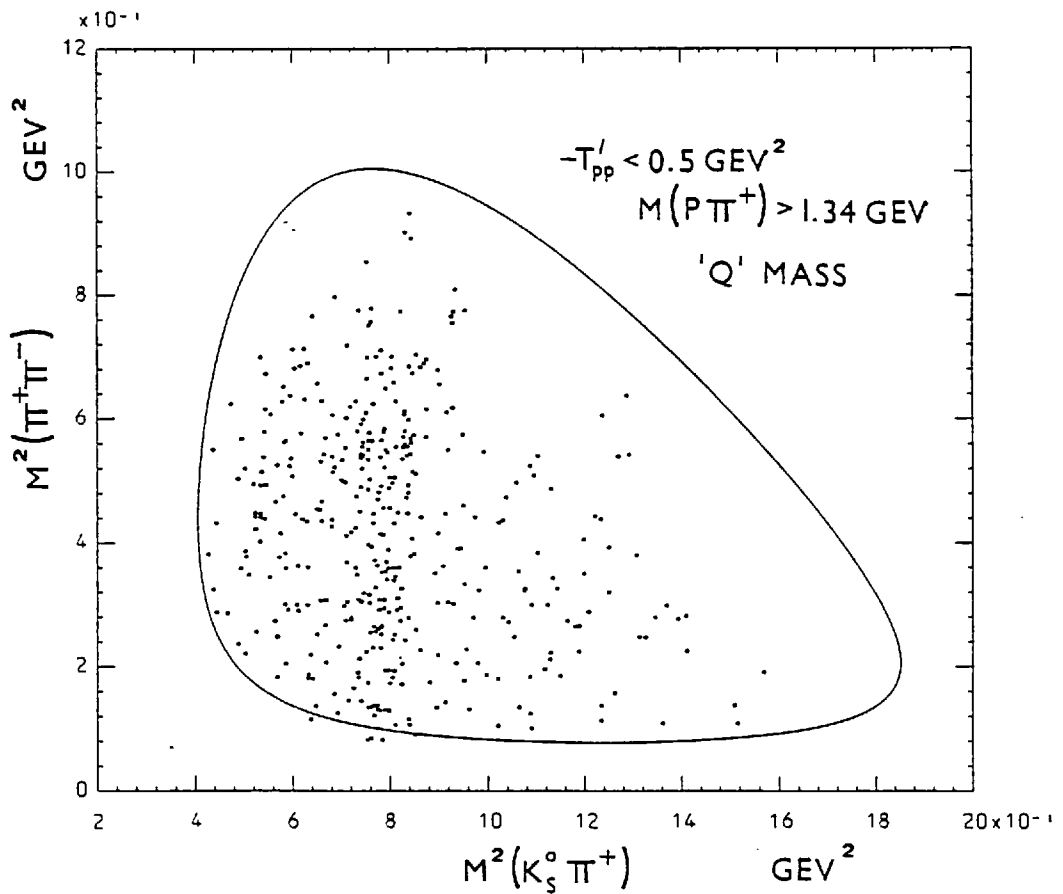
4.27



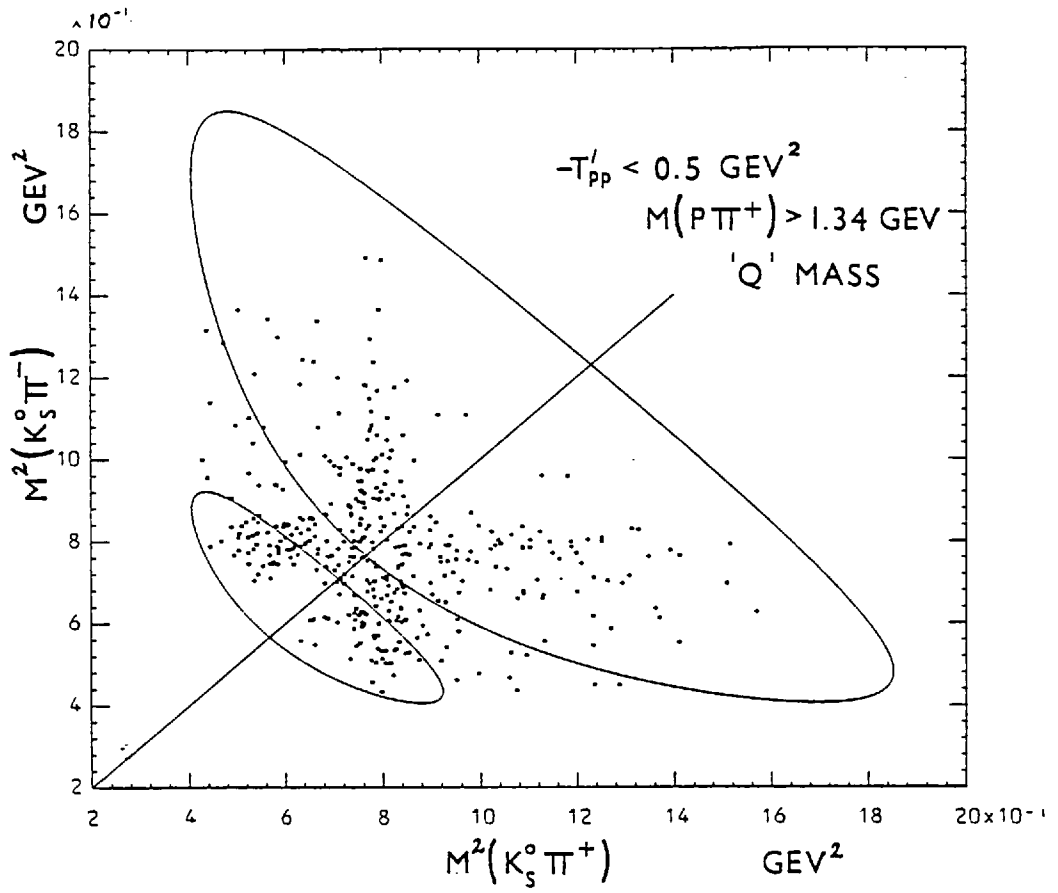
4.28



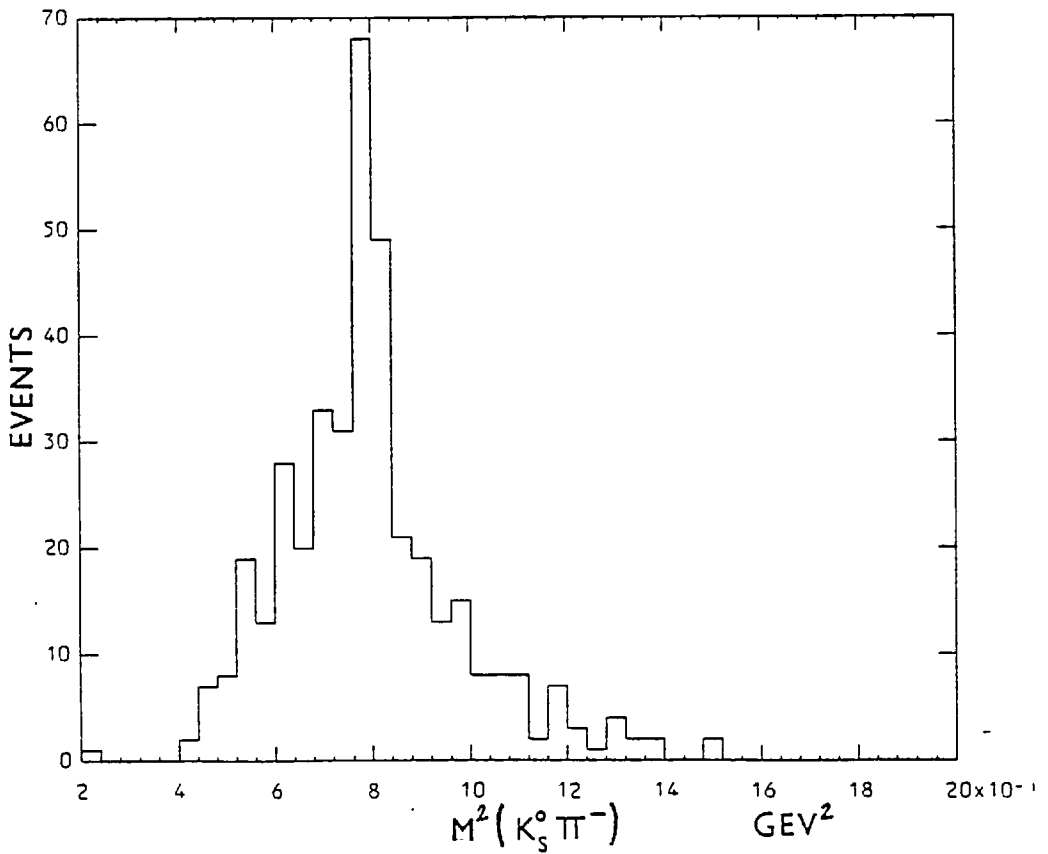
4.29



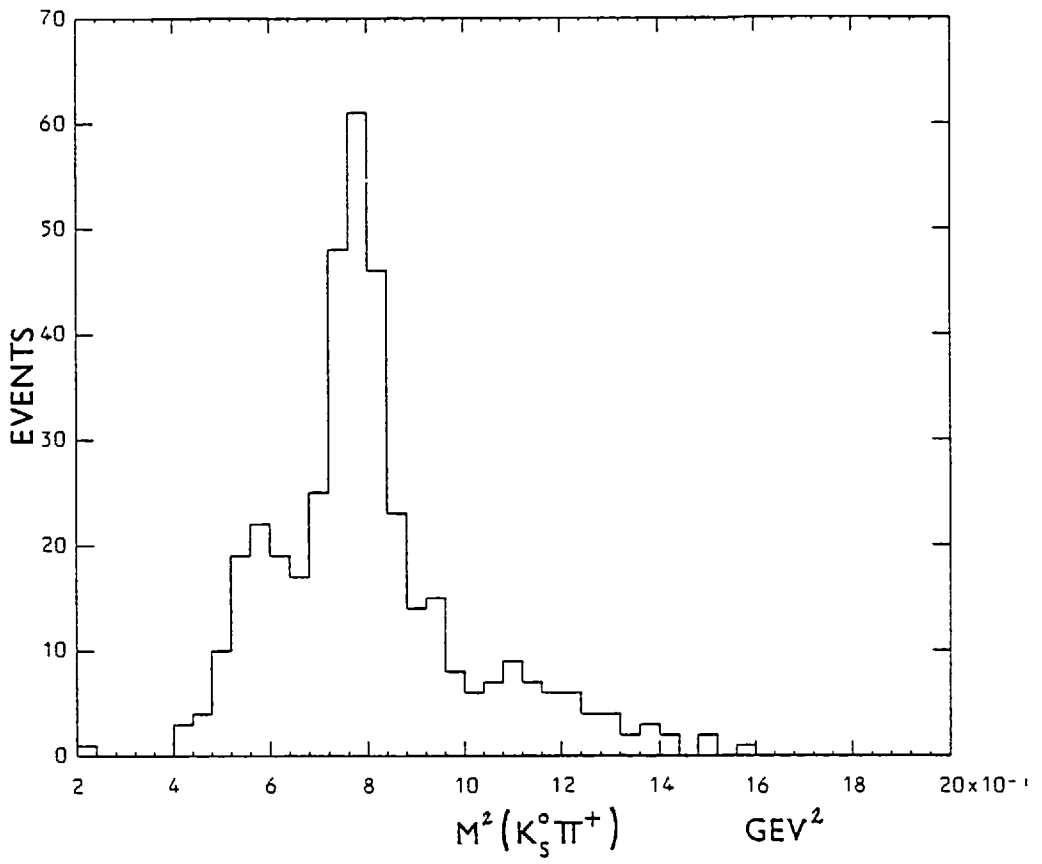
4.30



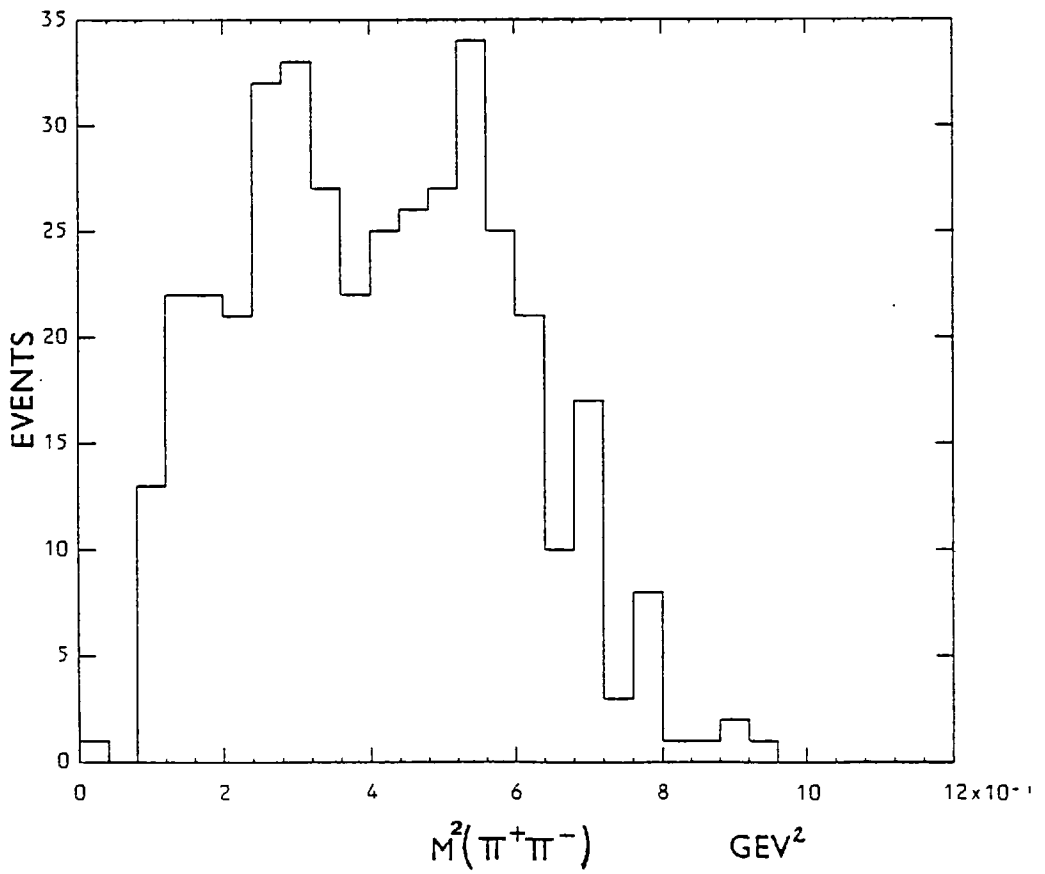
4.31



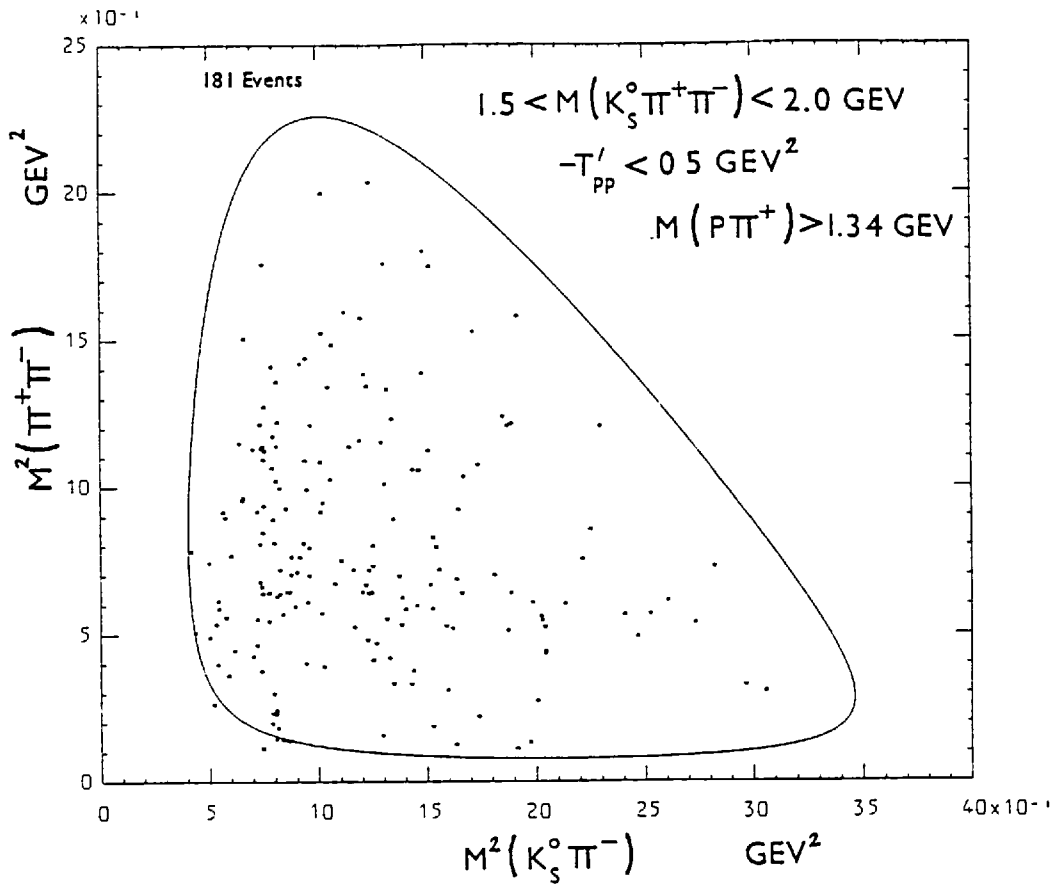
4.32



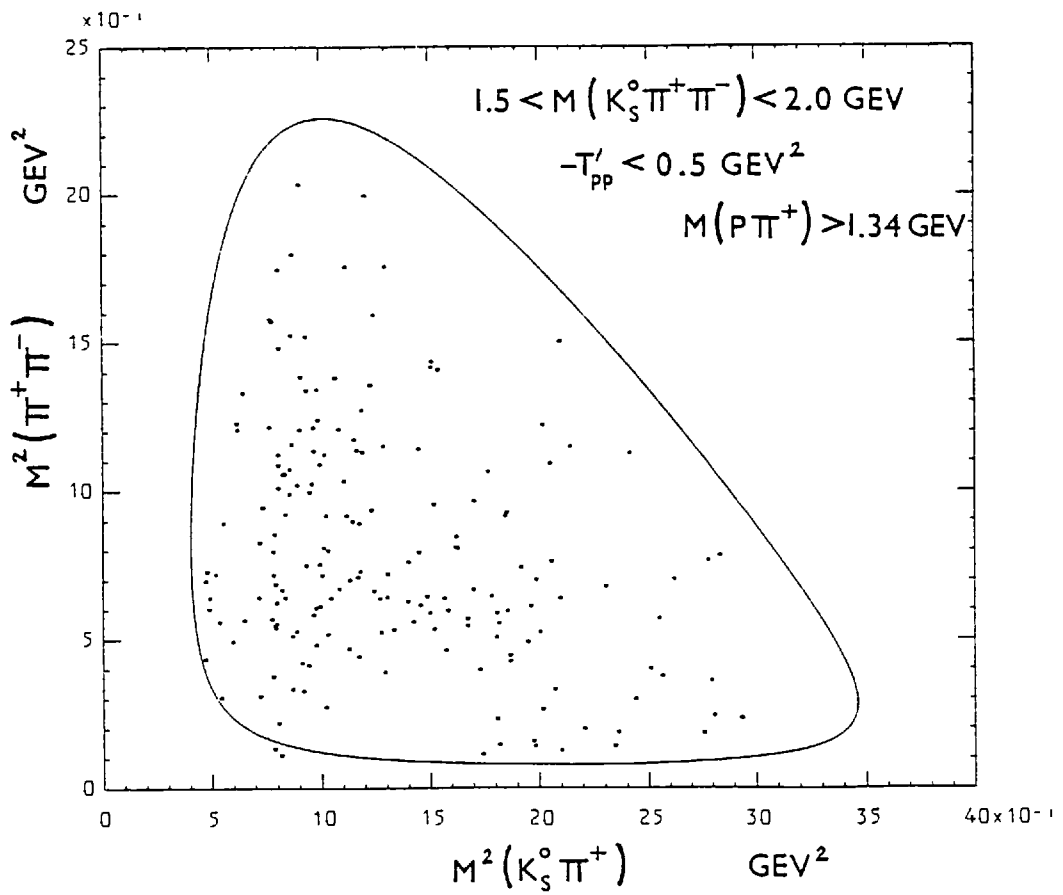
4.33



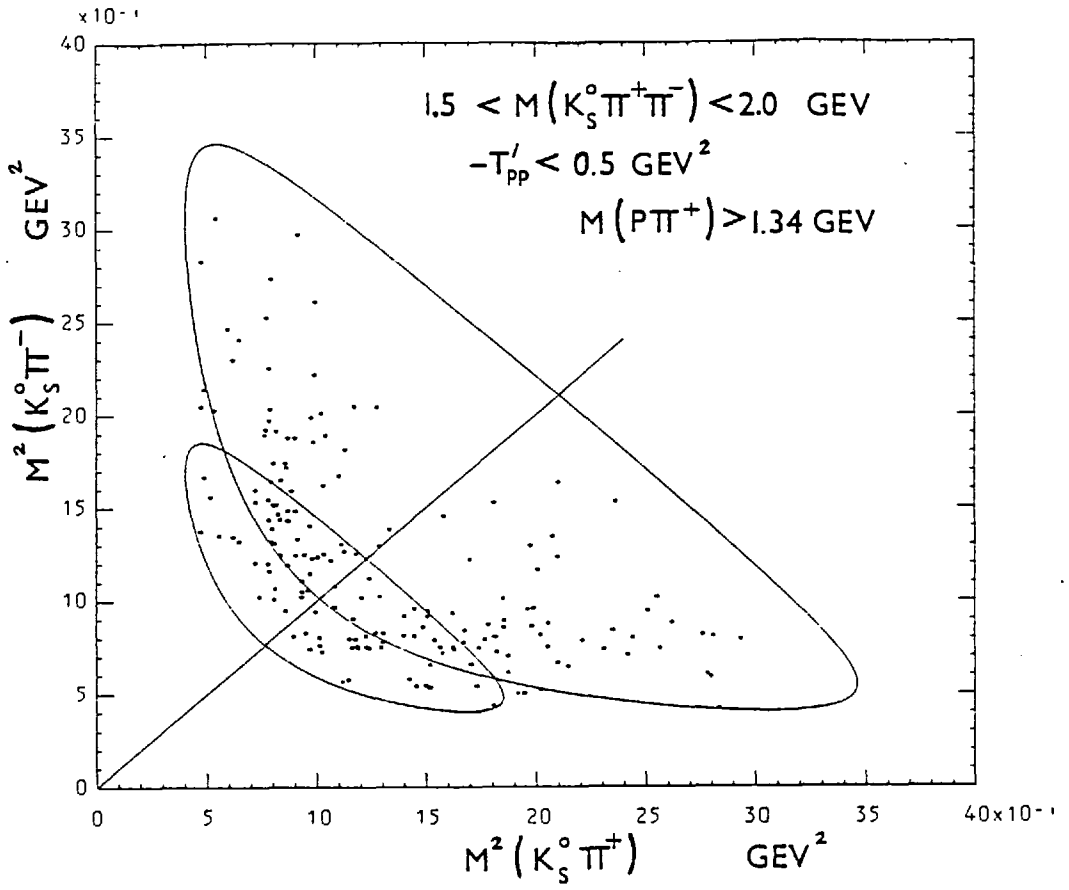
4.34



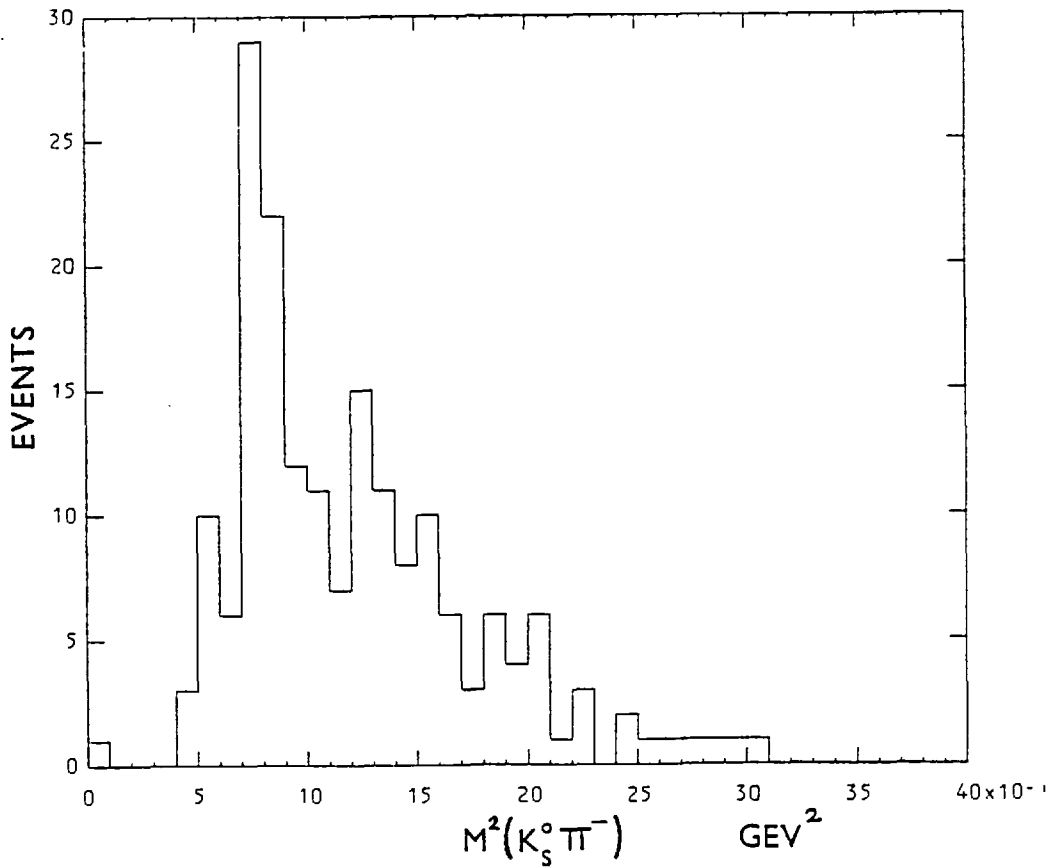
4.35



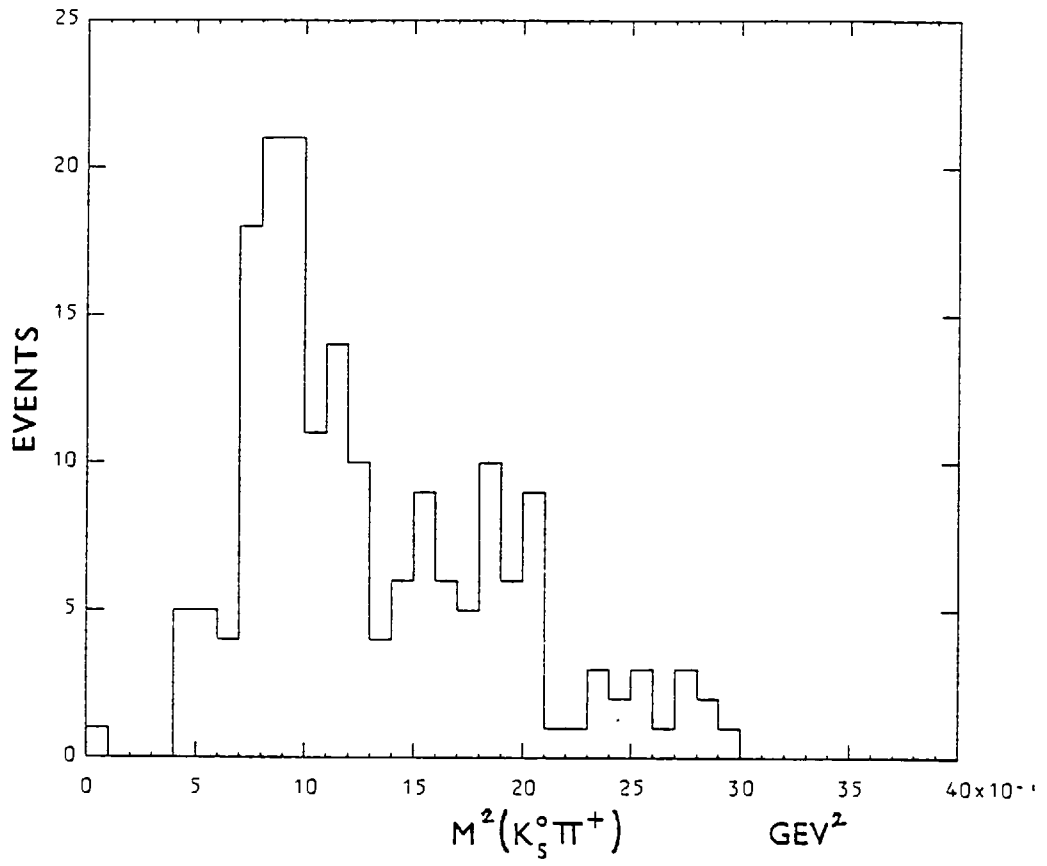
4.36



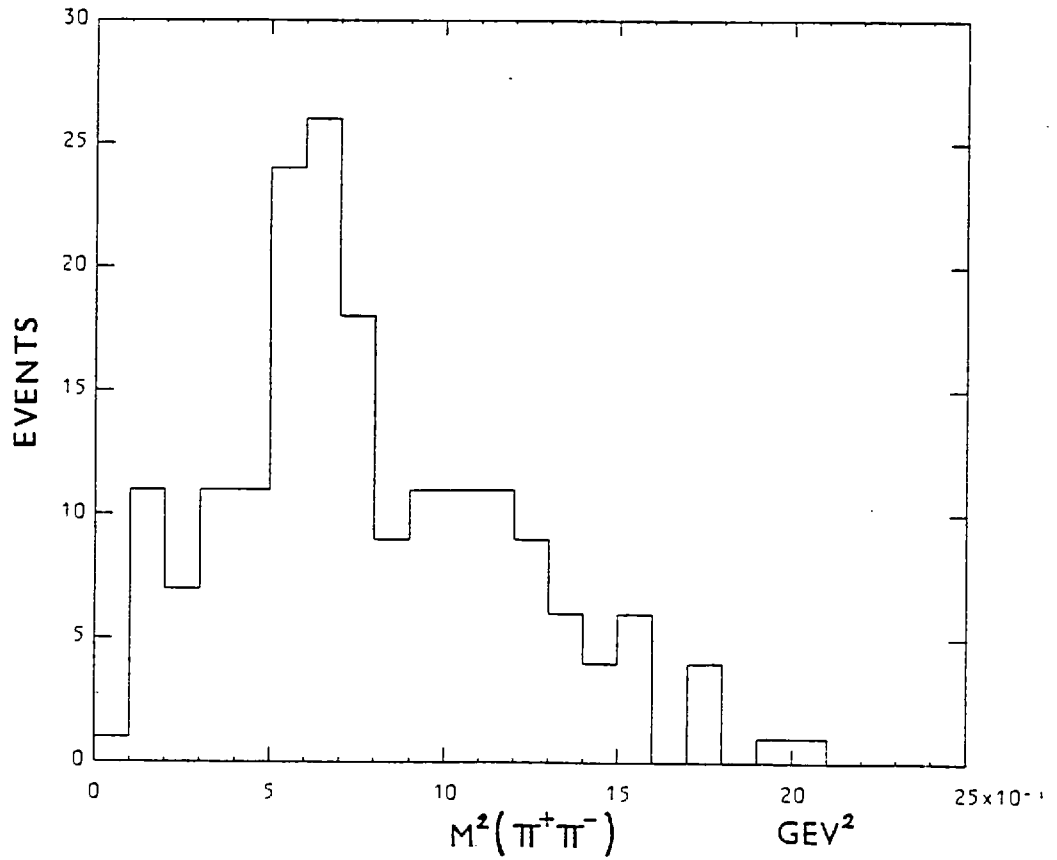
4.37



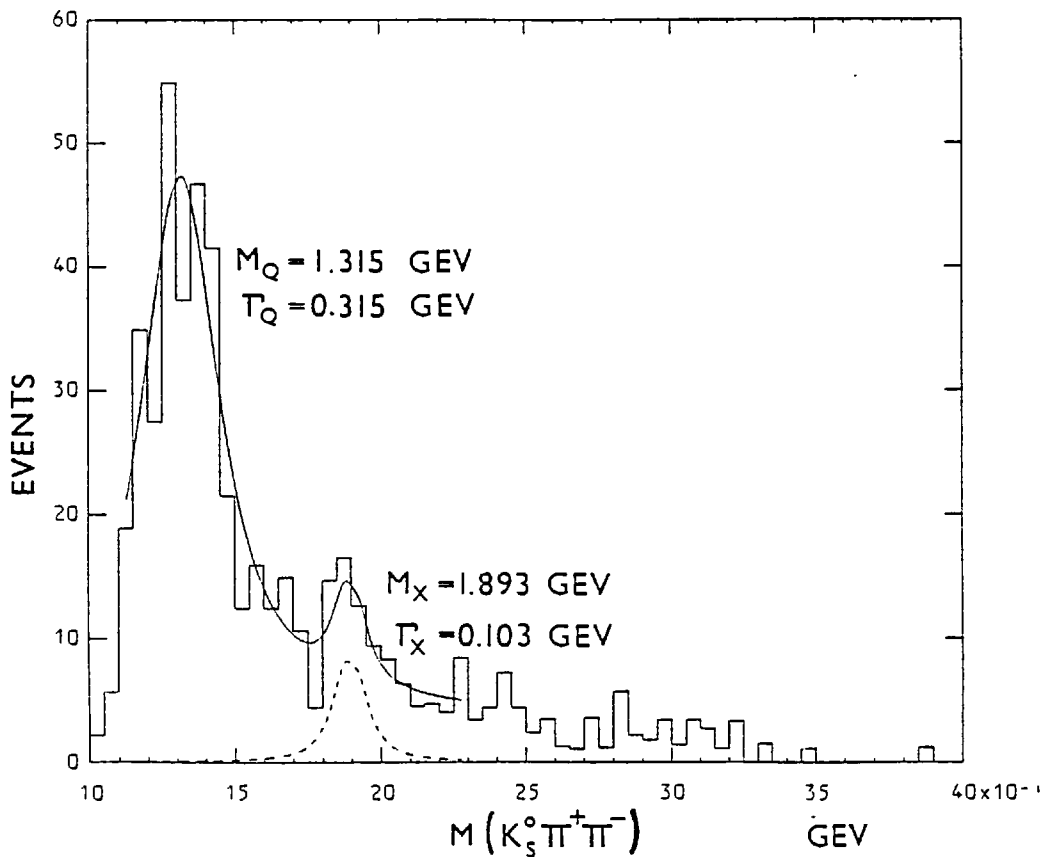
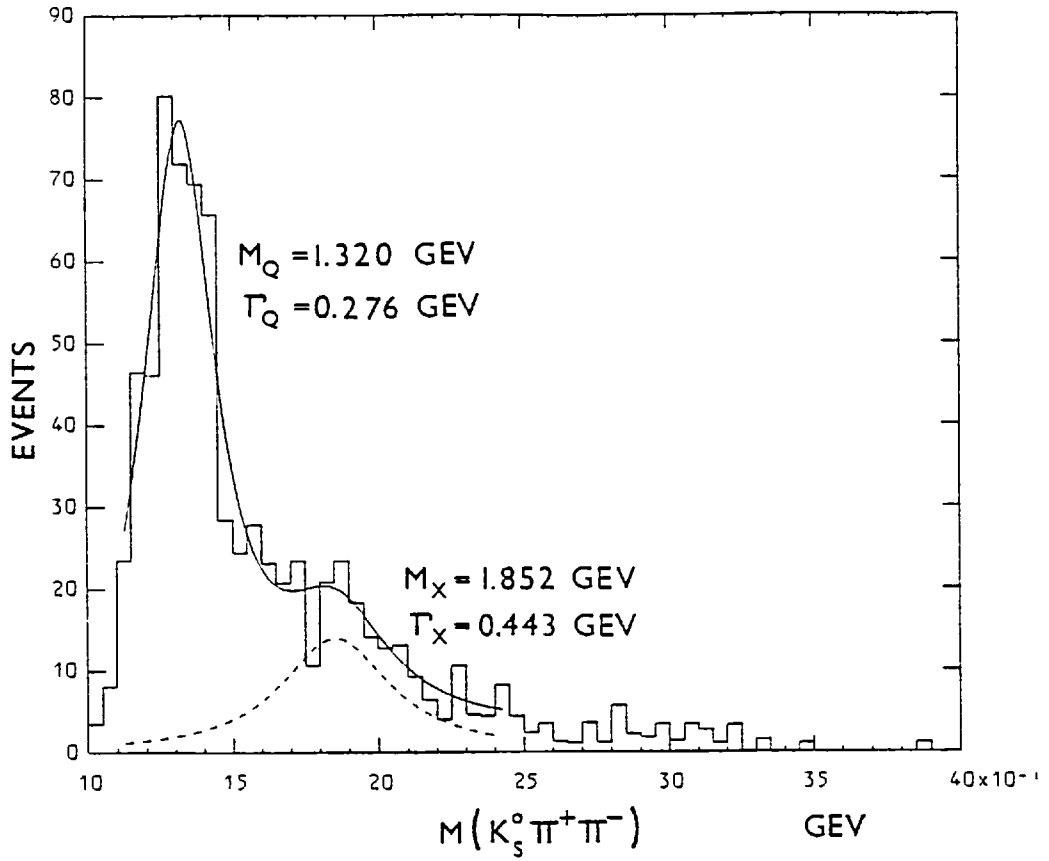
4.38



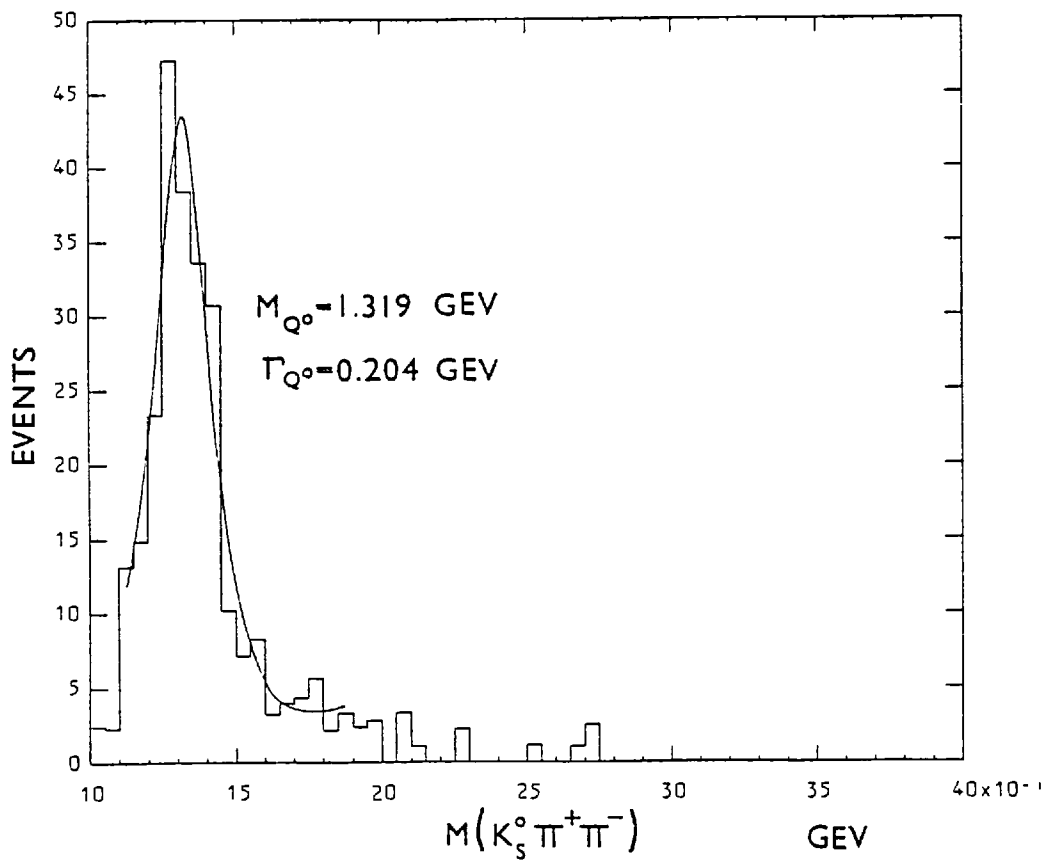
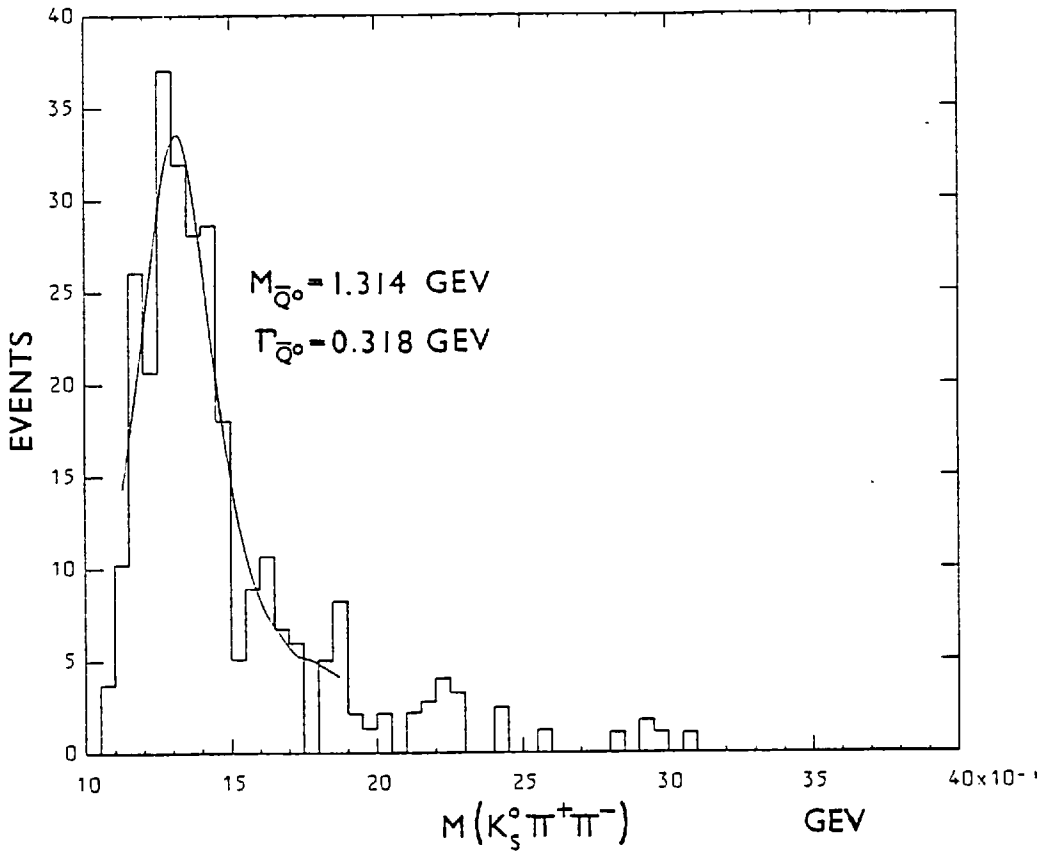
4.39



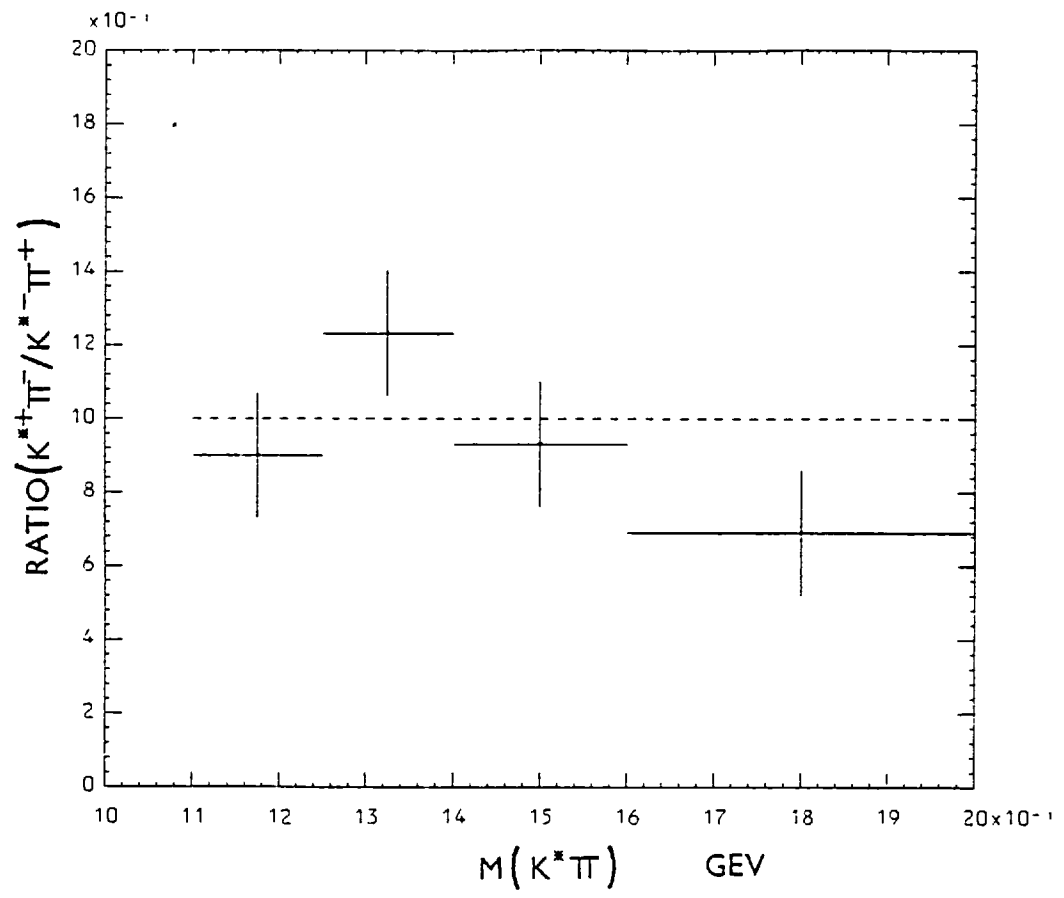
4.40



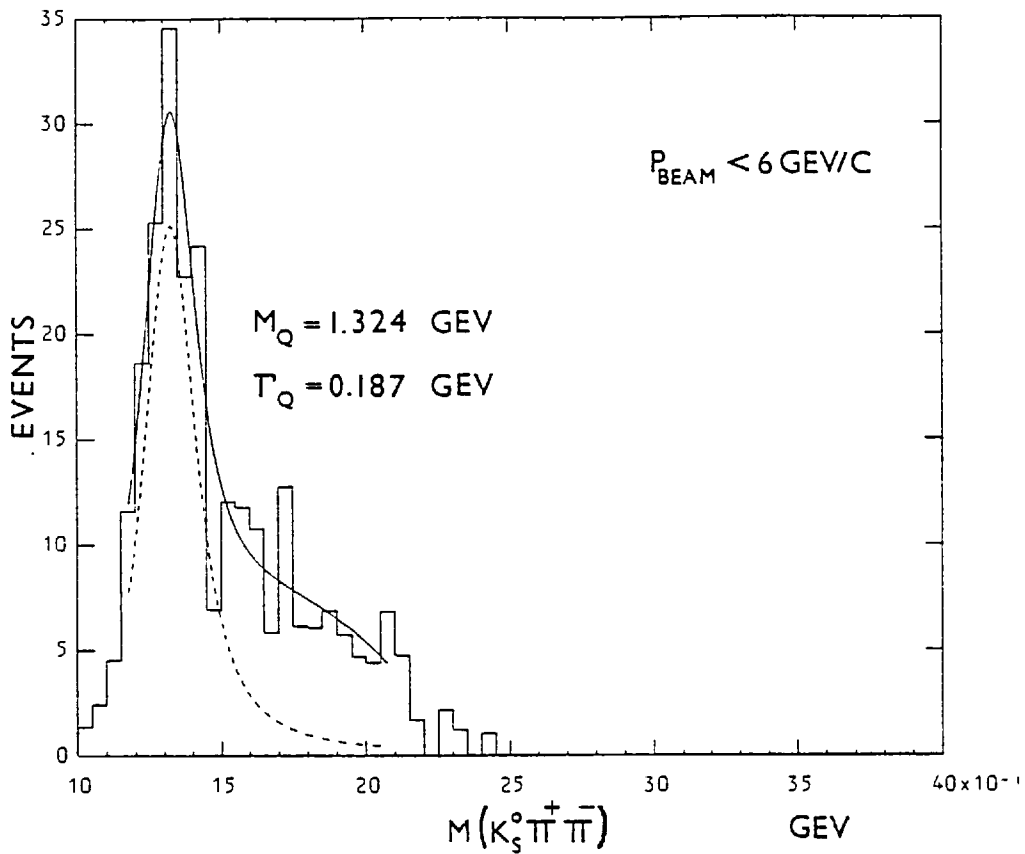
4.41



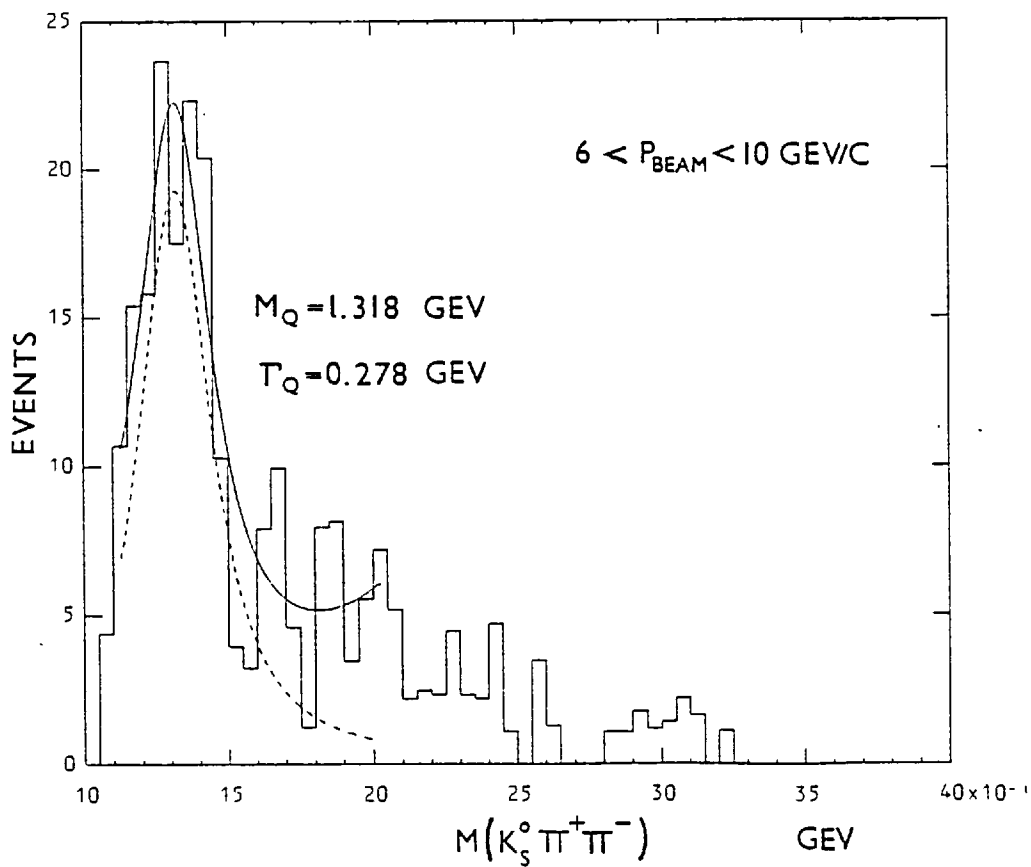
4.42



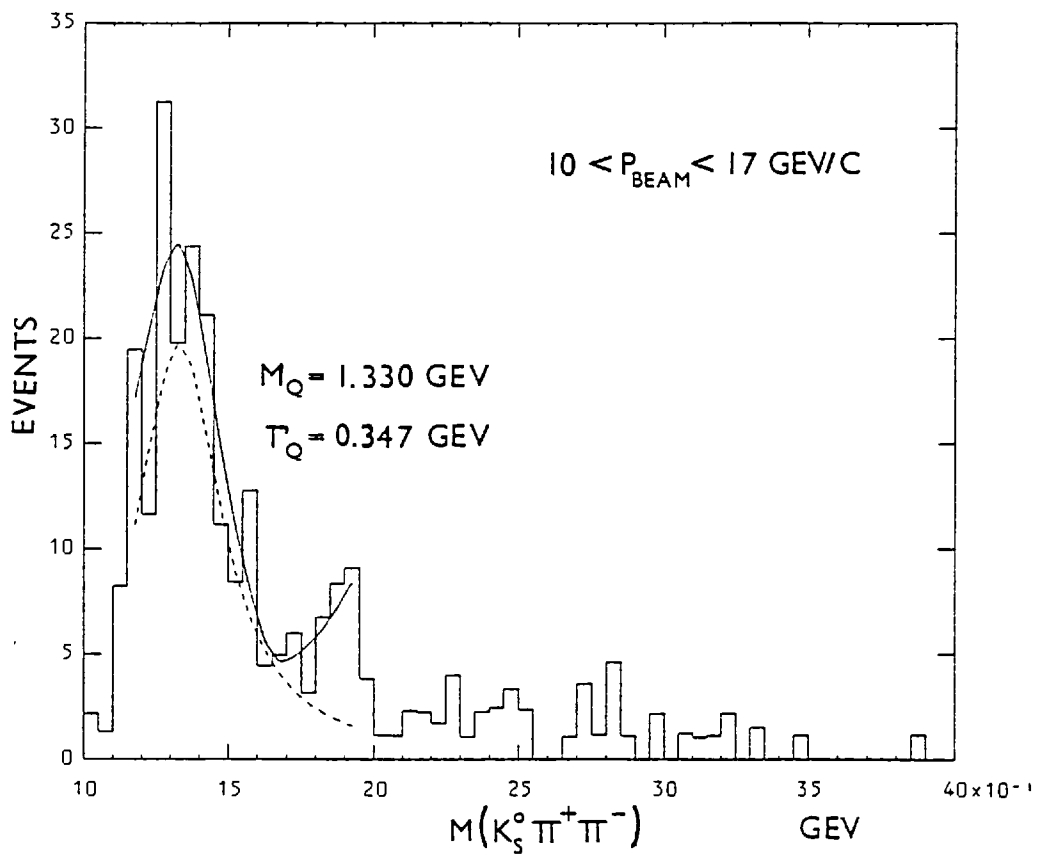
4.43



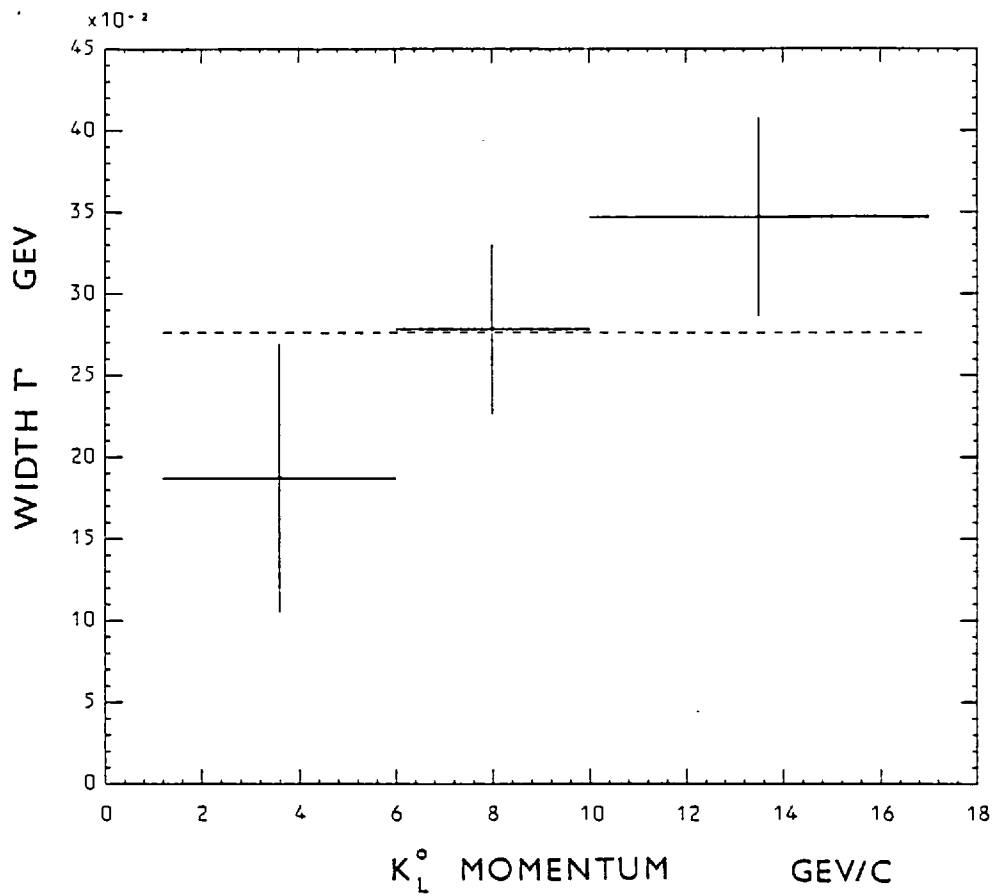
4.44a)



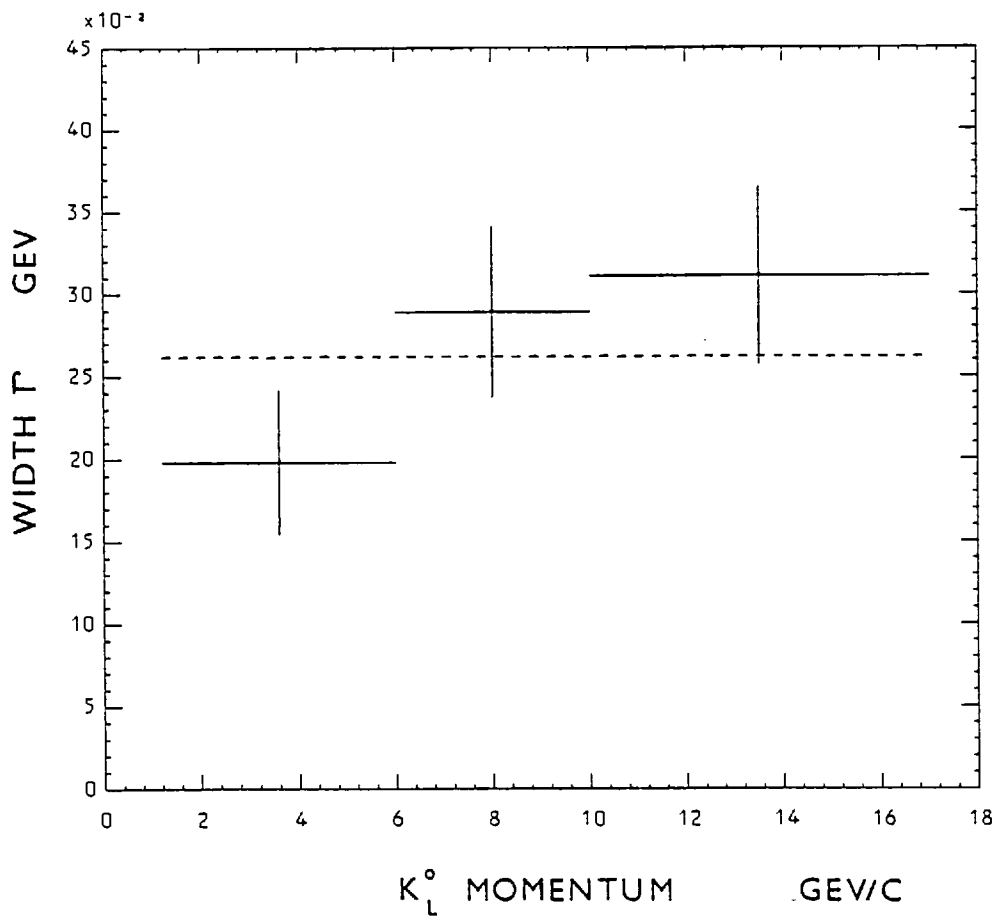
b)



c)

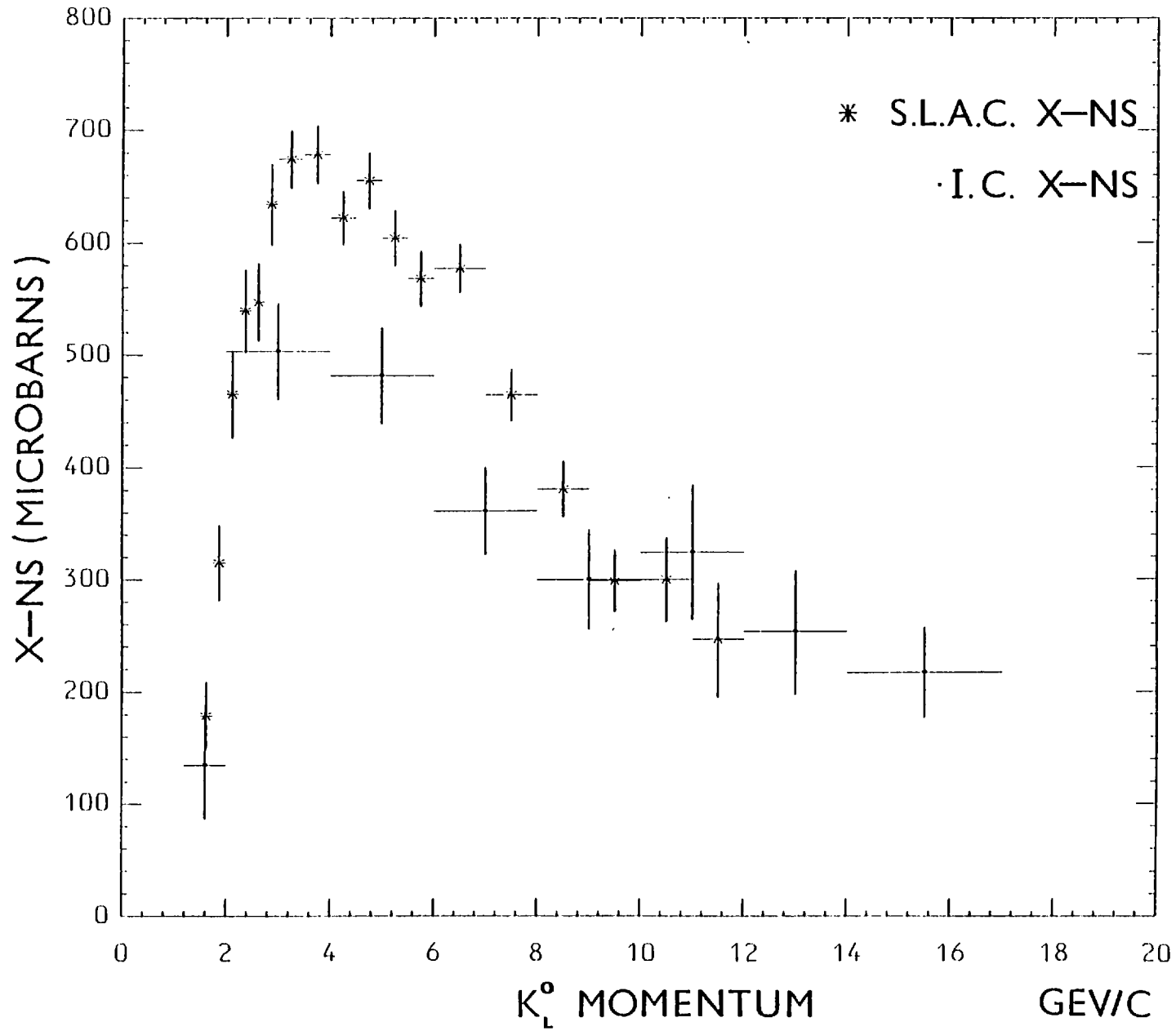


4.45a)

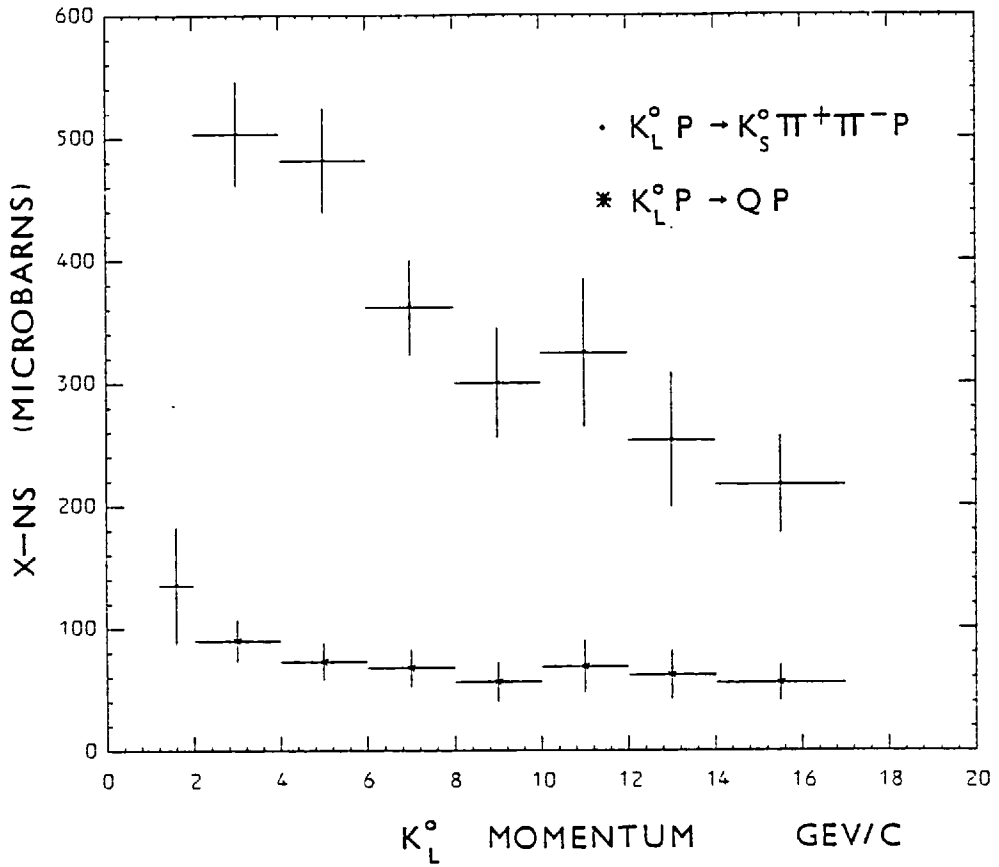


b)

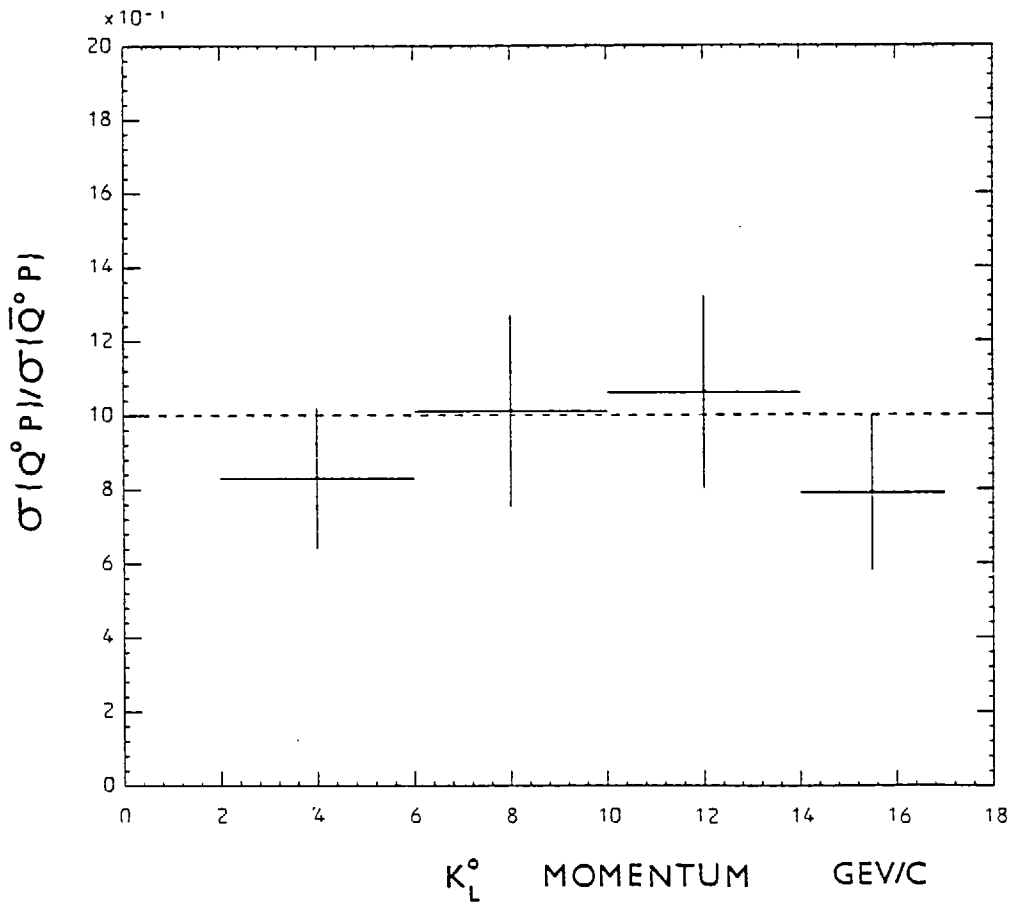
X-NS FOR $K_L^0 P \rightarrow K_S^0 \pi^+ \pi^- P$



4.46



4.47



4.48

Chapter 5

Momentum transfer studies

$$\text{in } K_L^0 p \rightarrow K_S^0 \pi^+ \pi^- p \quad (\text{Theory})$$

5.1 Introduction

Four-momentum transfer squared distributions are of considerable use in understanding many aspects of particle interactions, not only confined to diffractive processes and provide a valuable means with which to describe and explain the data. The four-momentum transfer squared 't' is a variable that is easily related to the kinematic data of each event and the subsequent experimental distribution provides an insight into the dynamics of the process, enabling a detailed model to be formulated describing the interaction in terms of the Lorentz invariant quantities 's' the centre of mass energy and 't', the four momentum transfer squared. The resulting model can in turn be used as a basis for theoretical predictions which can be experimentally tested.

In seeking a description of inelastic diffraction processes from such a model, one is guided by some common features of diffraction dissociation processes with those of elastic scattering of for example $\pi^{\pm} p$ and $K^{\pm} p$, such as similar behaviour of the differential cross-section with momentum transfer squared t ($d\sigma/dt$), both processes being steeply peripheral (ie. favouring low t) and being described by an exponential parameterization⁽²²⁾ for small t by

$$\frac{d\sigma}{dt} = \left. \frac{d\sigma}{dt} \right|_{t=0} e^{-bt} \quad (5.1)$$

with the slope 'b' in the range 7 - 12 (Gev^{-2}), depending on the particular value of s.

In addition elastic scattering and inelastic diffraction processes have cross-sections that show a weak dependence with c.m. energy s and slopes 'b' in equation (5.1) that exhibit 'shrinkage' that is an increase in 'b' with energy. An important common aspect of the t distributions for the two processes, which will form the focal point of this chapter, is the observation of a 'crossover' near $t = -0.2 \text{ GeV}^2$ in the particle and anti-particle differential cross-sections. The anti-particle process $(K, \bar{\pi}, \bar{p})$ as in $K\bar{p}$ elastic scattering having a steeper slope and higher intercept than the corresponding particle (K, π, p) process as in K^+p elastic scattering figure (5.1). Similar crossovers have been observed in the following inelastic diffractive processes,

$$K^\pm p \rightarrow Q^\pm p \quad (23)$$

$$\pi^\pm p \rightarrow A^\pm p \quad (24)$$

$$K_L^0 p \rightarrow Q p \quad (1)$$

which exhibit the same trend as their elastic counterparts, figures (5.2 - 5.4)

5.2

The Crossover Phenomenon

A simple explanation of the cross-over effect for elastic scattering can be made using a naive geometrical-optical model approach, which succeeds in describing the overall features. Assuming that the scattering is on a black totally absorbing disc of radius of interaction R , equation (5.1) can be rewritten⁽²⁵⁾ as

$$\frac{d\sigma}{dt} = \left. \frac{d\sigma}{dt} \right|_{t=0} e^{-R^2 t/4}$$

For complete absorption the forward amplitude is purely imaginary and the total cross-section $\sigma_T = 2\pi R^2$ (26). Using the optical theorem equation (5.2) can be rewritten as

$$\frac{d\sigma}{dt} = \frac{\sigma_T^2 e^{-\sigma_T/8\pi t}}{16\pi} \quad 5.3$$

The sign of the crossover follows from this expression since antiparticle induced processes as in K^-p elastic scattering have larger total cross-sections than the corresponding particle (K^+p) processes thus yielding higher slopes and intercepts. The model is only partially adequate since real amplitudes are also found experimentally to be non-zero and the total cross-section varies with energy, requiring R to change. (27)

The cross-over effect can also be understood quantitatively within the Regge-exchange framework, where Regge contributions odd under charge conjugation 'C' such as ρ, ω , contribute to the dominant Pomeron exchange amplitude, with opposite signs for the particle and anti-particle processes. Considering as an example π^+p and π^-p elastic scattering, the differential cross-sections can be expressed in terms of the t channel exchange amplitudes as (28)

$$\begin{aligned} \frac{d\sigma(\bar{X}p \rightarrow \bar{X}p)}{dt} &= \sum_{\lambda} |T_{\lambda} + V_{\lambda}|^2 \\ \frac{d\sigma(Xp \rightarrow Xp)}{dt} &= \sum_{\lambda} |T_{\lambda} - V_{\lambda}|^2 \end{aligned} \quad 5.4$$

λ = summation over helicities
in the t -channel.

T_{λ} represents the exchange amplitude for even C exchanges such as (Pomeron, A_2) and V_{λ} that for the odd C exchange (ω, ρ). The difference can be written after simplification as

$$D(X, \bar{X}, p) = 4 \operatorname{Re} \sum_{\lambda} T_{\lambda} V_{\lambda}^* \quad 5.5$$

Experimentally the dominant Pomeron Amplitude at small t is found to be mainly Imaginary and non-flip ⁽²⁹⁾ so that a good approximation to the above expression is given by

$$D(X, \bar{X}, p) = 4 \sum_{\text{non-flip}} \operatorname{Im} T \times \operatorname{Im} V \quad 5.6$$

The crossover corresponds to 'ImV' changing sign at the crossover point, 'ImT' remaining positive.

An extension to crossover predictions for inelastic diffractive processes can be made within the framework of the Reggeized Deck pion exchange model which has enjoyed some success in explaining certain features of the $(\pi\pi\pi)$ and $(K\pi\pi)$ mass spectrum in terms of a low mass kinematic enhancement, in $\pi p \rightarrow (\pi\pi\pi)p$ and $Kp \rightarrow (K\pi\pi)p$ diffractive processes. The crossover predictions that follow from the Deck model provide a further sensitive test of the internal dynamics of diffraction dissociation and give valuable clues to the nature of contributing exchanges. The existence of a crossover in

$$\begin{aligned} K_L^0 p \rightarrow Q^0 p &\rightarrow K_S^0 \pi^+ \pi^- p \\ \bar{K}_L^0 p \rightarrow \bar{Q}^0 p &\rightarrow K_S^0 \pi^+ \pi^- p \end{aligned} \quad 5.7$$

$K_L^0 p$ diffractive interactions, reactions (5.7) is of particular importance, not least because of the removal of relative normalization errors encountered in the equivalent charged kaon beam experiments, but also because the Deck effect is believed to contribute significantly in Q production.

5.3 The Reggeized Deck Model

The Reggeized Deck pion exchange model has been developed by Berger (30) in the study of 2 → 3 body inelastic processes and has usually been applied to diffractive processes represented by

$$ap \rightarrow (a^* \pi)p \rightarrow a\pi\pi p \quad 5.8$$

where 'a' represents the incident hadron, and the term in brackets (a* π) is the excited system decaying to aπ. As applied to the K_L^0 experiment the corresponding interaction for reaction (5.8) is

$$\begin{aligned} K^0 p &\rightarrow (K^{*+} \pi^-) p \rightarrow K^0 \pi^+ \pi^- p \\ \bar{K}^0 p &\rightarrow (K^{*-} \pi^+) p \rightarrow \bar{K}^0 \pi^+ \pi^- p \end{aligned} \quad 5.9$$

The Deck pion exchange graph is shown in figure (4.8), the beam particle dissociating at the upper vertex to an excited state a^* and a virtual pion, which then scatters elastically off the nucleon at the bottom vertex. Properties of this inelastic process are thus related to the known behaviour of the πp elastic scattering involved in the graph. In particular the crossover properties of the πN elastic scattering are reflected in the inelastic process.

To obtain some quantitative estimate for this effect, Berger has represented the 2 → 3 amplitude (31) in the form

$$A_\pi = g \frac{(s_{\pi a^*})^{\alpha_\pi}}{(m_\pi^2 - t_{aa^*})} e^{-i\pi\alpha_\pi/2} A_{\pi N}(s_{\pi N}, t_{pN}) \quad 5.10$$

where the 5 variables ($S, S_{\pi a}^*, S_{\pi N}, t_{pN}, t_{aa}^*$) needed for the full description of the $2 \rightarrow 3$ process are shown in figure (5.5). The propagator term $(m_{\pi}^2 - t_{aa}^*)^{-1}$ takes account of the emission of the virtual pion, 'g' the coupling constant at the $\pi a a^*$ vertex, and the terms $(S_{\pi a}^*)^{\alpha_{\pi}} e^{-i\pi\alpha_{\pi}/2}$ are the Regge energy and phase dependence of the pion exchange. The πN elastic scattering is accounted for by the term $A_{\pi N}(s_{\pi N}, t_{pN})$.

The resulting amplitude has been used by Berger as the basis for Monte-Carlo generation of events for $K_L^0 p \rightarrow K^* \pi p$ leading to numerical estimates for the slopes of the differential cross-sections⁽³²⁾ as a function of beam momentum as in figure (5.8). The slopes are obtained by fitting the differential cross-section for a fixed $M_{a\pi}^*$ to the form

$$\frac{d^2\sigma}{dt'dM_{a\pi}^*} = ce^{bt'_{pp}} \quad \begin{array}{l} |t'_{pp}| = |t_{pp} - t|_{\min} \\ \text{for } 0.02 < |t'_{pp}| < 0.5 \text{ Gev}^2 \end{array} \quad (5.11)$$

The two sets of curves display the variation of the slope b of equation (5.11) with momentum for $K_L^0 p \rightarrow K^* \pi p$, the $K^* \pi$ mass is restricted to be less than 1.5 Gev, in the 'Q' region for both (5.8a) and (5.8b) with the additional restriction that $M(p\pi^+)$ mass in figure (5.8b) is greater than 1.34 Gev. The Deck pion exchange graphs for $K^0 p \rightarrow K^{*+} \pi^- p$ and $\bar{K}^0 p \rightarrow K^{*-} \pi^+ p$ are shown in figure (5.6).

From an inspection of the two Deck graphs an immediate prediction is that the slopes $b(K^0 p \rightarrow K^{*+} \pi^- p)$ should be greater than $b(\bar{K}^0 p \rightarrow K^{*-} \pi^+ p)$, because of the known properties of $\pi^+ p$ and $\pi^- p$ elastic scattering, the $\pi^- p$ having a higher slope and intercept than $\pi^+ p$ ⁽³³⁾, with the crossover occurring at about $t_c = -0.2 \text{ Gev}^2$.

This observation is borne out by figure (5.8b) based on the theoretical calculation, where the slope for $K^0 p \rightarrow K^{*+} \pi^- p$ is greater than the slope for $\bar{K}^0 p \rightarrow K^{*-} \pi^+ p$ for all momenta. For figure (5.8a) no $M(p\pi^+) > 1.34$ Gev cut has been made corresponding to Δ^{++} exclusion and below beam momentum of 6 Gev/c, the slope for $\bar{K}^0 p \rightarrow K^{*-} \pi^+ p$ is greater than that of $K^0 p \rightarrow K^{*+} \pi^- p$ reversing the sign of the crossover.

The values of the slopes predicted are in reasonable agreement with data from $K^\pm p \rightarrow (K\pi\pi)^\pm p$ reactions and the corresponding Deck pion exchange graphs for $K^\pm p \rightarrow (K\pi\pi)^\pm p$ and $\pi^\pm p \rightarrow (\pi\pi\pi)^\pm p$ give the correct sign of the crossover, however data from the previous K_L^0 experiment at S.L.A.C. (34) is in serious disagreement with the pion exchange prediction, the slopes for $\bar{K}^0 p \rightarrow K^{*-} \pi^+ p$ being steeper and having a higher intercept than those for $K^0 p \rightarrow K^{*+} \pi^- p$, with the crossover occurring at $t_c' = -0.13$, figure (5.3). Berger suggested that the Δ^{++} (1236) reflection was responsible but it appears that events containing Δ candidates were removed from the sample. The trend of the S.L.A.C. data agrees with that found from elastic scattering and with the general systematics that the slope of the anti particle (K^-, \bar{K}^0, π^-) induced process is greater than that in the equivalent particle process (K^+, K^0, π^+).

5.4 The K^* Exchange Graph

In an attempt to further develop the Deck model and to explain the S.L.A.C. crossover data, Berger has considered the possibility of K^* exchange being present in addition to pion exchange in $K_L^0 p \rightarrow K^* \pi p$. The slope characteristics of $K^* p$ elastic scattering would presumably be similar to those of $K^\pm p$ elastic scattering with $b(K^{*-} p) > b(K^{*+} p)$, thus reversing the pion exchange Deck predictions, figure (5.7), the net crossover seen in the $K_L^0 p$ data presumably occurring because the difference in the K^* slopes is more pronounced than that between the corresponding pion exchange slopes, to give $b(\bar{K}^0 p \rightarrow K^{*-} \pi^+ p) > b(K^0 p \rightarrow K^{*+} \pi^- p)$. This hypothesis would not conflict with the observed crossovers in $K^\pm p \rightarrow (K\pi\pi)^\pm p$, and would reinforce the pion exchange predictions, although in ref.(35) some doubt is shed on this idea on the grounds that it would give too large a difference in slopes.

An attempt to reparametrize the Deck model in terms of K^* exchange meets with some difficulty due to lack of knowledge of off-shell K^* -nucleon scattering, so a less ambitious scheme has been adopted by Berger to try to isolate and provide evidence for this alternative exchange. As a result of this investigation Berger has claimed to have found a convenient way to separate the regions of phase space corresponding to different particle exchanges. The five basic kinematic variables used in the description of the $2 \rightarrow 3$ process are partially replaced by a newer set $(S, M_{a^* \pi}^2, t_{pN}, \theta_s, \phi_s)$ where θ_s and ϕ_s are the S-channel helicity angles of the decay of the a^* in the a^* rest frame. Applying this to the diffractive process $K_L^0 p \rightarrow K^* \pi p_{out}$, the angles ϕ_s and θ_s can be expressed (31) as in figure (5.9)

$$\cos\phi_s = \frac{(\vec{p}_{out} \times \vec{K}^*) \cdot (\vec{p}_{out} \times \vec{K}_L^0 in)}{|\vec{p}_{out} \times \vec{K}^*| \cdot |\vec{p}_{out} \times \vec{K}_L^0 in|} \quad 5.12$$

$$\cos\theta_s = \frac{\vec{K}^* \cdot \vec{p}_{out}}{|\vec{K}^*| \cdot |\vec{p}_{out}|} \quad \text{in the } K^*\pi \text{ rest frame}$$

With reference to figure (5.9), the two sets of variables $(t_{aa^*}, S_{\pi N})$ and $(t_{a\pi}, S_{a^*N})$ can be re-expressed⁽³¹⁾ in terms of the five basic variables of the new set. The variables appearing in the first set control the dynamics of pion exchange via equation (5.10), where t_{aa^*} appears in the propagator term $(m_\pi^2 - t_{aa^*})^{-1}$ and $S_{\pi N}$ is the Regge energy dependence of the term $A_{\pi N}(S_{\pi N}, t_{pN})$, and by analogy the second set would be expected to do the same for K^* exchange, where

$$S_{\pi N} = m_N^2 + m_\pi^2 + 2E_N E_\pi + 2|q_N| |q_\pi| \cos\theta_s \quad 5.13$$

$$S_{a^*N} = m_N^2 + m_{a^*}^2 + 2E_N E_{a^*} - 2|q_N| |q_{a^*}| \cos\theta_s$$

$$t_{aa^*} = m_a^2 + m_{a^*}^2 - 2E_a E_{a^*} + 2|q_a| |q_{a^*}| \{ \cos\theta_s \cos\chi + \sin\theta_s \sin\chi \cos\phi_s \} \quad 5.14$$

$$t_{a\pi} = m_a^2 + m_\pi^2 - 2E_a E_\pi - 2|q_a| |q_\pi| \{ \cos\theta_s \cos\chi + \sin\theta_s \sin\chi \cos\phi_s \}$$

in a more simplified form, these equations can be rewritten⁽³⁶⁾ as

$$S_{\pi N} = A_1 + B_1 \cos\theta_s \quad 5.15$$

$$S_{a^*N} = A_2 - B_1 \cos\theta_s$$

$$t_{aa^*} = a_1 + b_1 \cos\theta_s + c_1 \sin\theta_s \cos\phi_s \quad 5.16$$

$$t_{a\pi} = a_2 - b_1 \cos\theta_s - c_1 \sin\theta_s \cos\phi_s$$

The functions $A_1, A_2, B_1, a_1, a_2, b_1$ and c_1 depend only upon the three other variables in the basic set $S, M_{a^*\pi}^2$ and t_{pN} . Since the angular dependence of phase space is given by the term $'d(\cos\theta)d\phi'$, any structure in the ϕ_s angular distribution would provide some insight of the diffractive amplitude. The only dependence on ϕ_s is through equations (5.16) for t_{aa^*} and $(t_{a\pi})$ which appear in the propagator term for the virtual pion (K^*) exchanged. By varying ϕ_s from $\phi_s = 0$ where $-t_{aa^*}$ is smallest and the amplitude for pion exchange is large, to $\phi_s = \pi$ where $(-t_{a\pi})$ is smallest and a^* exchange would be expected to occur, the relative proportion of the two Deck graphs for π and a^* exchange can be changed. The distribution of ϕ_s obtained by Berger from Monte-Carlo simulations using the Deck-pion exchange amplitude, ⁽³¹⁾ shows just this peaking at $\phi_s = 0$. The experimental ϕ_s distribution would therefore show forward or backward peaking or some other structure depending upon the relative amount of π or a^* exchange present.

The important conclusion from this work, is that different parts of the ϕ_s angular distribution are characteristic of different exchanges and by selecting on different regions of ϕ_s the relative amount of a given exchange can be enhanced. Applying these ideas to the $K_L^0 p$ crossover problem, a more stringent test for the Deck model would be to select events with $\phi_s < \pi/2$ where π exchange predominates and with $\phi_s > \pi/2$ for K^* exchange. For the pion exchange region the slope prediction is $b(K^0 p \rightarrow K^{*+} \pi^- p) > b(\bar{K}^0 p \rightarrow K^{*-} \pi^+ p)$ and for the K^* region ---

$$b(\bar{K}^0 p \rightarrow K^{*-} \pi^+ p) > b(K^0 p \rightarrow K^{*+} \pi^- p).$$

Some confirmation for these ideas has come from an analysis of $\pi^\pm p \rightarrow \pi^\pm (\pi^- \Delta^{++})$ at 16 GeV/c. ⁽³⁷⁾ The relevant Deck graphs are illustrated in figure (5.10), where instead of beam dissociation, target dissociation here involves pion or baryon exchanges scattering off the projectile. If the assumption is made that $\pi^\pm \pi^-$ and $\pi^\pm \Delta^{++}$ elastic scattering show the same

cross-over systematics of $\pi^\pm p, K^\pm p$ and $p^\pm p$ scattering, then the crossover predictions follow from the two Deck graphs. For the total data no overall crossover is observed, however if selections on the s-channel helicity angle of the Δ^{++} in the $(\pi^- \Delta^{++})$ rest frame are made corresponding to mainly π exchange ($\phi_s < \pi/2$) then the slope for $\pi^+ p \rightarrow \pi^+(\pi^- \Delta^{++})$ is seen to be greater than that of $\pi^- p \rightarrow \pi^-(\pi^- \Delta^{++})$ as a reflection of $\pi^\pm \pi^-$ elastic scattering, with a crossover occurring at $t_c = -0.34 \text{ Gev}^2$. Similarly for ($\phi_s > \pi/2$) where baryon exchange of Δ^{++} predominates, the sign of the crossover is reversed with the slope of $\pi^- p \rightarrow \pi^-(\pi^- \Delta^{++})$ greater than $\pi^+ p \rightarrow \pi^+(\pi^- \Delta^{++})$, and the crossover point at $t_c = -0.15 \text{ Gev}^2$. The experimental ϕ_s distribution for both $\pi^+ p$ and $\pi^- p$ processes show a significant pion exchange peaking at $\phi_s = 0$, and the region for $\phi_s > \pi/2$ is suggestive of a non-negligible amount of Δ^{++} exchange.

5.5 Different Secondary Exchanges in the Q crossover

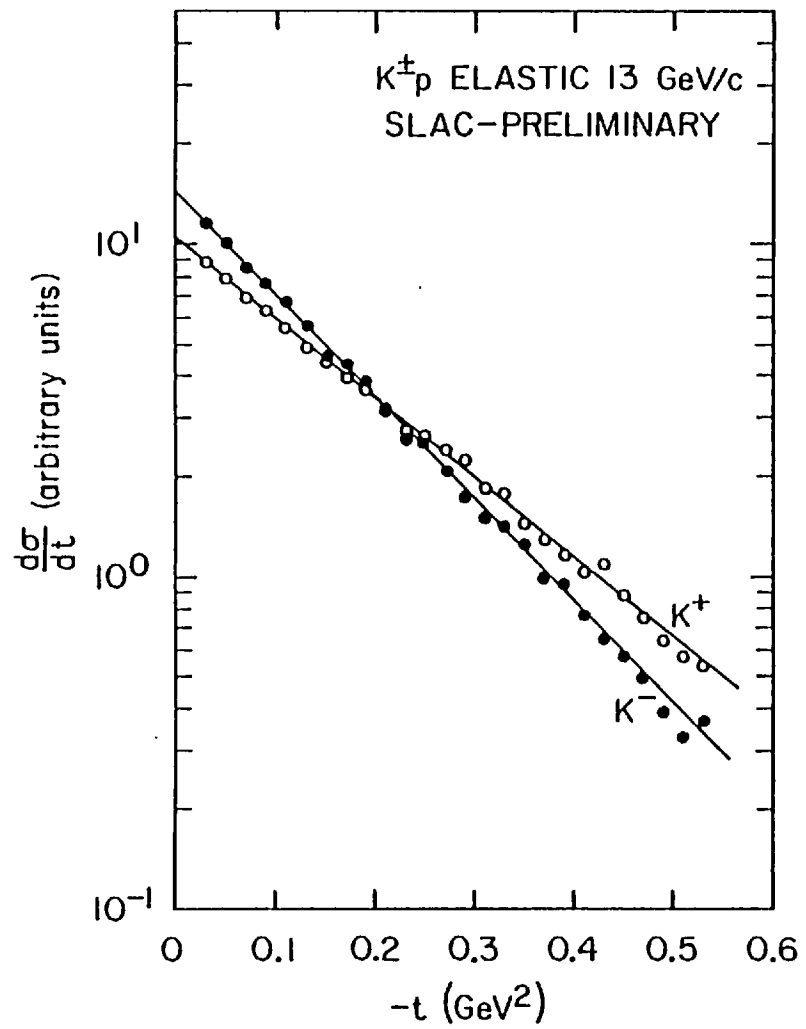
An alternative explanation of the Q crossover problem within the Deck framework, has been provided by Cohen-Tannoudji et al⁽³⁸⁾. Instead of adding K^* exchange graphs to the usual π exchange Deck graph, secondary contributions from B and ω are considered, figures (5.11). The duality diagrams for $K^0 p \rightarrow Q^0 p \rightarrow K^+ \pi^- p$ and $\bar{K}^0 p \rightarrow \bar{Q}^0 p \rightarrow K^{*-} \pi^+ p$ are shown in figure (5.12) and a study of the quark content exchanged, shows that the I=1 B(1235) meson (exchange degenerate with the pion) and I=0 ω meson can be present. G parity conservation permits the B and ω mesons to couple at the pion vertex. The amplitudes for the two processes can be expressed schematically in the form,

$$1) \quad A(\bar{K}^0_p \rightarrow K^{*-} \pi^+_p) = \pi P + B\omega \quad 5.17$$

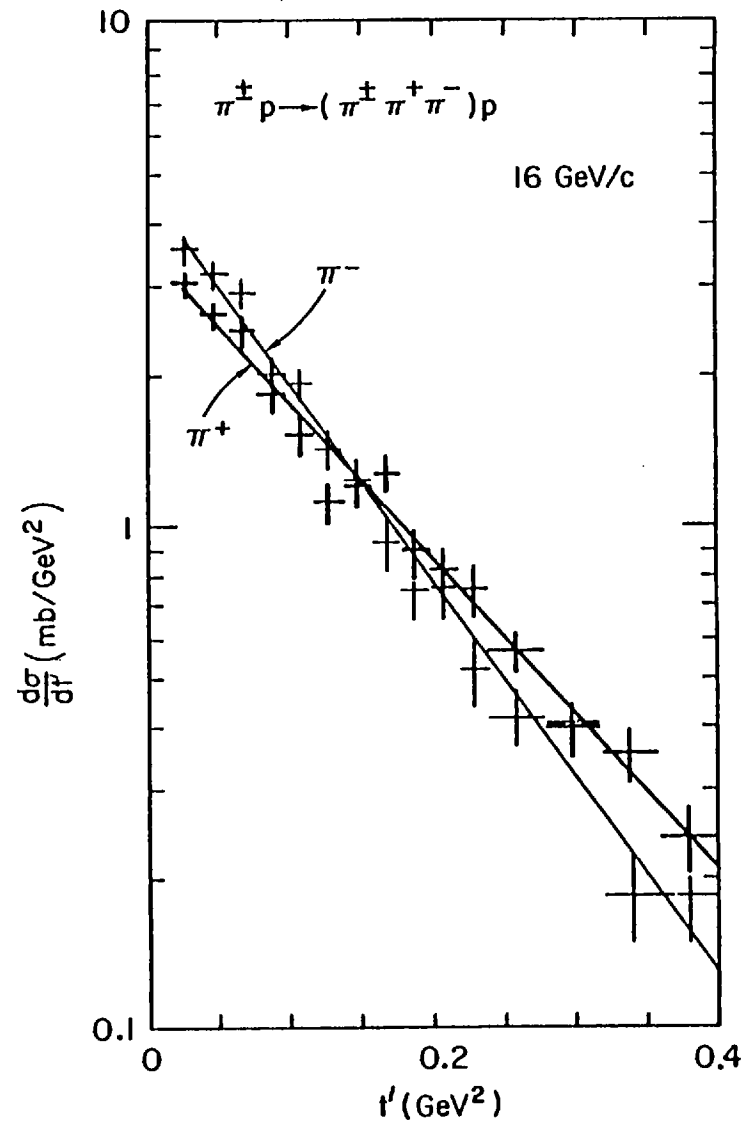
$$2) \quad A(K^0_p \rightarrow K^{*+} \pi^-_p) = \pi P - B\omega$$

P = Pomeron.

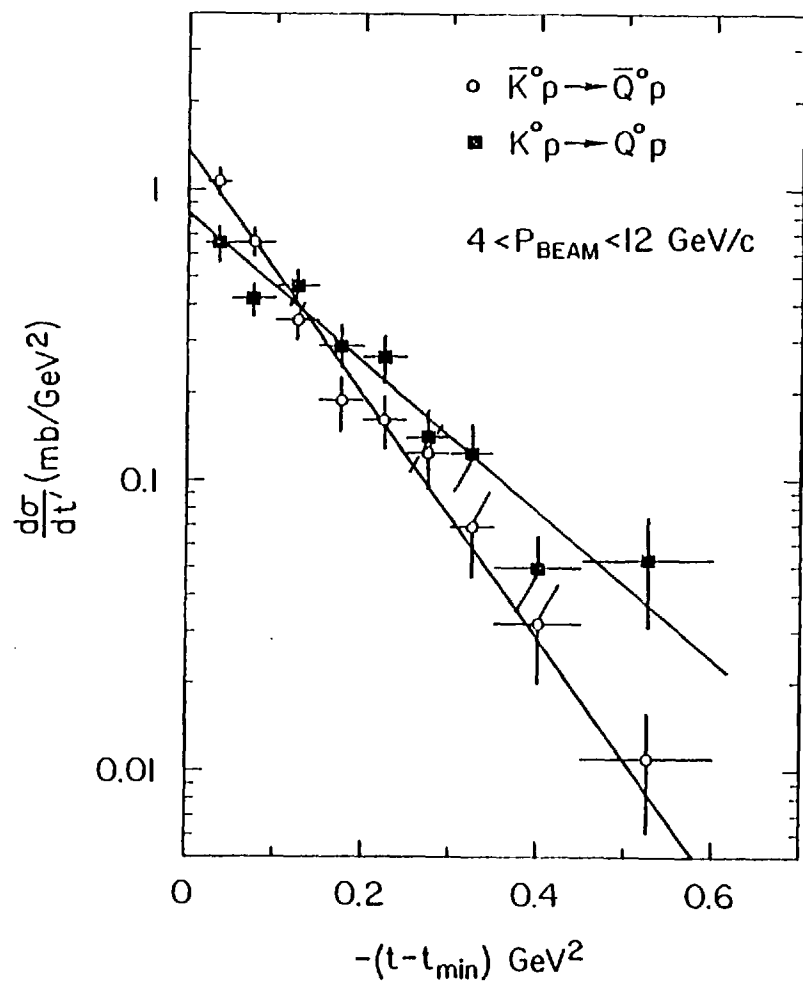
The sign of the $B\omega$ contribution is not affected by the charge of the 'Q', so the same arguments apply to charged $Q^+ - \bar{Q}$ as well as neutral $Q^0 - \bar{Q}^0$. After expressing 1) and 2) of equation (5.17) in terms of detailed Regge amplitudes and phases, the model is able to reproduce the experimentally observed sign of the crossover for Q^+/Q^- (in $14\text{Gev}/c \text{ } K^\pm p \rightarrow Q^\pm p$), with the crossover point occurring at $t \approx -0.2 \text{ Gev}^2$ and Q^- having a higher intercept and steeper slope than Q^+ . Moreover the simulated $(K\pi\pi)$ mass spectrum and variation of slopes with $(K\pi\pi)$ mass is in fair agreement with data from this experiment. A particularly relevant feature of the model is that the crossover should be the same over the complete $\cos\phi_s$ region, even for $\cos\phi_s > 0$ where according to Berger pion exchange is enhanced. The authors claim their model is also able to explain crossover effects of other diffractive processes $(KN, \pi N)$, the s -channel quantum numbers being 'dual' to the exchanges interfering with the Pomeron in the t -channel.



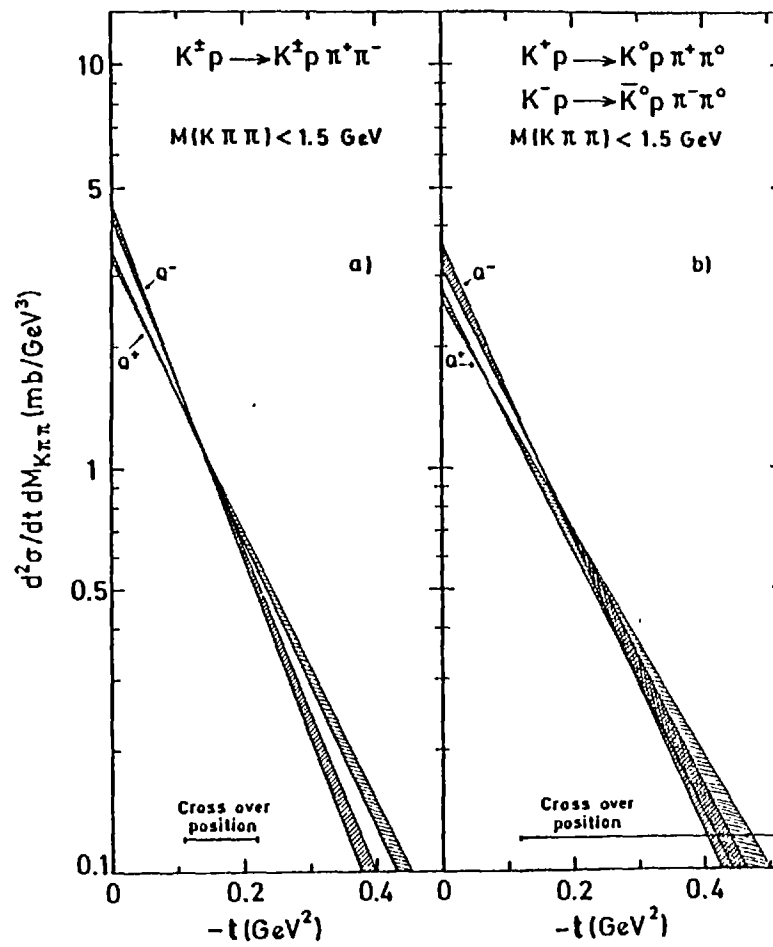
5.1



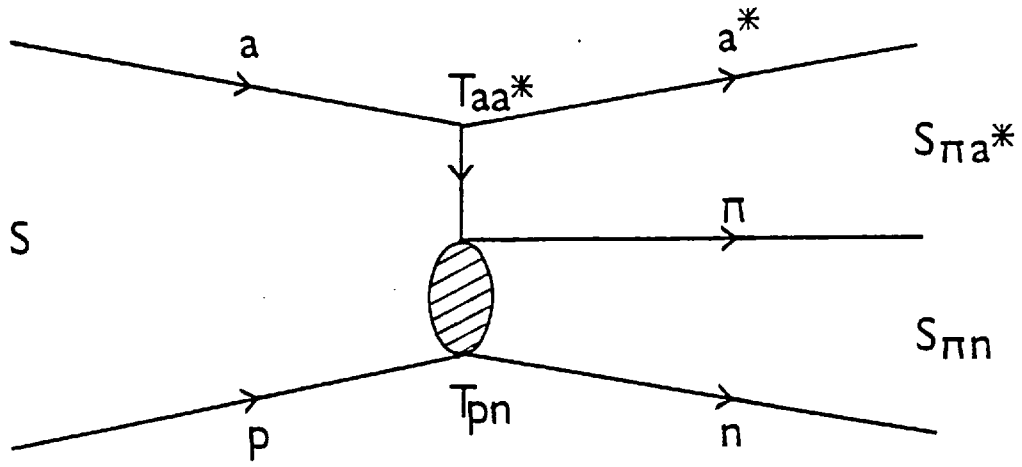
5.2



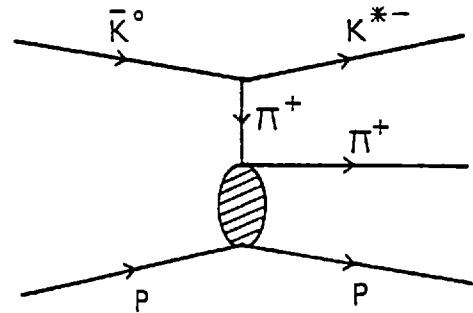
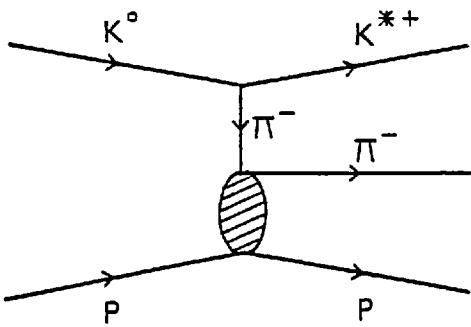
5.3



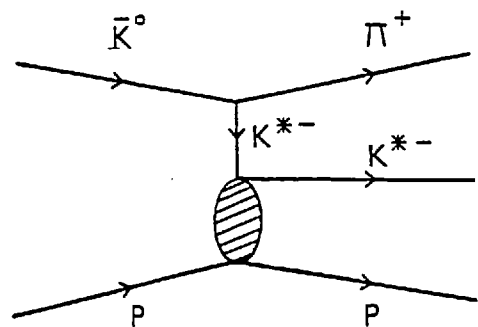
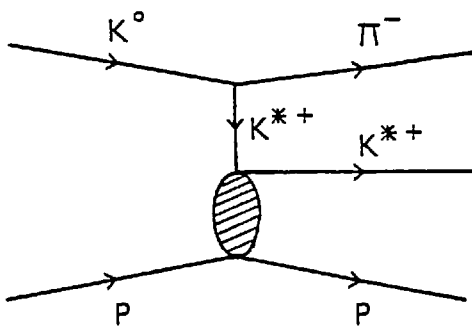
5.4



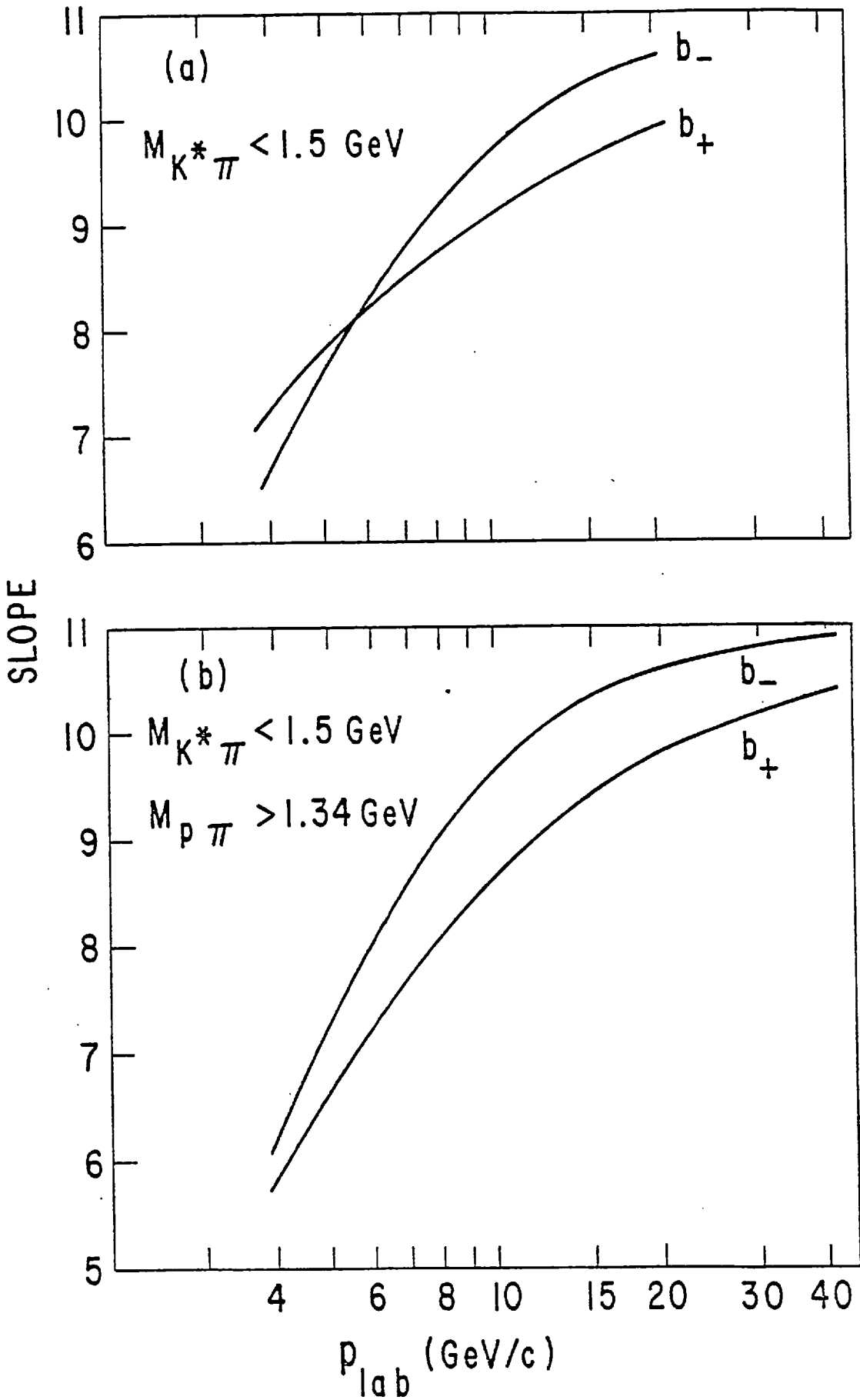
5.5



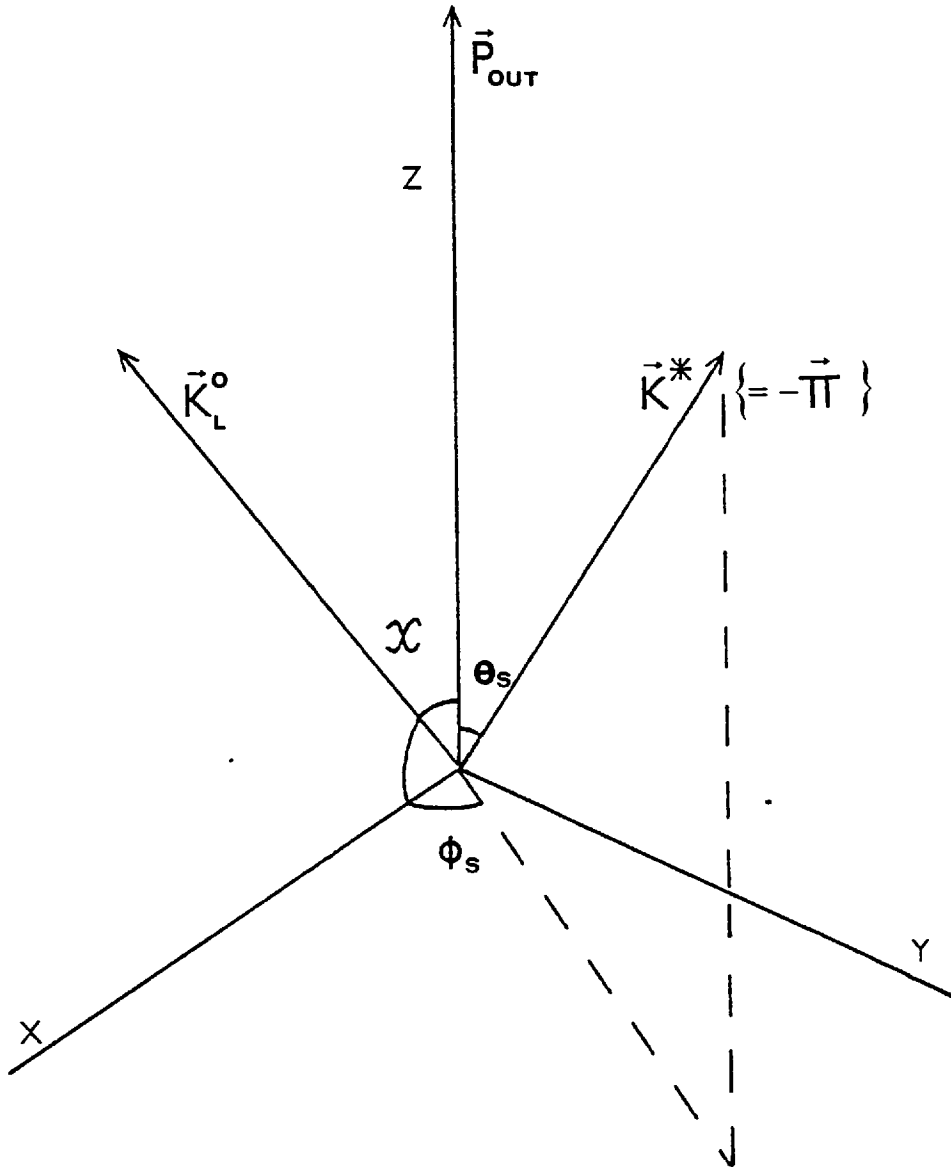
5.6



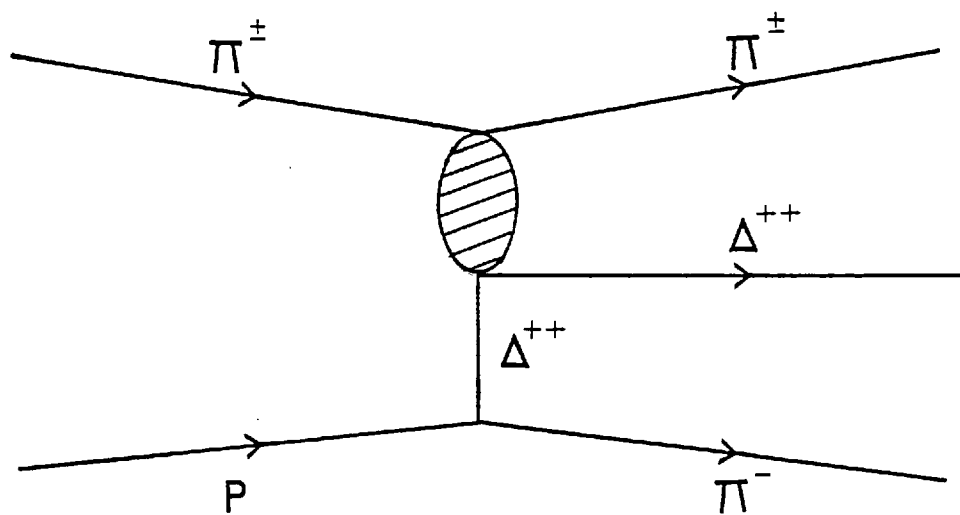
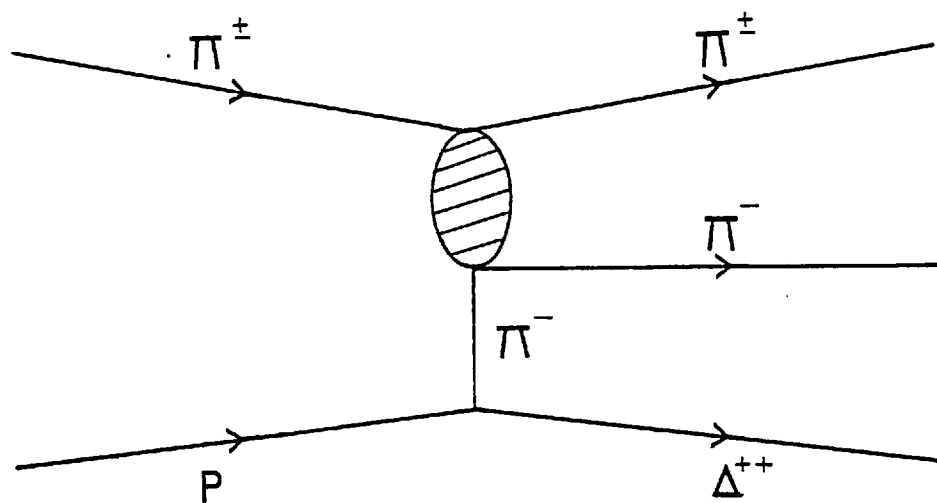
5.7



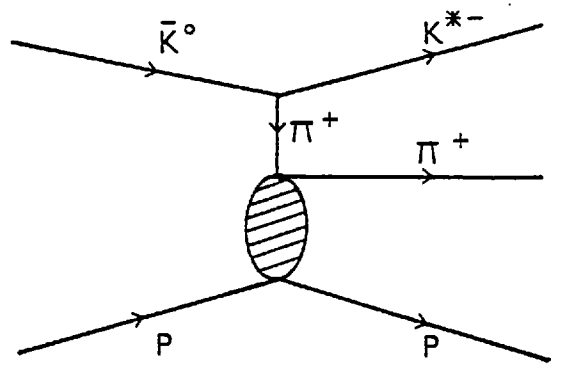
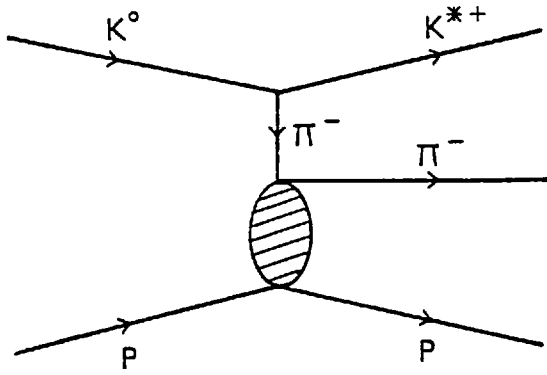
S-CHANNEL AXES



$$K_L^o P \rightarrow K^* \Pi P_{OUT}$$

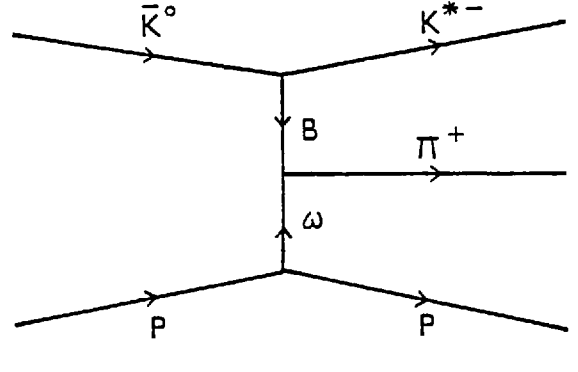
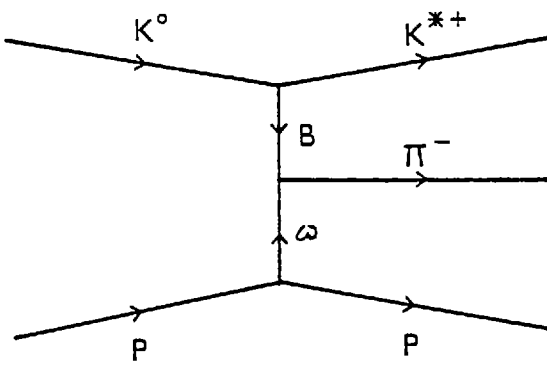


5.10

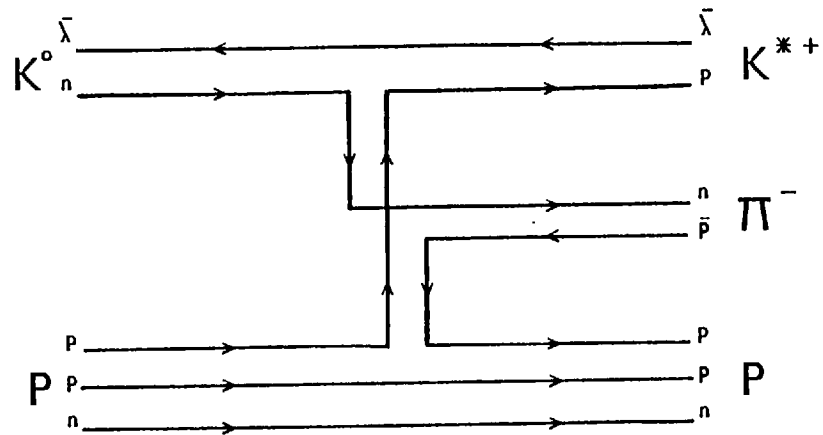
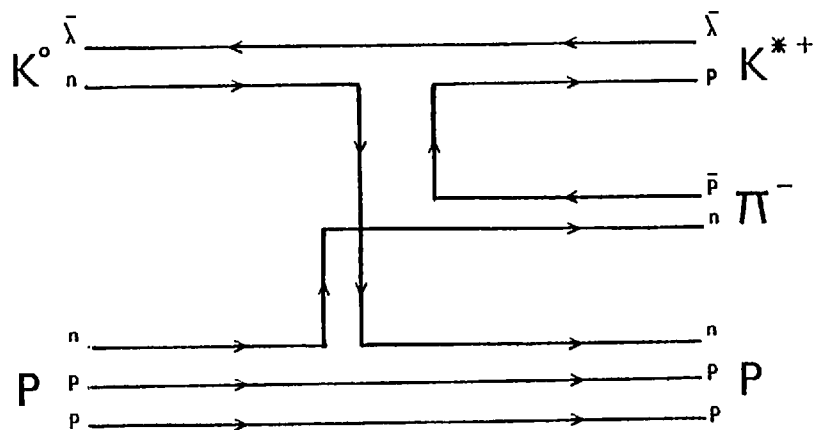
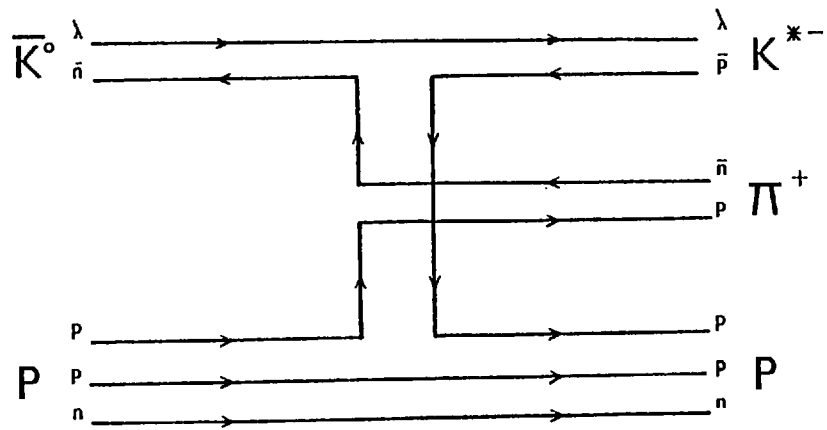
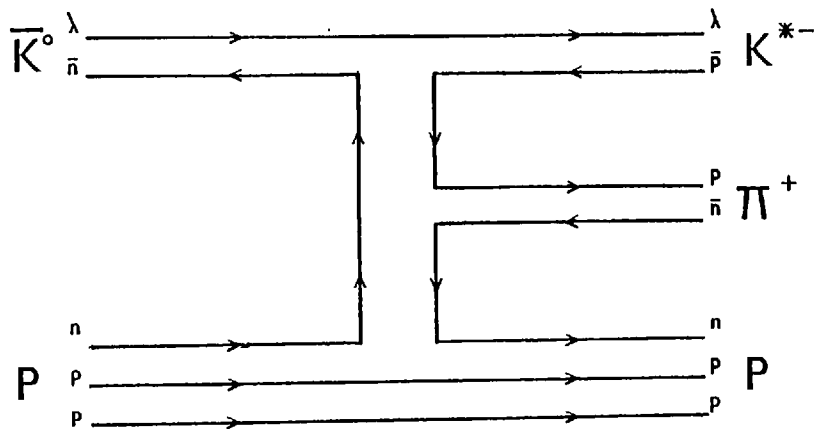


+

+



5.11



5.12

Chapter 6

Momentum transfer studies

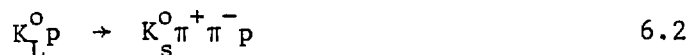
$$\text{in } K_L^0 p \rightarrow K_S^0 \pi^- \pi^+ p (\text{Experiment})$$

6.1 Introduction

Exponential fits to the four-momentum transfer squared distributions are presented in this chapter for the reactions



for various different cuts. Data is taken from three and six constraint fits to the channel



which survive the fiducial volume and projected length cuts outlined in Chapter 1. The four-momentum transfer squared distributions of reaction (6.2) for both laboratories, figures (4.1) show a loss in the first bin, for $|t_{pp}| < 0.04 \text{ Gev}^2$, corresponding to events with short recoil protons that are missed at the scanning stage. Therefore in fitting the t'_{pp} distributions of reactions (6.1) to exponentials, the interval of t'_{pp} selected is $0.02 < |t_{pp} - t_{\min}| < 0.5 \text{ Gev}^2$, where t_{\min} is the minimum kinematic t_{pp} value for the particular $(K_S^0 \pi^+ \pi^-)$ effective mass in question. The Q region of (6.1) is defined by the following sets of cuts on data of reaction (6.2).

- 1) $1.1 < M(K_S^0 \pi^+ \pi^-) < 1.5 \text{ Gev}$
- 2) $M(p\pi^+) > 1.34 \text{ Gev}$ 6.3
- 3) $0.02 < |\tau_{pp}^-| < 0.5 \text{ Gev}^2$

Separation into Q^0 and \bar{Q}^0 states is achieved by restricting the $K^{*+} \pi^-$ and $K^{*-} \pi^+$ masses of (6.1) within the Q region, where the K^* selection is $0.86 < M(K_S^0 \pi) < 0.92 \text{ Gev}$. Figure (6.1) shows the $K_S^0 \pi^+$ and $K_S^0 \pi^-$ mass distributions subject to the cuts in (6.3) and figure (6.2) shows the corresponding distributions when events with $K_S^0 \pi$ masses within both K^{*+} and K^{*-} mass intervals have been removed. The number of weighted events after the cuts in (6.3) have been applied to reactions (6.2) is given in the first column of table (6.1). Because of the low statistics it was decided not to immediately omit events with $(K_S^0 \pi)$ masses within both K^{*+} and K^{*-} mass intervals. Instead the fits to the τ' distributions containing these events have been compared to the corresponding quantities with these events removed, to ascertain if there was any significant shift in the slope parameters. No such change was observed for any τ' distribution, and apart from the lower numbers and higher statistical errors resulting from the removal of these 'ambiguous' events, the conclusions remain the same. This source of ambiguity has been reduced as far as possible by the choice of a narrow K^* cut. The second column of table (6.1) gives the number remaining when these ambiguous events have been removed. The cuts imposed on the data to isolate the 'Q' diffractive signal coincide with the cuts used in the S.L.A.C. K_L^0 data and by Berger in his model, thus enabling trends and comparisons easier to make.

6.2 Determination of the Slopes

The t' distributions for various cuts were fitted to exponential distributions of the form

$$\frac{dN}{dt}_{pp} = A e^{-bt'}_{pp} \quad \text{for } 0.02 < |t'_{pp}| < 0.5 \quad 6.4$$

To determine the slopes 'b' and intercepts 'A' of equation (6.4) from the data a maximum likelihood estimator was used in preference to a chi-squared minimization method, motivated in part by the need to extract as much information as possible from the low statistics data and also to avoid any difficulties over 'binning' events as in the chi-squared method. In the limit of high statistics both methods can be shown to be equivalent but for poor statistics a maximum likelihood method is more efficient⁽³⁹⁾. In order to use the maximum likelihood method the exponential distribution, equation(6.4), is normalized to unity within the t' interval, having the form

$$P(b) = \frac{b e^{-b(t'_2 - t'_1)}}{(1 - e^{-b(t'_2 - t'_1)})} \quad 6.5$$

where t'_1 and t'_2 are the lower and upper limits of the range of t' over which the fit is made. The fitted slope value b is taken as that value which maximizes

$$L = \prod_{i=1, n} P^i(b) \quad \begin{array}{l} i = i^{\text{th}} \text{ event} \\ n = \text{number of events} \end{array} \quad 6.6$$

or equivalently minimizes

$$- \log L = - \sum_{i=1, n} w_i \log P^i(b) \quad \begin{array}{l} w_i \text{ is the weight} \\ \text{for the } i^{\text{th}} \text{ event} \end{array} \quad 6.7$$

The error on the slope ' δb ' is defined to be that which increases the negative log-likelihood function (6.7) by 0.5 from that at minimum.

$$\delta b = \left(-\frac{d^2}{db^2} \log L \right)^{-\frac{1}{2}} \quad 6.8$$

Using the slope value from the fit, the intercept at $t'=t_1$ denoted by 'I' can be found by normalising the area under the exponential curve to the total number of events in the fit 'N' where

$$\int_{t_1}^{t_2} A e^{-bt'} dt' = N \quad 6.9$$

so that
$$I = \frac{Nb}{(1 - e^{-b(t_2 - t_1)})}$$

The error on the intercept ' δI ' is calculated from the error on the slopes ' δb ' and the statistical error of the weighted numbers of events in the fit. Using the principle of superposition of errors (40), the most probable error on the intercept is given by

$$\delta I^2 = \left(\frac{\partial I}{\partial b} \right)^2 \delta b^2 + \left(\frac{\partial I}{\partial N} \right)^2 \delta N^2 \quad 6.10$$

where
$$\delta N^2 = \sum_i w_i^2$$

in terms of N and b, the error on the intercept δI can be expressed as,

$$\delta I^2 = \left(\frac{N}{(1 - e^{-b(t_2 - t_1)})} - \frac{b(t_2 - t_1) N e^{-b(t_2 - t_1)}}{(1 - e^{-b(t_2 - t_1)})^2} \right)^2 \delta b^2 + \frac{b^2 \delta N^2}{(1 - e^{-b(t_2 - t_1)})^2} \quad 6.11$$

6.3 Slopes of the t' distribution for Q^0 and \bar{Q}^0

The t' distributions for the combined data sample which satisfied the diffractive 'Q' cuts outlined previously, were fitted to a single exponential using the method of maximum likelihood described in section (6.2). The data with error bars and the fitted curve are shown in figure (6.3). From figure (6.3) it is apparent that the slope and intercept of the antiparticle induced process $\bar{K}^0 p \rightarrow K^{*+} \pi^- p$ are larger than the corresponding particle process $K^0 p \rightarrow K^{*+} \pi^- p$ with a crossover in the differential cross-sections at $-t' = 0.14 \pm 0.07 \text{ Gev}^2$. The slope values are $b = 5.56 \pm 0.71$ and $b = 8.93 \pm 0.88 \text{ Gev}^{-2}$ for $Q^0 p$ and $\bar{Q}^0 p$ respectively. This result is in agreement with the general systematics obtained from elastic reactions, with antiparticle induced processes having steeper slopes and larger intercepts (at $t'=0$) than the corresponding particle processes. The sign of the crossover also confirms the lower momentum K_L^0 S.L.A.C. result,⁽³⁴⁾ where slope values $b = 5.9 \pm 0.5$ and $b = 9.7 \pm 0.7 \text{ Gev}^{-2}$ for $Q^0 p$ and $\bar{Q}^0 p$ were obtained, figure (5.3), and is in disagreement with the pion-exchange Deck model. The slope parameters and intercepts are given in table (6.2) together with those found using subsequent cuts described in this section.

The slope parameters were found to be insensitive to any additional cuts on the data. Specifically one could argue as the authors of 8.25 Gev/c $K^\pm p \rightarrow Q^\pm p$ do⁽⁴¹⁾ that in eliminating events where Δ^{++} production is evident, the comparison between particle and antiparticle distributions is being biased, that is to say the $M(p\pi^+) > 1.34 \text{ Gev}$ cut to remove Δ^{++} background does not affect K^0 and \bar{K}^0 induced processes equally and removes genuine 'Q' events.

In order to 'symmetrize' this bias between particle and antiparticle, a cut on $M(p\pi^-) > 1.34$ Gev was also made on the data and will be referred to as a Δ^0 cut. The slope values and crossover position as a result of this extra Δ^0 cut were unaltered within errors from their previous values and the corresponding slopes were $b = 5.70 \pm 0.76$ and $b = 8.57 \pm 0.94$ Gev⁻² for Q^0_p and \bar{Q}^0_p . Moreover for both these two different sets of cuts removal of events with $K^0_S \pi$ masses in both K^{*+} and K^{*-} intervals made no significant difference to the slope values. Figure (6.4) shows the crossover in the t' distributions obtained when this class of events have been removed. A similar sign in the crossover is seen in the data if the Δ^{++} background is not removed, figure (6.5), although the slopes are approaching common values and the crossover position has moved out to $-t' = 0.23$ Gev².

6.4 Strength of the Regge Contribution in the Q region

Diffraction dissociation like elastic scattering is believed to be dominated by a 'Pomeron' term with some Regge exchanges whose contribution diminishes with energy. This Regge contribution to diffraction dissociation processes can be isolated using a technique first applied to elastic scattering of $K^{\pm}p$ by Davier and Harari⁽⁴²⁾. In the same spirit as equation (5.6) for elastic scattering, the extension to diffraction dissociation of $K_L^0 p \rightarrow Qp$ can be written as

$$\frac{d\sigma}{dt'}(\bar{Q}^0 p) - \frac{d\sigma}{dt'}(Q^0 p) = 4 \sum_{\lambda\mu} (\text{Im}A_P^{\lambda\mu}) (\text{Im}A_V^{\lambda\mu}) \quad 6.12$$

- A_P = Pomeron exchange amplitude
- A_V = Regge exchange amplitude
- $\lambda(\mu)$ = helicity change at baryon(meson)vertex

Where the dominant Pomeron term is assumed to be purely imaginary and quadratic terms in the Regge amplitudes are ignored. As in elastic scattering the difference in the differential cross-sections is given by the Regge interference term, whose imaginary part changes sign at the crossover point. For the total momentum interval of this experiment $\sigma(Q^0 p) = \sigma(\bar{Q}^0 p)$, so that the interference term between the Pomeron and odd C Regge exchanges in equation (6.12) cancels over the total t' range. In the forward direction $t' = 0$ the helicity flip amplitudes are zero and duality considerations give a good approximation to the exotic channel $K^0 p \rightarrow Q^0 p$ as $|\text{Im}A_P|^2$.

Equation (6.12) can then be simplified to

$$\left. \frac{\frac{d\sigma}{dt'}(\bar{Q}^0 p) - \frac{d\sigma}{dt'}(Q^0 p)}{4 \frac{d\sigma}{dt'}(Q^0 p)} \right\}_{t'=0} = \frac{\text{Im } A_V^{\infty}}{\text{Im } A_P^{\infty}} \quad 6.13$$

Thus the ratio of Regge to Pomeron exchange can be found using data from the t' distributions for diffractive 'Q' production. For this experiment using the whole Q mass interval this ratio was found to be $0.19 \pm .09$. The previous K_L^0 S.L.A.C. experiment⁽¹⁾ obtained a value of 0.17 for $4 < p_{K_L^0} < 12$ Gev/c and for Q^+Q^- production the corresponding ratio is 0.07 at 14.3 Gev/c⁽⁴³⁾. In comparison $K^\pm p$ elastic scattering gives 0.085 at 13 Gev/c for this ratio.

6.5 Momentum Dependence of the Slopes

The momentum dependence of the slopes has been investigated to check for any change in sign of the crossover with energy. According to the pion exchange Deck model outlined in chapter 5 section (5.3), if no anti-selection on the Δ^{++} is made, the crossover should change sign below 6 GeV/c beam momentum, figure (5.8a), as π^+p elastic scattering below this momentum value and with $M(p\pi^+)$ in the $\Delta^{++}(1236)$ mass region has a steeper differential cross-section slope than π^-p . By contrast in figure (5.8b), if the Δ^{++} background is excluded then the prediction is that $b(K^0p \rightarrow K^{*+}\pi^-p) > b(\bar{K}^0p \rightarrow K^{*-}\pi^+p)$ for all momenta, with the slopes increasing and approaching a common value with increasing beam momentum. Berger has remarked⁽³¹⁾ that if no selection on the (πp) mass is made, then above a beam momentum of 8 GeV/c the effect on the slopes from resonance structure such as Δ^{++} and Δ^0 would be minimized and the crossover predictions from the Deck model at these 'asymptotic' energies would be unambiguous with $b(K^{*+}\pi^-p) > b(K^{*-}\pi^+p)$. This is indirectly supported by the observation in chapter (4) that above 8 GeV/c K_L^0 momentum, the Δ^{++} signal is much reduced in strength, figure (4.17), and the cut removes few true Q events.

In order to test these ideas the data has been divided into three momentum intervals between threshold and 17 GeV/c (as described in chapter 4, section(4.7)) and the t' distributions fitted to single exponentials. This has been done both including and excluding $(p\pi^+)$ masses within the Δ^{++} region in addition to the other cuts used in isolating the diffractive signal.

The fits have also been repeated excluding events with ($K_S^0\pi$) masses within both K^{*+} and K^{*-} mass intervals. The results of these fits are shown in figures (6.6 - 6.9) and are summarized in table (6.3). The slopes for ($K^{*-}\pi^+p$) and ($K^{*+}\pi^-p$) with Δ^{++} removed are consistent within errors with their average values (dashed line) and the slopes for ($K^{*+}\pi^+p$) are steeper than for ($K^{*+}\pi^-p$) for all momenta. If no Δ^{++} cut is made, then from figure (6.7) for momenta below 6 Gev/c the difference in slopes between ($K^{*-}\pi^+p$) and ($K^{*+}\pi^-p$) is almost zero but does not change sign. For the other two momentum intervals the slopes for ($K^{*-}\pi^+p$) are greater than ($K^{*+}\pi^-p$) and above 10 Gev/c K_L^0 momentum the difference in slopes is indistinguishable from figure (6.6) with the Δ^{++} anti-selection. The slopes for ($K^{*+}\pi^-p$) are consistent with their average values, whereas the ($K^{*-}\pi^+p$) slopes above 6 Gev/c differ from the average value because of the presence of the Δ^{++} signal. The slopes obtained for the overall data with no Δ^{++} removal are 5.25 ± 0.89 and $6.67 \pm 0.60 \text{ Gev}^{-2}$ for ($K^{*+}\pi^-p$) and ($K^{*-}\pi^+p$), figure (6.5).

These results are in clear disagreement with the slope values obtained from the pion exchange model, compare figure (5.8b) where for $M(p\pi^+) > 1.34 \text{ Gev}$ the slope for ($K^{*+}\pi^-p$) is predicted to be greater than for ($K^{*-}\pi^+p$) for all beam momenta between 4 and 40 Gev/c. The average difference between the slopes in figure (5.8b) corresponding to $(b(K^{*+}\pi^-p) - b(K^{*-}\pi^+p))$ is $\approx 1 \text{ Gev}^{-2}$ whereas a difference of $-4 \pm 1.2 \text{ Gev}^{-2}$ found from our data. The average difference from the S.L.A.C. data was $-3.8 \pm 0.8 \text{ Gev}^{-2}$. Corresponding to figure (5.8a) where there is no Δ^{++} anti-selection, no change in the sign of the crossover is observed below 6 Gev/c in figure (6.7) and above this momentum the slope for ($K^{*-}\pi^+p$) is again found to be greater (within errors) than for ($K^{*+}\pi^-p$). Similar conclusions can be drawn for figures (6.8 - 6.9) where events with ($K_S^0\pi$) masses within both K^* mass intervals were removed.

Comparisons with data from K^+ and K^- experiments can be hampered by different 'Q' region definitions and relative normalisation problems for different experiments, however using data from a 12 GeV/c K^+ experiment⁽⁴⁴⁾ and a 14 GeV/c K^- experiment⁽⁴³⁾, a crossover can be seen in the $d\sigma/dt$ distributions for the reactions $K^\pm p \rightarrow K^\pm \pi^+ \pi^- p$ figure (5.4a) and $K^\pm p \rightarrow K^0 p \pi^\pm \pi^0$ figure (5.4b). Considering the process $K^\pm p \rightarrow K^\pm \pi^+ \pi^- p$ and using data from the whole 'Q' ($K\pi\pi$) mass interval, the slopes for $K^- p \rightarrow Q^- p$ are found to be $9.6 \pm 0.3 \text{ GeV}^{-2}$ and for $K^+ p \rightarrow Q^+ p$ $7.9 \pm 0.1 \text{ GeV}^{-2}$ with the crossover at $-t = 0.17 \pm 0.05 \text{ GeV}^2$. This is to be compared with the crossover position for Q^0 and \bar{Q}^0 in this experiment at $-t' = 0.14 \text{ GeV}^2$. The crossover point for $K^+ p \rightarrow K^0 \pi^+ \pi^0 p$ and $K^- p \rightarrow \bar{K}^0 \pi^- \pi^0 p$ is not so well determined, as the slopes for these processes are closer (7.9 ± 0.5 and $6.9 \pm 0.5 \text{ GeV}^{-2}$) and figure (5.4b) reflects the uncertainty in the crossover position. Slope parameters from $K^\pm p \rightarrow Q^\pm p$ are generally in better agreement with the predicted values from figure (5.8b) than their K_L^0 counterparts, for example from the 8.25 GeV/c $K^\pm p \rightarrow Q^\pm p$ experiment⁽⁴¹⁾, slopes of 7.72 ± 0.67 and $8.7 \pm 0.67 \text{ GeV}^{-2}$ were obtained for Q^+ and Q^- . Slope differences for Q^\pm production ($\approx 2 \text{ GeV}^{-2}$) are smaller than for Q^0, \bar{Q}^0 production ($\approx 4.0 \text{ GeV}^{-2}$) for this experiment and for the S.L.A.C. K_L^0 experiment. In comparison, $K^\pm p$ elastic scattering has a difference in slopes of ($\approx 1.5 \text{ GeV}^{-2}$) at 14 GeV/c similar to Q^+, Q^- production, with slope values being two units less than in $Q^\pm p$ ⁽⁴⁴⁾. On the basis of the pion exchange Deck model one would expect the difference in slopes between Q^- and Q^+ , ($b(Q^-) - b(Q^+)$), to be opposite the slope difference from \bar{Q}^0 and Q^0 , ($b(\bar{Q}^0) - b(Q^0)$), because of the reflection of $\pi^+ p$ and $\pi^- p$ elastic scattering, however this is not found to hold experimentally .

6.6 Mass Dependence of the Slopes

A common property among diffractive processes is a strong dependence of the slopes of the differential cross-sections with mass of the dissociating system, the slopes being larger near threshold and decreasing with increasing mass. Figure(6.10) illustrates this variation using data from the previous S.L.A.C. K_L^0 experiment, with the slopes of the antiparticle induced process (\bar{K}^0) being steeper than that of the particle process (K^0) for all ($K^*\pi$) masses. Figure(6.11) also shows data from a 14 GeV/c K^-p experiment⁽⁴³⁾, where a similar variation is seen. Data from this experiment which satisfied the diffractive cuts was divided into four ($K^*\pi$) mass intervals from $1.0 < M(K_S^0 \pi^+ \pi^-) < 2.2$ Gev and the slopes of the t' distributions fitted to single exponentials in these regions. The resultant slope-mass plot is shown in figures (6.12 - 6.13) and table (6.4) with the overall trend of the slopes similar to that in other experiments. Apart from the first ($K^*\pi$) mass interval, where the statistics are poor and errors on the slopes large, the slope for $K^{*-} \pi^+ p$ is steeper than that of $K^{*+} \pi^- p$.

The traditional explanation advanced for the slope-mass behaviour, in terms of a kinematic correlation in the Deck model between t_{aa^*} and t_{pN} , figure(5.5), for masses near threshold has been shown by Pirilä and Miettinen to be wrong⁽⁴⁵⁾. Analyses⁽⁴⁶⁾ on subsequent diffractive data, which have included all the variables needed to fully describe the amplitude, have shown that the Deck or other multiperipheral models cannot at present reproduce the observed slope-mass variation.

6.7 Selection on angles

As described in section (5.4) of the previous chapter, angular selections on diffractive data such as $K_L^0 p \rightarrow Qp$, have been advocated by Berger as a means of enhancing the contribution of specific exchanges, with a view to testing cross-over predictions of the Deck model. This is particularly relevant for $K_L^0 p \rightarrow Qp$, where as has been seen the Deck model incorporating only pion exchange fails to explain the sign and magnitude of the crossover in the data. The possibility that other exchanges such as K^* are present which 'over-compensate' for the incorrect sign of the crossover from π exchange, can be tested by appropriate cuts on the s-channel helicity angles ϕ_s and θ_s defined by equations (5.12). The success of the ϕ_s selection in $\pi^\pm p \rightarrow \pi^\pm (\pi^- \Delta^{++})$ crossover predictions encourages a study of the usefulness of this variable in the diffractive process $K_L^0 p \rightarrow Qp$.

The ϕ_s distributions using K^{*+} and K^{*-} as analyzer, figure (5.9), are shown in figures (6.14) for events satisfying the diffractive 'Q' cuts. Parity conservation for strong interactions enables the total 2π kinematic range of ϕ_s to be folded into the interval $0 < \phi_s < \pi$ radians. Within the available statistics of this experiment no prominent peaking at $\phi_s = 0$ corresponding to pion exchange or $\phi_s = \pi$ for K^* exchange is visible for either strangeness state. Data from the higher statistics 8.25 GeV/c $K^\pm p \rightarrow Q^\pm p$ experiment and $K^- p \rightarrow Q^- p$ at 16 GeV/c are also compatible with a flat ϕ_s distribution. The numbers of events for $\phi_s < \pi/2$ is the same (within statistics) as for $\phi_s > \pi/2$ for both Q^0 and \bar{Q}^0 distributions. These observations are interpreted by Berger as implying equal amounts of pion and $K^*(890)$ exchanges present such that the overall ϕ_s distribution shows no peaking.

The t' distributions for events satisfying the diffractive Q cuts were fitted to single exponentials within the regions $\phi_s < \pi/2$ or $\cos \phi_s > 0$ and $\phi_s > \pi/2$ or $\cos \phi_s < 0$. The resulting fits to the data are shown in figure (6.15) and the values are summarized together with those from subsequent cuts in table (6.5). For the interval $\cos \phi_s > 0$ where the contribution from the pion exchange Deck graph should predominate, the slope of $(\bar{K}^0 p \rightarrow K^{*-} \pi^+ p)$ is steeper than the slope for $(K^0 p \rightarrow K^{*+} \pi^- p)$, the difference in slopes being $2.97 \pm 1.54 \text{ Gev}^{-2}$. For $\cos \phi_s < 0$, where K^* exchange is thought to occur, a similar result is found that $(\bar{K}^0 p \rightarrow K^{*-} \pi^+ p)$ has a steeper slope than $(K^0 p \rightarrow K^{*+} \pi^- p)$, where the difference in slopes is $3.86 \pm 1.66 \text{ Gev}^{-2}$.

The fits have been repeated with the Δ^0 cut and excluding those events with $K_s^0 \pi$ masses within both K^{*+} and K^{*-} mass intervals but apart from the larger statistical errors from the fewer surviving events, the slopes and crossover sign remain the same in both $\cos \phi_s$ regions. The observation that the crossover does not change sign for $\cos \phi_s > 0$ in the pion exchange sector, where $b(K^{*+} \pi^- p)$ is predicted to be greater than $b(K^{*-} \pi^+ p)$ when Δ^{++} masses are excluded is a serious blow to the model. Although the statistical significance of the data is not very high and the difference in slopes is not at the three standard deviation level required for convincing evidence, the trend of the data is in disagreement with Berger's predictions. This is supported by the observation of almost equal slopes for $(K^{*-} \pi^+ p)$ and $(K^{*+} \pi^- p)$ for $\cos \phi_s > 0$ where no Δ^{++} anti-selection has been made and the beam momentum is less than 6 Gev/c, table (6.5). Under these conditions a clear sign of a crossover reversal should have been apparent. For beam momenta greater than 6 Gev/c for both $\cos \phi_s > 0$ and $\cos \phi_s < 0$ segments, the slope of $(K^{*-} \pi^+ p)$ is greater than that of $(K^{*+} \pi^- p)$.

The Deck pion exchange amplitude, equations (5.10), also shows an angular dependence in addition to that on ϕ_s in the s-channel angle ' θ_s ' via the subenergy variable $s_{\pi N}(s_{a^*N})$, equation (5.15), which governs the off-shell pion (K^*)-nucleon elastic scattering, represented by the term $A_{\pi N}(s_{\pi N}, t_{pN})$ (or $A_{a^*N}(s_{a^*N}, t_{pN})$ for K^* exchange). On the basis of equations (5.15 - 5.16) for the subenergy and momentum transfer squared variables, the Deck amplitude will concentrate events at high energy (such that $s \gg M_{a^*\pi}^2$) in the corners of the $\cos \theta_s - \phi_s$ phase space plot, figure (6.16a). The top left hand corner corresponding to a large amplitude for pion exchange where $|t_{aa^*}|$ is smallest and $s_{\pi N}$ is large and the bottom right hand corner for K^* exchange where $|t_{a\pi}|$ is smallest and s_{a^*N} large. By selecting events in these two corners one should in principle be able to enhance pion or K^* exchange more efficiently than by the $\cos \phi_s$ cuts alone. The scatter plots of $\cos \theta_s - \phi_s$ for both strangeness states are shown in figures (6.17). Because of the poor statistics the line boundaries of the two different exchange sectors have been extended to cover the complete diagonal of the $\cos \theta_s - \phi_s$ plot, figure (6.16a). The t' distributions have been fitted to single exponentials in the two regions and the slope parameters summarized in table (6.5). For the total momentum interval and for both pion and K^* exchange regions the slope of $\bar{K}^0 p \rightarrow K^{*-} \pi^+ p$ is greater than that of $K^0 p \rightarrow K^{*+} \pi^- p$. For momenta greater than 10 Gev/c such that $s \gg M_{a^*\pi}^2$ a similar result is obtained in the pion exchange corner, where $b(K^{*-} \pi^+ p) - b(K^{*+} \pi^- p)$ is $4.41 \pm 2.52 \text{ Gev}^{-2}$ and for the K^* corner, $b(K^{*-} \pi^+ p) - b(K^{*+} \pi^- p)$ is $4.01 \pm 2.86 \text{ Gev}^{-2}$.

Angular selections on the data have been repeated using the 't-channel' set of axes, where ϕ_t and θ_t in figure (6.18) are the t-channel angles defined in the rest frame of the $(K^*\pi)$ system. On the basis of the momentum transfer squared and sub-energy variables of the Deck amplitude, the π and K^* exchanges can also be shown⁽³¹⁾ to be concentrated in the top left and bottom right corners of the $\cos \theta_t - \phi_t$ scatter plot, figure (6.16b). After selecting events in the two diagonal segments of the $\cos \theta_t - \phi_t$ scatter plot, the t' distribution slopes for $\bar{K}^0 p \rightarrow K^{*-} \pi^+ p$ were found to be greater than that for $K^0 p \rightarrow K^{*+} \pi^- p$ in both regions in agreement with the previous results for the $\cos \theta_s - \phi_s$ selections. The slope parameters from the fits are summarized in table (6.5) and figures (6.19) show the experimental $\cos \theta_t - \phi_t$ scatter plots for both Q^0 and \bar{Q}^0 together with the ϕ_t distributions in figure (6.20). The numbers of events in the pion and K^* exchange corners of the $\cos \theta_s - \phi_s$ and $\cos \theta_t - \phi_t$ scatter plots are shown schematically in figures (6.21 - 6.22) for various momentum cuts. With present statistics figures (6.21 - 6.22) show little evidence of any clustering of events in these corners.

6.8 Summary and Conclusions

A study of the overall data has clearly shown that $\bar{K}^0 p \rightarrow \bar{Q}^0 p$ has a steeper slope and higher intercept than $K^0 p \rightarrow Q^0 p$, with the crossover occurring at $-t'_c = 0.14 \pm 0.07 \text{ Gev}^2$. The momentum dependence of the slopes has been investigated and the slope for $\bar{Q}^0 p$ is greater than that for $Q^0 p$ over the total K_L^0 momentum interval of the experiment. If no Δ^{++} anti-selection is made, the slope for $\bar{K}^0 p \rightarrow K^{*-} \pi^+ p$ is found to be greater than that for $K^0 p \rightarrow K^{*+} \pi^- p$, with the difference in slopes being smaller than in the diffractive process $K_L^0 p \rightarrow Qp$. The momentum dependence of the slopes without removal of the Δ^{++} signal shows no sign of a crossover reversal from above to below 6 Gev/c beam momentum as predicted in figure (5.8a). The proportion of Regge to Pomeron exchange in $K_L^0 p \rightarrow Qp$ (0.19 ± 0.09) is similar to that found in the S.L.A.C. K_L^0 experiment (0.17). The slopes for $K^0 p \rightarrow K^{*+} \pi^- p$ and for $\bar{K}^0 p \rightarrow K^{*-} \pi^+ p$ diminish with increasing $K^* \pi$ masses, with the slope for $(K^{*-} \pi^+ p)$ remaining greater than for $(K^{*+} \pi^- p)$ for $K^* \pi$ mass greater than 1.2 Gev. The crossover shows no sign of a reversal under the ϕ_s angular selections, and the slope for $\bar{Q}^0 p$ is greater than that of $Q^0 p$ for both $\cos \phi_s < 0$ and $\cos \phi_s > 0$ regions. The experimental ϕ_s and ϕ_t angular distributions appear uniform and show no peaking at $\phi_s = 0$ and $\phi_s = \pi$ radians, corresponding to π and K^* exchanges and there is no concentration of events in the opposite Deck corners of the $\cos \theta_s - \phi_s$ and $\cos \theta_t - \phi_t$ scatter plots.

These observations taken together provide no evidence for the existence of the extra K^* exchange Deck Graph as postulated by Berger, and do not resolve the Q crossover problem. Although the model of the Q crossover formulated by Cohen-Tannoudji, which invokes B and ω exchange in addition to the normal pion-exchange Deck Graph, predicts the correct sign of the cross-

over and does not have any $\cos \phi_s$ dependence, criticism has been levelled against it by Berger on account of the sensitive balance of Regge amplitudes and phases involved. The lack of any slope dependence on the decay angles $(\cos \theta_s, \phi_s)$ and $(\cos \theta_t, \phi_t)$ together with the absence of any concentration of events in the Deck corners of these plots strengthens an alternative resonant interpretation of the Q enhancement. The observed mass variation of the slopes, which on the basis of the pion-exchange Deck model would be very small, points to the need for a sizeable extra contribution to be present.

At issue in the Q enhancement is the problem of distinguishing a resonant signal from a large Deck type background which has many features in common. One would expect the non-resonant component to depend upon the form of the production amplitude in direct contrast to the resonant part. The mass distributions (of the $K_S^0 \pi^+ \pi^-$ system) like the slope parameters, on the basis of the Deck model, might then show significant differences for various regions of the $\cos \theta_s - \phi_s$ and $\cos \theta_t - \phi_t$ phase space. This has been briefly investigated but within the available statistics of the experiment no difference has been observed.

Table 6.1

Numbers of events in $K_L^0 p \rightarrow Qp$

Channel	<u>K^{*+}/K^{*-} events not removed</u>	<u>K^{*+}/K^{*-} events removed</u>
$K^0 p \rightarrow Q^0 p$	141.1	115.3
$\bar{K}^0 p \rightarrow \bar{Q}^0 p$	139.5	113.7

Table 6.2

Slope and intercept parameters for the total data

Final State	<u>K^{*+}/K^{*-} events not removed</u>		<u>K^{*+}/K^{*-} events removed</u>	
	Slopes (Gev^{-2})	Intercepts (Events/ Gev^2)	Slopes (Gev^{-2})	Intercepts (Events/ Gev^2)
$Q^0 p,$	5.56 ± 0.71	843 ± 116	5.0 ± 0.77	634 ± 98
$\bar{Q}^0 p,$	8.93 ± 0.88	1263 ± 116	8.99 ± 0.98	1037 ± 151
$Q^0 p, \Delta^0 \text{ cut}$	5.70 ± 0.76	755 ± 110	5.23 ± 0.81	586 ± 95
$\bar{Q}^0 p, \Delta^0 \text{ cut}$	8.57 ± 0.94	1003 ± 145	8.61 ± 1.04	823 ± 132
$K^{*+} \pi^- p, \text{Qin}$ Δ^{++} not removed	5.25 ± 0.59	1123 ± 132	4.82 ± 0.67	799 ± 110
$K^{*-} \pi^+ p, \text{Qin}$ Δ^{++} not removed	6.67 ± 0.60	1520 ± 165	6.66 ± 0.68	1187 ± 145

'Qin' = denotes the cut $1.1 < M(K^* \pi) < 1.5 \text{ Gev}$.

Table 6.3

Momentum dependence of the slopes

Final State	<u>K*⁺/K*⁻ events not removed</u>		<u>K*⁺/K*⁻ events removed</u>	
	Slopes (Gev ⁻²)	Intercepts (Events/Gev ²)	Slopes (Gev ⁻²)	Intercepts (Events/Gev ²)
Q ^o p, p _{K_L} ^o <6 Gev/c	4.69±1.24	221±57	4.24±1.35	166±48
Q ^o p, p _{K_L} ^o <6 Gev/c	7.94±1.49	351±84	8.22±1.65	294±77
Q ^o p, 6 < p _{K_L} ^o <10 Gev/c	7.10±1.32	359±80	6.17±1.39	253±64
Q ^o p, 6 < p _{K_L} ^o <10 Gev/c	9.64±1.61	437±98	9.01±1.76	319±82
Q ^o p, p _{K_L} ^o >10 Gev/c	4.97±1.17	273±65	4.63±1.24	219±58
Q ^o p, p _{K_L} ^o >10 Gev/c	9.23±1.46	478±105	9.67±1.63	426±102
<u>Δ⁺⁺ not removed</u>				
K* ⁺ π ⁻ p, Qin, p _{K_L} ^o <6 Gev/c	4.48±0.87	437±81	4.41±1.04	299±66
K* ⁻ π ⁺ p, Qin, p _{K_L} ^o <6 Gev/c	4.66±0.75	594±94	4.67±0.86	454±81
K* ⁺ π ⁻ p, Qin, 6 < p _{K_L} ^o <10 Gev/c	6.72±1.14	424±85	5.55±1.23	283±66
K* ⁻ π ⁺ p, Qin, 6 < p _{K_L} ^o <10 Gev/c	9.92±1.52	536±110	9.06±1.64	370±88
K* ⁺ π ⁻ p, Qin, p _{K_L} ^o >10 Gev/c	4.96±1.17	273±65	4.63±1.24	219±57
K* ⁻ π ⁺ p, Qin, p _{K_L} ^o >10 Gev/c	9.23±1.46	479±105	9.67±1.63	426±102

Table 6.4

Mass dependence of the slopes

Final State	<u>K^{*+}/K^{*-} events not removed</u>		<u>K^{*+}/K^{*-} events removed</u>	
	Slopes (Gev^{-2})	Intercepts (Events/ Gev^2)	Slopes (Gev^{-2})	Intercepts (Events/ Gev^2)
<u>$1.0 < M(K_S^0 \pi^+ \pi^-) < 1.2 \text{ Gev}$</u>				
$K^{*+} \pi^- p, \Delta^{++}$ removed	9.3 ± 2.31	202 ± 67	10.68 ± 2.54	220 ± 73
$K^{*-} \pi^+ p, \Delta^{++}$ removed	6.89 ± 1.68	212 ± 63	7.51 ± 1.77	221 ± 66
<u>$1.2 < M(K_S^0 \pi^+ \pi^-) < 1.35 \text{ Gev}$</u>				
$K^{*+} \pi^- p, \Delta^{++}$ removed	6.17 ± 1.0	490 ± 91	5.47 ± 1.05	383 ± 79
$K^{*-} \pi^+ p, \Delta^{++}$ removed	10.19 ± 1.55	528 ± 119	9.63 ± 1.68	398 ± 96
<u>$1.35 < M(K_S^0 \pi^+ \pi^-) < 1.5 \text{ Gev}$</u>				
$K^{*+} \pi^- p, \Delta^{++}$ removed	3.76 ± 1.16	209 ± 53	2.32 ± 1.32	110 ± 36
$K^{*-} \pi^+ p, \Delta^{++}$ removed	8.55 ± 1.29	530 ± 105	8.76 ± 1.53	415 ± 96
<u>$1.5 < M(K_S^0 \pi^+ \pi^-) < 2.2 \text{ Gev}$</u>				
$K^{*+} \pi^- p, \Delta^{++}$ removed	4.47 ± 1.41	166 ± 49	4.47 ± 1.41	165 ± 49
$K^{*-} \pi^+ p, \Delta^{++}$ removed	4.96 ± 1.24	240 ± 61	4.96 ± 1.24	240 ± 61

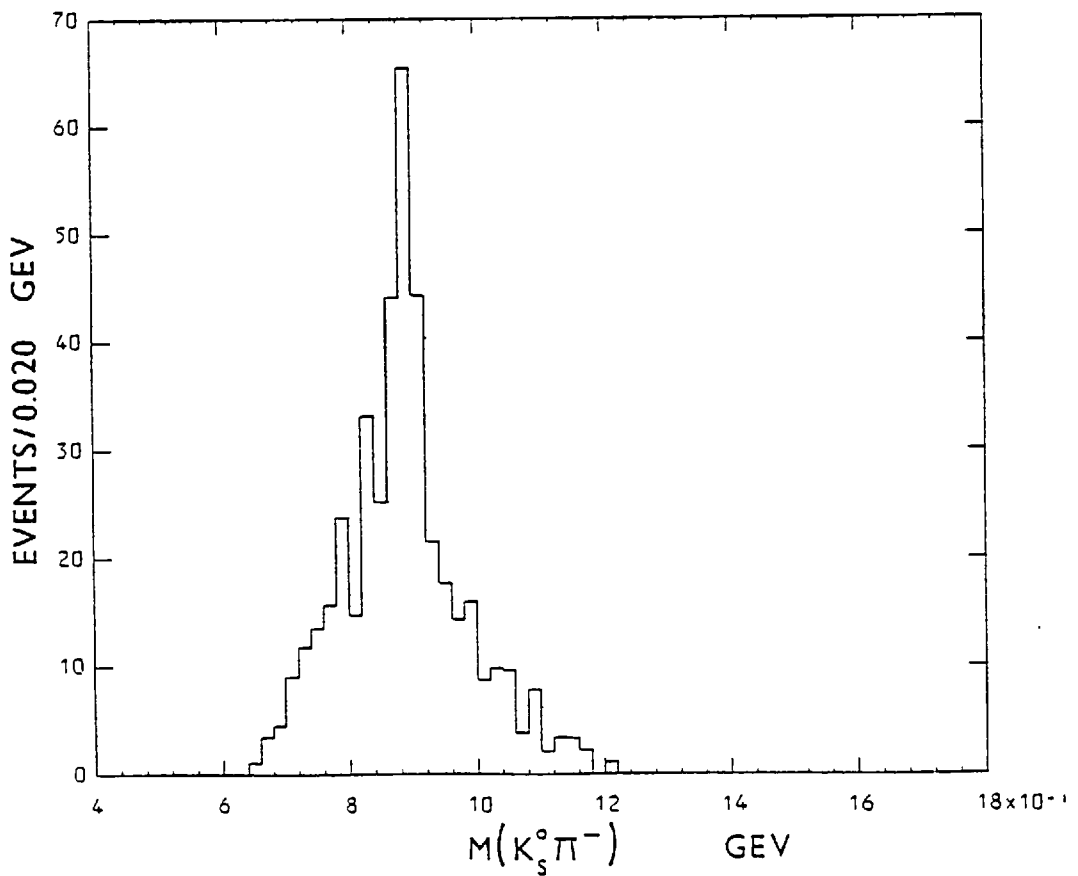
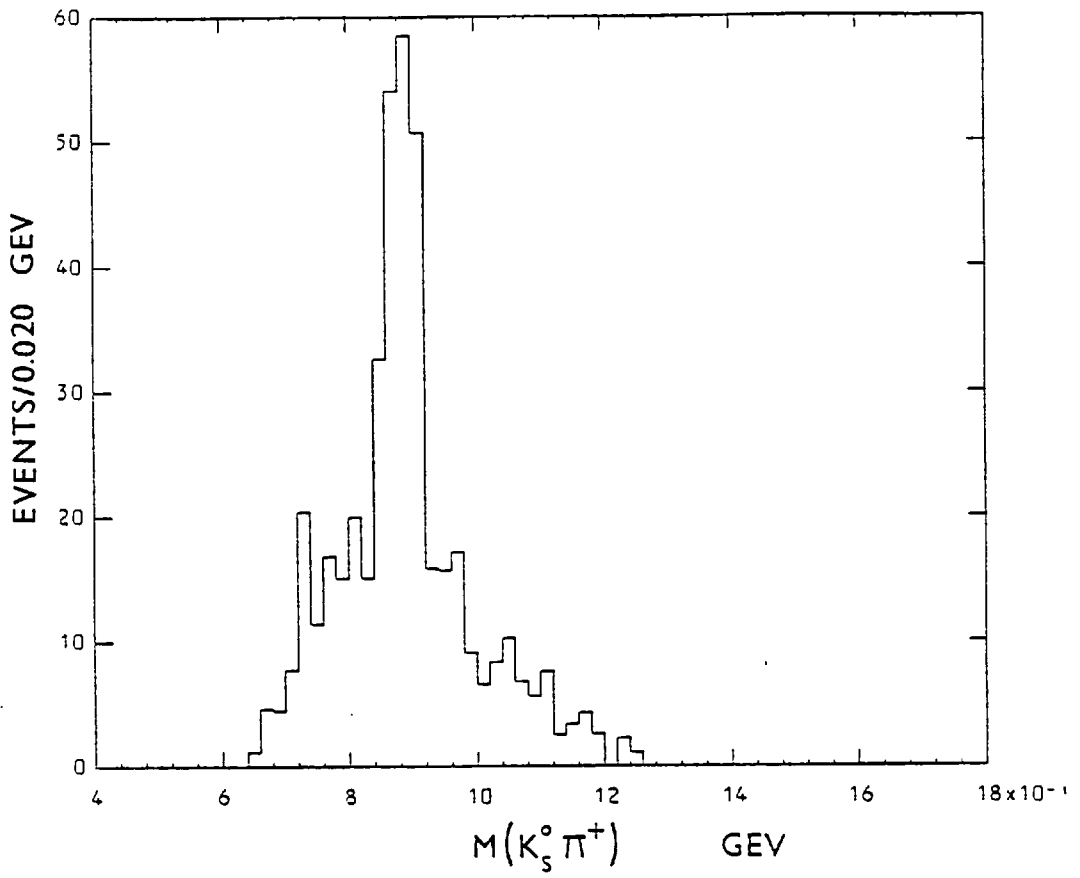
Table 6.5

Angular dependence of the slopes

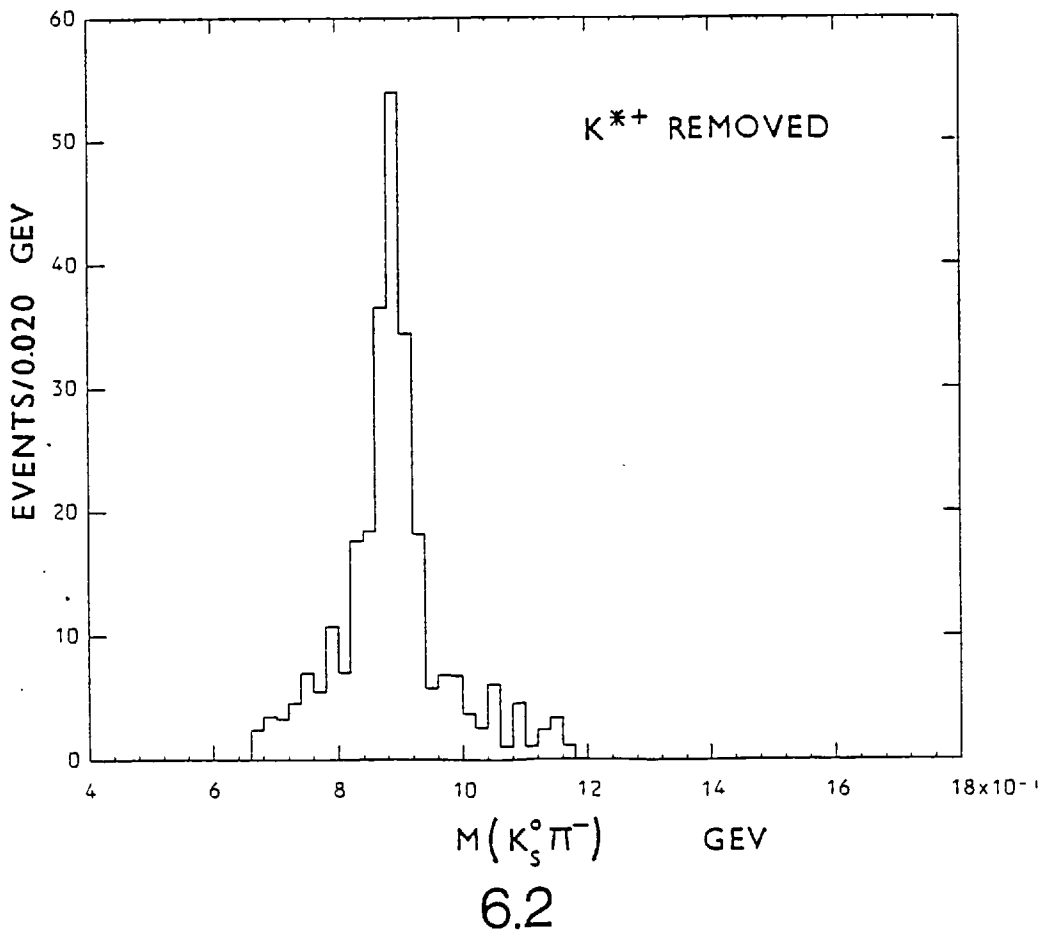
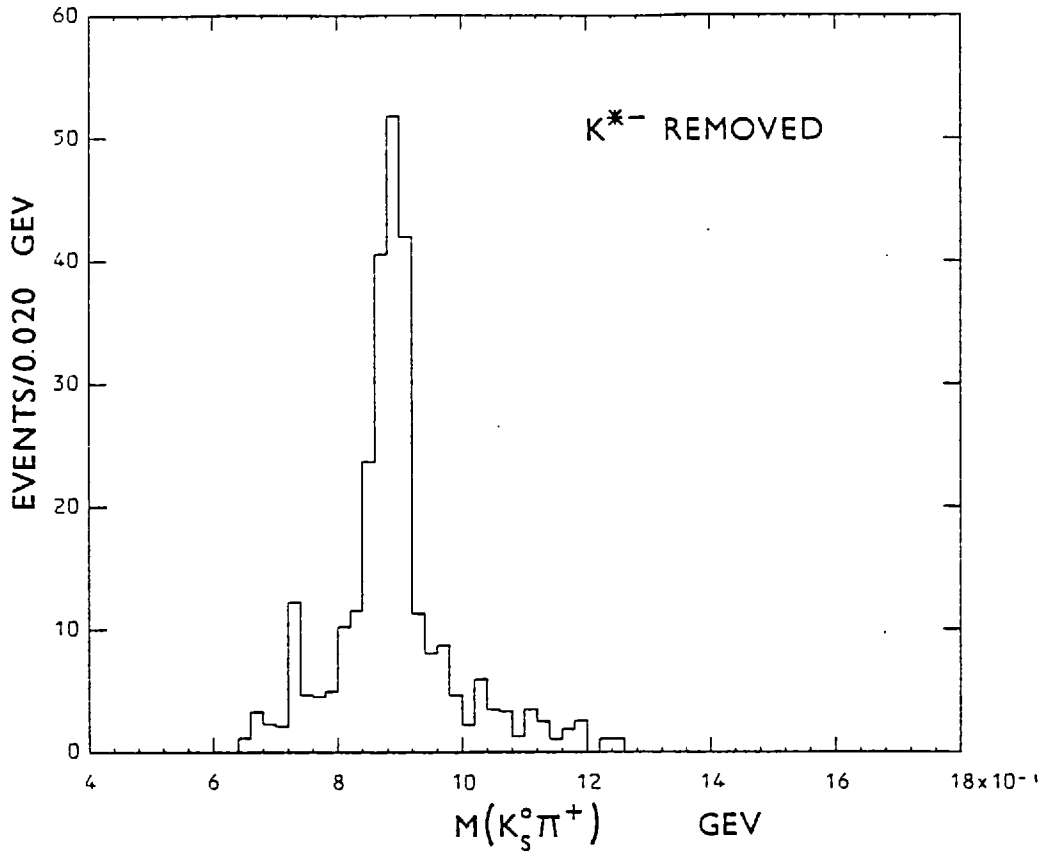
Final State	<u>K*⁺/K*⁻ events not removed</u>		<u>K*⁺/K*⁻ events removed</u>	
	Slopes (Gev ⁻²)	Intercepts (Events/Gev ²)	Slopes (Gev ⁻²)	Intercepts (Events/Gev ²)
Q ^o _p , cosφ _s >0	5.39±0.99	417±82	4.97±1.07	324±71
Q ^o _p , cosφ _s >0	8.36±1.18	620±114	8.51±1.32	506±104
Q ^o _p , cosφ _s <0	5.74±1.0	426±83	5.04±1.10	310±69
Q ^o _p , cosφ _s <0	9.60±1.32	646±121	9.55±1.45	533±110
Q ^o _p , Δ ^o cut, cosφ _s >0	5.70±1.07	380±78	5.34±1.15	310±71
Q ^o _p , Δ ^o cut, cosφ _s >0	8.02±1.26	495±100	8.32±1.45	410±94
Q ^o _p , Δ ^o cut, cosφ _s <0	5.69±1.08	374±78	5.12±1.17	276±65
Q ^o _p , Δ ^o cut, cosφ _s <0	9.23±1.41	511±106	8.92±1.54	413±95
<u>cosθ_s - φ_s plot</u>				
Q ^o _p , π exchange corner	5.62±0.98	449±85	5.07±1.05	340±73
Q ^o _p , π exchange corner	8.75±1.03	771±127	8.41±1.18	630±115
Q ^o _p , K* exchange corner	5.50±1.04	394±79	4.92±1.12	294±66
Q ^o _p , K* exchange corner	9.32±1.44	491±105	10.2 ±1.76	412±100
<u>cosθ_t - φ_t plot</u>				
Q ^o _p , π exchange corner	5.24±0.99	396±78	4.26±1.07	279±63
Q ^o _p , π exchange corner	8.09±1.14	605±110	8.15±1.29	479±98
Q ^o _p , K* exchange corner	5.88±1.02	447±86	5.77±1.13	359±77
Q ^o _p , K* exchange corner	9.96±1.4	666±126	9.96±1.48	565±117

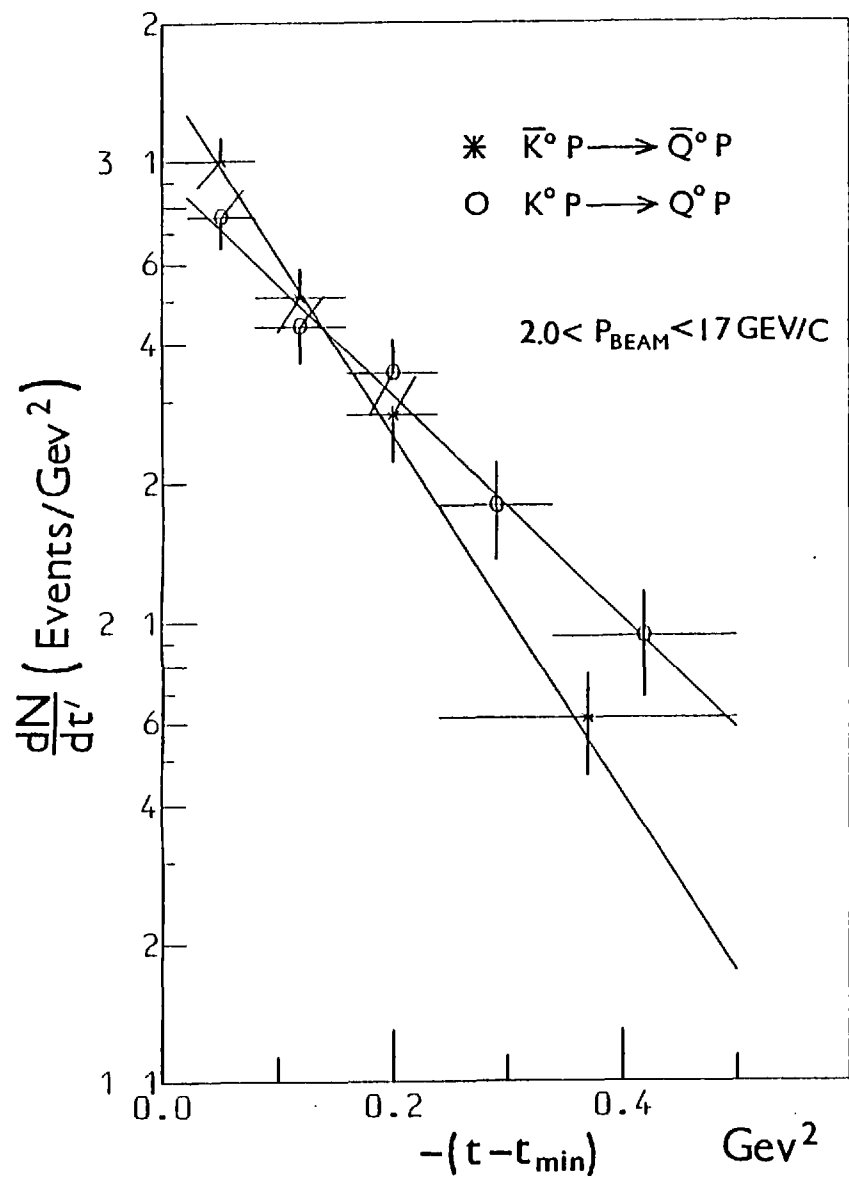
Table 6.5 contd.,

Final State	<u>K*⁺/K*⁻ events not removed</u>		<u>K*⁺/K*⁻ events removed</u>	
	Slopes (Gev ⁻²)	Intercepts (Events/Gev ²)	Slopes (Gev ⁻²)	Intercepts (Events/Gev ²)
$\cos\theta_s - \phi_s$ plot $p_{K_L^0} > 10$ Gev/c <hr/>				
Q ^o _{p,π} exchange corner	5.04±1.62	143±47	4.32±1.73	106±40
\overline{Q}^o _{p,π} exchange corner	9.45±1.93	296±84	9.44±2.04	265±80
Q ^o _{p,K*} exchange corner	4.89±1.68	129±45	4.95±1.81	113±42
\overline{Q}^o _{p,K*} exchange corner	8.90±2.32	183±65	10.08±2.80	161±64
$\cos\theta_t - \phi_t$ plot $p_{K_L^0} > 10$ Gev/c <hr/>				
Q ^o _{p,π} exchange corner	4.48±1.71	112±40	3.80±1.81	85±34
\overline{Q}^o _{p,π} exchange corner	6.09±1.78	153±52	6.65±1.92	150±53
Q ^o _{p,K*} exchange corner	5.37±1.60	162±51	5.34±1.75	135±47
\overline{Q}^o _{p,K*} exchange corner	13.60±2.66	374±11	14.54±3.16	320±107
Δ^{++} not removed $p_{K_L^0} < 6$ Gev/c <hr/>				
K* ⁺ π ⁻ _{p,Qin,cosφ_s} >0	4.09±1.20	207±54	3.95±1.41	146±44
K* ⁻ π ⁺ _{p,Qin,cosφ_s} >0	4.32±1.04	298±65	4.56±1.17	244±59
K* ⁺ π ⁻ _{p,Qin,cosφ_s} <0	4.91±1.26	232±60	4.95±1.55	154±48
K* ⁻ π ⁺ _{p,Qin,cosφ_s} <0	5.06±1.13	296±69	4.79±1.31	210±57
Δ^{++} not removed $p_{K_L^0} > 6$ Gev/c <hr/>				
K* ⁺ π ⁻ _{p,Qin,cosφ_s} >0	5.55±1.14	328±73	4.78±1.24	234±60
K* ⁻ π ⁺ _{p,Qin,cosφ_s} >0	8.55±1.36	481±101	8.23±1.47	372±88
K* ⁺ π ⁻ _{p,Qin,cosφ_s} <0	6.23±1.16	364±78	5.42±1.25	266±65
K* ⁺ π ⁻ _{p,Qin,cosφ_s} <0	10.90±1.68	542±117	10.88±1.88	433±105

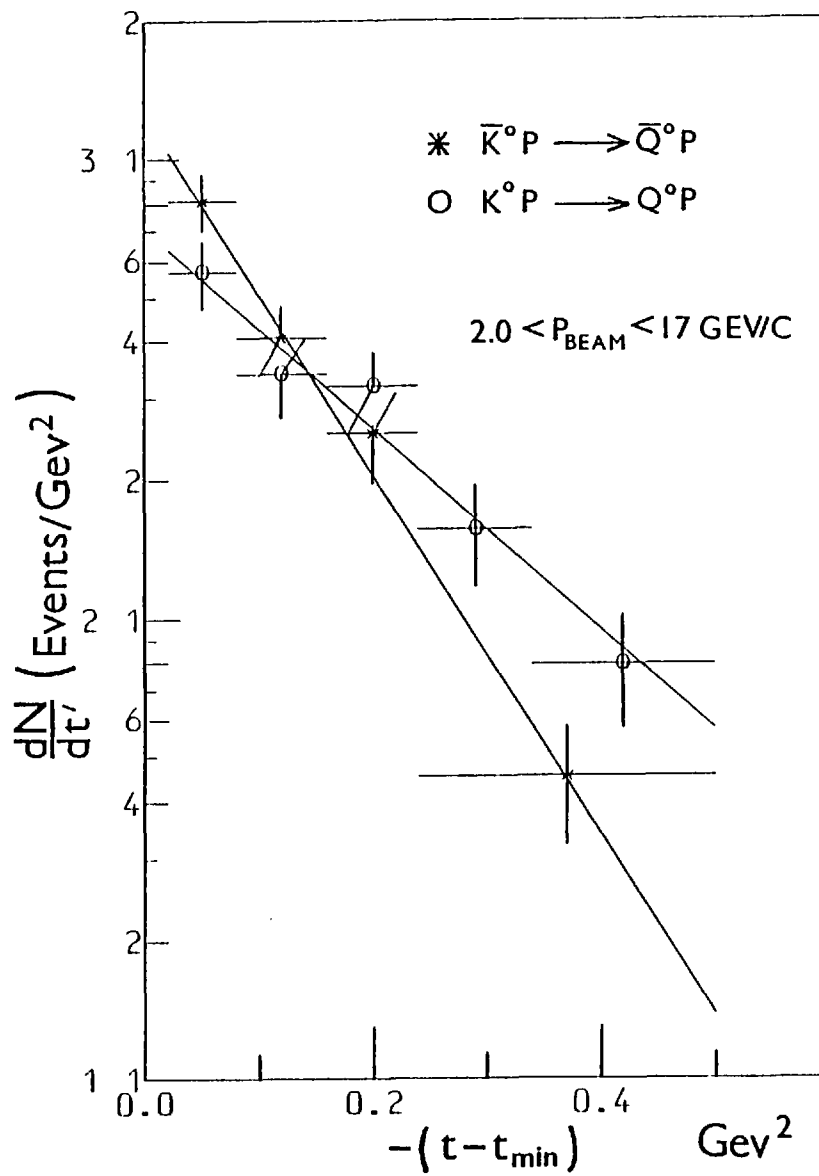


6.1

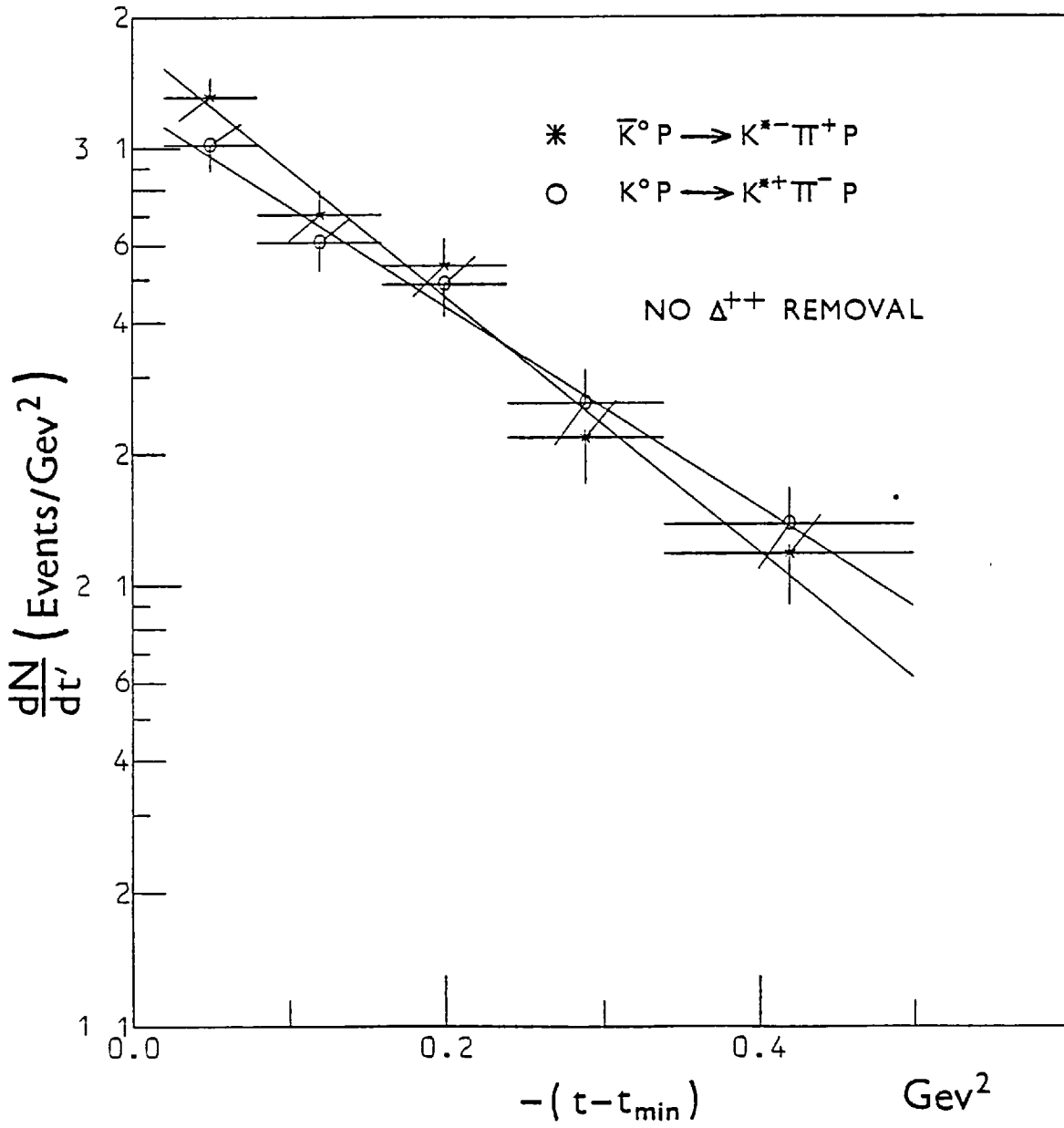




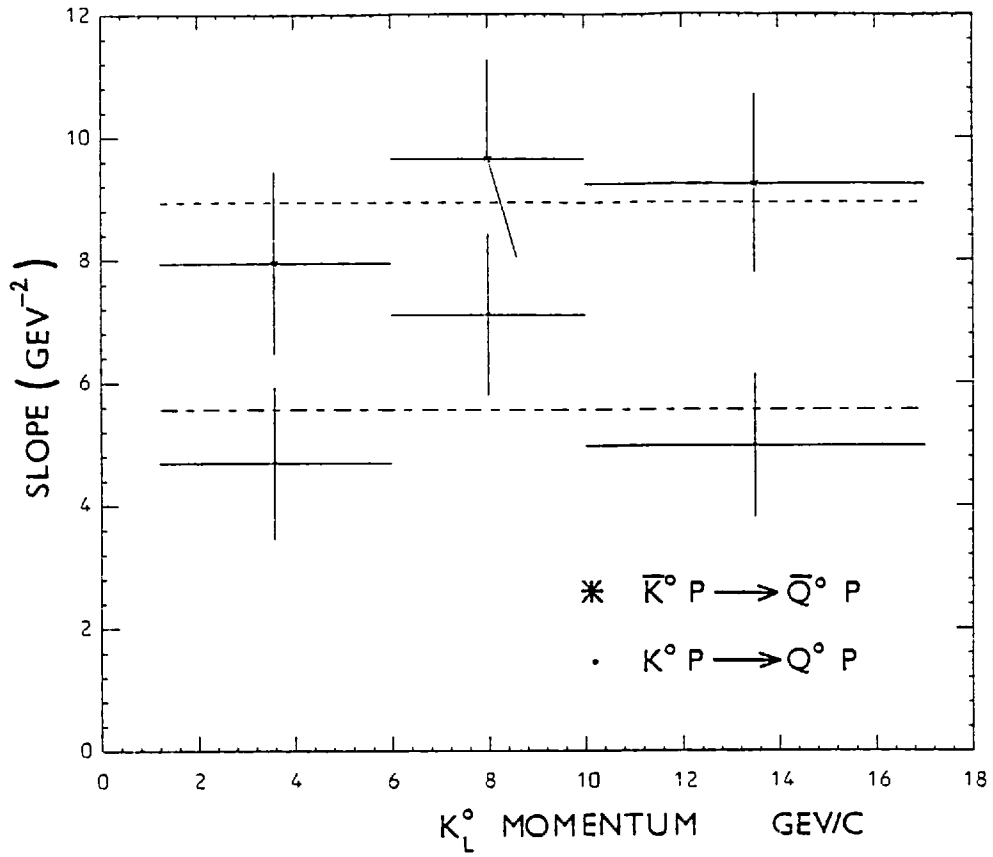
6.3



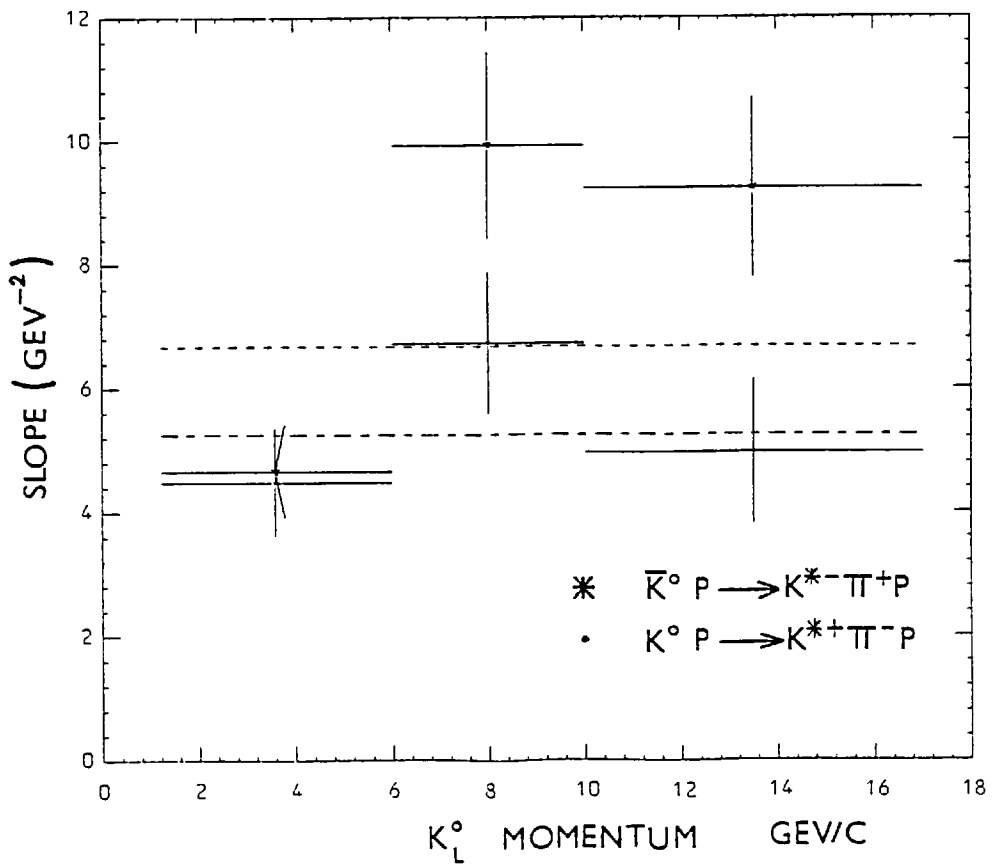
6.4



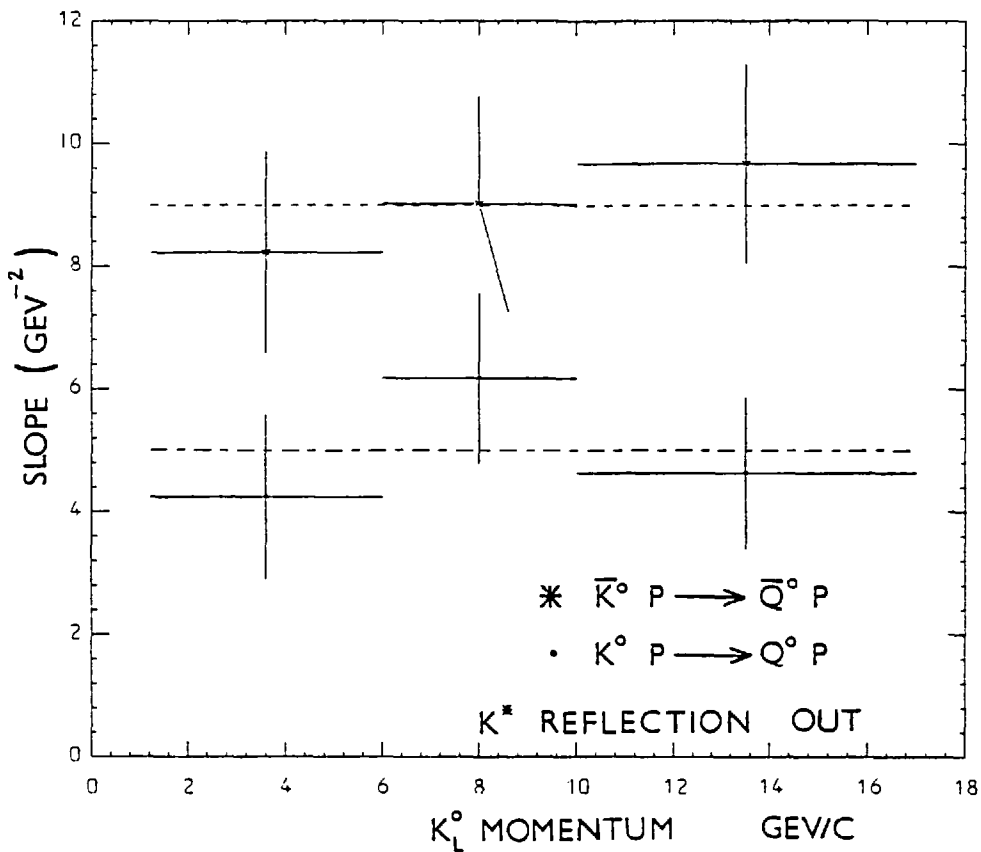
6.5



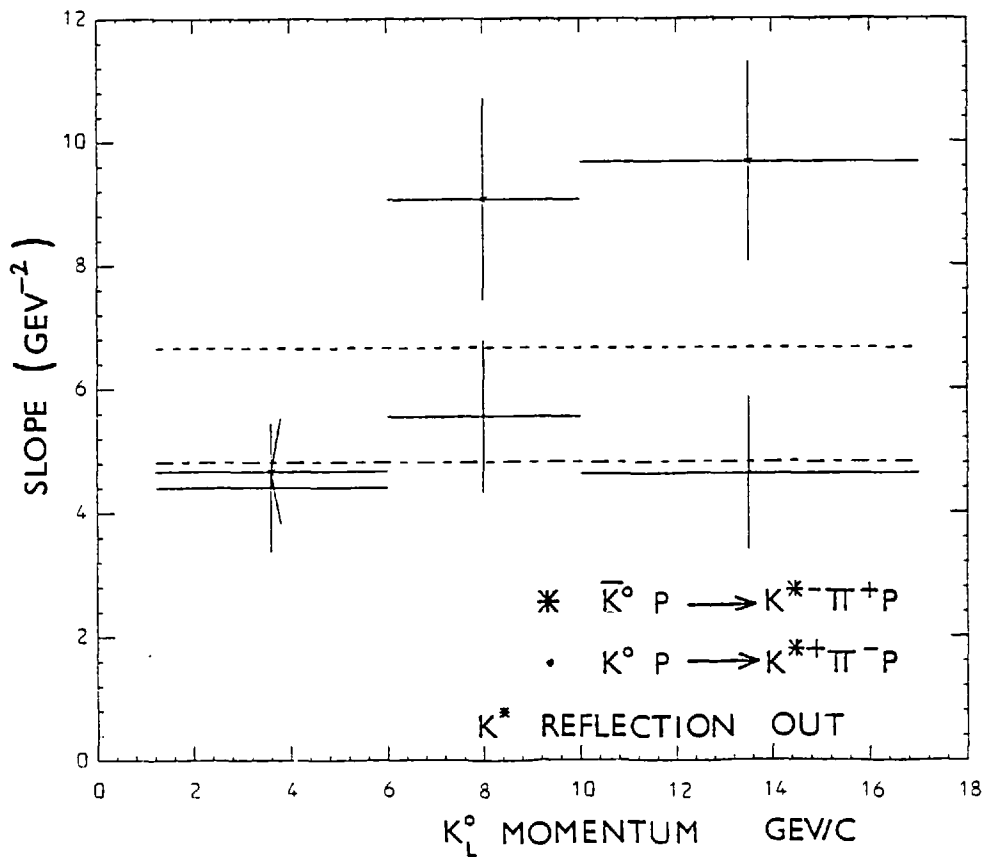
6.6



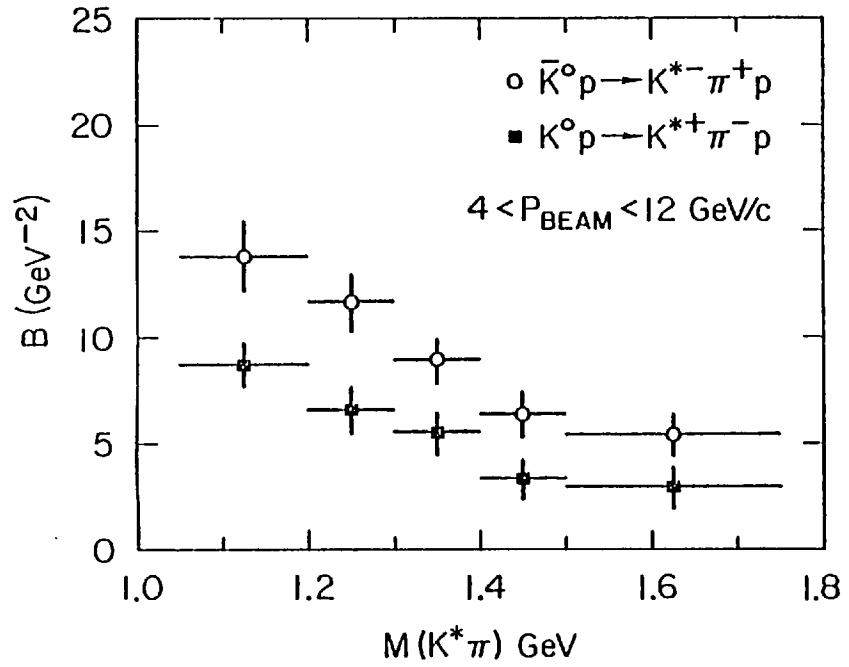
6.7



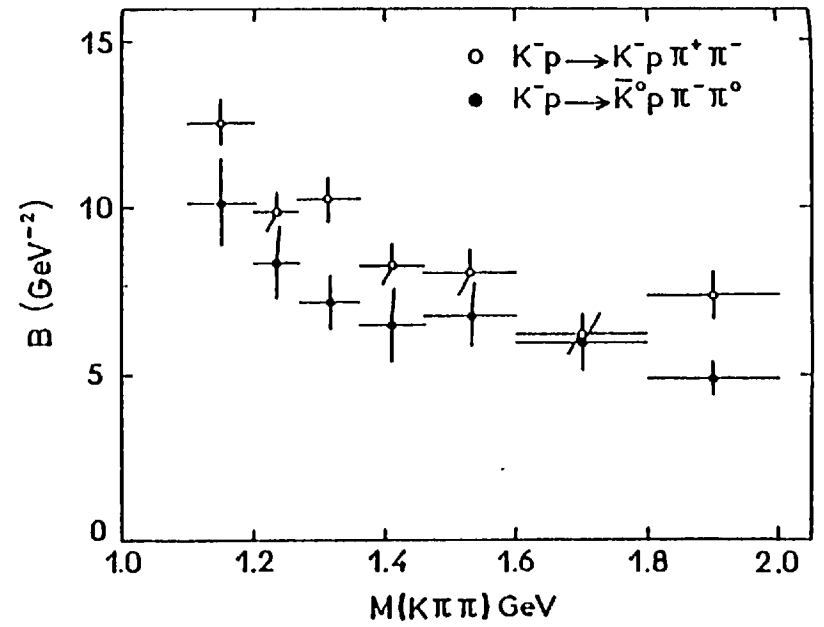
6.8



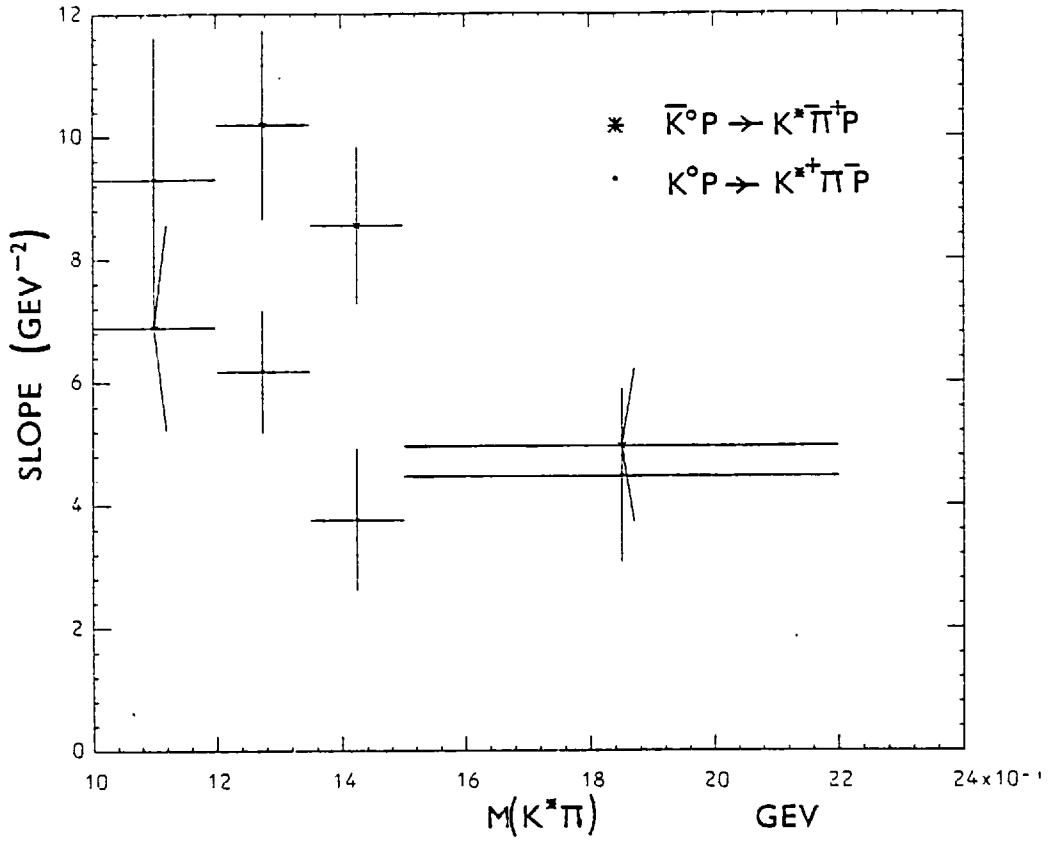
6.9



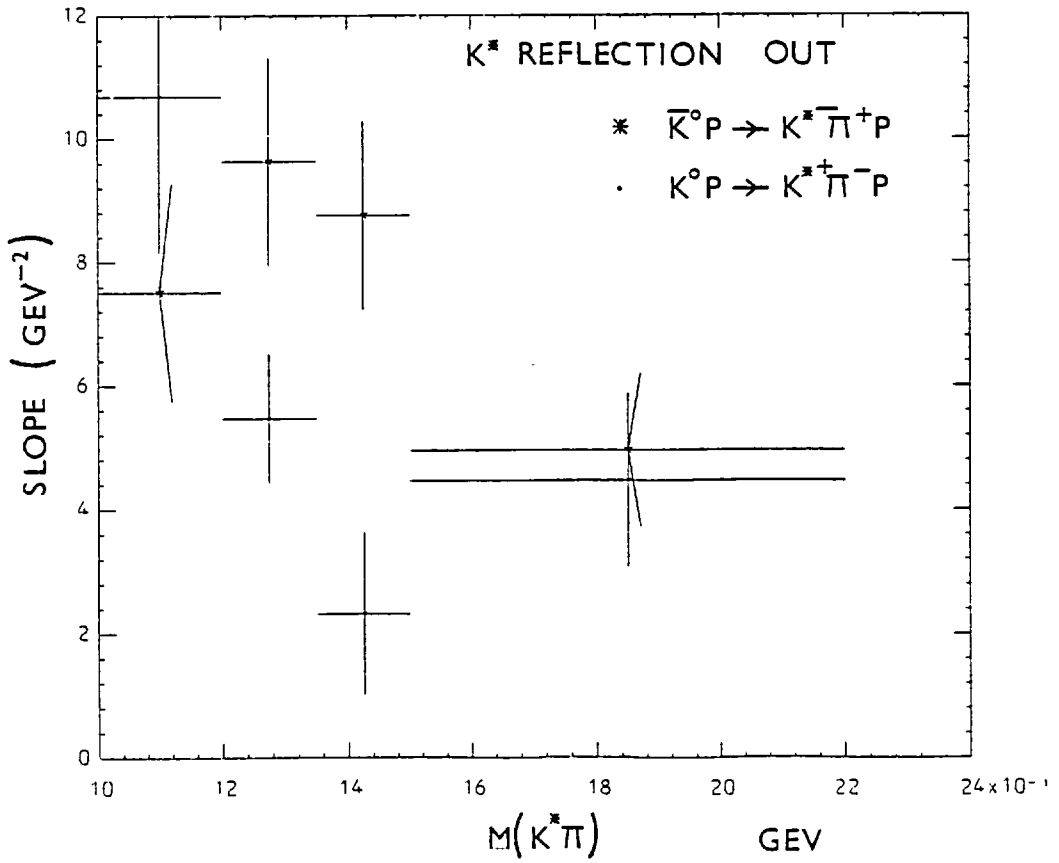
6.10



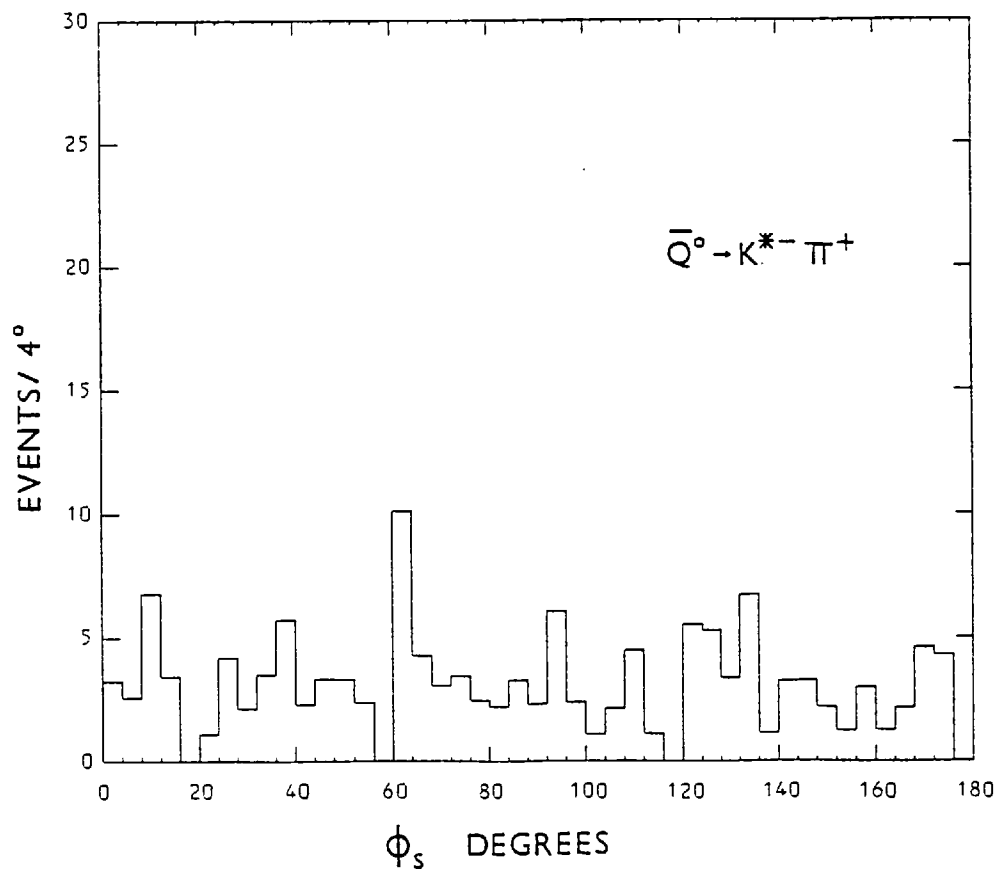
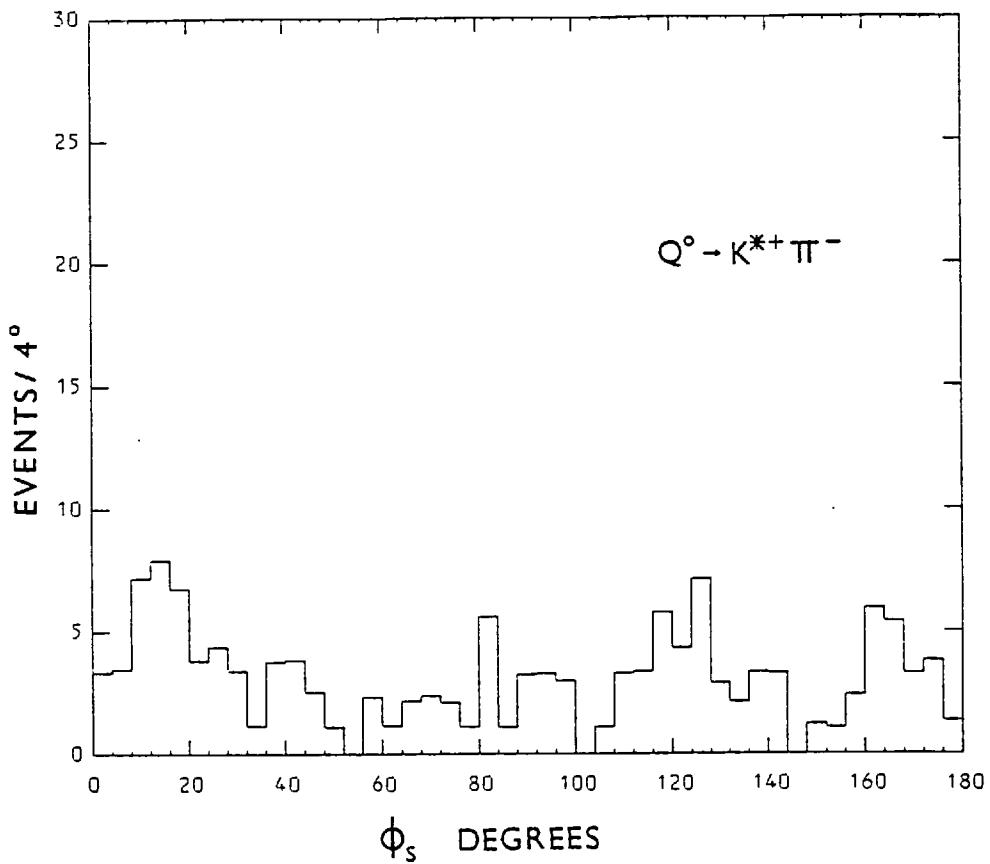
6.11



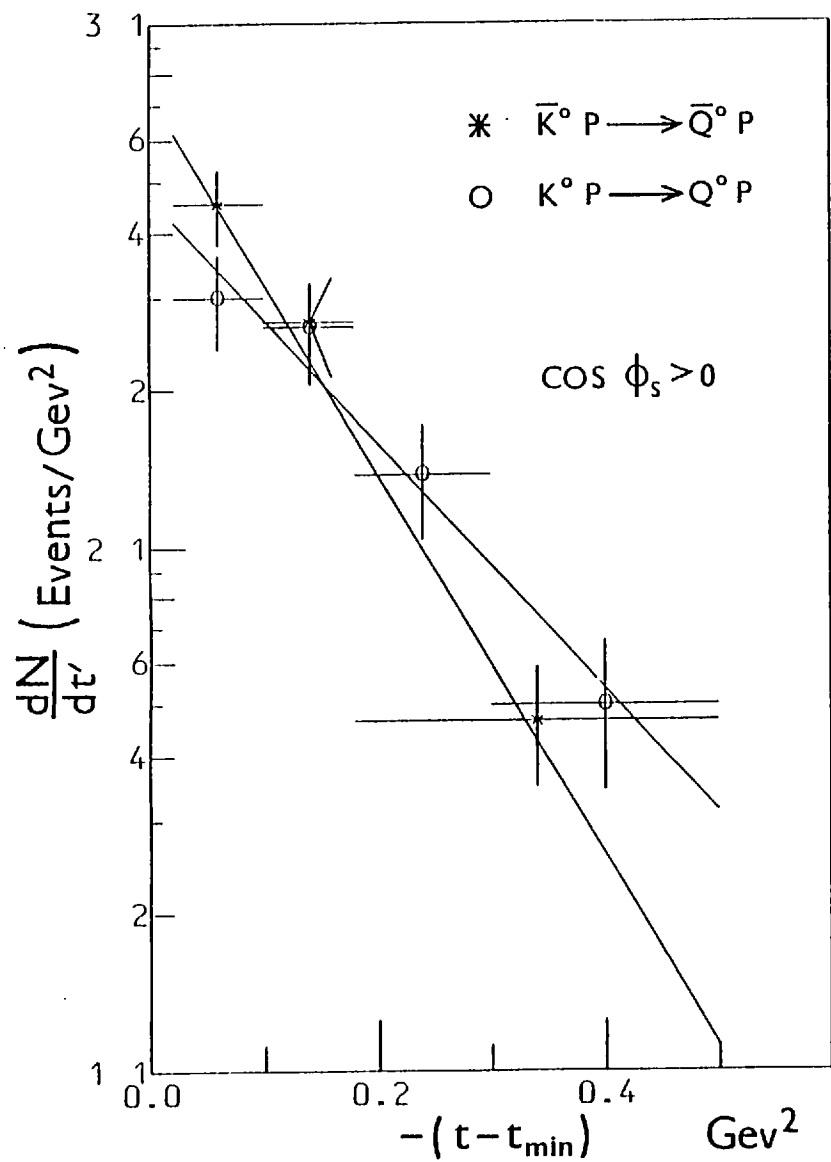
6.12



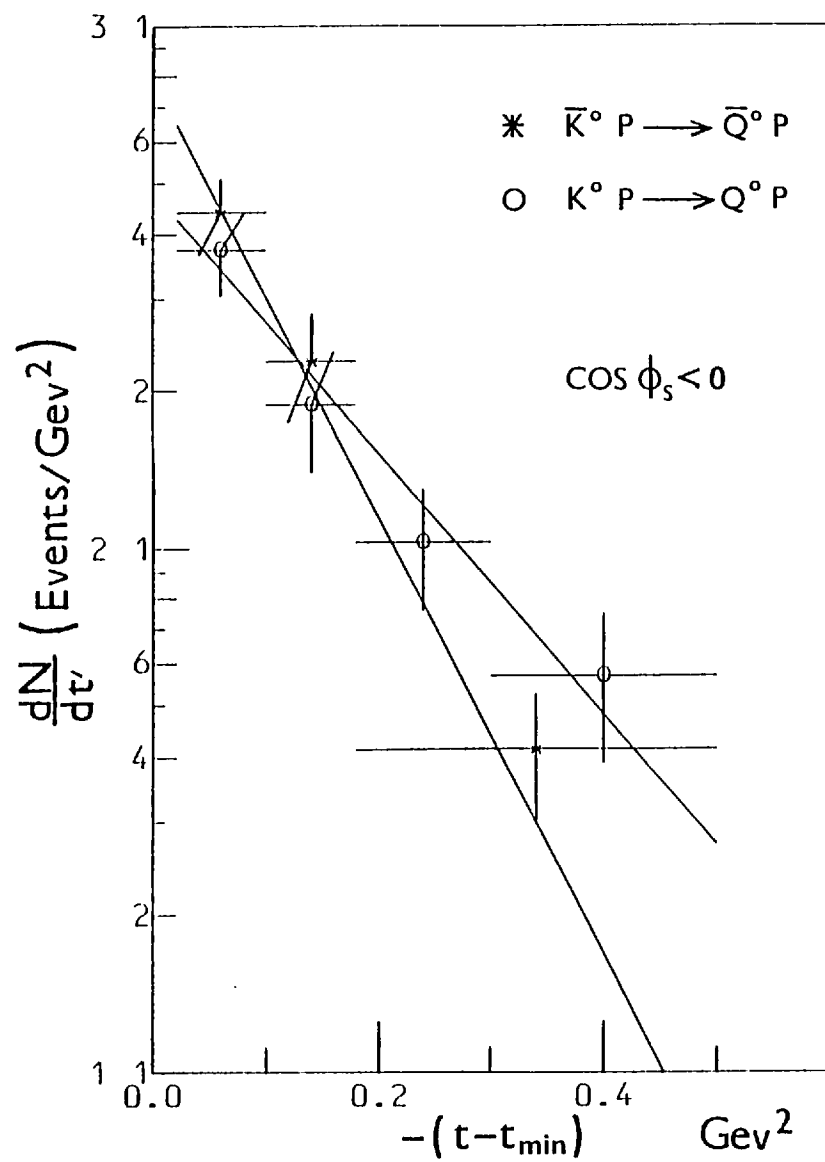
6.13



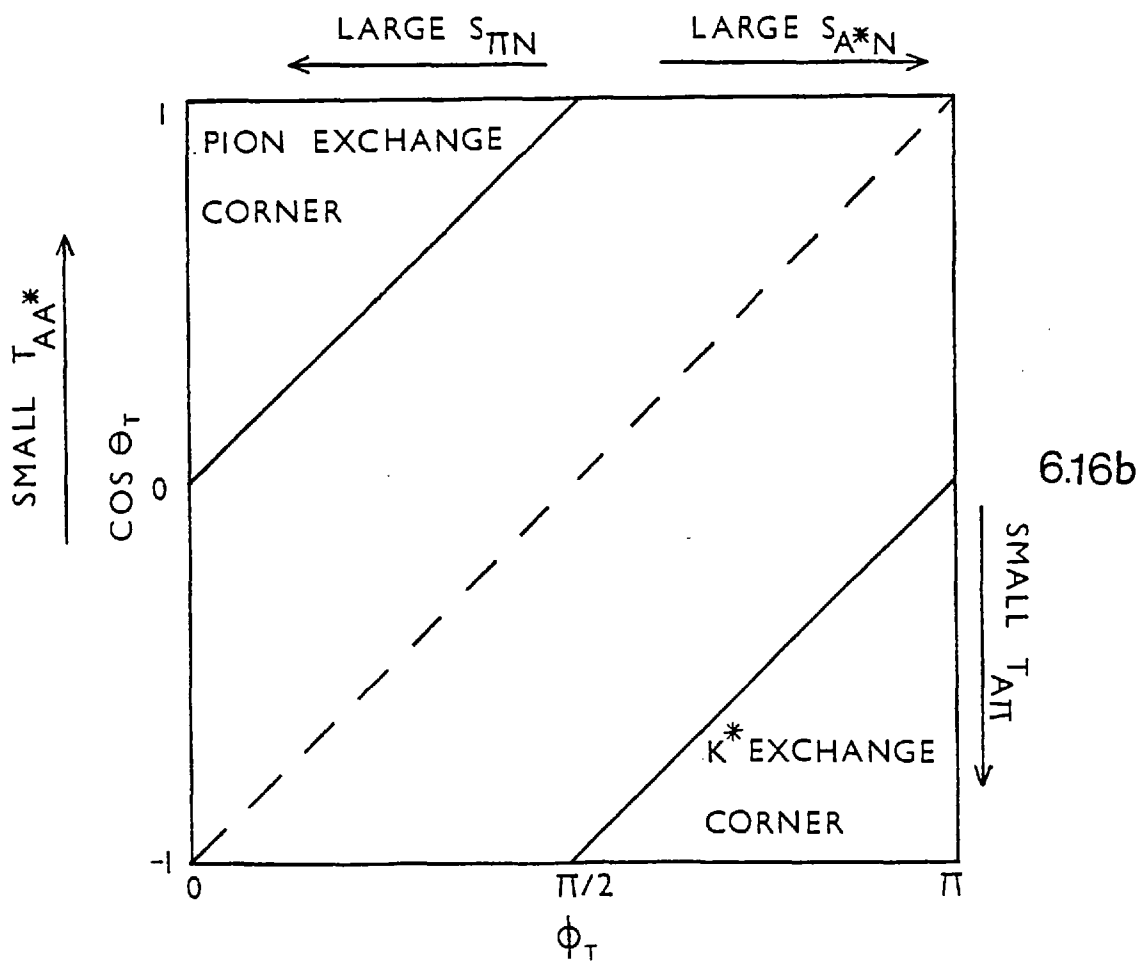
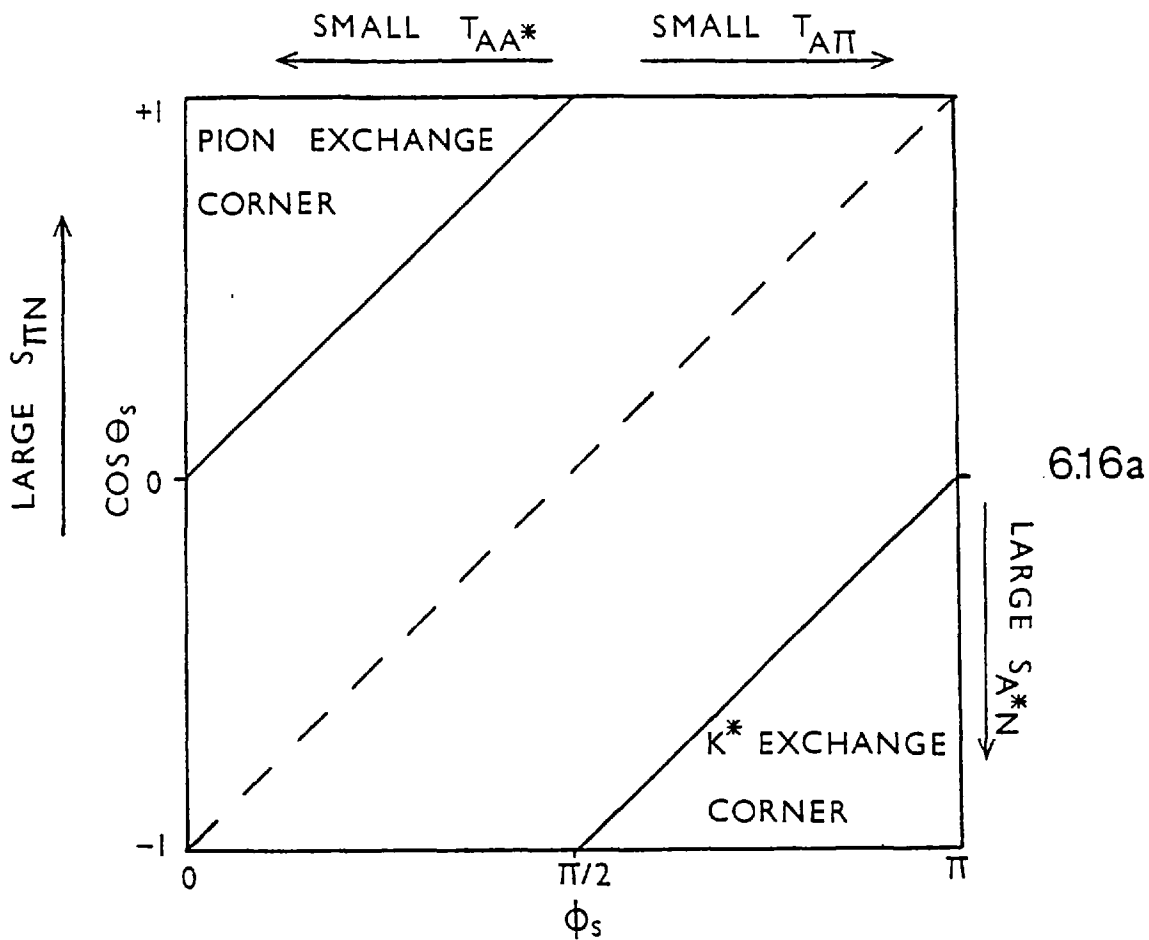
6.14

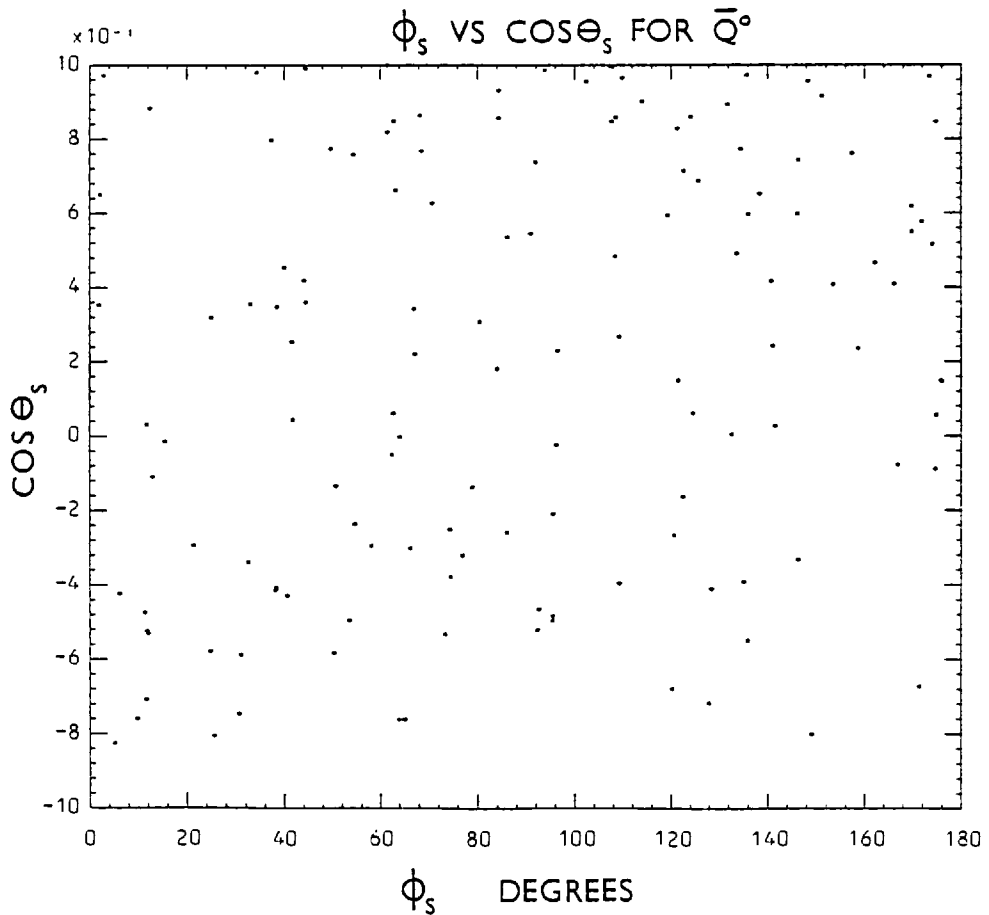
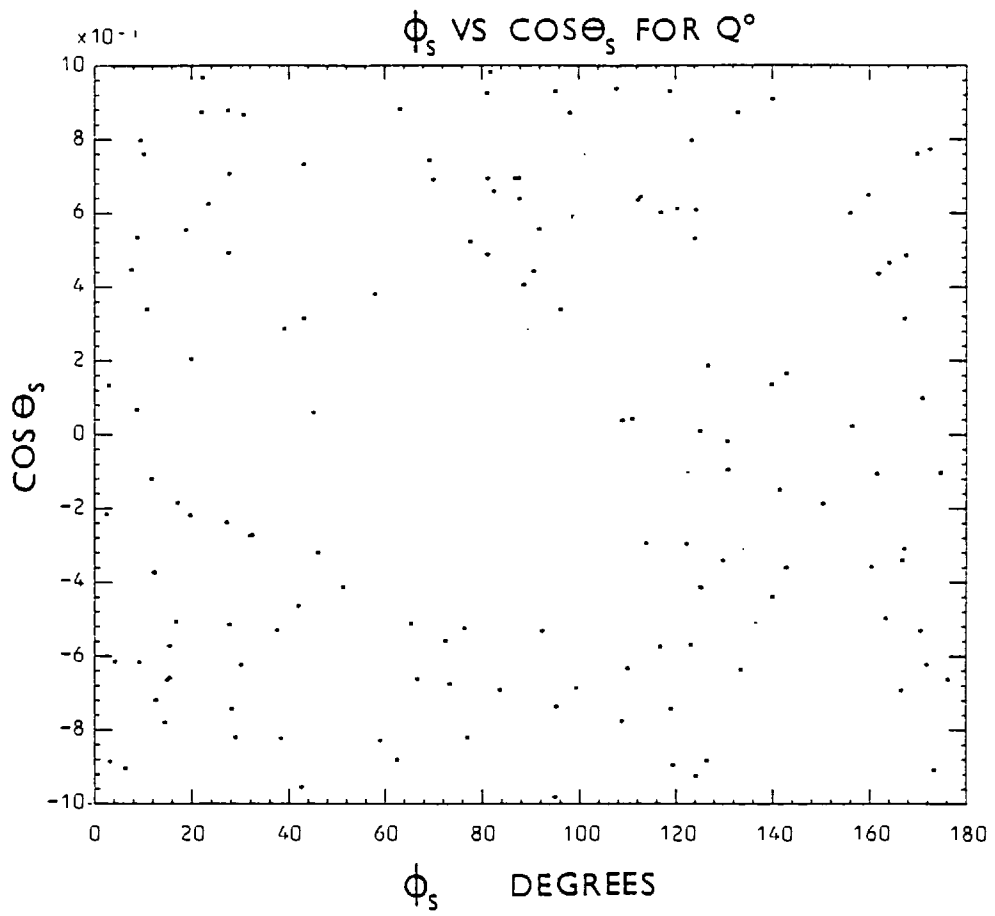


6.15



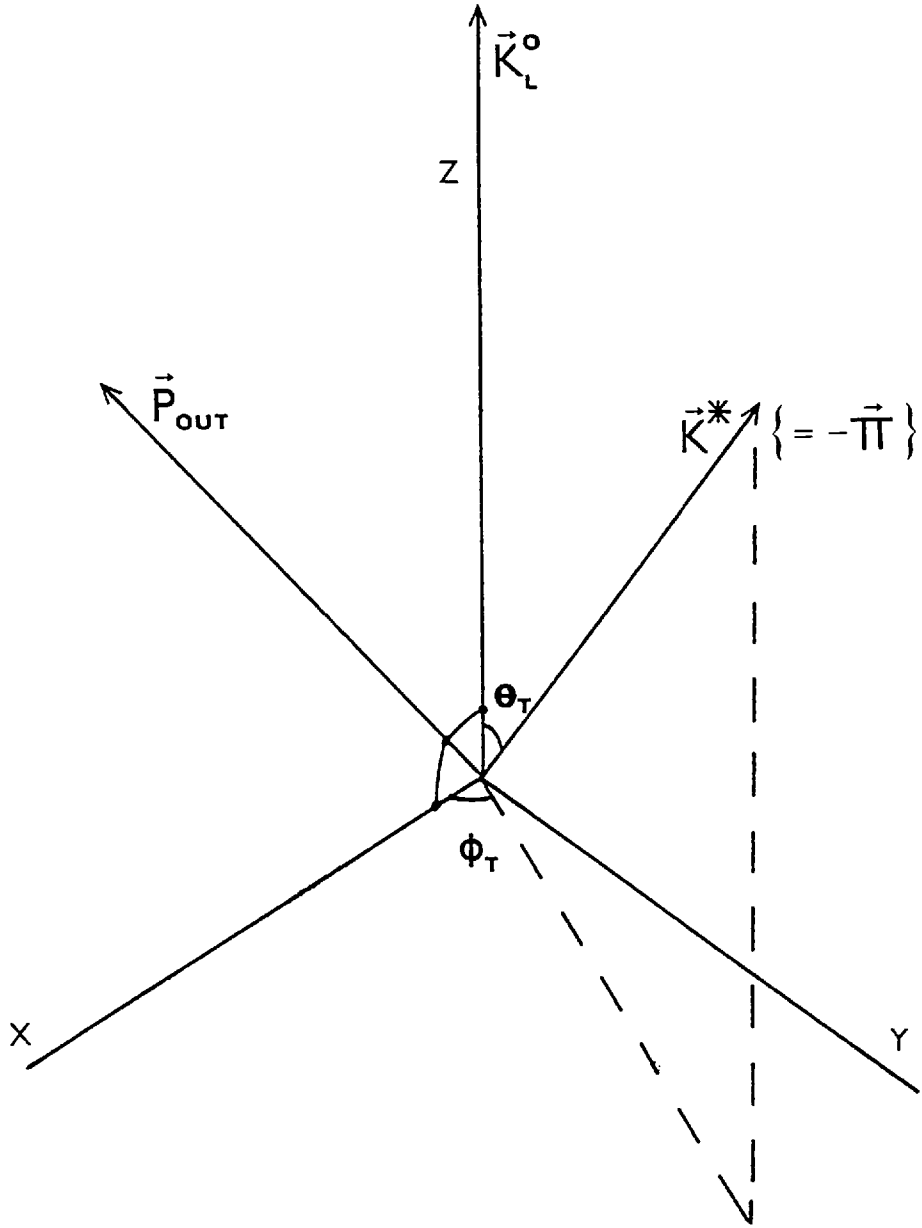
6.15



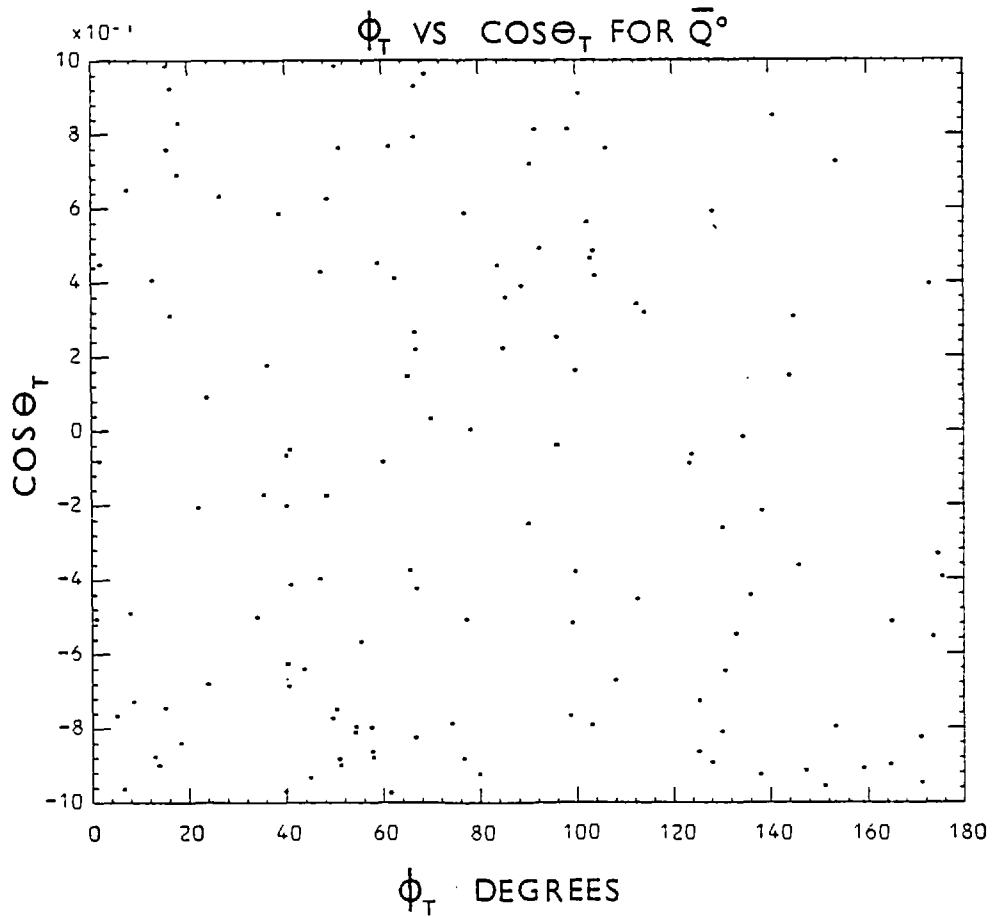
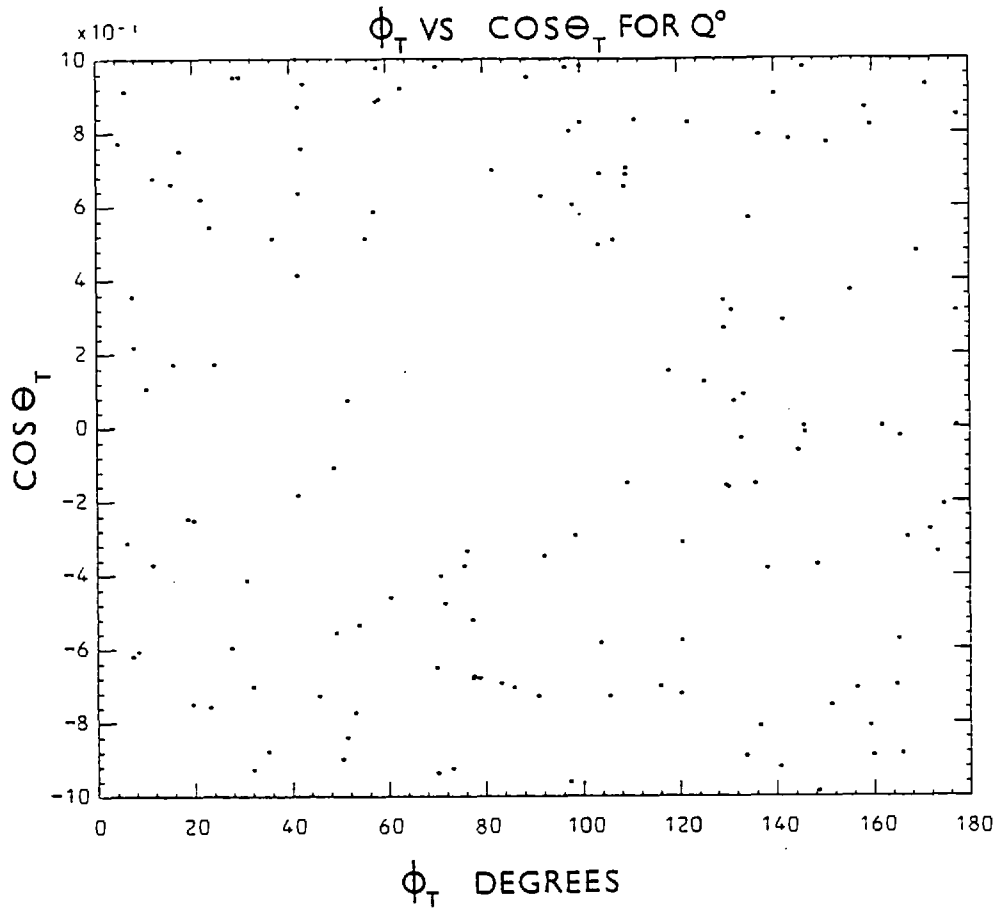


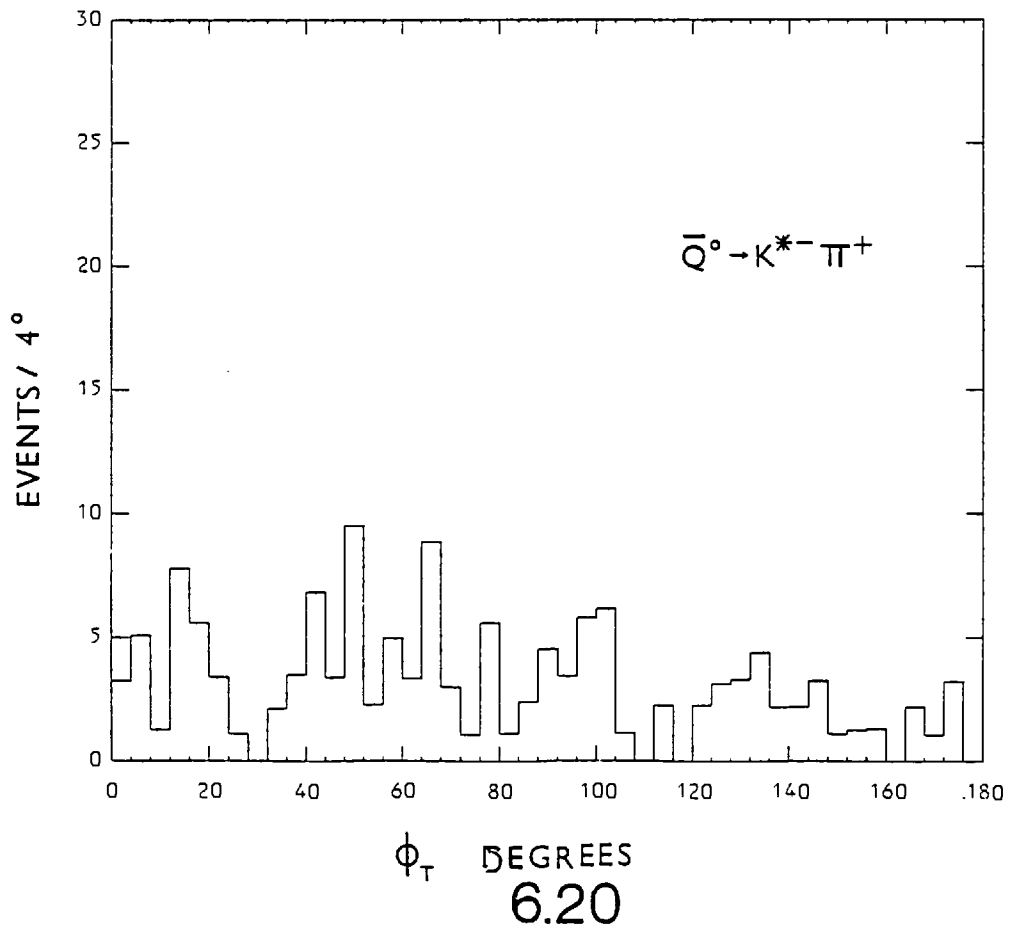
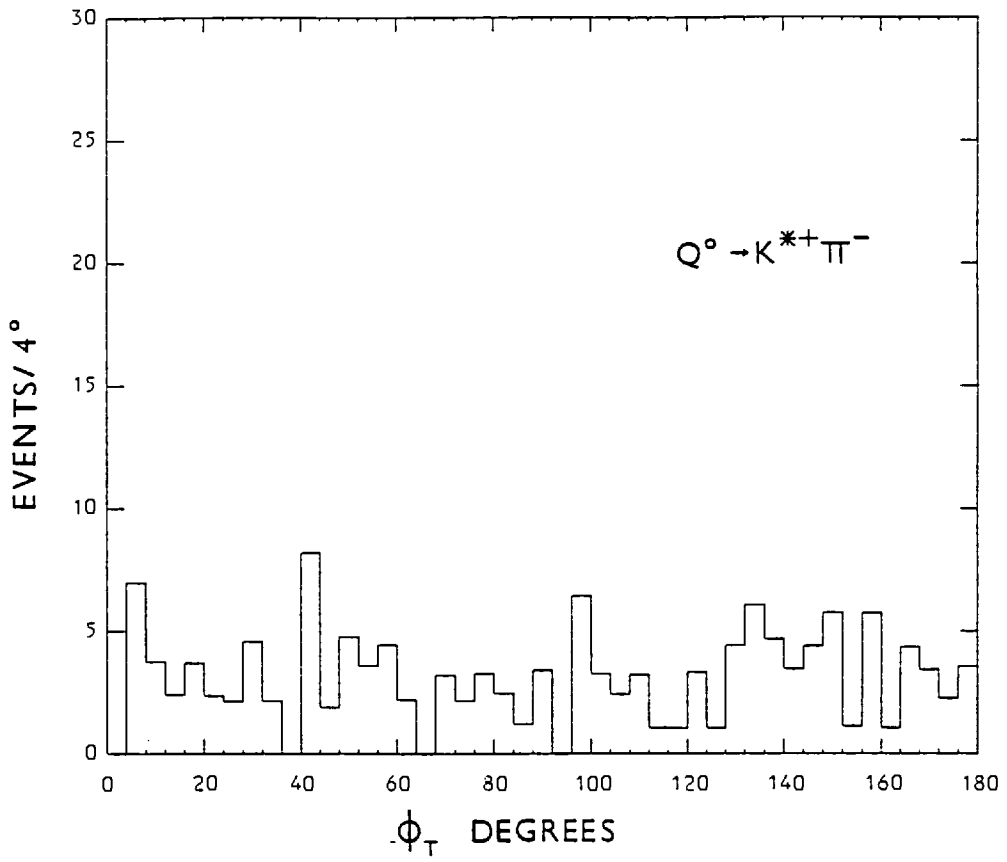
6.17

T-CHANNEL AXES

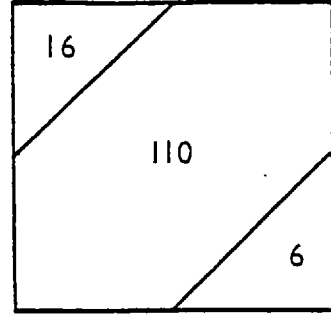
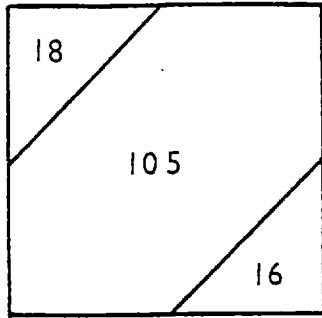


$$K_L^0 P \rightarrow K^* \pi P_{OUT}$$

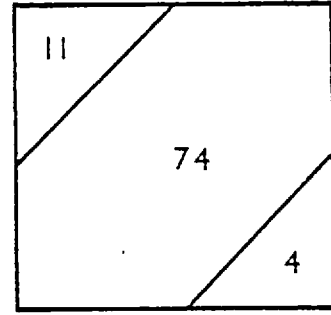
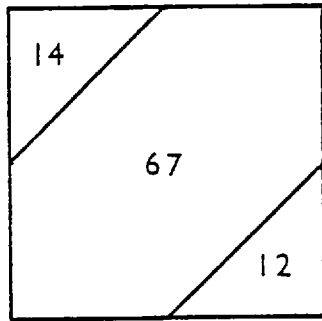




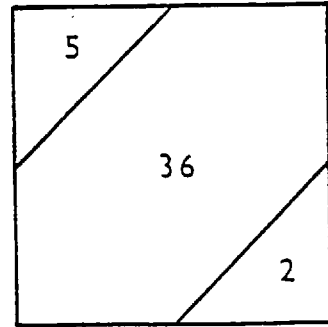
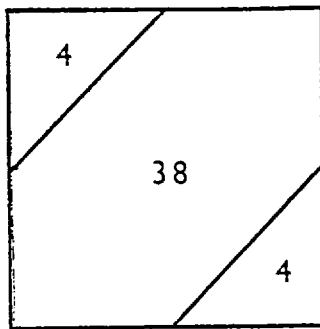
Q^0 TOTAL DATA \bar{Q}^0



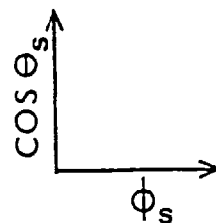
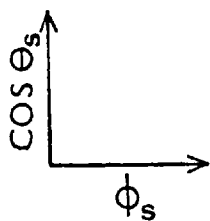
Q^0 $P_{K_L^0} < 10$ GEV/C \bar{Q}^0



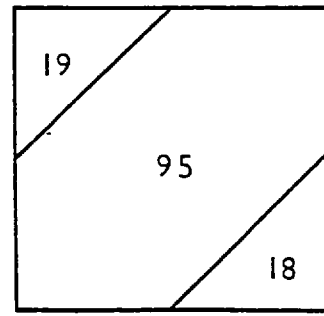
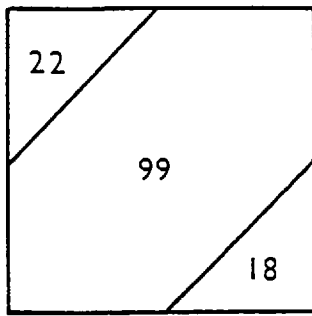
Q^0 $P_{K_L^0} > 10$ GEV/C \bar{Q}^0



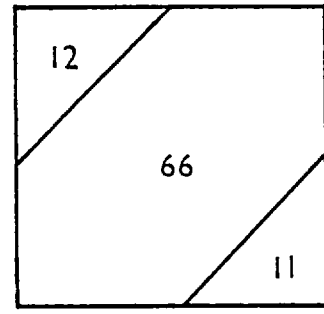
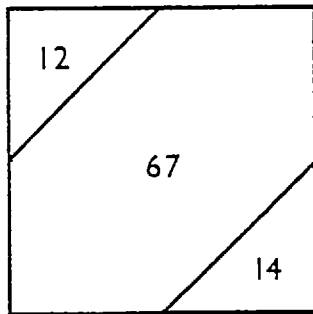
6.21



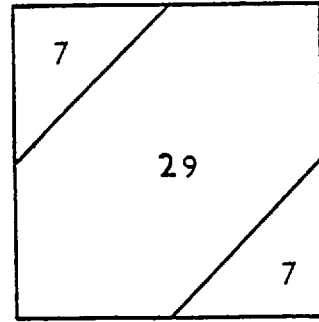
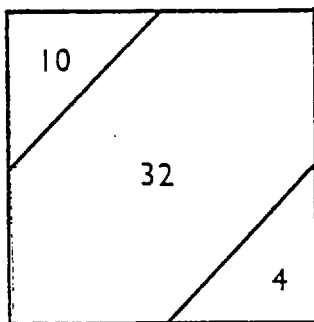
Q° TOTAL DATA \bar{Q}°



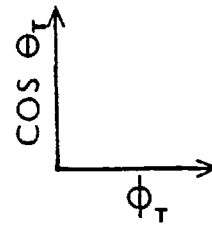
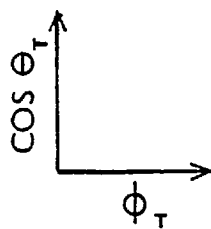
Q° $P_{K_L^{\circ}} < 10$ GEV/C \bar{Q}°



Q° $P_{K_L^{\circ}} > 10$ GEV/C \bar{Q}°



6.22



REFERENCES

Chapter 1

- 1 P.Bosetti et al., Nucl. Phys. B94, 21, (1975) and
J.V.Beapre et al., Nucl. Phys. B30, 381, (1971)
- 2 HYDRA GEOMETRY, CERN T.C. Program Library
- 3 GRIND KINEMATICS, CERN T.C. Program Library
- 4 Particle Properties Handbook; Review of Particle Properties.
Physics Letters, Vol. 75B, No.1 April (1978)
- 5 Methods in Subnuclear Physics (Herceg-Noví), M.Nikolić,
Vol.IV, 413, Part 3
- 6 M.Tyndel; private communication
- 7 R.J.Yamartino et al., Phys.Rev. D10, No.1, 9, (1974)
- 8 SLICE, CERN T.C. Program Library

Chapter 2

- 1 A.D.Brody et al., Phys. Rev. Lett. Vol.22, No.18, 966, (1969)
- 2 FOWL, CERN T.C. Program Library
- 3 Particle Data Group, Reviews of Modern Physics, Vol.48
No.2, Part 2, 66, (1976)
- 4 M.K.Gaillard, K_{ℓ_3} Form Factors, C.E.R.N. Yellow Report 70-14 (1970)
- 5 L.M.Chounet et al., Physics Reports 4C, 199, 252, (1972)
- 6 Particle Data Group, Reviews of Modern Physics, Vol.48
No.2, Part 2, 71, (1976)
- 7 MINUIT, CERN T.C. Program library
- 8 For example :- B.C.Erricker, Advanced General Statistics,
(The English Universities Press Ltd.,) Page 189.
- 9 G.W.Brandenburg et al., Phys. Rev. D7, No.3, 708, (1973)

Chapter 3

- 1 D.Luers et al., Phys. Rev. Vol.133 No.5B, B1276, (1964)
- 2 G.W.Brandenburg et al., Phys. Rev. D8 No.7, 1978, (1973)
- 3 FAKE, CERN T.C. Program library
- 4 Particle Data Group, Reviews of Modern Physics, Vol.48
No.2, Part 2, 77, (1976)

Chapters 4,5,6

- 1 G.W.Brandenburg et al., Nucl. Phys. B45, 397, (1972)
- 2 B.French, Mesons, CERN Report 75-38 (1975)
- 3 K.W.J.Barnham et al., Nucl. Phys. B25, 49, (1970)
- 4 I.Butterworth, Boson Resonances, Annual Review of Nuclear Science, Vol.19, 179, (1969)
- 5 R.J.Hemingway, Classical Mesons, C.E.R.N. report 75-38 (1977)
- 6 J.Hansen et al., Nucl. Phys. B81, 403, (1974)
- 7 M.Deutschmann et al., Phys. Lett. Vol.49B No.4, 388, (1974)
- 8 M.G.Bowler et al., Nucl. Phys. B74, 493, (1974)
- 9 G.Otter et al., Nucl. Phys. B93, 365, (1975)
- 10 U.Amaldi, M.Jacob, and G.Matthiae, Diffraction of Hadronic Waves, Annual Review of Nuclear Science, Vol.26, 82, (1976)
- 11 B.Conforto and G.Conforto, Rutherford Laboratory Report,
RL - 77 - D24/A
- 12 G.Otter et al., Nucl. Phys. B106, 77, (1976) and
Nucl. Phys. B96, 29, (1975)
- 13 G.W.Brandenburg et al., Phys.Rev. Lett. Vol.36, no.13, 703, (1976)

- 14 M.G.Bowler, Journal of Physics G, Vol.3, No.6, 775, (1977)
and R.K.Carnegie et al., S.L.A.C. - Pub. - 1767, (1976)
- 15 H.J.Lipkin, FERMILAB publication, 77/84, (1977)
- 16 D.W.G.S.Leith, S.L.A.C. - Pub. - 1980.
- 17 B.H.Bransden, D.Evans and J.V.Major, The Fundamental Particles,
(Van Nostrand, Rheinhold Company, 1973), page 181.
- 18 H.I.Miettinen, Diffractive Processes and the Triple-Pomeron,
C.E.R.N. report TH.2072.
- 19 G.Otter et al., Nucl. Phys. B.87, 1, (1975)
- 20 G.Goldhaber et al., Phys. Rev. Lett. Vol.19, No.17, 972, (1967)
- 21 G.Goldhaber, C.E.R.N. Yellow Report, 67-24, (1967)
- 22 W.S.C.Williams, An Introduction to Elementary Particles,
(Academic Press, 2nd edition, 1971), page 406.
- 23 D.W.G.S.Leith, Strong Interactions, Proceedings of Summer
Institute on Particle Physics, S.L.A.C. - 179, 132, (1974)
- 24 D.W.G.S.Leith, Diffraction Dissociation, Proceedings of XVI
International Conference on High Energy Physics, Vol.3, 321, (1972)
- 25 V.Barger and D.Cline, Phenomenological Theories of High Energy
Scattering, (W.A.Benjamin, Inc, 1969), page 29.
- 26 B.E.Y.Svensson, C.E.R.N. Yellow Report, 67-24 (1967)
- 27 E.H.S.Burhop, High Energy Physics, Vol. III (Academic Press, 1967),
page 139.
- 28 N.Schmitz, High Energy Reactions, D.E.S.Y. Report.
- 29 V.Barger and D.Cline, Phenomenological Theories of High Energy
Scattering, page 100.

- 30 E.L.Berger, Phys. Rev. 186, No.5, 1525, (1968) and 179, No.5, 1567,(1969)
- 31 E.L.Berger, A Critique of the Reggeized Deck Model, Proceedings of the Daresbury Study Weekend, DL/R34 No.8, 35, (1975)
- 32 E.L.Berger, Systematics of Cross-over effects in Inelastic Diffraction Dissociation, Argonne, ANL/HEP 7464 and Phys. Rev. D11 No.11, 3214,(1975)
- 33 I.Ambats et al., Phys. Rev. D9 No.5, 1179, (1974)
- 34 G.W.Brandenburg et al., Phys. Rev. Lett. Vol.28, No.14, 932. (1972)
- 35 G.L.Kane, Phenomenology of Diffractive Reactions, Acta Physica Polonica, Vol.B3, No.6, 845, (1972)
- 36 E.L.Berger, VI International Colloquium on Multiparticle Reactions at Oxford, RL - 75 - 143, 193, (1975)
- 37 P.Bosetti et al., Nucl. Phys. B103, 189, (1976)
- 38 G.Cohen-Tannoudji et al., Nucl. Phys. B95, 445, (1975)
- 39 W.T.Eadie, D.Drijard, F.E.James, M.Roos, Statistical Methods in Experimental Physics (North-Holland,1971), page 156.
- 40 J.Topping, Errors of Observation and Their Treatment, (Chapman and Hall Ltd.), page 20.
- 41 A.Stergiou et al., Nucl. Phys. B102, 1, (1976)
- 42 M.Davier and H.Harari, Phys. Lett. Vol.35B, No.3, 239, (1971) and H.Harari, Annals of Physics, 63, 432, (1971)
- 43 R.Barloutaud et al., Nucl. Phys. B59, 374, (1973)
- 44 P.J.Davis et al., Phys. Rev. D5, No.11, 2683, (1972) and H.Bingham et al., Nucl. Phys. B48, 591, (1972)
- 45 P.Pirilä and H.Miettinen, Phys. Lett. Vol.40B, No.1, 127, (1972)
- 46 G.Vassiliadis et al., Nucl. Phys. B103, 1, (1976)

ACKNOWLEDGEMENTS

First and foremost I would like to thank my supervisor Dr.T.C.Bacon for his guidance and counsel throughout the duration of my research in the department.

I also express my appreciation to Dr.M.E.Mermikides for his efforts in setting up the Data Reduction programs for the K_L^0 experiment, to Dr.B.Pollock for aid in the determination of the scanning efficiencies and to Dr.Y.Oren for advice and the use of some computer programs in the Data Analysis. I am indebted to the scanning and measuring staff in the H.E.N.P. department, particularly Pat Hurst, Christine Page and Margaret Urquhart for efficient management and book-keeping of the K_L^0 Bubble Chamber film and to Dr.P.Newham for assistance with the SMOG graphics system.

I would also like to thank Professor I.Butterworth for an opportunity to do research and I am grateful to the Science Research Council and my parents for financial support.